2018

# Mechanisms Of Decarboxylation In The CYP152 Family Of Cytochrome P450S

José Armando Amaya
*University of South Carolina*

# MECHANISMS OF DECARBOXYLATION IN THE CYP152 FAMILY OF CYTOCHROME P450S

by

José Armando Amaya

Bachelor of Science
Université Joseph Fourier, 2010

Master of Science
Université Joseph Fourier, 2012

---

Submitted in Partial Fulfillment of the Requirements

For the Degree of Doctor of Philosophy in

Chemistry

College of Arts and Sciences

University of South Carolina

2018

Accepted by:

Thomas Makris, Major Professor

Maksymilian Chruszcz, Committee Member

Qian Wang, Committee Member

Rekha Patel, Committee Member

Cheryl L. Addy, Vice Provost and Dean of the Graduate School

# DEDICATION

This achievement could not have been possible without the support of the many people in my life who are invaluable. To my beautiful wife Amada, who has been a continuous source of support during these past five years, even in the most difficult times. Her incredible passion and dedication to her work, as well as her values as a person have been a source of inspiration to me. To my parents, whose unconditional support and effort have made all my career choices possible. Their work ethic and principles have set an example of whom I want to be as a person. To both my sisters, who have shown me to always persist and never give up. Finally, to all my friends and family who have supported me during these times.

# ACKNOWLEDGEMENTS

First and foremost, I would like to thank my mentor Dr. Thomas Makris who has truly been a tremendous source of knowledge and enrichment during my time as a graduate student. Thank you for helping me grow as a scientist and thank you for all the times you put up with my crazy ideas, writing and loud music; I don't think I could have asked for a better mentor. I would also like to thank Jason Hsieh whose work was invaluable in all the projects I carried out. I would like to thank my lab family Job, Steve, Courtney and Olivia who always made the lab feel like a second home. Thank you for putting up with me, for your friendship and for all the advice you have given me. I would like to thank all the undergraduates who have worked in the lab, specially the ones I have mentored: Cooper, Nic, Julia and Aubrey; I don't think this thesis would have been possible without your help, you guys are truly the workforce behind all these projects. Finally, I would like to thank everyone else who has been involved in the projects I have worked, specially Dr. John Dawson, Dr. Maksymilian Chruszcz, Dr. James Sodetz, Dr. Mike Walla and Dr. William Cotham, whose input has been invaluable in my work.

# ABSTRACT

Intense interest has focused on the development of enzymes as next-generation catalysts for the production of molecules with biotechnological potential. $OleT_{JE}$, a member of the cytochrome P450 CYP152 family is an excellent candidate for the generation of advanced biofuels. $OleT_{JE}$ catalyzes the hydrogen peroxide-dependent decarboxylation of $C_n$ fatty acids to produce $C_{n-1}$ terminal alkenes. Despite the ability of this enzyme to yield long chain alkenes with nearly exclusive chemoselectivity, its reactivity towards shorter chain length substrates results in undesired levels of hydroxylated side-products, limiting its industrial potential. Previous transient kinetic studies have demonstrated that, despite its unusual chemistry, the reaction is initiated by canonical substrate hydrogen-atom abstraction by an iron(IV)-oxo intermediate (compound I) followed by the formation of a hyperstable iron(IV)-hydroxide species (compound II). The origin of chemoselectivity in $OleT_{JE}$, and CYP152s in general, has been probed by a coordinated study of several CYP152 family members, including $OleT_{JE}$, P450-BSβ, CYP-MP, and the newly characterized $OleT_{SA}$. Spectroscopically labeled substrates, in concert with UV-Vis spectroscopy, EPR spectroscopy and transient kinetic studies show that substrate constriction is necessary for alkene production, but compromises the rate of product egress. Moreover, alteration of the environment surrounding the axial thiolate ligand in $OleT_{SA}$ via mutagenesis has allowed the establishment of a platform to extend research towards the electronic characterization of the catalytically relevant intermediates, compound I and compound II.

TABLE OF CONTENTS

# LIST OF TABLES

# LIST OF FIGURES

# CHAPTER 1

## MIXED REGIOSPECIFICITY COMPROMISES ALKENE SYNTHESIS BY A CYTOCHROME P450 PEROXYGENASE FROM METHYLOBACTERIUM POPULI[‡]


**Abstract**

Intensive interest has focused on enzymes that are capable of synthesizing hydrocarbons, alkenes and alkanes, for sustainable fuel production. A recently described cytochrome P450 (OleT-JE) from the CYP152 family catalyzes an unusual carbon-carbon scission reaction, transforming $C_n$ fatty acids to $C_{n-1}$ 1-alkenes. Here, we show that a second CYP152, CYP-MP from *Methylobacterium populi* ATCC BAA 705, also catalyzes oxidative substrate decarboxylation. Alkene production is accompanied with the production of fatty alcohol products, underscoring the mechanistic similarity of the decarboxylation reaction with canonical P450 monooxygenation chemistry. The branchpoint of these two chemistries, and regiospecificity of oxidation products, is strongly chain length dependent, suggesting an importance of substrate coordination for regulating alkene production.


---


[‡]Amaya, J. A.; Rutland, C. D.; Makris, T. M., Mixed regiospecificity compromises alkene synthesis by a cytochrome P450 peroxygenase from *Methylobacterium populi*. *J Inorg Biochem* **2016,** *158*, 11-6.

Reprinted here with permission of publisher.

## 1. Introduction

Widespread biotechnological interest has focused on the identification [1-4] and reconstitution of enzymes capable of synthesizing gaseous [5-6] or liquid hydrocarbon fuels in microbial hosts [5, 7-9]. A recently discovered cytochrome P450 isolated from *Jeotgalicoccus* sp. ATCC 8456, termed OleT-JE [2] (or CYP152L1) [10], catalyzes the hydrogen peroxide dependent cleavage of $C_n$ fatty acids for the synthesis of $C_{n-1}$ alkenes and a carbon dioxide co-product [11]. The OleT-JE reaction converts a biologically abundant feedstock into a hydrocarbon (and useful commodity chemical for organic synthesis) in a one-step reaction that consumes an inexpensive co-substrate. Given its tremendous potential for advanced biofuel production, a number of recent efforts have focused on the optimization of OleT-JE catalysis. These include the development of alternative photo- [12] and bio- [13-14] catalytic turnover methods to maximize alkene production *in vitro*, thereby potentially bypassing the requirement for $H_2O_2$, which may prove to be more difficult to leverage in a microbial platform.

The oxidative decarboxylation reaction catalyzed by OleT-JE is highly atypical, although not unprecedented [15-16], for P450s, which typically catalyze the monooxygenation of substrates (reviewed in [17-18]). Primary sequence analysis places OleT-JE as a member of the CYP152 family, which includes the fatty acid hydroxylases P450 SPα [19-22], P450 BSβ [23] and P450 CLA [24]. The structure of OleT-JE, solved by the Munro and Leys groups, has confirmed a high degree of structural similarity of the OleT-JE active-site [10] with BSβ[23] and SPα [25], including direct interaction of the fatty acid carboxylate necessary for the efficient utilization of $H_2O_2$ with an active site arginine (Arg245 in OleT-JE). A large steady-state substrate $^2H$ kinetic isotope effect (KIE) [26] for SPα and BSβ hydroxylations

indicates that the peroxygenase reaction proceeds by substrate C-H bond abstraction by a high-valent iron(IV)-oxo π cation radical Compound I intermediate [27]. Ensuing oxygen rebound [28-29] results in a distribution of α and β mono-hydroxylated products.

In recent work by our laboratory [11], we evaluated the mechanism of the OleT-JE alkene forming reaction with an eicosanoic ($C_{20}$) fatty acid substrate, a chain length which is presumed to approximate the native substrate of OleT-JE based on identification of 18-methyl-nonadecene as the predominant alkene found in *Jeotgalicoccus* [2]. Substrate and $H_2O_2$ labeling studies confirmed that alkene formation is accompanied with the formation of a carbon dioxide co-product that derives from the fatty acid terminal carboxylate. Significantly, no oxygen insertion was observed in the $CO_2$ co-product, hinting at a clear mechanistic deviation of alkene forming and P450 monooxygenation chemistries. Further evaluation of the OleT-JE reaction by single-turnover stopped flow kinetics, however, strongly links the two mechanisms [11]. Rapid mixing of per-deuterated $C_{20}$ fatty acid bound with $H_2O_2$ resulted in the direct observation of a catalytically competent Compound I species [27, 30-31] on route to alkene formation. These species did not significantly accumulate in parallel reactions with protiated substrate, suggesting that alkene formation also proceeds by substrate hydrogen atom abstraction. Taken together, the mechanisms for P450 aliphatic hydroxylations, and the initial steps for OleT-JE oxidative decarboxylation, provides evidence for branching following an initial C-H bond abstraction event, as depicted in Figure 1.1. This scheme is additionally supported by altered product profiles observed for OleT-JE in reactions with shorter fatty acid substrates. Although OleT-JE predominantly generates 1-nonadecene in single [11] and multiple turnover [2, 13] reactions with

eicosanoic acid ($C_{20}$), the metabolism of shorter chain length substrates often results in an increased production of hydroxylated fatty acid side products [13, 32].

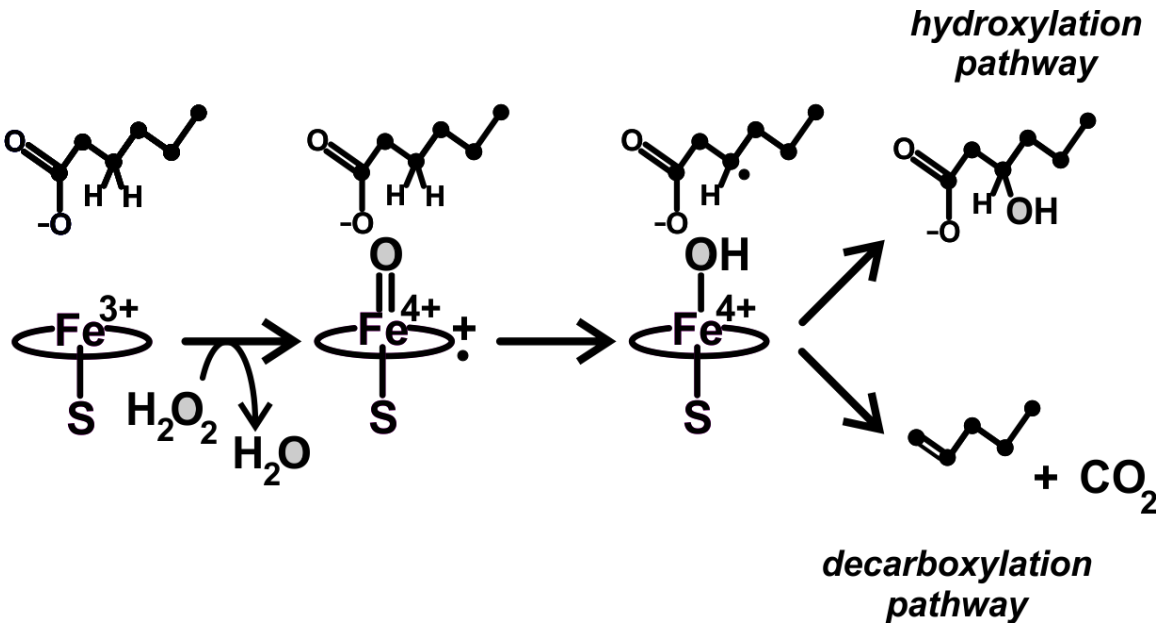


**Figure 1.1** Proposed mechanistic branching for fatty acid hydroxylation and decarboxylation catalyzed by OleT-JE[11]

Important questions remain regarding the relative importance of electronic and active-site structural contributions on the hydroxylation/decarboxylation branchpoint in OleT-JE, which would potentially aid in leveraging its catalysis further. This has prompted us to reexamine the efficiency of alkene production by CYP152 orthologs. While OleT-JE is the founding member for P450 fatty acid decarboxylases, work by Rude et al.[2] previously demonstrated that other CYP152 enzymes may also have the capacity to produce alkenes [2]. Among a series of CYP152 enzymes tested towards palmitic acid ($C_{16}$) decarboxylation in that study, a P450 from *Methylobacterium populi* ATCC BAA 705 (accession number ZP_02200540), which we denote hereafter as CYP-MP, was found to produce

pentadecene. The reported high chemoselectivity of CYP-MP towards palmitic acid decarboxylation, and low sequence identity of CYP-MP to OleT-JE (31%), including significant differences in active-site, made it an attractive system to begin to evaluate structural contributions on alkene formation. Here, we have cloned, overexpressed, and characterized CYP-MP reactivity towards a panel of fatty acid chain length substrates. Analytical experiments provide evidence for low alkene yields, and a large distribution of hydroxylation products that surprisingly extends beyond the fatty acid Cβ position. Product yield, efficiency of alkene formation, and the regioselectivity of products show significant chain length dependence. We have additionally examined the proposed role of an active-site histidine in OleT-JE, thought to be important for alkene production, through its introduction into CYP-MP.

## 2. Experimental procedures

### 2.1 Reagents

Ni-NTA and Butyl Sepharose resins were obtained from Qiagen and GE Healthcare respectively. An *E. coli* codon optimized gene of Mpop_1292, the orf encoding CYP-MP from *Methylobacterium populi* (ATCC BAA-705) was synthesized by DNA 2.0 (Menlo Park, CA). The original construct contained a C-terminal TEV cleavage site followed by a $His_6$ tag. Fatty acids and N,O-Bis (trimethylsilyl) trifluoroacetamide (BSTFA) were purchased from the Supelco Analytical branch of Sigma Aldrich. Hydrogen peroxide was obtained from Sigma Aldrich. The pDB-HisGST and pMHTDelta238 (expressing tobacco

etch virus (TEV) protease [33]) plasmids were obtained from the DNASU plasmid repository. Expression and purification of TEV followed described protocols.[33]

### 2.2 Subcloning, heterologous expression and purification of Mpop_1292

The original CYP-MP expression plasmid was digested using NdeI and XhoI, excising the Mp_1292 gene, and ligated into a similarly digested pDB-HisGST. Cloning was verified by sequencing at ACGT Inc. Heterologous expression was performed in *E. coli* BL21 (DE3) cells using modified Terrific broth (consisting of 12 g yeast extract, 6 g tryptone and 1 g bactopeptone, 125 mg thiamine, trace metals and 50 mg kanamycin per liter of culture). Cells were grown at 37 °C at 220 rpm, and the temperature was reduced to 20 °C at $OD_{600}$ ~ 0.4 and supplemented with 10 mg/L delta aminolevulinic acid. At an $OD_{600}$ ~ 1, cultures were induced with 0.1 mM IPTG. Cells were harvested after 24 hours, centrifuged and stored at -80 °C. Preliminary expression trials indicated that the P450 was exclusively localized in the membrane fraction. As a result, the pellet was resuspended in lysis buffer containing detergent (50 mM potassium phosphate (KPi) pH 8, 10 mM imidazole, and 0.1 M NaCl, containing 0.8% w/v cholate, 1 mM PMSF and 15 % (v/v) glycerol) (buffer A), and stirred for 2 hours at 4 °C. Cells were disrupted using a Branson sonifier and allowed to stir for an additional hour. Following centrifugation for 45 minutes at 17,000 g, the supernatant was loaded onto a Ni-NTA column, washed with 10 column volumes of buffer A containing 30 mM imidazole, and eluted with buffer A with 250 mM imidazole. Cleavage of the N-terminal GST tag was performed by addition of 1 mg of TEV protease per 25 mg of P450 and proteolysis was allowed to proceed for 16 hours at 4 °C. Ammonium sulfate was subsequently added to 25 % saturation and the protein was loaded onto a butyl sepharose column equilibrated in 50 mM KPi pH 8, 0.1 M NaCl, 25 % ammonium sulfate,

and 15 % glycerol (buffer B). The column was washed with 5 column volumes of buffer B and eluted with 50 mM KPi pH 8, 0.4 % cholate and 15 % glycerol. SDS-PAGE confirmed that the GST leader had been completely removed and that the protein was highly homogeneous. The final yield of purified P450 was roughly 40 mg per liter of culture.

### 2.3 Spectroscopy

Optical spectroscopy was performed on an Agilent 8453 spectrophotometer. An extinction coefficient of CYP-MP ($\varepsilon$ = 104 $mM^{-1}$ $cm^{-1}$ at 422 nm) was determined using the pyridine hemochromagen method [34]. The ferrous carbonmonoxy P450 adducts were prepared by the addition of carbon monoxide gas to a solution of ferric P450, and subsequent reduction of the protein with sodium dithionite. EPR spectra were recorded using an X-band Bruker EMXplus spectrometer equipped with an Oxford Instruments ESR900 liquid helium continuous flow cryostat. Spectra were recorded at a temperature of 20 K, a 1 mT modulation amplitude, and 1 mW microwave power. The concentration of protein was 200 µM.

### 2.4 Site Directed Mutagenesis

Site directed mutagenesis of the Met96His CYP-MP variant was performed using the following primer and its reverse complement:

5’ GATCATGGTTCTGTGCATGTTCTGGATGGTGCC 3’

Mutation was confirmed by gene sequencing at EtonBio Inc.

### 2.5 Optimizing turnover yields in OleT-JE

OleT-JE was expressed, purified, and adventitiously bound *E. coli* derived fatty acids were removed as described [11]. The effect of the rate of hydrogen peroxide addition on turnover efficiency was analyzed by mixing 2 mL of 5 mM hydrogen peroxide to a 2 mL reaction containing 200 mM KPi pH 7.5, 5 µM OleT-JE and 500 µM eicosanoic acid (prepared as a 10 mM stock solution in DMSO). $H_2O_2$ was added either by fast addition or by calibrated delivery over the course of 30, 60 or 120 minutes using a New Era NE-1000 syringe pump. The reactions were quenched with 6 M HCl after 2 total hours (including addition time) and products were analyzed on gas chromatography as described in more detail below.

### 2.6 CYP-MP Activity Assays

Hydrogen peroxide (2 mL, 5 mM) was slowly added over the course of one hour to a 2 mL reaction containing 200 mM KPi pH 7.5, 5 µM CYP-MP and 500 µM fatty acid (prepared as a 10 mM stock in DMSO) using a New Era NE-1000 syringe pump. Products were extracted by adding an equal volume of chloroform to the resulting reaction mixture. In order to account for differential response factors of alkenes, fatty acids and OH-fatty acids for accurate product quantitation, two internal standards (500 nmoles of each) were added upon reaction completion. These consisted of 1-hexadecene throughout and a fatty acid two carbons shorter than the substrate. Following extraction, the organic phase was derivatized by adding 250 molar equivalents of BSTFA (to initial substrate concentration) and incubated for 20 minutes at 60 °C. The derivatization mixture was dried using a stream of $N_2$ and re-dissolved in 100 µL $CHCl_3$. For gas chromatography (GC), 3 µL was analyzed on an Hewlett-Packard 5890 gas chromatograph using an HP-5 column with the following

oven conditions: 170 °C for 3 minutes, a 10 °C/min to 220 °C, a 5 °C/min to 320 °C, and 320 °C for 3 minutes. The response factors between fatty acids, hydroxy fatty acids and alkenes were determined by analyzing known authentic fatty acids (C20-C10), 2-hydroxyhexadecanoic acid and 1-hexadecene standards.

### 2.7 GC Mass-Spectrometry (GC-MS)

Gas chromatography mass spectrometry (GC-MS) was performed at the University of South Carolina Mass Spectrometry facility with a Hewlett Packard HP5890 GC and a 30-meter Rbx-5 column. Mass spectra were recorded on a Waters VG 705 magnetic sector mass spectrometer using 70 eV electron impact energy.

## 3. Results

### 3.1 Heterologous expression and membrane localization of CYP-MP

A C-terminal hexahistidine tagged CYP-MP synthetic gene, with a T5 promoter, showed poor expression in *E. coli* BL21(DE3), which did not improve upon alteration with a T7 promoter. In order to maximize expression, a TEV cleavable Glutathione-S-Transferase (GST) solubility tag was introduced at the N-terminus of CYP-MP by sub-cloning into the pDB-HisGST vector. Expression trials indicated a high level of protein production, and that the fusion was contained in the membrane fraction. In order to confirm subcellular localization, a membrane fraction was prepared by isolating spheroplasts, which were shown to contain at least 90 % of CYP-MP (Figure 1.2).

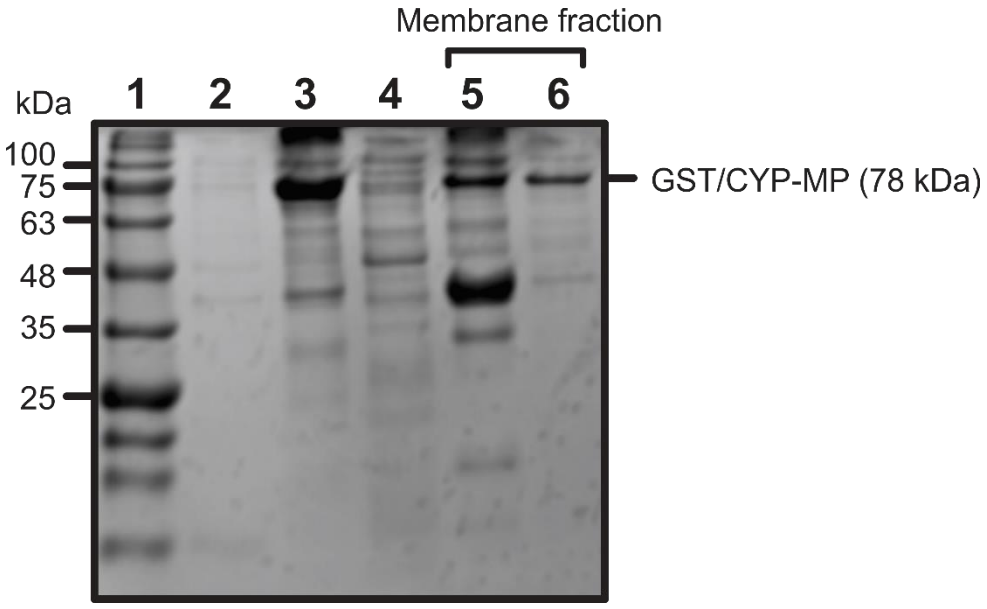


**Figure 1.2** SDS PAGE showing the membrane localization of GST tagged CYP-MP. Molecular weight markers in kDa shown to the left (lane 1); soluble fraction after lysozyme treatment (lane 2); spheroplasts (lane 3); soluble fraction after sonication of spheroplasts (lane 4); insoluble fraction after sodium cholate treatment (lane 5); soluble fraction after sodium cholate treatment.

Treatment of spheroplasts with detergent (0.8 % sodium cholate) led to efficient solubilization of the fusion protein, which could be subsequently purified by affinity chromatography in the presence of detergent. The GST tag was cleaved as described in Methods, and CYP-MP was purified from the GST fragment using hydrophobic interaction chromatography (Figure 1.3). Native, untagged CYP-MP, which has a high predicted pI (~9.6), was found to require the presence of detergent in order to remain in a soluble, non-aggregated form. This feature suggests that the membrane localization of the full-length construct is likely not attributable to the presence of the N-terminal GST, but is rather a general feature of CYP-MP.

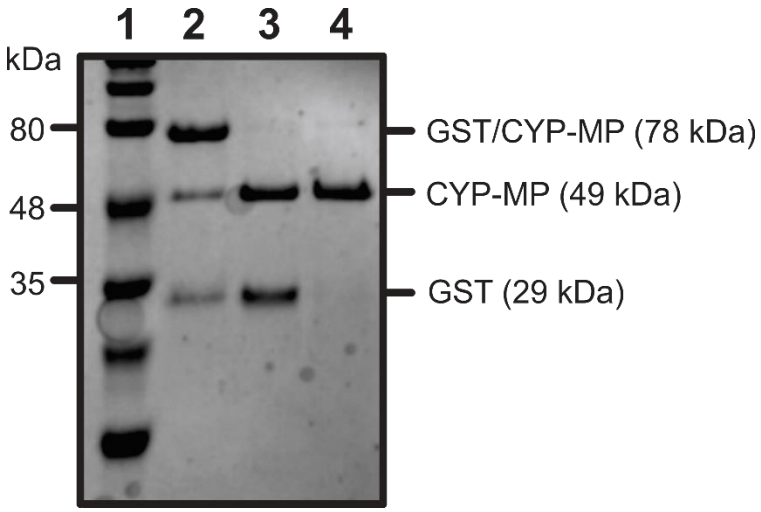


**Figure 1.3** SDS PAGE showing TEV cleavage and purification of CYP-MP. Molecular weight markers in kDa shown to the left (lane 1); GST/CYP-MP as purified from affinity Ni-NTA (lane 2); GST/CYP-MP after TEV cleavage (lane 3); purified CYP-MP after hydrophobic interaction chromatography (lane 4).

### 3.2 Spectroscopic characterization of CYP-MP

The optical spectrum of untagged, cholate solubilized CYP-MP at pH 8.0 is shown in Figure 1.4A and the inset. The purified ferric form of CYP-MP (solid line) has a perturbed red shifted Soret maximum at 422 nm, versus 417 nm that is typical for low-spin (LS) water bound P450s, a prominent α band at 545 nm and a significantly weaker β band at 575 nm. Significant hyper-porphyrin characteristics [35] are also visible at ~360 nm. These spectroscopic features are indicative of an altered coordination environment in CYP-MP, possibly deriving from binding of an alternative axial ligand [36] [37], or protonation of the proximal thiolate to the inactive neutral thiol form [38]. The latter possibility is ruled out through examination of the optical spectrum of the ferrous carbonmonoxy-bound form of CYP-MP (Figure 1.4A, dashed line), which displays the characteristic spectrum ($\lambda_{max}$ ~ 448 nm) for thiolate ligated $Fe^{2+}$-CO complexes. Only minor contributions (<15 %) from

the catalytically inactive 'P420' form is observed. Addition of excess fatty acid ($C_{12}$ to $C_{18}$ chain lengths) to the ferric enzyme resulted in no detectable optical spectroscopic changes (Figure 1.4B), such as the low to high spin-state conversion that is readily observed in OleT-JE and other P450s upon substrate binding [10-11].

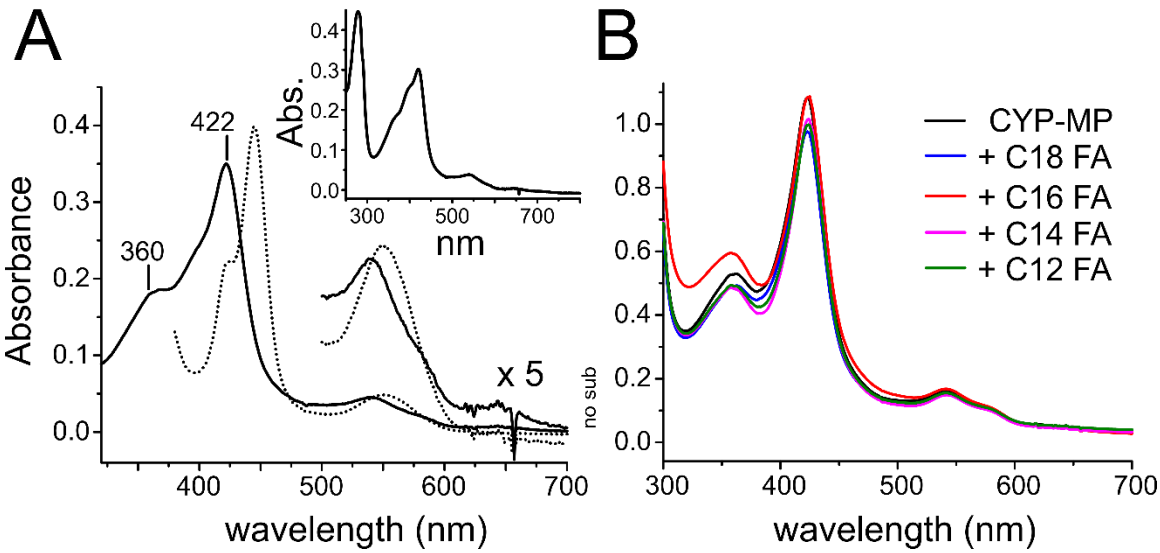


**Figure 1.4** UV/Vis absorption spectra of CYP-MP in ferric (solid and inset) and ferrous carbonmonoxy-bound (dashed) forms (A). UV-Vis absorption spectra of as isolated CYP-MP, and upon addition of 80 µM fatty acids of varying chain-lengths.

The active-site structure of CYP-MP was further probed by X-band electron paramagnetic resonance (EPR) spectroscopy (Figure 1.5). The EPR spectrum of the isolated enzyme (Figure 1.5, top trace) is comprised of one major form with g-values at 2.49, 2.26, and 1.87. The $g_z = 2.49$ for CYP-MP is higher than those typically observed for ferric water-ligated P450s, that usually fall in the range of $g_z \leq 2.45$ [39-40]. Similarly large $g_z$ values have been previously observed for P450s with nitrogen or anionic oxygen donors bound trans to the cysteine thiolate [36, 40]. As there is no amino acid in the modeled active-site of CYP-MP (Figure 1.14) that could readily provide such a ligand to the heme iron, we assign these

spectroscopic features as most likely deriving from a ferric-hydroxide bound form of the enzyme. No high spin signals are observed upon the addition of any chain length fatty acid to the enzyme, in agreement with optical spectroscopic data. However, the addition of 4 molar equivalents of stearic ($C_{18}$) acid to the enzyme results in the conversion of a fraction of the enzyme to a new low-spin ferric form with g values of 2.52, 2.26, and 1.87. This new species could in principle derive either from subtle changes in hydroxide ligand geometry, or from direct coordination of the fatty acid carboxylate to the heme. However, this latter scenario would seem unlikely based on the lack of significant optical spectroscopic changes upon fatty acid addition to CYP-MP (Figure 1.4B), and known structures of fatty acid bound CYP152 enzymes [10, 23, 25], in which the fatty acid carboxylate forms a salt bridge with a conserved active site arginine (retained as Arg256 in CYP-MP). Accordingly, the addition of shorter chain length substrates (ex. $C_{16}$) which are readily metabolized by CYP-MP fail to reproduce the g = 2.52 signal that is specifically observed upon stearic acid binding.

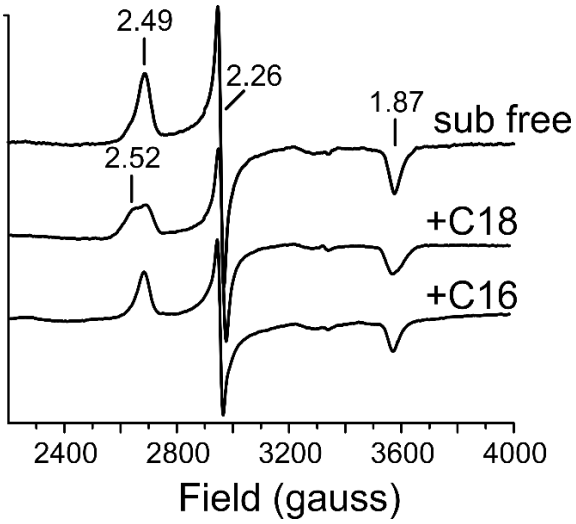


**Figure 1.5** X-band EPR of CYP-MP as purified (top trace) and upon the addition of 4 molar equivalents of C18 and C16 chain length fatty acids (middle and lower traces, respectively)

### 3.2 Characterization of CYP-MP Reaction Products

Previous multiple turnover studies of OleT-JE have shown that the addition of excess hydrogen peroxide results in low conversion of substrate [32]. The addition of excess peroxide to CYP-MP in the presence of fatty acids resulted in similarly poor product yields (<10%) despite long incubation times, suggesting possible inactivation of the enzyme. We explored whether a slow addition of $H_2O_2$ would circumvent these issues in OleT-JE, and by extension CYP-MP, enabling both higher turnover numbers and more accurate product quantitation.

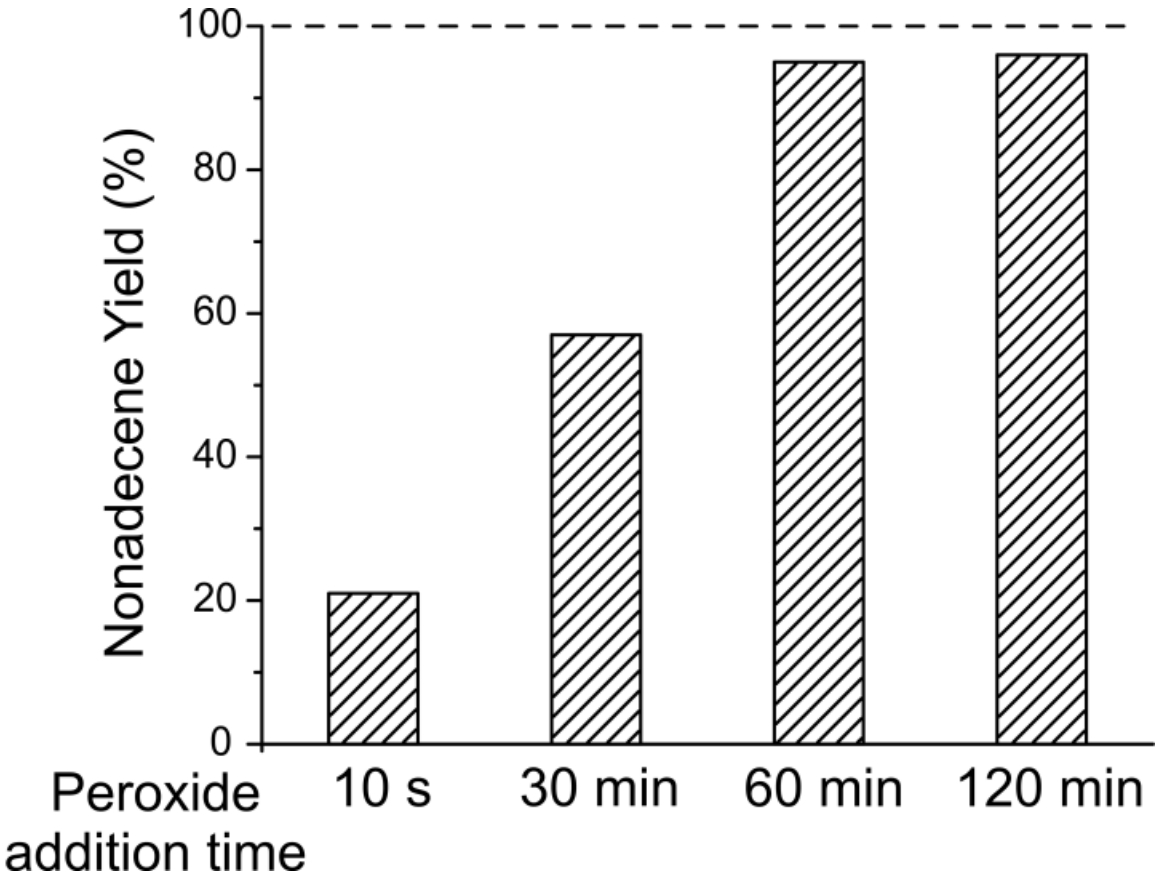


**Figure 1.6** Effect of varying the peroxide addition time on the efficiency of OleT-JE metabolism of eicosanoic acid to nonadecene. Final concentrations after mixing are 2.5 µM OleT-JE, 250 µM fatty acid and 2.5 mM hydrogen peroxide.

Assays were performed with OleT-JE and eicosanoic acid, in which a fixed amount of oxidant (ten-fold molar excess to fatty acid), was added at varying rates, maintaining a total incubation time of 2 hours. Figure 1.6 demonstrates the effect of this slow $H_2O_2$ perfusion technique on OleT-JE turnover yields. Nonadecene yields are maximized, and approach completion when $H_2O_2$ is added over a 60-minute period. Nonadecene is the only product detected under these turnover conditions (Figure 1.7), in accordance with single turnover studies reported earlier by our group [11].

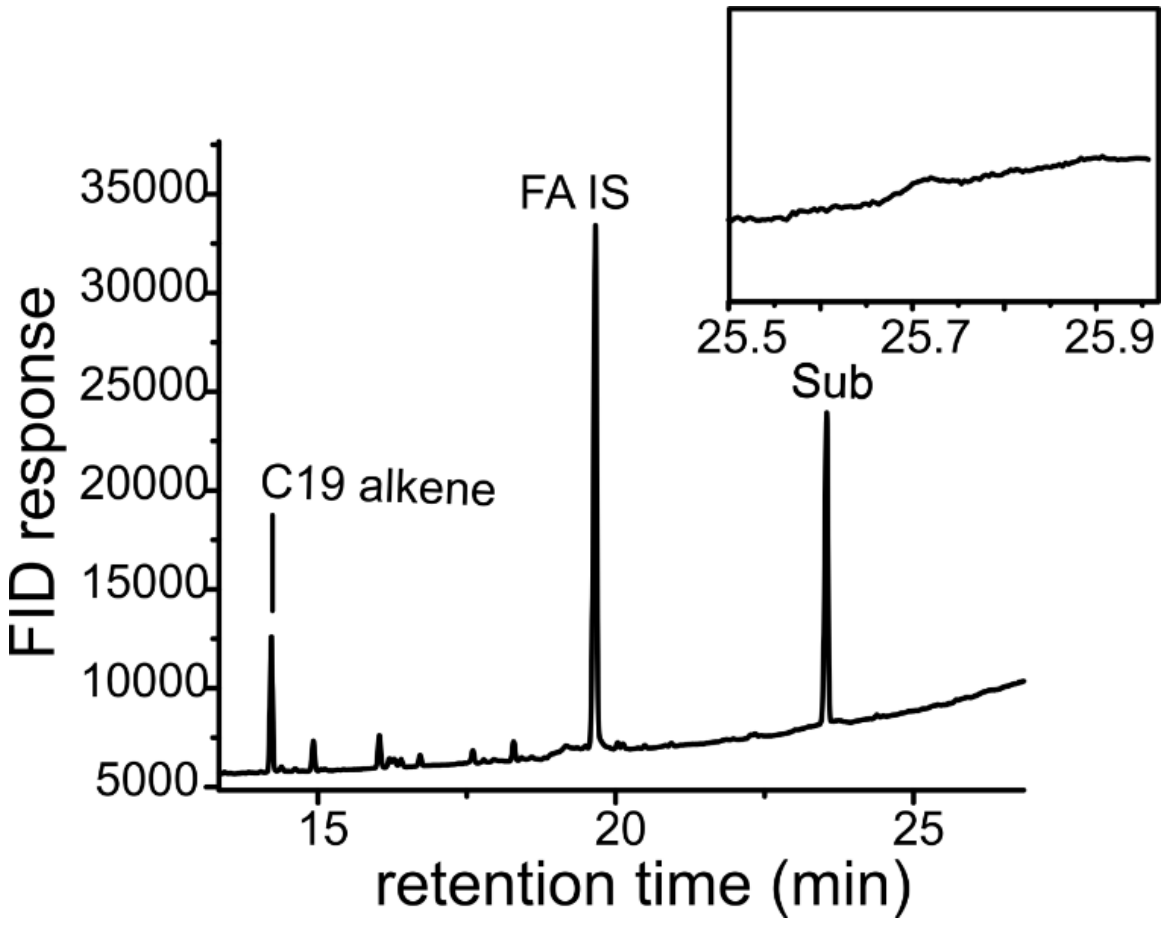


**Figure 1.7** Representative GC chromatogram for the reaction of OleT-JE, $H_2O_2$ and $C_{20}$ fatty acid. No appreciable signal at a retention time corresponding for β-hydroxy $C_{20}$ fatty acid (RT = 25.7 min) is observed (inset).

Similar turnover methods were tested with CYP-MP and a panel of fatty acid chain length substrates. Following extraction, samples were derivatized by silylation with BSTFA to enable the detection of non-metabolized substrate (mono-), and hydroxylated (di-silylated) fatty acids, together with 1-alkene. Two internal standards, consisting of a fatty acid of similar chain length as the substrate ($C_{n-2}$) and hexadecane, were included to ensure accurate quantitation of all product forms. The response factors of each were determined through analysis of authentic alkene, fatty acid, and α-OH fatty acid standards. Representative chromatograms for the metabolism of each substrate are included in Supplementary information (Figures 1.8 to 1.10) and the results are summarized in Table 1. Unlike OleT-JE, CYP-MP poorly metabolizes eicosanoic acid, and only β hydroxylated products were detected.

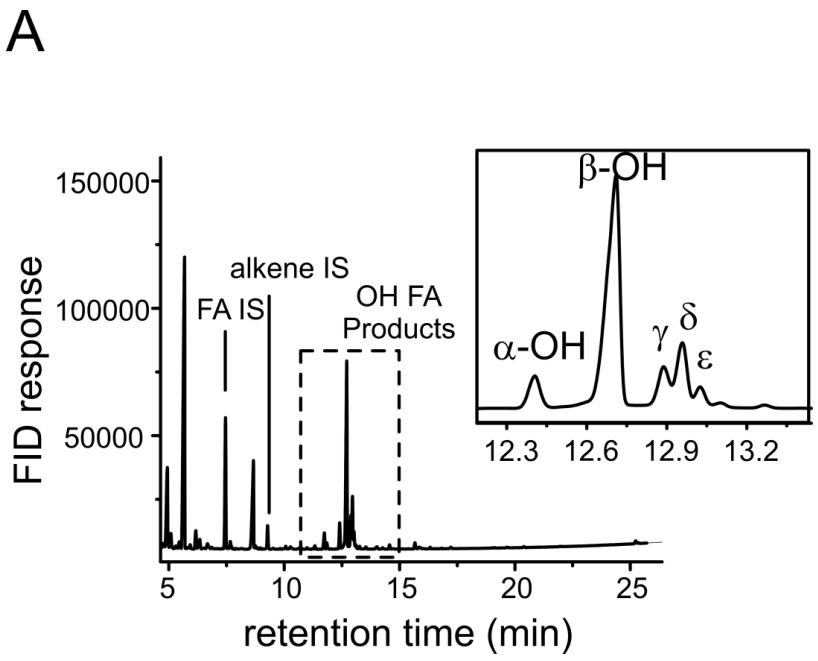


**Figure 1.8** Representative GC chromatogram for the reaction of CYP-MP, $H_2O_2$, and $C_{20}$ (A) or $C_{18}$ (B) fatty acid substrates

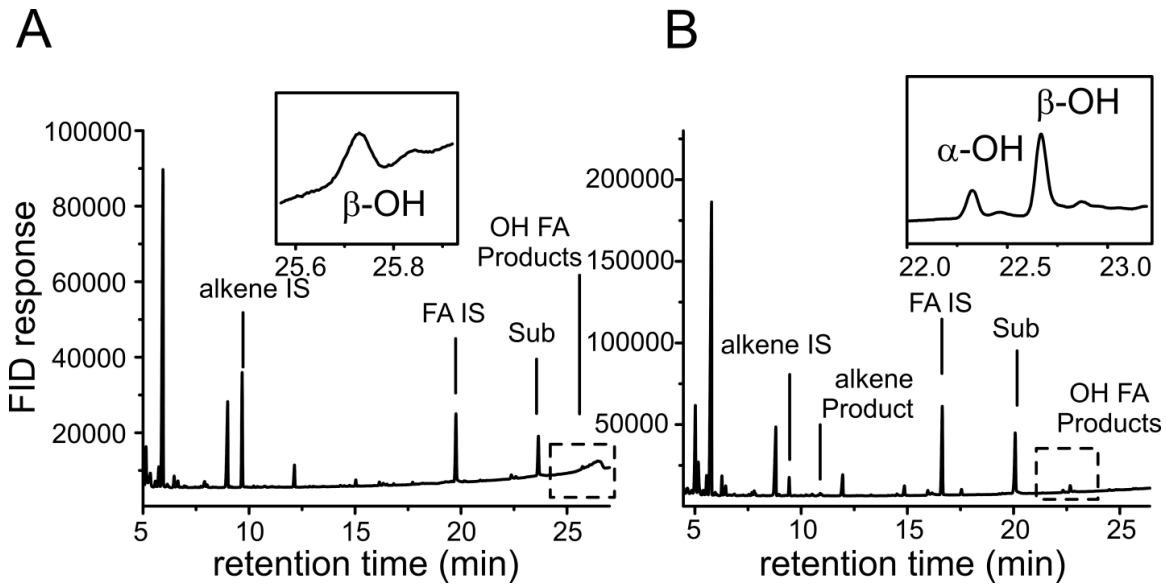


**Figure 1.9** Representative GC chromatogram for the reaction of CYP-MP, $H_2O_2$ and $C_{16}$ (A) or $C_{14}$ (B) fatty acid substrates

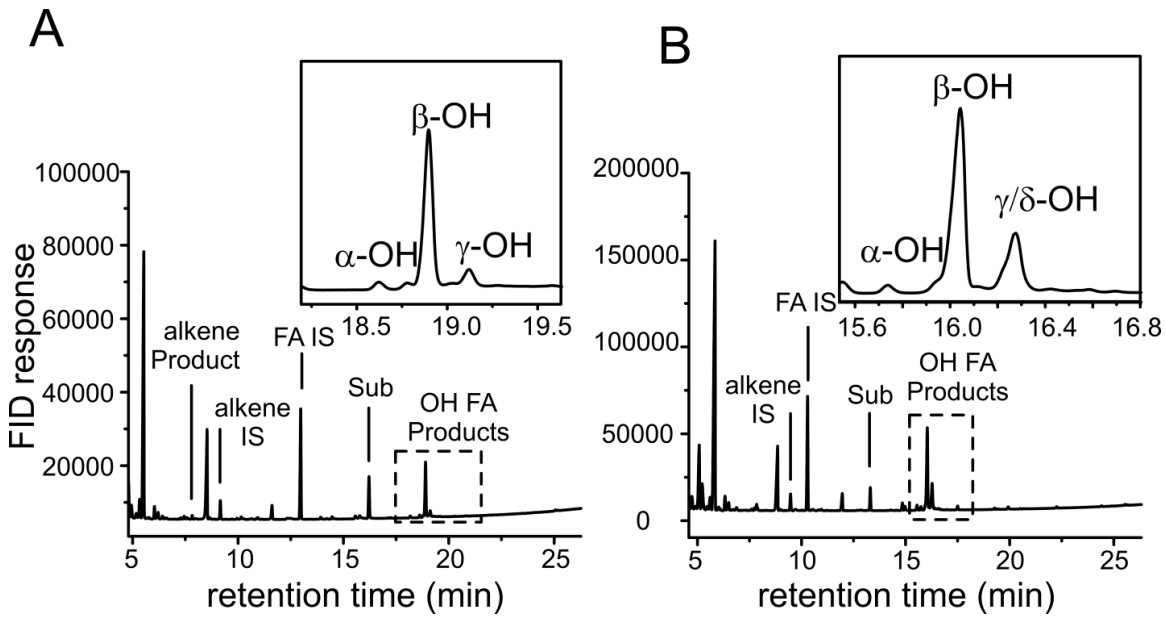


**Figure 1.10** Representative GC chromatogram for the reaction of CYP-MP, $H_2O_2$ and a $C_{12}$ fatty acid substrate

**Table 1.1**: Fatty acid metabolism and product distribution of WT and M96H CYP-MP

| Cytochrome P450 | Substrate | Conversion (%) | Product distributions (%) | | | |
|---|---|---|---|---|---|---|
| | | | 1-alkene | α -OH | β -OH | γ, δ, ε -OH |
| WT CYP-MP | $C_{20}$ | < 1% [a] | | | | |
| | $C_{18}$ | 18.4 ± 1.2 | 38.3 ± 4.7 | 8.4 ± 5.8 | 48.3 ± 6.7 | 5.0 ± 0.8 |
| | $C_{16}$ | 64.0 ± 4.8 | 23.9 ± 0.9 | 3.4 ± 0.1 | 65.4 ± 1.1 | 7.3 ± 0.2 |
| | $C_{14}$ | 88. 9 ± 2.7 | n.d. | 3.4 ± 0.4 | 69.3 ± 2.6 | 27.3 ± 2.8 |
| | $C_{12}$ | 99.9 ± 0.1 | n.d. | 7.9 ± 0.7 | 71.0 ± 5.5 | 21.1 ± 6.2 |
| Met96His | $C_{12, 14, 16}$ | < 1% [b] | | | | |

[a] only β-hydroxylated fatty acid products were detected

[b] mostly β-alcohol fatty acids n.d. not detected

The conversion yields considerably improve with a decrease in substrate chain length, and result in nearly stoichiometric products formed from reactions of CYP-MP and lauric acid ($C_{12}$). Detectable, albeit low, levels of alkene are observed in reactions of $C_{18}$ and $C_{16}$ substrates. As previously reported for OleT-JE [13, 32], decarboxylation chemoselectivity decreases with a reduction in carbon number, and is completely abolished in reactions of $C_{14}$ and $C_{12}$ substrates with CYP-MP.

Although hydroxylation at the Cβ position forms the major product across the $C_{20}$ to $C_{12}$ series, the turnover of short chain fatty acids, particularly $C_{16}$ and below, results in the appearance of large distribution of products in respective chromatograms (Figure 1.9 and 1.10). The retention times of these peaks, shortly following α and β di-silylated hydroxylated fatty acid products, suggested that they may correspond to hydroxylated

derivatives that extended beyond the Cβ position. In order to unambiguously identify these putative oxidation products, GC-MS was performed. Representative mass fragmentation patterns of hydroxylated products that derive from reactions with $C_{16}$ and $C_{14}$ substrates are presented in Figure 1.11 and Figure 1.12 respectively.

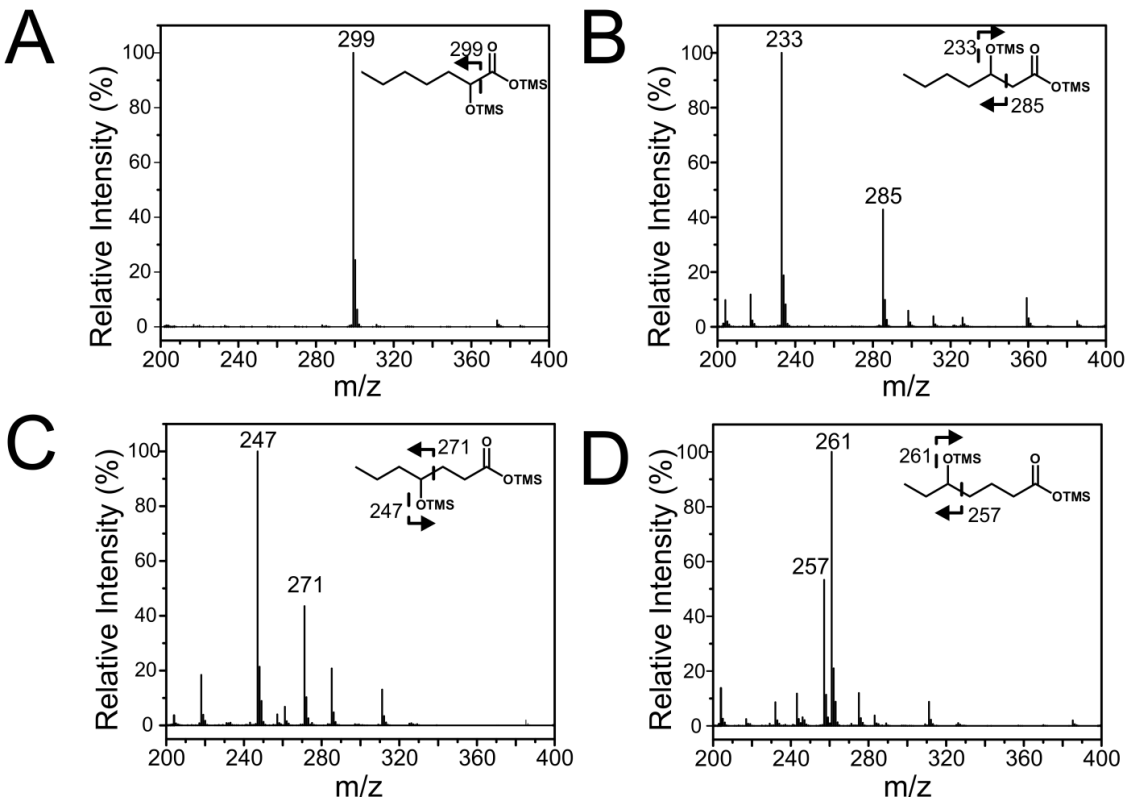


**Figure 1.11** GC/MS fragmentation patterns of derivatized (di-silylated) hydroxy-fatty acid products in reactions of CYP-MP, $C_{16}$ fatty acid, and $H_2O_2$ showing α (A), β (B), γ (C) and δ (D) forms. The mass of major fragment ions is indicated with respective assignments in the inset

The mass fragmentation patterns of the products that result from reactions of CYP-MP with $C_{16}$ and $C_{14}$ clearly show that γ and δ OH-fatty acids are formed. In the case of $C_{14}$ and $C_{12}$, these products extend as far as the ε position, suggesting a number of substrate binding

modes afforded by the CYP-MP active site. To our knowledge, these distal oxidation products have not been observed in reactions of other CYP152 enzymes, which have only been shown to form α and β fatty alcohols.

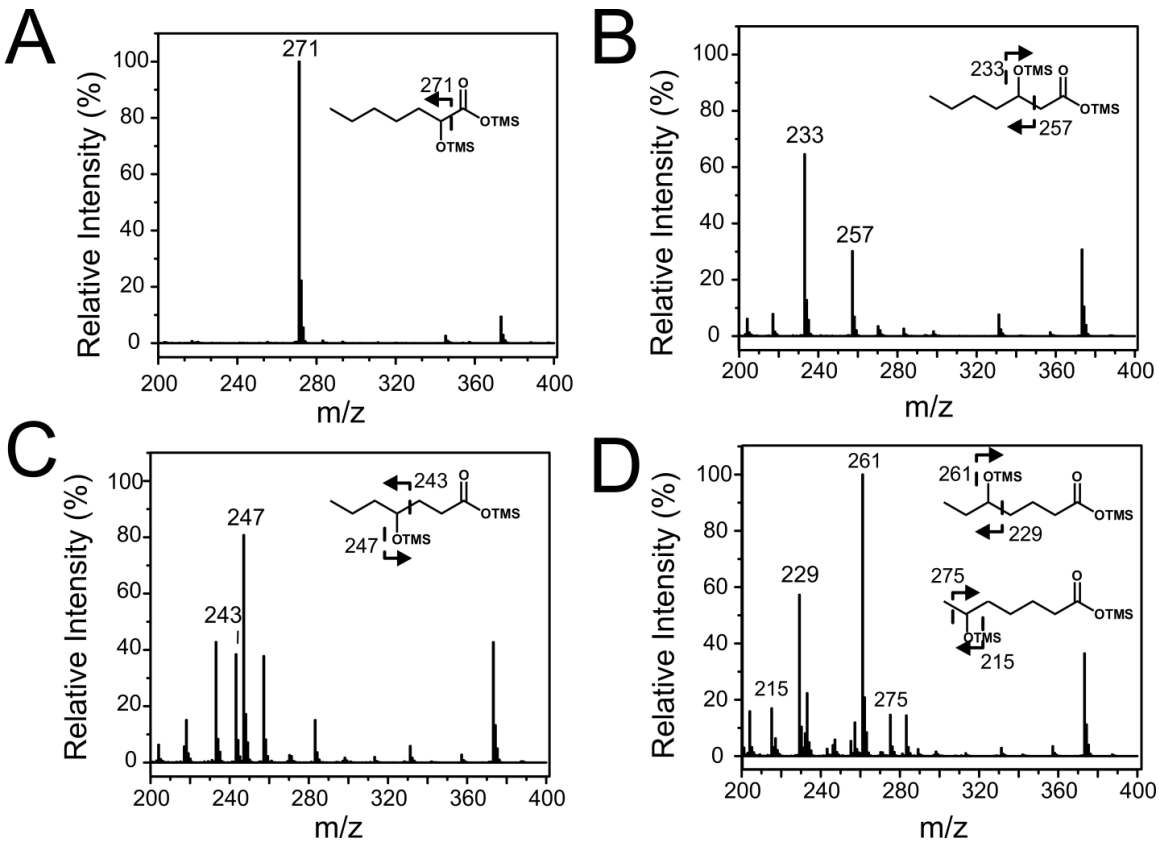


**Figure 1.12** Representative GC chromatogram for the reaction of CYP-MP, $H_2O_2$ and $C_{12}$ fatty acid substrate

Given the relatively poor alkene formation by CYP-MP relative to OleT-JE, we tested whether an active-site mutation may be able to rescue its activity. A noted difference from a pairwise structural comparison of OleT-JE, BSβ, and SPα is the presence of an active-site histidine in OleT-JE (His85) that is replaced by a glutamine in BSβ and SPα. In OleT-JE, the His85 Nε2 group is positioned ~ 5.9 Å from the heme iron and could possibly serve a role to promote the decarboxylation pathway through hydrogen bonding interaction, or

possible proton donation, to an incipient iron(IV)-hydroxide formed as a result of C-H bond abstraction. This residue is replaced by a methionine (Met96) in CYP-MP, which is incapable of forming such a hydrogen bond. The Met96His mutant was generated, characterized by optical spectroscopy, and has similar general optical features as the wild-type enzyme in the ferric state, including a similar Soret maximum, prominent β band, and a second absorption band at 360 nm (Figure 1.13). Reduction with dithionite in the presence of CO reveals that the enzyme is partially (~40 %) in the inactive P420 form, observed in multiple preparations of the enzyme. The results of turnover studies with $C_{12}$, $C_{14}$, and $C_{16}$ substrates (Table 1) show that introduction of an active-site histidine does not restore alkene production. The CYP-MP Met96His mutant displays poor metabolism of fatty acids, resulting in less than <1 % conversion. The meager levels of product that are detectable only comprise hydroxylated fatty acid products.

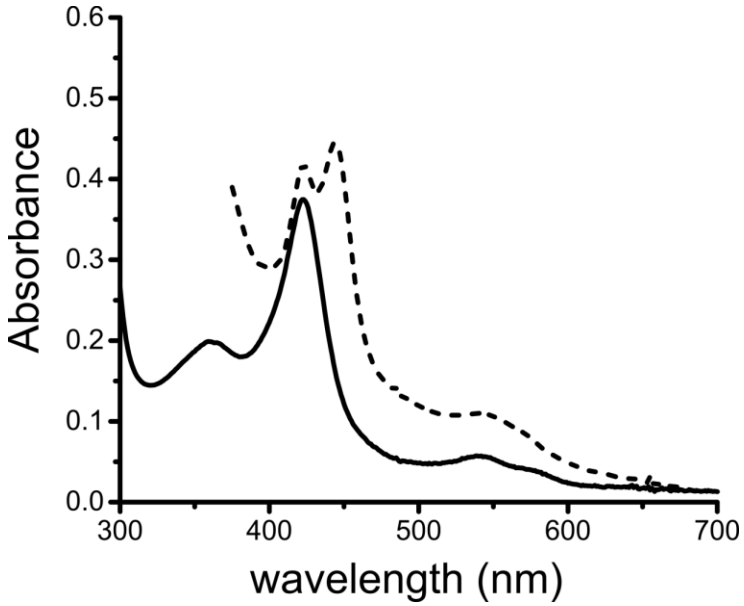


**Figure 1.13** UV-Vis absorption spectra of the CYP-MP Met96His mutant in ferric (solid) and ferrous carbon-monoxy forms

## 4. Discussion

It is shown here that CYP-MP is capable of producing alkenes, extending the unusual OleT-JE oxidative decarboxylation reaction to a second CYP152. The observation of alcohol products, in addition to alkenes, is consistent with previous proposals that very similar chemical mechanisms give rise to both products.[11] Production of an alkene necessitates the loss of a hydrogen from the Cβ position. Therefore, it would seem logical that the decarboxylation reaction is initiated by C-H bond abstraction by Compound I at this position. Unfortunately, the perdeuterated fatty acid probe utilized in our previous transient kinetics studies of OleT-JE does not allow for precise targeting of this abstraction to a Cβ-H. In light of this, it is notable that Cβ alcohols are the predominant CYP-MP reaction product in reactions of all chain length (CL) substrates. C-H bond abstraction at Cβ is not the sole requirement for efficient decarboxylation. Additional structural or electronic factors are likely required to inhibit an oxygen rebound step following the formation of Compound II.

The native substrate for CYP-MP is not currently known. Given the high abundance of mono-unsaturated (largely $C_{18}$) fatty acids found in many *Methylobacteria* [41], it is possible that the native substrate of CYP-MP may not be among those tested in this study. Nonetheless, the spectroscopic and activity assays reported here begin to provide a more detailed framework for understanding the active site requirements for alkene formation. The capacity of CYP-MP to catalyze decarboxylation demonstrates that an active-site histidine is not an obligate requirement for substrate carbon-carbon scission. Nonetheless, CYP-MP is much less productive than OleT-JE for the synthesis of alkenes from longer ($C_{18}$ and $C_{20}$) substrates. The strict chain length dependence of CYP-MP decarboxylase

activity also alludes to an importance of substrate identity in controlling the monooxygenation/decarboxylation branchpoint. For comparison, there is some ambiguity regarding the CL dependence of OleT-JE, which may result from variations in reaction conditions, the oxidant utilized ($O_2$/electrons versus $H_2O_2$), and analytical methods employed [13-14, 32]. Although reported yields vary significantly in these studies, OleT-JE has been shown to produce increasing amounts of α and β OH-fatty acids, and consequently less alkene, upon CL reduction from $C_{20}$ to $C_{16}$. An associated decreased capacity for shorter chain fatty acids to induce a low- to high-spin state conversion in OleT-JE [10] may signal the presence of multiple substrate coordination modes within the active-site, leading to an increased accessibility of the heme iron to water. These relationships have been extensively studied in other P450s, including CYP101 mutants and substrate analogs (ex. [42-45]). While optical spin-state transitions are not directly observable for CYP-MP upon the binding of substrates, it is notable that perturbation of the ferric-hydroxide EPR spectrum is only observed upon binding of a substrate ($C_{18}$) that shows the largest efficiency for alkene formation. Likewise, the product distributions for shorter chain fatty acids, extending as far as the Cε position for $C_{12}$, clearly demonstrate that shorter CL substrates adopt a variety of conformations within the CYP-MP active site. As for OleT-JE, decreased regiospecificity compromises the efficiency of the alkene forming pathway in CYP-MP.

In order to identify the possible structural factors that may give rise to a large distribution of CYP-MP oxidation products, a homology model (based on the $C_{20}$ fatty acid bound X-ray structure of OleT-JE, PDB 4L40 [10]) was generated using the I-TASSER server [46]. An overlay of the two active sites is shown in Figure 1.14. Assuming that fatty acids bind in a similar orientation to CYP-MP as OleT-JE, smaller hydrophilic side chains

replace the phenylalanine residues found in OleT-JE (Phe79 and 172) that lie in close contact with the substrate. Without the anchoring of these residues in CYP-MP, the fatty acid may be able to shift more readily, allowing for a greater propensity for target C-H bond abstraction and incipient oxygen rebound. Controlling substrate binding modes, in this case, may serve as a guide for understanding the differential alkene-producing ability of different CYP152 enzymes. They may also serve as a template for improving the efficiency of OleT-JE with alternative substrates.

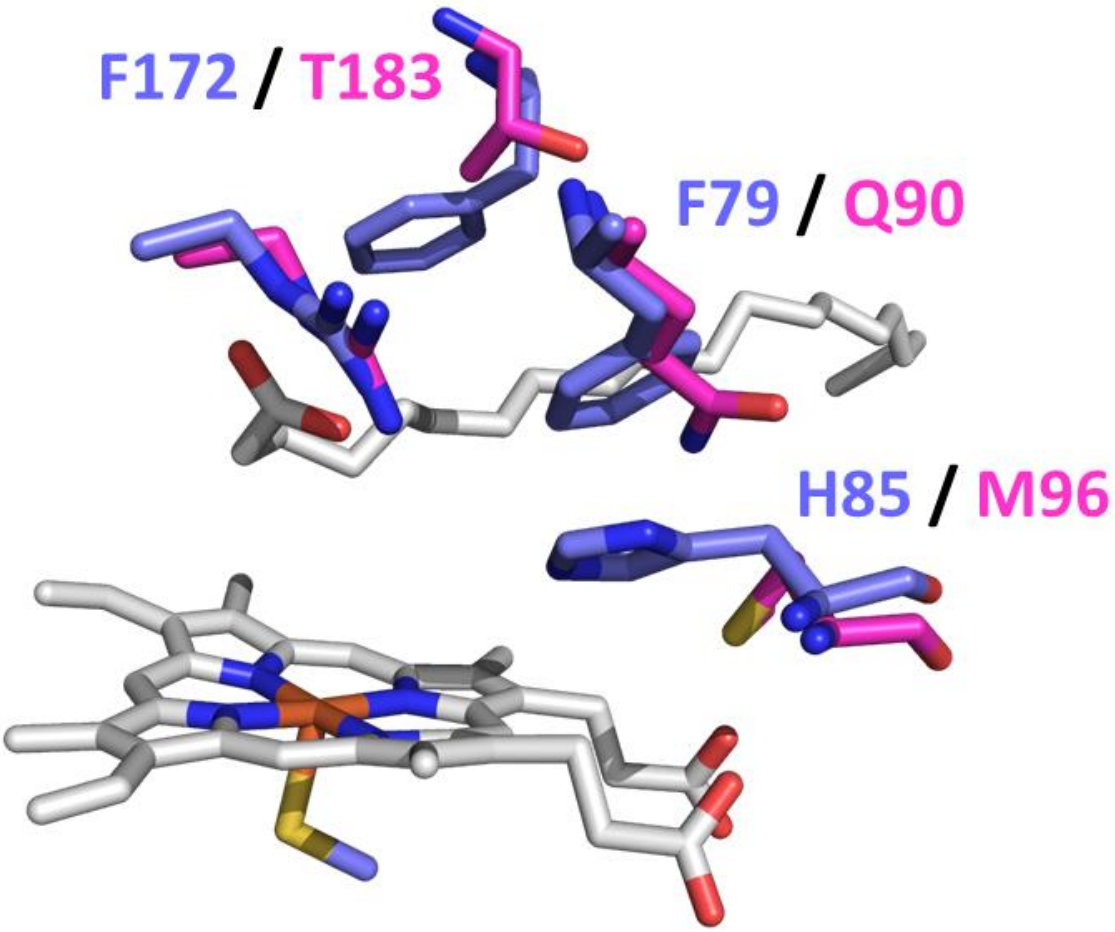


**Figure 1.14** Overlay of the predicted active-site structure of CYP-MP (pink) and eicosanoic acid ($C_{20}$) bound OleT-JE (purple) PDB: 4L40

## 5. Acknowledgments

We thank Michael Walla for assisting with the GC-MS analysis of alkene and hydroxylated fatty acid products. This work is supported by startup funds from the University of South Carolina and funding from the U.S.C. Office of Research through the Aspire program to T.M.M.

## 6. References

1. Qiu, Y.; Tittiger, C.; Wicker-Thomas, C.; Le Goff, G.; Young, S.; Wajnberg, E.; Fricaux, T.; Taquet, N.; Blomquist, G. J.; Feyereisen, R., An insect-specific P450 oxidative decarbonylase for cuticular hydrocarbon biosynthesis. *P Natl Acad Sci USA* **2012,** *109* (37), 14858-14863.

2. Rude, M. A.; Baron, T. S.; Brubaker, S.; Alibhai, M.; Del Cardayre, S. B.; Schirmer, A., Terminal Olefin (1-Alkene) Biosynthesis by a Novel P450 Fatty Acid Decarboxylase from Jeotgalicoccus Species. *Appl Environ Microb* **2011,** *77* (5), 1718-1727.

3. Rui, Z.; Li, X.; Zhu, X.; Liu, J.; Domigan, B.; Barr, I.; Cate, J. H. D.; Zhang, W., Microbial biosynthesis of medium-chain 1-alkenes by a nonheme iron oxidase. *Proceedings of the National Academy of Sciences of the United States of America* **2014,** *111* (51), 18237-18242.

4. Schirmer, A.; Rude, M. A.; Li, X.; Popova, E.; del Cardayre, S. B., Microbial biosynthesis of alkanes. *Science* **2010,** *329* (5991), 559-62.

5. Kallio, P.; Pasztor, A.; Thiel, K.; Akhtar, M. K.; Jones, P. R., An engineered pathway for the biosynthesis of renewable propane. *Nature communications* **2014,** *5*, 4731.

6. Khara, B.; Menon, N.; Levy, C.; Mansell, D.; Das, D.; Marsh, E. N.; Leys, D.; Scrutton, N. S., Production of propane and other short-chain alkanes by structure-based engineering of ligand specificity in aldehyde-deformylating oxygenase. *Chembiochem : a European journal of chemical biology* **2013,** *14* (10), 1204-8.

7. Choi, Y. J.; Lee, S. Y., Microbial production of short-chain alkanes. *Nature* **2013,** *502* (7472), 571-576.

8. Harger, M.; Zheng, L.; Moon, A.; Ager, C.; An, J. H.; Choe, C.; Lai, Y. L.; Mo, B.; Zong, D.; Smith, M. D.; Egbert, R. G.; Mills, J. H.; Baker, D.; Pultz, I. S.; Siegel, J. B., Expanding the Product Profile of a Microbial Alkane Biosynthetic Pathway. *Acs Synth Biol* **2013,** *2* (1), 59-62.

9. Howard, T. P.; Middelhaufe, S.; Moore, K.; Edner, C.; Kolak, D. M.; Taylor, G. N.; Parker, D. A.; Lee, R.; Smirnoff, N.; Aves, S. J.; Love, J., Synthesis of customized petroleum-replica fuel molecules by targeted modification of free fatty acid pools in Escherichia coli. *Proceedings of the National Academy of Sciences of the United States of America* **2013,** *110* (19), 7636-7641.

10. Belcher, J.; McLean, K. J.; Matthews, S.; Woodward, L. S.; Fisher, K.; Rigby, S. E. J.; Nelson, D. R.; Potts, D.; Baynham, M. T.; Parker, D. A.; Leys, D.; Munro, A. W., Structure and Biochemical Properties of the Alkene Producing Cytochrome P450 OleTJE (CYP152L1) from the Jeotgalicoccus sp. 8456 Bacterium. *Journal of Biological Chemistry* **2014,** *289* (10), 6535-6550.

11. Grant, J. L.; Hsieh, C. H.; Makris, T. M., Decarboxylation of fatty acids to terminal alkenes by cytochrome P450 compound I. *Journal of the American Chemical Society* **2015,** *137* (15), 4940-3.

12. Zachos, I.; Gassmeyer, S. K.; Bauer, D.; Sieber, V.; Hollmann, F.; Kourist, R., Photobiocatalytic decarboxylation for olefin synthesis. *Chemical Communications (Cambridge, United Kingdom)* **2015,** *51* (10), 1918-1921.

13. Dennig, A.; Kuhn, M.; Tassoti, S.; Thiessenhusen, A.; Gilch, S.; Bulter, T.; Haas, T.; Hall, M.; Faber, K., Oxidative Decarboxylation of Short-Chain Fatty Acids to 1-Alkenes. *Angewandte Chemie* **2015,** *54*, 8819-8822.

14. Liu, Y.; Wang, C.; Yan, J.; Zhang, W.; Guan, W.; Lu, X.; Li, S., Hydrogen peroxide-independent production of alpha-alkenes by OleTJE P450 fatty acid decarboxylase. *Biotechnology for biofuels* **2014,** *7* (1), 28.

15. Fujii, T.; Nakamura, K.; Shibuya, K.; Tanase, S.; Gotoh, O.; Ogawa, T.; Fukuda, H., Structural characterization of the gene and corresponding cDNA for the cytochrome P450rm from Rhodotorula minuta which catalyzes formation of isobutene and 4-hydroxylation of benzoate. *Mol Gen Genet* **1997,** *256* (2), 115-120.

16. Fukuda, H.; Fujii, T.; Sukita, E.; Tazaki, M.; Nagahama, S.; Ogawa, T., Reconstitution of the isobutene-forming reaction catalyzed by cytochrome P450 and P450 reductase from Rhodotorula minuta: decarboxylation with the formation of isobutene. *Biochemical and Biophysical Research Communications* **1994,** *201* (2), 516-22.

17. de Montellano, P. R. O., Hydrocarbon Hydroxylation by Cytochrome P450 Enzymes. *Chem Rev* **2010,** *110* (2), 932-948.

18. Denisov, I. G.; Makris, T. M.; Sligar, S. G.; Schlichting, I., Structure and chemistry of cytochrome P450. *Chem Rev* **2005,** *105* (6), 2253-2277.

19. Imai, Y.; Matsunaga, I.; Kusunose, E.; Ichihara, K., Unique heme environment at the putative distal region of hydrogen peroxide-dependent fatty acid alpha-hydroxylase from Sphingomonas paucimobilis (peroxygenase P450(SPalpha). *Journal of biochemistry* **2000,** *128* (2), 189-94.

20. Matsunaga, I.; Sumimoto, T.; Ueda, A.; Kusunose, E.; Ichihara, K., Fatty acid-specific, regiospecific, and stereospecific hydroxylation by cytochrome P450 (CYP152B1) from Sphingomonas paucimobilis: substrate structure required for alpha-hydroxylation. *Lipids* **2000,** *35* (4), 365-71.

21. Matsunaga, I.; Yamada, M.; Kusunose, E.; Miki, T.; Ichihara, K., Further characterization of hydrogen peroxide-dependent fatty acid alpha-hydroxylase from Sphingomonas paucimobilis. *Journal of biochemistry* **1998,** *124* (1), 105-10.

22. Matsunaga, I.; Yokotani, N.; Gotoh, O.; Kusunose, E.; Yamada, M.; Ichihara, K., Molecular cloning and expression of fatty acid alpha-hydroxylase from Sphingomonas paucimobilis. *The Journal of biological chemistry* **1997,** *272* (38), 23592-6.

23. Lee, D. S.; Yamada, A.; Sugimoto, H.; Matsunaga, I.; Ogura, H.; Ichihara, K.; Adachi, S.; Park, S. Y.; Shiro, Y., Substrate recognition and molecular mechanism of fatty acid hydroxylation by cytochrome P450 from Bacillus subtilis - Crystallographic, spectroscopic, and mutational studies. *Journal of Biological Chemistry* **2003,** *278* (11), 9761-9767.

24. Girhard, M.; Schuster, S.; Dietrich, M.; Durre, P.; Urlacher, V. B., Cytochrome P450 monooxygenase from Clostridium acetobutylicum: a new alpha-fatty acid hydroxylase. *Biochem Biophys Res Commun* **2007,** *362* (1), 114-9.

25. Fujishiro, T.; Shoji, O.; Nagano, S.; Sugimoto, H.; Shiro, Y.; Watanabe, Y., Crystal Structure of H2O2-dependent Cytochrome P450(SP alpha) with Its Bound Fatty Acid Substrate. Insight into the regioselective hydroxylation of fatty acids at the alpha position. *Journal of Biological Chemistry* **2011,** *286* (34), 29941-29950.

26. Matsunaga, I.; Yamada, A.; Lee, D. S.; Obayashi, E.; Fujiwara, N.; Kobayashi, K.; Ogura, H.; Shiro, Y., Enzymatic reaction of hydrogen peroxide-dependent peroxygenase cytochrome P450s: kinetic deuterium isotope effects and analyses by resonance Raman spectroscopy. *Biochemistry* **2002,** *41* (6), 1886-92.

27. Rittle, J.; Green, M. T., Cytochrome P450 compound I: capture, characterization, and C-H bond activation kinetics. *Science* **2010,** *330* (6006), 933-7.

28. Groves, J. T.; McClusky, G. A., Aliphatic Hydroxylation Via Oxygen Rebound - Oxygen-Transfer Catalyzed by Iron. *Journal of the American Chemical Society* **1976,** *98* (3), 859-861.

29. Groves, J. T.; McClusky, G. A.; White, R. E.; Coon, M. J., Aliphatic Hydroxylation by Highly Purified Liver Microsomal Cytochrome P-450 - Evidence for a Carbon Radical Intermediate. *Biochemical and Biophysical Research Communications* **1978,** *81* (1), 154-160.

30. Kellner, D. G.; Hung, S. C.; Weiss, K. E.; Sligar, S. G., Kinetic characterization of Compound I formation in the thermostable cytochrome P450 CYP119. *Journal of Biological Chemistry* **2002,** *277* (12), 9641-9644.

31. Wang, X.; Peter, S.; Kinne, M.; Hofrichter, M.; Groves, J. T., Detection and Kinetic Characterization of a Highly Reactive Heme-Thiolate Peroxygenase Compound I. *Journal of the American Chemical Society* **2012,** *134* (31), 12897-900.

32. Zachos, L.; Gassmeyer, S. K.; Bauer, D.; Sieber, V.; Hollmann, F.; Kourist, R., Photobiocatalytic decarboxylation for olefin synthesis. *Chem Commun* **2015,** *51* (10), 1918-1921.

33. Blommel, P. G.; Fox, B. G., A combined approach to improving large-scale production of tobacco etch virus protease. *Protein Expres Purif* **2007,** *55* (1), 53-68.

34. Berry, E. A.; Trumpower, B. L., Simultaneous Determination of Hemes-a, Hemes-B, and Hemes-C from Pyridine Hemochrome Spectra. *Anal Biochem* **1987,** *161* (1), 1-15.

35. Adak, S.; Crooks, C.; Wang, Q.; Crane, B. R.; Tainer, J. A.; Getzoff, E. D.; Stuehr, D. J., Tryptophan 409 controls the activity of neuronal nitric-oxide synthase by regulating nitric oxide feedback inhibition. *The Journal of biological chemistry* **1999,** *274* (38), 26907-11.

36. Agmon, N., The Grotthuss mechanism. *Chemical Physics Letters* **1995,** *244* (5,6), 456-62.

37. Austin, R. N.; Groves, J. T., Alkane-oxidizing metalloenzymes in the carbon cycle. *Metallomics : integrated biometal science* **2011,** *3* (8), 775-87.

38. Adams, P. A.; Louw, J., Dioxygen bond scission and heme degradation in hemoproteins: a kinetic study of chemical model systems using ferrimyoglobin and hemepeptide: non-hemepeptide complexes as catalysts for 'peroxidasic' reduction of hydrogen peroxide. *Journal of the Chemical Society, Perkin Transactions 2: Physical Organic Chemistry* **1995,** (8), 1683-90.

39. Baas, B. J.; Denisov, I. G.; Sligar, S. G., Homotropic cooperativity of monomeric cytochrome P450 3A4 in a nanoscale native bilayer environment. *Archives of Biochemistry and Biophysics* **2004,** *430* (2), 218-228.

40. Barr, D. P.; Mason, R. P., Mechanism of radical production from the reaction of cytochrome c with organic hydroperoxides. An ESR spin trapping investigation. *The Journal of biological chemistry* **1995,** *270* (21), 12709-16.

41. Wellner, S.; Lodders, N.; Kampfer, P., Methylobacterium cerastii sp nov., isolated from the leaf surface of Cerastium holosteoides. *Int J Syst Evol Micr* **2012,** *62*, 917-924.

42. Carver, T. E.; Brantley, R. E., Jr.; Singleton, E. W.; Arduini, R. M.; Quillin, M. L.; Phillips, G. N., Jr.; Olson, J. S., A novel site-directed mutant of myoglobin with an unusually high O2 affinity and low autooxidation rate. *The Journal of biological chemistry* **1992,** *267* (20), 14443-50.

43. Bonfils, C.; Saldana, J. L.; Debey, P.; Maurel, P.; Balny, C.; Douzou, P., Fast photochemical reactions of cytochrome P450 at subzero temperatures. *Biochimie* **1979,** *61* (5-6), 681-7.

44. Bonfils, C.; Debey, P.; Maurel, P., Highly purified microsomal P-450: the oxyferro intermediate stabilized at low temperature. *Biochem Biophys Res Commun* **1979,** *88* (4), 1301-7.

45. Bonfils, C.; Debey, P.; Maurel, P., Highly-purified microsomal P-450: the oxyferro intermediate stabilized at low temperature. *Biochemical and Biophysical Research Communications* **1979,** *88* (4), 1301-7.

46. Chen, K.; Que, L., Jr., Stereospecific alkane hydroxylation by non-heme iron catalysts: mechanistic evidence for an Fe(V)=O active species. *Journal of the American Chemical Society* **2001,** *123* (26), 6327-37.

# CHAPTER 2

## A DISTAL LOOP CONTROLS PRODUCT RELEASE, CHEMO- AND REGIO-SELECTIVITY IN CYTOCHROME P450 DECARBOXYLASES

**Abstract**

The cytochrome P450 OleT-JE utilizes hydrogen peroxide ($H_2O_2$) to catalyze the decarboxylation or hydroxylation of fatty acid (FA) substrates. Both reactions are initiated through the abstraction of a substrate hydrogen atom by the high-valent iron-oxo intermediate known as Compound I. Here, we specifically probe the influence of substrate coordination on OleT-JE reaction partitioning through the combined use of fluorescent and EPR-active FAs, and mutagenesis of structurally disordered F-G loop that is far removed from the heme-iron active-site. The labeled probes are efficiently metabolized and reveal a slow product release step, mediated by the F-G loop, that limits OleT-JE turnover. A single amino acid change or truncation of the loop reveals that this region establishes critical interactions to anchor FA substrates in place and allow for regiospecific C-H abstraction and decarboxylation to occur.

---

Amaya, J. A.; Rutland, C. D.; Leschinsky, N.; Makris, T. M., A Distal Loop Controls Product Release and Chemo- and Regioselectivity in Cytochrome P450 Decarboxylases. *Biochemistry* **2018,** *57* (3), 344-353

## 1. Introduction

High-valent iron-oxo species have been directly implicated in a plethora of important biosynthetic transformations. In addition to more common monooxygenase reactions that result from the integration of one atom of atmospheric dioxygen into substrates, recent studies have established the intermediacy of iron-oxo intermediates for catalyzing substrate halogenations,[1] epimerizations,[2] dehydrogenations,[3] and heterocyclic ring formation[4] in non-heme iron enzymes. Following the abstraction of a scissile substrate C-H bond, these enzymes have evolved complex mechanisms that can change the nature of the ensuing rebound reaction by altering both the efficiency and sometimes the identity of the activated radical species. The analogous iron(IV)-oxo unit in heme enzymes, commonly referred to as Compound I, has a substantially more rigid structure from invariable ligands provided by the porphyrin cofactor and axial ligand, and would thus appear to offer less catalytic flexibility. Nonetheless, heme-containing enzymes, particularly cytochrome P450s (CYPs), have been implicated in diverse set of chemistries that can include oxidative desaturations [5] and decarboxylations, [6-7] among others.

Until very recently, the highly reactive [8] nature of CYP Compound I intermediate has prohibited its direct visualization in a reaction other than the archetypal monooxygenation. This has limited understanding the origins for heme-enzyme reaction diversification. The CYP OleT-JE, named for its olefin-forming capacity, catalyzes the decarboxylation of fatty acid substrates using $H_2O_2$ as a co-substrate.[7] The substrate-assisted mechanism that allows for the efficient activation of peroxide in OleT-JE, and is very likely common to other CYP152 orthologs, has enabled isolation of Compound I (Ole-I) [9] in the OleT-JE C-C cleavage reaction and revealed a significant substrate $^2H$ kinetic

isotope effect (KIE) for Ole-I decay. This, and subsequent observation of the OleT-JE Compound II intermediate (Ole-II) [10] has demonstrated that oxygen insertion and decarboxylation both proceed from the same substrate hydrogen atom transfer step (Scheme 2.1).

A number of studies have sought to clarify the important regulatory elements required to sufficiently hamper oxygen rebound in OleT-JE and route the enzyme towards further oxidation of the substrate in order to allow decarboxylation to occur. Inspiration has largely derived from comparison of the OleT-JE structure with CYP152 orthologs with variable abilities to navigate the decarboxylation/hydroxylation branchpoint, in particular, the archetypal CYP152 hydroxylase BSβ.[11] As a result, mutagenesis experiments have targeted active site residues and the immediate microenvironment that differ between the two enzymes.[7, 12-13] Although this line of inquiry, augmented by theory, [14-15] has identified possible roles for proton donation pathways and solvent in mediating the switch, growing evidence has suggested that additional elements may be required to reinforce decarboxylation.

Several lines of evidence have alluded to a sophisticated interplay of substrate binding modes and mobility, mediated by the protein scaffold, for controlling the fate of activated oxygen species in OleT-JE. Primarily, OleT-JE exhibits mixed chemoselectivity [7, 12-13, 16-17] and hydroxylates some non-native chain length substrates with variable proficiency through a canonical rebound mechanism.[18] This mixed functionality is reiterated in CYP-MP, another CYP152 ortholog that is devoid of an active site histidine (H85 in OleT-JE) that has been highlighted as a principle difference between BSβ and OleT-JE. [19] Introduction of the activating substrate-acid required for efficient $H_2O_2$

utilization by active site mutation [20] or via a substrate misrecognition strategy [18] allows OleT-JE to insert oxygen into an even broader range of hydrocarbons. The radical recombination efficiencies measured from radical clock studies using the latter approach are indistinguishable from those measured for CYP monooxygenases. [18]

Here, we have adopted a new strategy to examine OleT-JE reaction partitioning that preserves the active site features of OleT-JE, but introduces variations to the fatty acid (FA) substrate at positions of the protein that are far removed from the heme-iron active site. Using fatty acid substrates with spectroscopically-active probes appended to different points along the acyl chain, we have identified a slow product release step that limits OleT-JE turnover. These probes indicate that a structurally disordered region of OleT-JE known

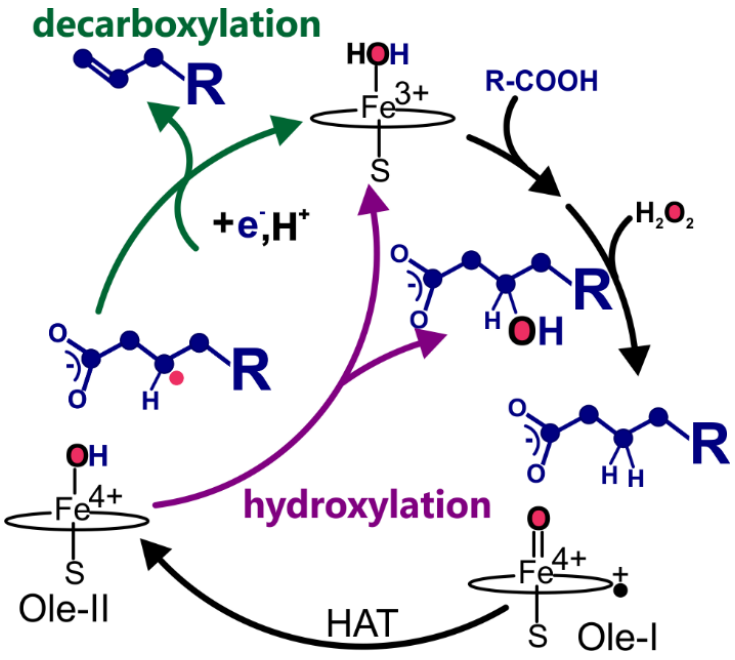


**Scheme 2.1** Proposed mechanism for the atypical decarboxylation (green) and canonical hydroxylation (purple) reactions catalyzed by the cytochrome P450 OleT-JE. Following the binding of the fatty acid substrate and activation of $H_2O_2$, both reactions are initiated via hydrogen atom transfer (HAT) to OleT-JE compound I (Ole-I) to form Ole-II. The reaction then bifurcates, depending on the nature of the substrate. Either an electron from the substrate is abstracted that is coupled to proton transfer, resulting in decarboxylation to an alkene, or oxygen rebound occurs, forming a fatty alcohol.

as the F-G loop is critical for mediating product release. This same region is critical for anchoring the FA substrate. Disruption of the interactions of the F-G loop and substrate, with as little as a single amino acid change, converts OleT-JE from a decarboxylase into a monooxygenase, even though the active site structure has been left completely preserved.

## 2. Experimental Procedures

### 2.1 Reagents and chemicals

All buffers used in this study were purchased from BDH Chemicals. Peptone, tryptone, yeast extract and thiamine were purchased from Research Products International (Mt. Prospect, IL, USA). Antibiotics were purchased from BioBasic Inc (Markham, ON Canada). Hydrogen peroxide and 11-(dansylamino)undecanoic acid (DAUDA) were obtained from Sigma Aldrich. Protiated fatty acids, N,O-Bis(trimethylsilyl)trifluoroacetamide (BSTFA) and trimethylchlorosilane (TMCS) (99:1) were purchased from Supelco (Bellefonte, PA, USA). 16-doxylstearic acid was purchased from Santa Cruz Biotechnology (Dallas, TX, USA). 11-aminoundecanoic acid was obtained from Acros Organics (Morris, NJ, USA). Dansyl chloride and alkene standards were purchased from TCI Chemicals (Portland, OR, USA). The pChuA expression vector was obtained from Addgene (plasmid #42539) and was a kind gift from Alan Jasanoff. [21]

### 2.2 Fluorescent fatty acid synthesis

The dansylated fatty acid derivative 11-(dansylamino)-undecanoic acid (DAUDA) was synthesized by dissolving 11-aminoundecanoic acid (2 mmol) in 90 mL of $H_2O$ with

sodium bicarbonate (20 mmol). To this suspension, 24 mL of a 1:6 solution of triethylamine:acetone (vol:vol) containing dansyl chloride (1 mmol) was added dropwise over the course of one hour while stirring at room temperature. The reaction was then acidified with 0.5 M HCl to pH 2 and extracted with three times 75 mL of ethyl acetate. The organic phase was completely evaporated under a stream of $N_2$. The resulting white solid was resuspended in 50 mL EtOH and stored at -20 °C. The concentration of DAUDA was determined by optical spectroscopy using an extinction coefficient ($\varepsilon_{335\ nm}$ = 4800 $M^{-1}$ $cm^{-1}$). Final yields were typically 80 – 90 %.

**2.3 OleT-JE mutagenesis**

*OleT-JE L176G*: Site-directed mutagenesis employed standard molecular biology procedures and partially overlapping primers. The following primers were utilized with the newly-introduced codon underlined:

5'GTGCGGGCGGTGGTGCGTGGAAGGGCTATAAGGCG 3'

5' CCACCGCCCGCACGAAAGCTATCGATCATGATGTCCATATCG 3'.

*OleT-JE Δ3aa:* The deletion mutant to truncate the F-G loop was generated using restriction-free cloning with the following megaprimer and its reverse complement: 5'TAGCTTTCGTGCGCTGGGTGGTAAGGGCTATAAGGCGAAAGAGGCGCGTCG TCGTGTTG 3'.

All mutations were verified by sequencing at EtonBio Inc (Durham, NC, USA).

### 2.4 Heterologous expression and purification of OleT-JE

The expression and purification of wild-type OleT-JE, L176G, and the Δ3aa mutant, were identical. The OleT-JE-containing plasmid was co-transformed into BL21(DE3) with the hemin importer ChuA and the pG-TF2 plasmid (Takara Bio) that encodes for GroEL, GroES and Tig chaperones. One colony was inoculated in 100 mL of modified Terrific Broth (24 g of yeast extract, 12 g of tryptone and 1 g of bactopeptone per liter) that was supplemented with 100 µg/mL ampicillin, 20 µg/mL chloramphenicol and 50 µg/mL kanamycin and grown overnight at 37 °C. The following day, 10 mL of starter culture was used to inoculate 500 mL cultures of Terrific Broth supplemented with 100 µg/mL ampicillin, 20 µg/mL chloramphenicol, 50 µg/mL kanamycin, 125 mg/L thiamine and trace metals. Cultures were grown at 37 °C until $OD_{600nm}$ = 0.6 was reached, and the temperature was reduced to 18 °C and grown for an additional hour until the $OD_{600nm}$ reached ~ 1.5. Cells were then induced with 10 ng/mL tetracycline, 50 µM IPTG and 5 mg/L hemin and grown overnight at 18 °C. The following day, cells were harvested by centrifugation at 6000 g for 10 minutes and the pellet was frozen at -80 °C until further use. Cells were resuspended in 4 mL of Buffer A (50 mM $K_2HPO_4$ pH 8, 300 mM NaCl and 10 mM imidazole) per gram of pellet. Cells were disrupted using a Branson sonifier and stirred for an hour before centrifuging 30 minutes at 16,000 rpm. The supernatant was loaded onto a previously equilibrated nickel-nitriloacetic acid (Ni-NTA) column, washed with buffer A + 25 mM imidazole and eluted with buffer A + 250 mM imidazole. The eluate was diluted 1:1 (vol:vol) with Buffer B (50 mM $K_2HPO_4$ pH 8, 300 mM NaCl, 60 % ammonium sulfate) to reach a final concentration of 30 % ammonium sulfate. The protein was then loaded onto a Butyl-S-Sepharose column equilibrated in buffer C (50 mM

$K_2HPO_4$ pH 8, 300 mM NaCl, 30 % ammonium sulfate), washed with 10 column volumes of the same buffer and subsequently eluted with a linear gradient to 50 mM $K_2HPO_4$ pH 8 over 8 column volumes. Fractions with an absorbance ratio ($A_{418nm}/A_{280nm}$) higher than 0.9 were pooled and dialyzed against 200 mM $K_2HPO_4$ pH 7.5. The protein was concentrated, flash frozen in liquid nitrogen and stored at -80 °C.

### 2.5 UV-Visible Spectroscopy

Optical spectra were obtained using an HP 8453 spectrophotometer. Fatty acid titrations were performed using 6 - 10 µM OleT-JE in 200 mM $K_2HPO_4$ pH 7.5 and the sequential addition of substrate from a 10 mM stock solution. Unlabeled fatty acid substrates ($C_{20}$ through $C_{12}$) were dissolved in a 70:30 (v:v) mix of ethanol and Triton X-100. The labeled 16-doxylstearic acid and DAUDA fatty acids were dissolved in DMSO and ethanol respectively. The amount of solvent added never exceeded 5 % of the total volume of the solution during the course of the titration. The substrate-induced absorption changes at 417 nm were plotted as a function of total substrate concentration. The high affinity of these substrates warrants fitting to a Morrison quadratic expression [22] in order to determine a dissociation constant ($K_D$). We [9, 18-19] and others [13, 23] have described these fitting procedures in previous substrate-binding studies of OleT-JE.

### 2.6 Fluorescence binding experiments

Fluorescence spectroscopy was performed on a Cary Varian Eclipse fluorimeter with conditions identical to the UV-Vis titrations. In experiments that probed the local

environment of DAUDA, an excitation wavelength of 340 nm was used. In studies used to selectively probe OleT-JE-bound DAUDA for binding studies, a Forster Resonance Energy Transfer (FRET) approach was used. The fluorescence from tryptophans of OleT-JE ($\lambda_{excitation}$ = 280 nm, $\lambda_{emission}$ ~ 340 nm) was used to excite bound DAUDA ($\lambda_{emission}$ = 500 - 550 nm). The fluorescence intensity at 500 nm was plotted as a function of the concentration of DAUDA and fit in a similar fashion to the UV/Vis titration data.

### 2.7 Steady-state turnover

Steady-state activity assays were performed as previously described.[24] OleT-JE (10 nmol) was mixed with substrate (1 µmol) in 200 mM $K_2HPO_4$ pH 7.5 in a total volume of 2 mL. 1000 µmol of $H_2O_2$ (also in 2 mL of 200 mM $K_2HPO_4$ pH 7.5) was slowly added over the course of one hour using a syringe pump after which the reaction was immediately quenched with 100 µL of 12 M HCl. For samples analyzed by gas chromatography (GC), unlabeled fatty acids and the 16-DSA probe, internal standards (alkene and fatty acid) were subsequently added and the reaction was extracted with an equal volume of chloroform. The organic phase was concentrated and derivatized with 250 molar equivalents of BSTFA:TMCS (99:1). Samples were incubated at 60 °C for 30 minutes and analyzed by Gas Chromatography-Mass Spectrometry (GC-MS). GC-MS was performed at the University of South Carolina Mass Spectrometry facility with a Hewlett-Packard HP5890 Gas Chromatograph and an Agilent HP-5 column. The following oven conditions were used to detect the products from $C_{20}$ through $C_{16}$ fatty acid metabolism: 170 °C for 3 min, a 10 °C/min linear gradient to 220 °C, a 5 °C/min to 320 °C, and 320 °C for 3 min. The

following oven conditions were used to detect the products obtained from $C_{14}$ and $C_{12}$ fatty acid metabolism: 100 °C for 3 min, a 5 °C/min gradient to 250 °C and a 250 °C for 3 min. Analysis of DAUDA metabolites was done by LC/MS using a Dionics 3000RS and a Chromegabond WR C18 column using absorbance detection at 340 nm. The identity of hydroxylated and alkene products was determined by LC-MS using a Waters QTOF APIUS.

### 2.8 Stopped-flow transient kinetics

#### *2.8.1 Enzyme Preparation*

All P450s were initially peroxide-treated with 15 molar equivalents of $H_2O_2$ and desalted into 200 mM $K_2HPO_4$ pH 7.5 on a PD-10 desalting column (GE Healthcare) to remove adventitiously bound fatty acids. The protein was then concentrated to ~ 200 µM and diluted in 200 mM $K_2HPO_4$ pH 7.5 to a final concentration of 20 µM. Three molar equivalents of fatty acid were subsequently added from a 10 mM stock and incubated at 4 °C for at least 4 hours to ensure complete fatty acid binding. A stock of 10 mM $H_2O_2$ was prepared in $K_2HPO_4$ pH 7.5 and incubated at 4 °C for 4 hours.

#### *2.8.2 Data collection and kinetic analysis*

Stopped-flow experiments were carried out on an Applied Photophysics Ltd. SX20 stopped-flow spectrophotometer. Briefly, each protein stock was rapidly mixed 1:1 with $H_2O_2$ in 200 mM KPi pH 7.5. Single wavelength traces were collected using a photomultiplier tube (PMT) and full spectral data was acquired using photodiode array (PDA) detection. OleT-JE Compound I (Ole-I) and Compound II (Ole-II) decay rates were

obtained by fitting the PMT time courses at 370 nm or 440 nm. The data can be analyzed in ProData software using the following two-summed exponential expression:

$$A_{t,obs} = A_\infty + a_1 e^{-t/t_1} + a_2 e^{-t/t_2} \quad \text{(Eq. 1)}$$

$A_{t,obs}$ is the observed absorbance, *1/t* is the reciprocal relaxation time (RRT) of a particular phase (in $s^{-1}$), *a* is the amplitude of that phase, *t* is time (s) and $A_\infty$ is the final absorbance. The RRTs can be evaluated using the following kinetic model where $Fe^{3+}$(HS) and $Fe^{3+}$(LS) are the high-spin and low-spin forms of the enzyme. Ole-I and Ole-II have their usual designations:

$$Fe^{3+}(HS) + H_2O_2 \underset{k_{-1}}{\overset{k_1}{\rightleftarrows}} Ole-I \overset{k_2}{\rightarrow} Ole-II \overset{k_3}{\rightarrow} Fe^{3+}(LS) \quad \text{(Eq. 2)}$$

Both Ole-I and Ole-II have significant absorption contributions at both 370 and 440 nm wavelengths. However, the RRTs can be assigned based on their amplitudes and apparent rates. The fast phase with larger amplitude ($RRT_1$) can be ascribed to Ole-I decay (also Ole-II formation) where the slower, smaller amplitude phase ($RRT_2$) represents Ole-II decay. The two steps can also be delineated on the basis of the dependence on $H_2O_2$ concentration. In reactions with protiated fatty acids, such as the DAUDA and 16-DSA employed in this study, we have empirically determined that the $RRT_1$ versus [$H_2O_2$] plots yield a linear concentration dependence while $RRT_2$ is $H_2O_2$ independent due to the irreversibility of the C-H bond cleavage in the preceding step. The linear dependence of $RRT_1$ arises from a rate-limiting $H_2O_2$ binding step. As a result, the apparent $K_D$ for $H_2O_2$ binding can be determined by dividing the intercept ($k_{-1}$) by the slope ($k_1$) of the $RRT_1$ versus $H_2O_2$ plot.

### *2.8.3 Transient fluorescence*

Stopped-flow fluorescence studies were performed using the FRET approach described above. The prepared OleT-JE:DAUDA complex was mixed with $H_2O_2$ and data was collected using a fluorescence PMT equipped with a 510 nm bandpass filter. The fluorescence data could be fit to a two-summed expression with RRTs that are significantly slower than those measured for Ole-I and Ole-II decay and are independent of $H_2O_2$. The slower RRT with a positive amplitude corresponds to a decrease in fluorescence (i.e. loss of FRET between OleT-JE and the metabolized DAUDA) and gives the rate of product release from the enzyme.

## 2.9 Spin-probe EPR spectroscopy

### *2.9.1 Sample preparation*

OleT-JE (wild-type or variants) was desalted in 200 mM $K_2HPO_4$ pH 7.5 and diluted to a final concentration of 100 µM. One molar equivalent of 16-doxylstearic acid (16-DSA) from a 26 mM stock prepared in DMSO was added (final DMSO concentration never exceeded 5%). After incubating for 1 hour at 4 °C to ensure complete binding, 0 - 30 molar equivalents of hydrogen peroxide were added. The final OleT-JE and 16-DSA concentrations were 75 µM. The reaction was allowed to incubate for one hour prior to data collection. The samples, approximately 40 µL each, were loaded into glass capillaries and EPR was recorded at room temperature (298 K) using an X-band Bruker EMXplus spectrometer with a microwave power of 5 mW and a modulation amplitude of 0.4 mT.

*2.9.2 Spectral fitting*

EPR simulations were performed using EPRSIM-C developed by Strancar et al.[25] In an aqueous environment, the nitroxide label can freely rotate in any given x, y or z direction giving rise to a sharp three-line spectrum. The rotational correlation time ($\tau_c$) corresponds to the average time it takes to rotate on a single axis before changing directions and can be directly correlated to the hyperfine coupling tensor A and the linewidth of the central line. An isotropic label-label exchange (LLE) model was used to determine the appropriate fitting parameters for free 16-DSA, including the rotational correlation time ($\tau_c$), spin exchange rate ($W_{ex}$), and corrections for polarity. The parameters for OleT-JE-bound 16-DSA were determined using a stoichiometric enzyme:substrate complex fitted to an anisotropic tumbling model (MES) that accounts for the restricted rotational motion of the label with a partial averaging of all rotations. These parameters were determined individually for wild-type OleT-JE and the F-G helix mutants. For the simulation of spectra following the addition of $H_2O_2$, the spectra were decomposed into two components (the bound and free label) using fixed parameters for each species but allowing the weight of each to vary. The goodness-of-fit for all simulations was determined as $\chi^2 < 10$, representing a 95% confidence interval.

## 3. Results

### 3.1 Fluorescent- and EPR-active fatty acids are competent OleT-JE substrates

In order to ensure that the labeled fatty acid (FA) analogs utilized in this study report on structural configurations that are similar to those of prototypical OleT-JE

substrates, the binding and metabolism of the fluorescent FA probe 11-(dansylamino)-undecanoic acid (DAUDA) and the EPR-active 16-doxylstearic acid (16-DSA) were measured using transient and steady-state methods. The structures of these probes are shown at the top of Figure 2.1. The addition of either FA analog to substrate-free OleT-JE resulted in a shift of the Soret maximum from 418 to 392 nm, resulting from the conversion of the enzyme from the low- (LS) to high-spin (HS) ferric state that arises from displacement of the axial water ligand (Figure 2.1A and 2.1B). The measured efficiencies for high-spin conversion at saturating substrate concentrations, roughly 70% for DAUDA

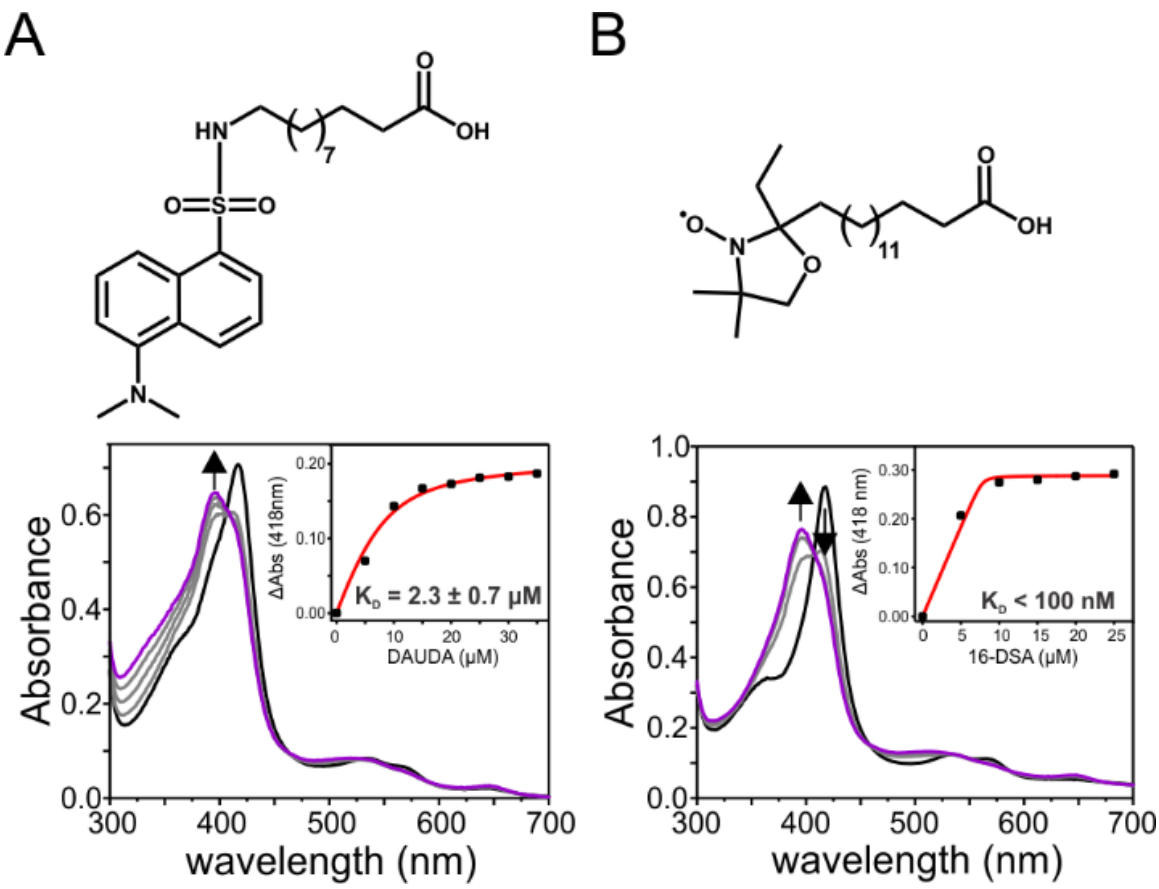


**Figure 2.1** Structure of the (A) 11-(dansylamino)undecanoic acid (DAUDA) and (B) 16-doxylstearic acid (16-DSA) probes utilized in this study (top). UV-Visible binding titrations of DAUDA and 16-DSA with wild-type OleT-JE. The optical changes at 418 nm were fit to a Morrison tight-binding quadratic expression to determine the dissociation constant of each probe with the enzyme (inset).

and 85% for 16-DSA respectively, are comparable to FA substrates of similar chain lengths. The readily observable absorption changes at 418 nm were used to measure the dissociation constant ($K_D$) of both molecules with OleT-JE (Figure 2.1 inset). Typically, the binding free energy of FA substrates to OleT-JE scales with chain length (CL). [9, 18, 23] The $K_D$ values of the probes, summarized in Table 2.1, show a similar trend and have affinities that are very comparable to prototypical long (e.g. $C_{20}$ in the case of 16-DSA) [9, 23] and short ($C_{10}$ and $C_{12}$ for DAUDA) [18, 23] FA substrates that are efficiently decarboxylated by the enzyme. The high-affinity and efficient propensity for spin-state conversion suggest that the probes utilized in this study may adopt very similar configurations within the active-site pocket as OleT-JE substrates. The precise mechanism for substrate-assisted iron-oxo formation from $H_2O_2$ in CYP152 enzymes has yet to be fully clarified. However, it has been proposed, based on analogy to a similar role proposed for an active-site glutamate for chloroperoxidase (CPO) [26-27] and unspecific peroxygenases (UPO),[28] that the substrate-acid is required to facilitate the proton-mediated rearrangement of the ferric-peroxide intermediate through either a hetero- [29] or homo-lytic [30] pathway that generates Compound I. Both mechanisms rely on the positioning of the substrate-carboxylate in close proximity to the heme-iron for the iron-oxo intermediate to rapidly form, in accordance with transient kinetic studies of OleT-JE. [9-10, 18] The OleT-JE:DAUDA and OleT-JE:16-DSA ternary complexes were rapidly mixed with varying amounts of $H_2O_2$, and the reactions were monitored using stopped-flow absorbance spectroscopy. The photodiode array spectra obtained when using a large excess of $H_2O_2$ (5 mM) to trigger the reaction are shown in Figures 2.2A, 2.2B, 2.3A and 2.3B. In both reactions, the high-spin signal had completely disappeared within the 1 millisecond deadtime and was replaced by

traces of Compound I but predominantly the Compound II and ferric low-spin forms of the enzyme. The kinetics for the formation and decay of the Ole-I and Ole-II intermediates were followed at 370 nm and 440 nm. All single wavelength time courses were biphasic in nature and could be fit using two-summed exponential expressions (Figures 2.2 and 2.3, C and D).

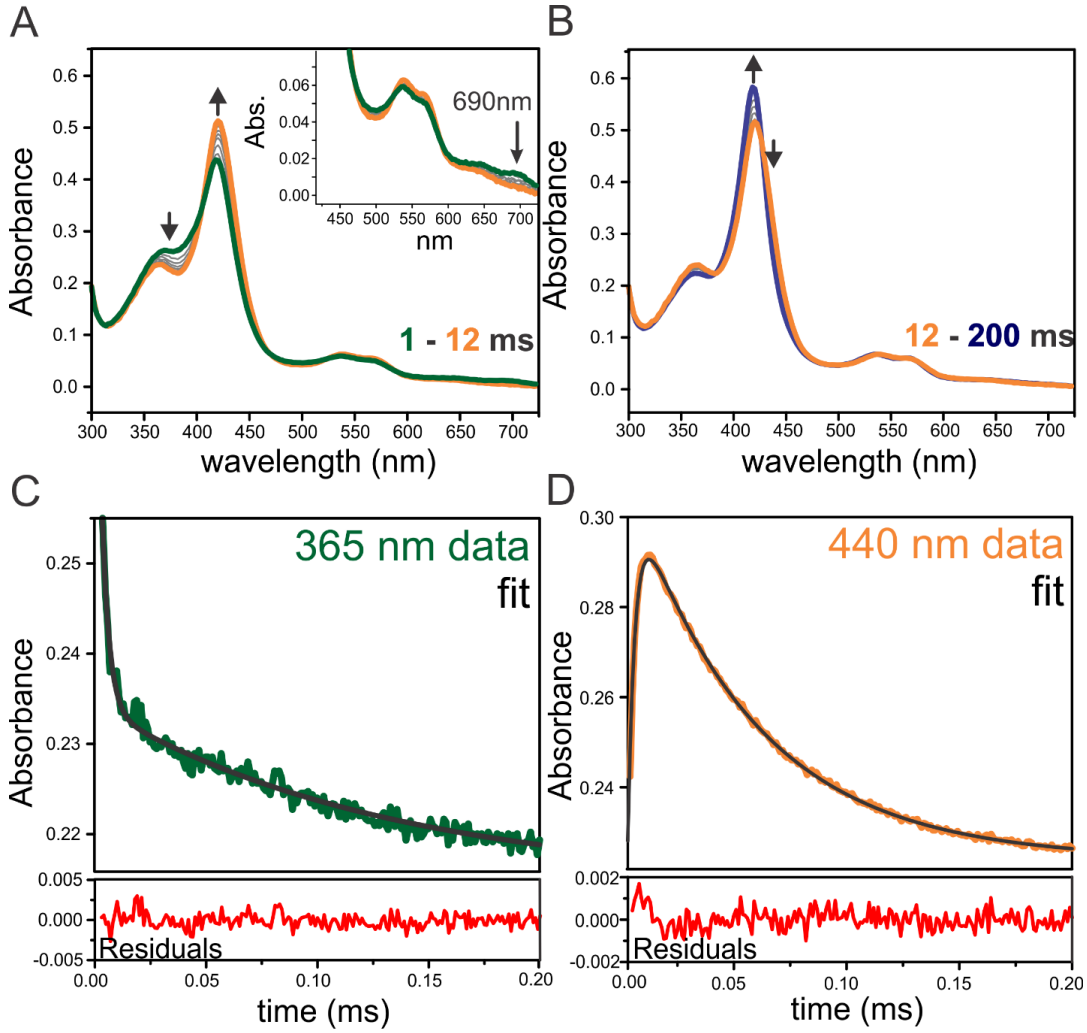


**Figure 2.2** Transient kinetic studies of the reaction of the OleT-JE:DAUDA ternary complex and $H_2O_2$ at 4 °C. Concentrations after mixing were 6 µM and 5 mM respectively. (A, B) Photodiode array spectra show the rapid decay of OleT-JE Compound I (Ole-I) to Compound II over 12 ms followed by the decay of the latter species to the ferric low-spin resting state of the enzyme over 200 ms. (C, D) The decay rate constants of the Ole-I and Ole-II intermediates were measured using a two-summed exponential expression. The decay rate constant of Ole-I (using the first phase at 440 nm or 370 nm) was 400 ± 40 $s^{-1}$, and the decay of Ole-II (using the decay phase of the 440 nm trace) was 13 ± 2 $s^{-1}$.

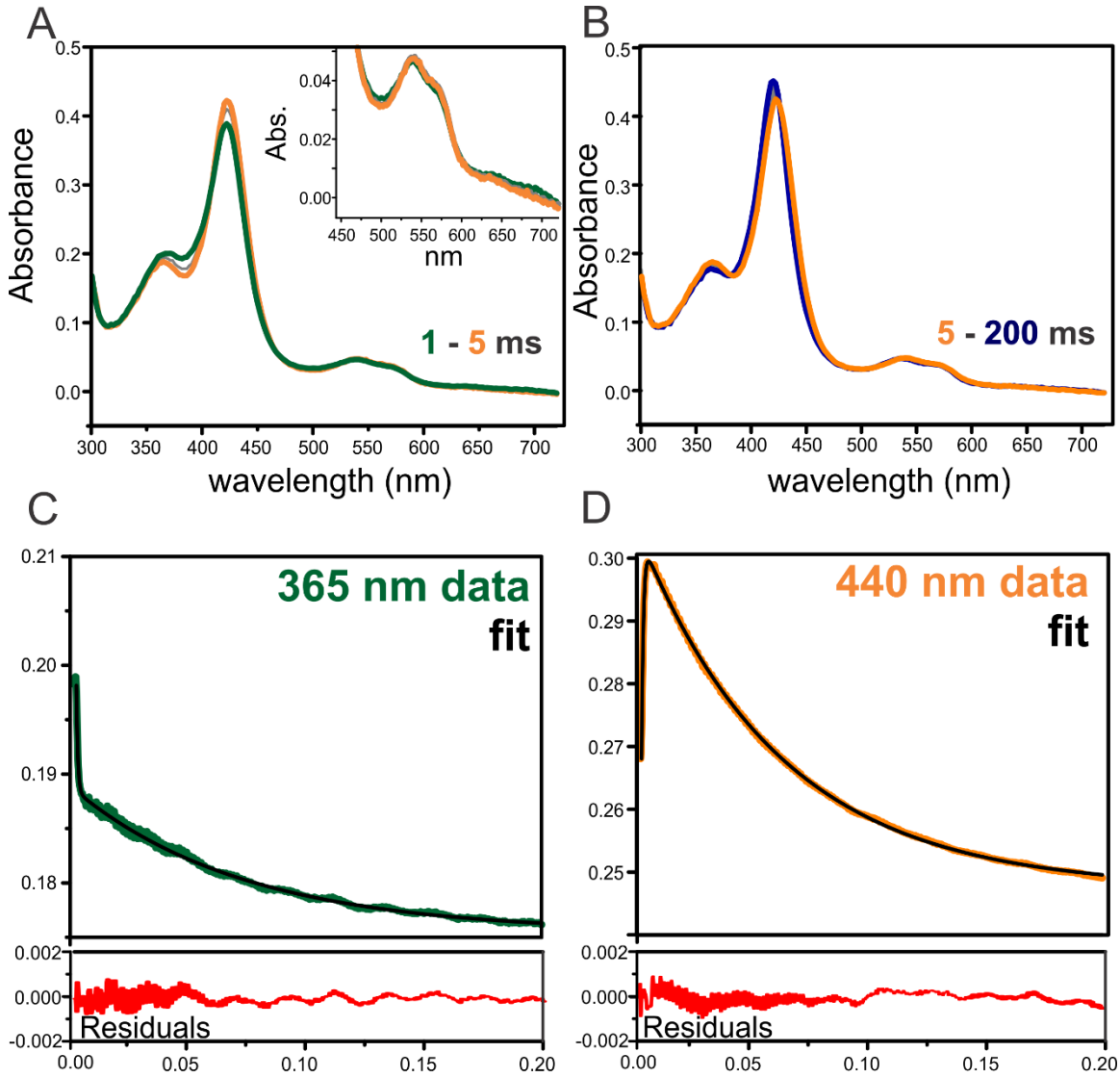


**Figure 2.3** Transient kinetic studies of the reaction of the OleT-JE:16-DSA ternary complex and $H_2O_2$ at 4 °C. Concentrations after mixing were 5 µM and 5 mM respectively. (A, B) Photodiode array spectra show the rapid decay of OleT-JE Compound I (Ole-I) to Compound II over 5 ms followed by the decay of the latter species to the ferric low-spin resting state of the enzyme over 200 ms. (C, D) The decay rate constants of the Ole-I and Ole-II intermediates were measured using a two-summed exponential expression. The decay rate constant of Ole-I (using the first phase at 440 nm or 370 nm) was ≥ 700 $s^{-1}$, and the decay of Ole-II (using the decay phase of the 440 nm trace) was 9 ± 1$s^{-1}$.

As in reactions of $C_{20}$ [10] and $C_{12}$ [18] FAs, there was excellent agreement between the measured reciprocal relaxation times (RRT) corresponding to the decay of Ole-I,

monitored at 370 nm, and the formation of Ole-II at 440 nm, reflecting a direct conversion of the two species. The apparent rates for Ole-I decay were 400 ± 40 $s^{-1}$ for DAUDA and in excess of 700 $s^{-1}$, the fastest RRT that can be accurately measured, for 16-DSA. The rate constants for Ole-II decay were 13 ± 2 $s^{-1}$ and 9 ± 1 $s^{-1}$ respectively. The ability of the probes to efficiently trigger the activation of $H_2O_2$ was further evaluated by plotting the RRT corresponding to Ole-II formation at 440 nm versus $H_2O_2$ concentration. In both cases, the plots revealed a linear relationship with the concentration of oxidant and a non-zero y-intercept (Figure 2.4). We have interpreted this kinetic behavior, which differs from

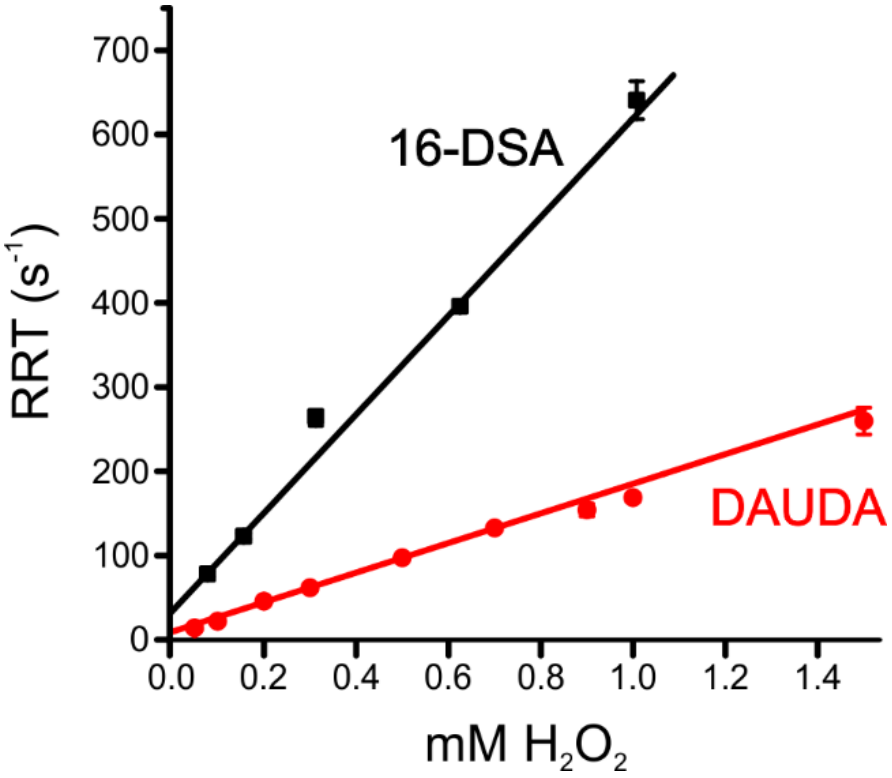


**Figure 2.4** $H_2O_2$ concentration dependence of Ole-II formation. The OleT:DAUDA or OleT:16-DSA complexes were mixed in a 1:1 ratio with varying concentrations of $H_2O_2$ and the reaction was monitored at 440 nm. The reciprocal relaxation time (RRT) corresponding to Ole-II formation was obtained from a two-exponential fitting of the time-course and was plotted vs. $H_2O_2$ concentration. Both substrates showed a linear relationship and a $k_1$ = 585 ± 22 $mM^{-1}$ $s^{-1}$ (16-DSA) and 176 ± 4 $mM^{-1}$ $s^{-1}$ (DAUDA) were obtained from the slopes of the plots. The y-intercept provides the off-rate for $H_2O_2$ binding, $k_{-1}$ = 33 ± 8 $s^{-1}$ (16-DSA) and 9 ± 2 $s^{-1}$ (DAUDA). These values are used to calculate the apparent dissociation constants ($K_D^{H_2O_2}$) shown in Table 2.1.

deuterated substrates that instead exhibit a hyperbolic dependence, as resulting from more facile cleavage of the C-H bond and at least partially rate-limiting $H_2O_2$ activation. The rate constants derived from these plots provide a peroxide on- ($k_1$) and off-rate ($k_{-1}$) that are listed in the legend of Fig. 2.4. These rates were subsequently used to calculate an apparent dissociation constant for $H_2O_2$ ($K_D^{H_2O_2}$). The values, shown in Table 2.1, are very similar to those measured for other OleT-JE substrates. This intimates that the carboxylate of DAUDA (or 16-DSA) enters the active site and very likely adopts a typical binding mode whereby it is stabilized via electrostatic interactions with an active site arginine (Arg245 in OleT-JE), a configuration that is common to all CYP152 enzymes that have been structurally characterized to date. [11, 23, 31]

**Table 2.1.** Comparison of equilibrium substrate dissociation constants and kinetic parameters for $H_2O_2$ activation for wild-type OleT-JE with the probe molecules used in this study and prototypical long- and short-chain length fatty acids.

| Substrate | $K_D$ Substrate (μM) | High-Spin Heme (%) | $K_D$ ($H_2O_2$) (μM) | Reference |
|---|---|---|---|---|
| DAUDA | 2.3 ± 0.7 | 70 | 45 ± 5 | this study |
| 16-DSA | < 0.1 | 85 | 54 ± 20 | this study |
| $C_{20}$ | 0.1 – 0.3[9, 23] | > 95[9, 23] | 100[10] | 9, 10, 23 |
| $C_{12}$ | 2.8 ± 0.4 | 61 | n.d. | 18 |
| $C_{10}$ | 25 ± 8 | 19 | 81 ± 23 | 18 |

The DAUDA and 16-DSA probes were further evaluated as substrates for OleT-JE using steady-state methods. After the controlled addition of $H_2O_2$ over one hour to a reaction mixture containing the wild-type enzyme and DAUDA, the metabolites were analyzed through liquid chromatography mass spectrometry (LC-MS). The absorbance chromatograms and MS profiles of products are shown in Figure 2.5A and 2.5B. DAUDA was completely metabolized by the enzyme and was converted to a single product that eluted later than the substrate. The MS chromatogram of the product (m/z = 389), 46 mass

units smaller than DAUDA, was diagnostic for an alkene that formed from a decarboxylation reaction.

Turnover studies of 16-DSA resulted in a slightly more complex profile of metabolites. Following extraction and derivatization by trimethylsilylation, the resulting products were analyzed by gas chromatography (GC). Assignments were made based on

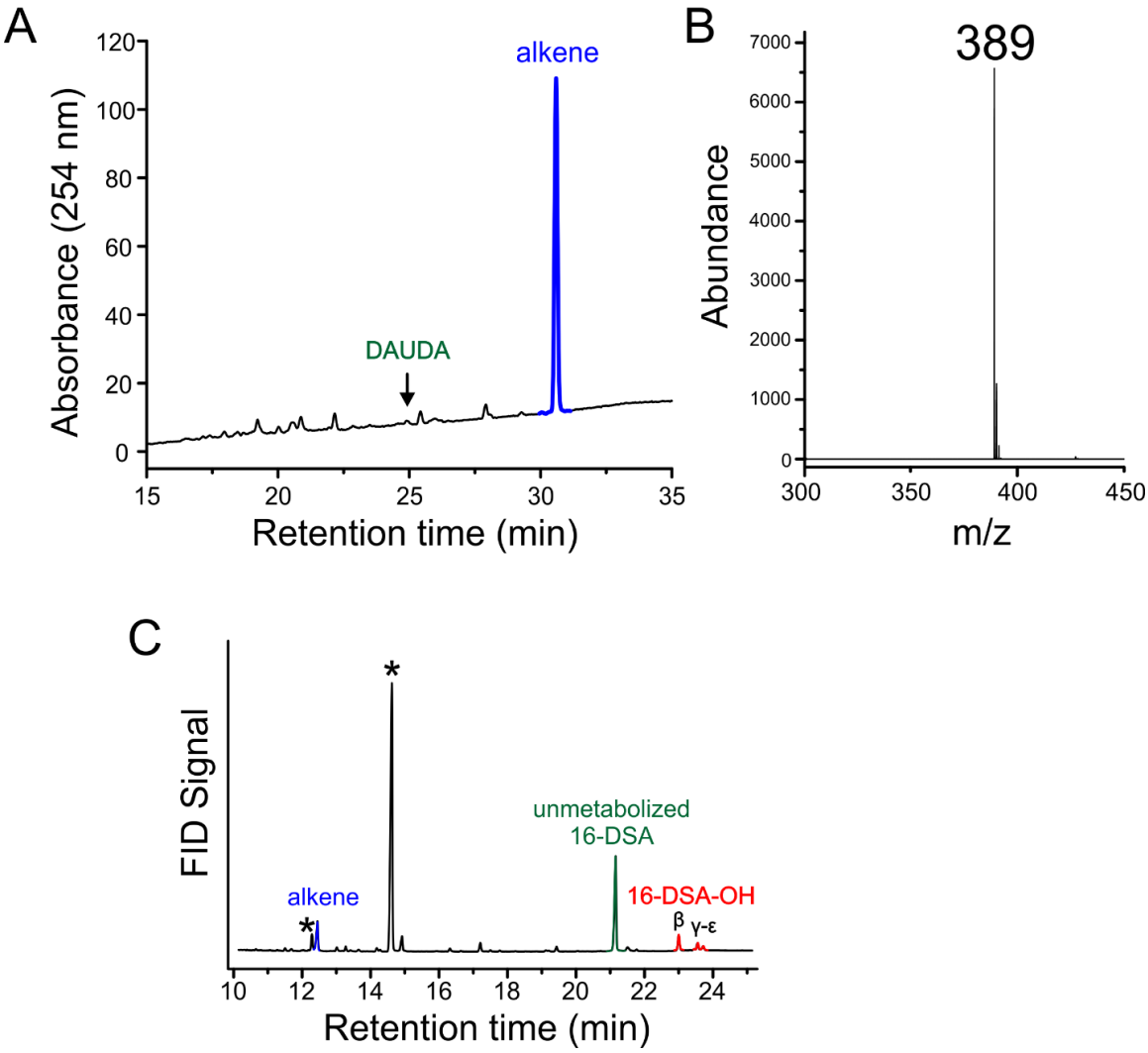


**Figure 2.5** Wild-type OleT metabolism of DAUDA and 16-DSA. Liquid chromatography absorbance chromatograms of the metabolism of DAUDA (A) and mass spectral fragmentation pattern of the decarboxylated DAUDA product (B). Gas chromatogram of the reaction of 16-DSA following extraction with $CHCl_3$ and trimethylsilylation (C). The peaks that are designated by asterisks were also present in control reactions where $H_2O_2$ was omitted.

the characteristic retention patterns we have made for unlabeled FA substrates in prior studies.[18-19] Formation of the alkene product, 15-doxyl-pentadecene, was accompanied by fatty-alcohols that were equally distributed at the Cβ and Cγ positions.

In sum, the product distributions from both labeled substrates confirm that the chemoselective and regioselective features of the enzyme are largely preserved for the probes despite the addition of the bulkier dansyl- and doxyl- groups appended to the FA tail (Table 2.2).

**Table 2.2.** Metabolic profiles of the OleT-JE wild-type and mutant enzymes in steady-state turnover studies of the DAUDA and 16-DSA reporter probes following analysis by LC-MS and GC. Alcohol and alkene products are expressed as a fractional percentage of total products formed. The composition of individual alcohol products is shown in parentheses. The $C_\beta$ regiospecificity is defined as the fractional percentage of alkenes and $C_\beta$ alcohols over total products formed by the enzyme.

| Enzyme | Substrate | Alcohol (%) | Alkene (%) | Cβ Regio-selectivity (%) | Conv. (%) |
|---|---|---|---|---|---|
| Wild-Type | DAUDA | 0 | 100 | 100 | 100 |
| | 16-DSA | 72.2 (0 % α, 52% β, 48 % γ) | 27.8 | 65.3 | 29.1 |
| L176G | DAUDA | 47.5 (n.d.) | 52.5 | n.d. | 98.3 |
| | 16-DSA | 100 (18 % α, 65 % β, 17 % γ+δ) | 0 | 65.0 | 45.9 |
| Δ3aa | DAUDA | 73 (n.d.) | 27 | n.d. | 28.0 |
| | 16-DSA | 100 (0 % α, 95 % β, 5 % γ+δ) | 0 | 95.0 | 87.0 |

n.d. MS methods do not resolve the absolute regiospecificity of the DAUDA alcohols, but place the major hydroxylated species at Cβ or further

### 3.2 Conformational changes and slow product-release in the metabolism of DAUDA

The solvatochromic nature of the dansyl fluorophore of DAUDA was used as a reporter for any structural changes that may accompany binding or metabolism by OleT-JE. The emission profile of free DAUDA upon excitation at $\lambda_{ex}$ = 340 nm is compared to that of the probe when it is bound to the enzyme. The latter was prepared through the addition of a small molar excess of DAUDA to OleT-JE followed by desalting unbound probe. As a result, the fluorescence spectra only reflect the emissive properties of the bound substrate. In an aqueous environment, the dansyl group has an emission maximum ($\lambda_{em}$) ~ 560 nm. The emission spectrum of free DAUDA in aqueous buffer is shown in Fig. 2.6A as a reference (grey spectrum). When the environment surrounding the dansyl group becomes less polar, the $\lambda_{em}$ typically shifts to a lower wavelength and is often accompanied by a large increase (as much as 50-fold) in emission intensity. Such changes have been well-documented for the binding of DAUDA to hydrophobic sites in proteins such as albumin. [32] The maximum emission wavelength of the OleT-JE:DAUDA complex exhibits a 60 nm red-shift to $\lambda_{em}$ ~ 500 nm but the fluorescence intensity remains relatively unchanged relative to that of the free probe (Fig. 2.6A, red spectrum). Immediately upon the addition of $H_2O_2$ to the enzyme:substrate complex, however, a large increase in the fluorescence (approximately 5-fold) was observed (Fig. 2.6A, blue spectrum). The origin for the apparent structural rearrangements that occur during the turnover of DAUDA was further probed by stopped-flow fluorescence measurements at 4 $^{o}$C. In order to specifically

probe the fluorescence of the bound DAUDA during catalysis and to minimize possible photobleaching, a Förster resonance energy transfer (FRET) approach was used. At least 8 tryptophans are estimated to be within the 20 Å Förster distance to the dansyl group and were used as donors ($\lambda_{ex}$ = 280 nm, $\lambda_{em}$ ~ 300 nm) to excite DAUDA when it was bound in close proximity. Rapid mixing of the DAUDA:OleT-JE complex with excess $H_2O_2$ under conditions that matched those of the stopped-flow absorption experiments described earlier (5 mM $H_2O_2$ post-mix at 4 °C) revealed a relatively rapid increase in fluorescence intensity (k ~ 1.8 $s^{-1}$) followed by a much slower rate of decay (k ~ 0.1 $s^{-1}$) that could be approximated by a two-summed expression (Figure 2.6B). The RRT for the loss of fluorescence in particular is much slower than that measured for the rate limiting step (Ole-II decay) from stopped-flow absorption measurements of the DAUDA single turnover reaction.

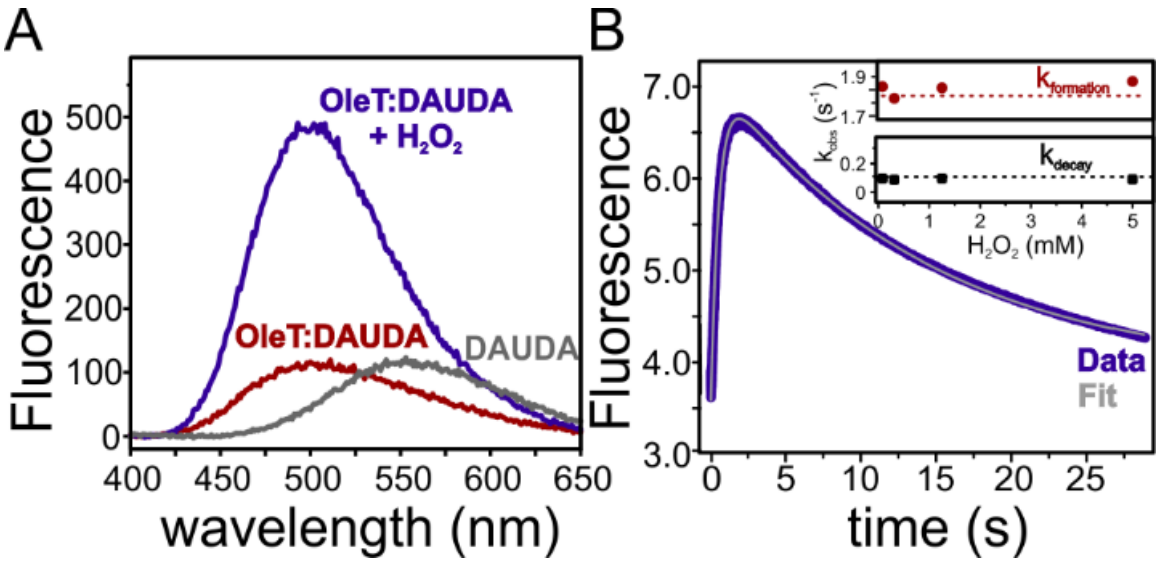


**Figure 2.6** Fluorescence changes in the OleT metabolism of DAUDA. (A) Comparison of the emission spectra of a 35 μM solution of DAUDA in solution (grey), bound to OleT (red), and immediately following the addition of 5 mM $H_2O_2$ to initiate decarboxylation. (B) Rapid mixing of a 10 μM OleT:DAUDA with 5 mM $H_2O_2$ at 4 °C. The fluorescence time-course is fit to a two-summed exponential expression. The observed rates associated with large fluorescence changes are plotted as a function of $H_2O_2$ (inset).

If either phase in the transient fluorescence profile corresponds to a step in the reaction that follows the irreversible abstraction of the substrate Cβ hydrogen atom, it should be kinetically separated from the $H_2O_2$ binding event. The inset to Figure 2.6B shows that this is indeed the case and that both rates are insensitive to oxidant concentration.

### 3.3 The OleT-JE F-G loop regulates product egress

The increase in fluorescence during DAUDA metabolism by OleT-JE is most easily interpreted as a change in the local environment of the dansyl probe that is coincident with, or shortly follows, the decay of Ole-II. This is proceeded by the slow release of the product from the enzyme, resulting in a large loss of FRET efficiency. Intriguingly, sluggish steady-state turnover rates (~ 0.2 $s^{-1}$) have been measured for the turnover of palmitic acid ($C_{16}$) by OleT-JE. [7] This is several orders of magnitude slower than the rate of hydroxylation of myristate ($C_{14}$) by the CYP152 hydroxylase P450 BSβ. [33] A pairwise comparison of the crystal structures of eicosanoic ($C_{20}$) acid-bound OleT-JE[23] and the palmitate- ($C_{16}$) bound BSβ hydroxylase[11] reveal interesting differences in FA coordination (Figure 2.7). In particular, the binding of the longer CL substrate in OleT-JE is accommodated by an F-G loop that is two amino acids longer than that of the corresponding region of BSβ. In OleT-JE, a hydrophobic interaction between L176 and the FA helps to reinforce a kink in the substrate acyl-chain that originates at the $C_{12}$ position. Provided that the binding of DAUDA adopts a similar arrangement, as steady state and transient studies would seem to indicate, the surrounding polarity of the dansyl fluorophore would be expected to be largely influenced by L176 and neighboring residues.

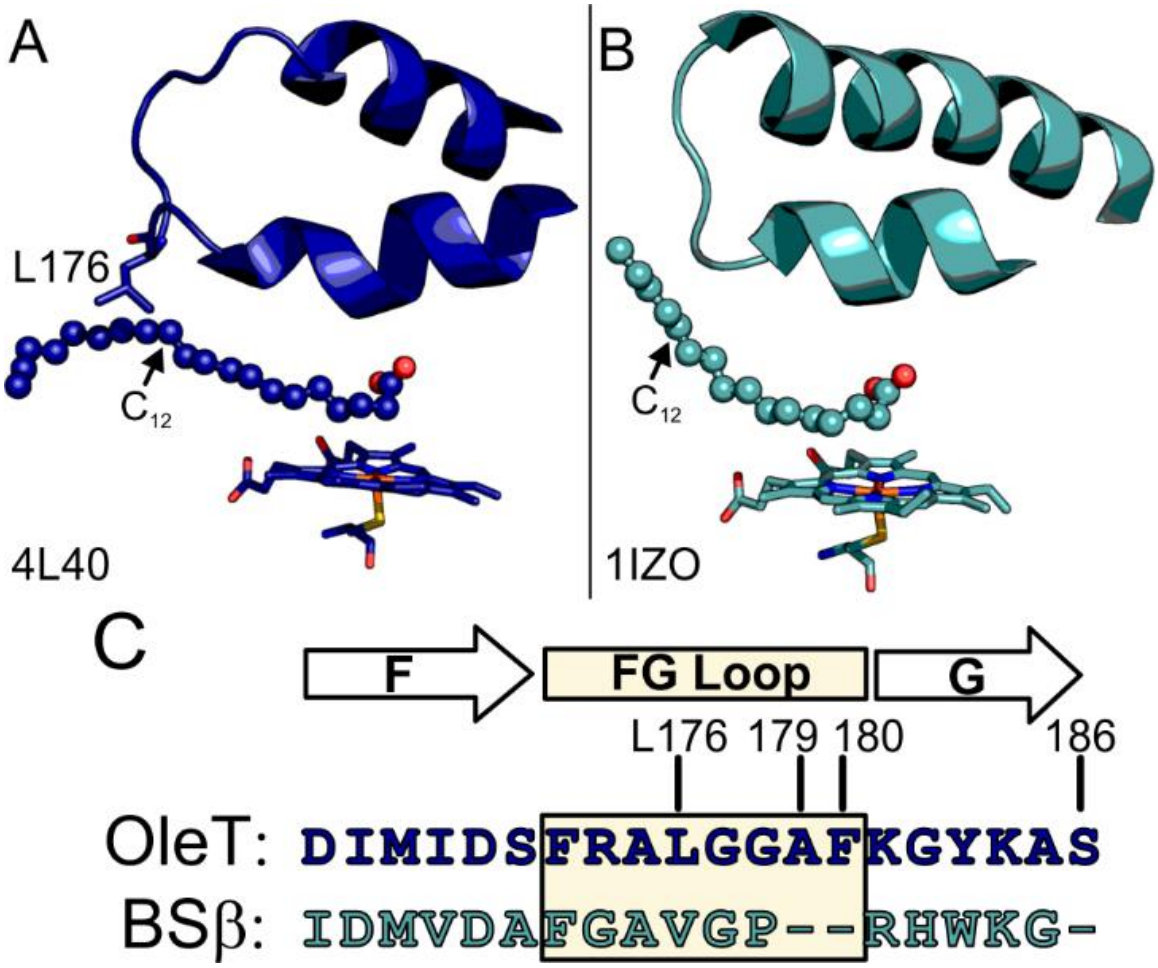


**Figure 2.7** Comparison of the crystal structures of (A) eicosanoic acid-bound OleT (PDB: 4L40) and (B) palmitate-bound cytochrome P450 BSβ. The $C_{12}$ position of the substrate is indicated as well as L176 on the FG loop. (C) Sequence alignment of the F-G loop and adjoining F and G helices of OleT and BSβ. The sites of mutagenesis explored in this study are indicated.

The F-G loop and adjoining helices have been shown to undergo large structural changes in several CYPs including CYP101,[34-37] P450 BM3, [38-39] CYP119,[40] and CYP2B4,[41] upon the binding of substrate. In addition to playing a crucial role in regulating substrate access, recent mutagenesis studies by Arnold and colleagues, guided by molecular dynamics calculations, have shown that relatively minor substitutions in this

flexible region also influence CYP regiospecificity.[42] For OleT-JE, turnover studies conducted by several laboratories have shown that the chemoselectivity of the enzyme generally shows a bimodal distribution with substrate CL. The enzyme efficiently decarboxylates long ($C_{18}$ – $C_{20}$) and short ($C_{10}$) CLs but the metabolism of $C_{12}$ – $C_{16}$ substrates is accompanied by the production of variable amounts of fatty-alcohols, typically at the Cβ position. [7, 9, 13, 17-18, 23] This implies that additional anchoring of the substrate from the F-G loop may be an important point of contact for controlling the chemical outcome, particularly for mid-CL substrates. A relatively conservative mutation was generated that was designed to limit van der Waals interaction between the F-G loop and the FA (L176G). This was accompanied by the design of a triple-deletion mutant (ΔA179, ΔF180, ΔS186) to approximate the loop structure of BSβ by removing the extra two residues of the FG loop and adjoining G-helix (Figure 2.7C). For simplicity, we refer to the latter construct as Δ3aa hereafter. Both mutants were successfully expressed and purified and exhibited typical low-spin heme spectra. The binding of eicosanoic acid (EA), DAUDA, and 16-DSA was tested by optical absorption spectroscopy. Unlike the wild-type enzyme, all three substrates failed to induce any significant spin-shift in the L176G or Δ3aa OleT-JE mutants (Figure 2.8). To verify that the variants did not introduce any wholesale structural changes that eliminated FA binding altogether, the FRET approach was used to interrogate the binding of DAUDA to OleT-JE. Upon the addition of the fluorescent substrate, efficient quenching of the tryptophan fluorescence at 300 nm was observed and accompanied by an emission from DAUDA at $\lambda_{em} \sim 500$ nm (Figure 2.9A).

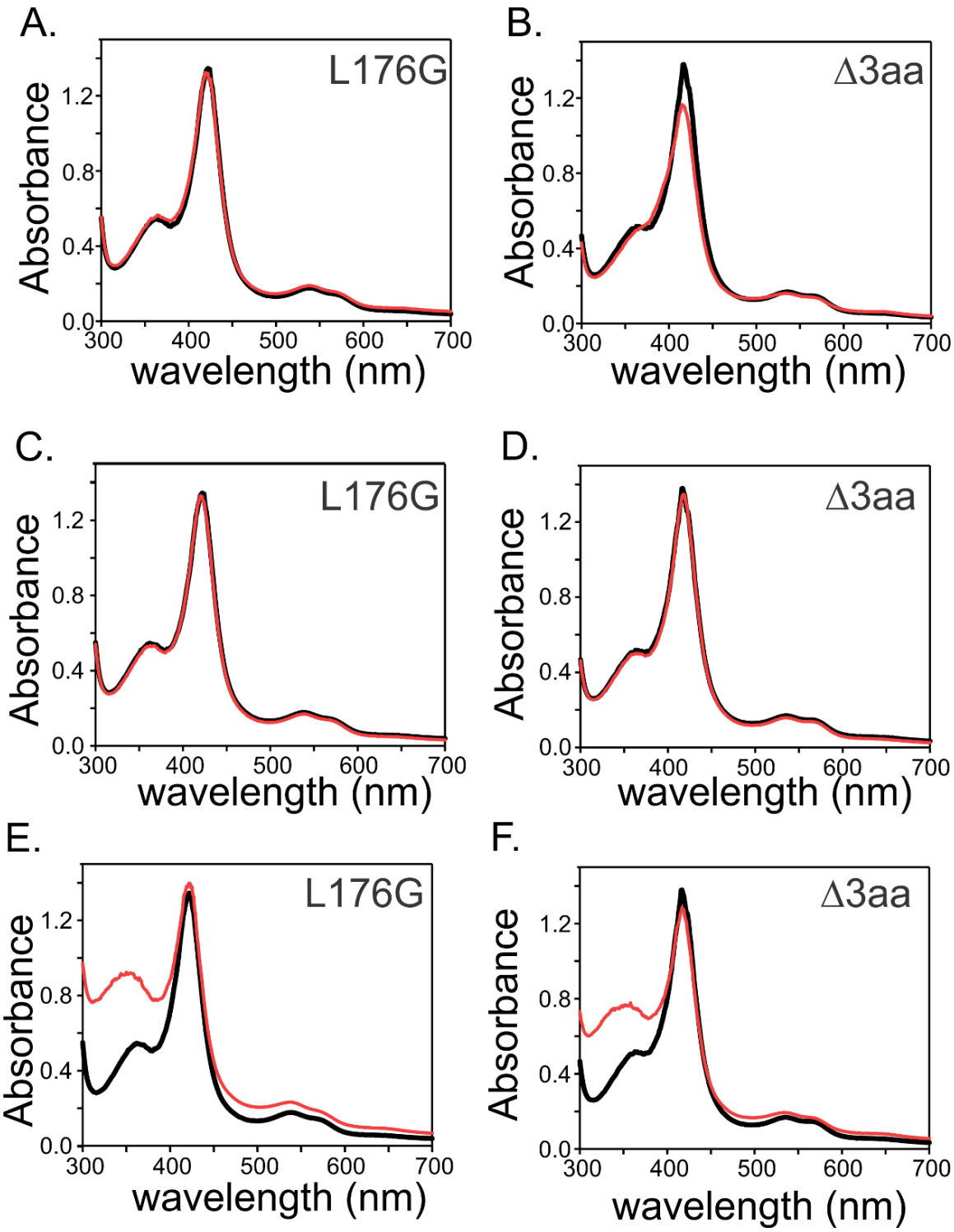


**Figure 2.8** Optical absorption spectroscopy of the L176G and Δ3aa mutant in the absence (black) and upon the addition (red) of various fatty acids. (A, B) 50 μM eicosanoic acid; (C, D) 50 μM 16-DSA; or (E,F) 300 μM DAUDA was added to 12 μM OleT. The 350 nm absorbance in E and F derives from excess free DAUDA.

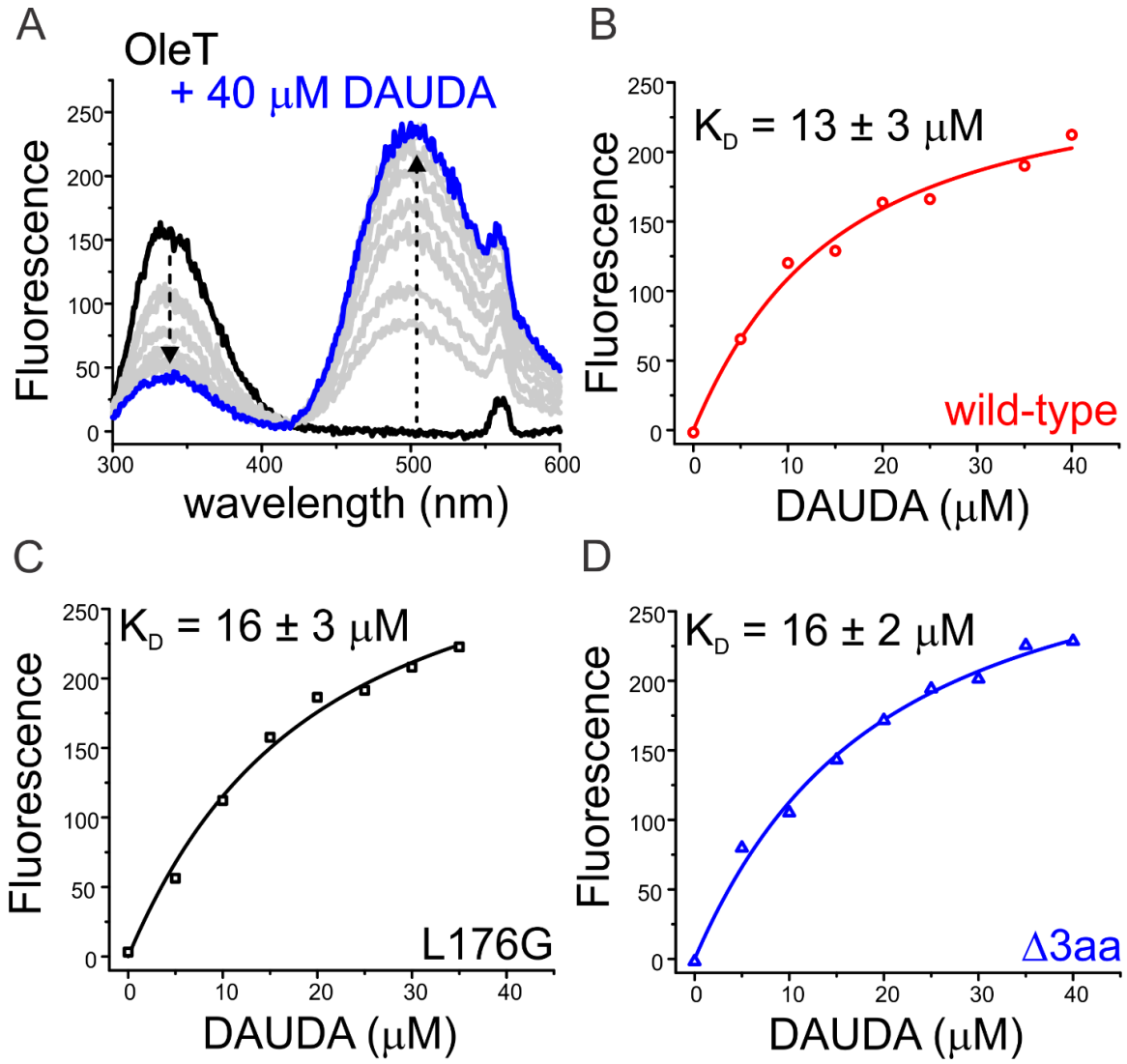


**Figure 2.9** Fluorescence titration studies of wild-type (WT), L176G, and Δ3aa OleT-JE with DAUDA. The fatty acid was titrated into 5 μM OleT-JE and the emission spectrum, using $\lambda_{ex}$ = 280 nm was collected. The fluorescence intensity at 500 nm was plotted as a function of DAUDA concentration and dissociation constants ($K_D$) were determined by fitting the data to a Morrison quadratic function.

Using the FRET response as a binding-probe, the dissociation constants of DAUDA with wild-type OleT-JE and the two variants were measured. The $K_D$ values were similar for all three enzymes, demonstrating that the variants were able to bind the labeled-FA with an affinity comparable to wild-type OleT-JE (Figure 2.9B-D). The L176G:DAUDA and

Δ3aa:DAUDA complexes were subsequently mixed with excess $H_2O_2$ under the same conditions used for the wild-type enzyme in Figure 2.6, and the fluorescence at $\lambda_{em} > 500$ nm was monitored by stopped-flow fluorescence. Both mutants exhibited a drastic reduction in the maximal emission intensity that could be observed. Notably, the fluorescence decay was also much faster in the mutants (Figure 2.10). This implies that the structural changes accompanied with formation of the stable enzyme:product complex in the wild-type enzyme either did not occur or were much more transient in nature, resulting in more facile release of product from the active site.

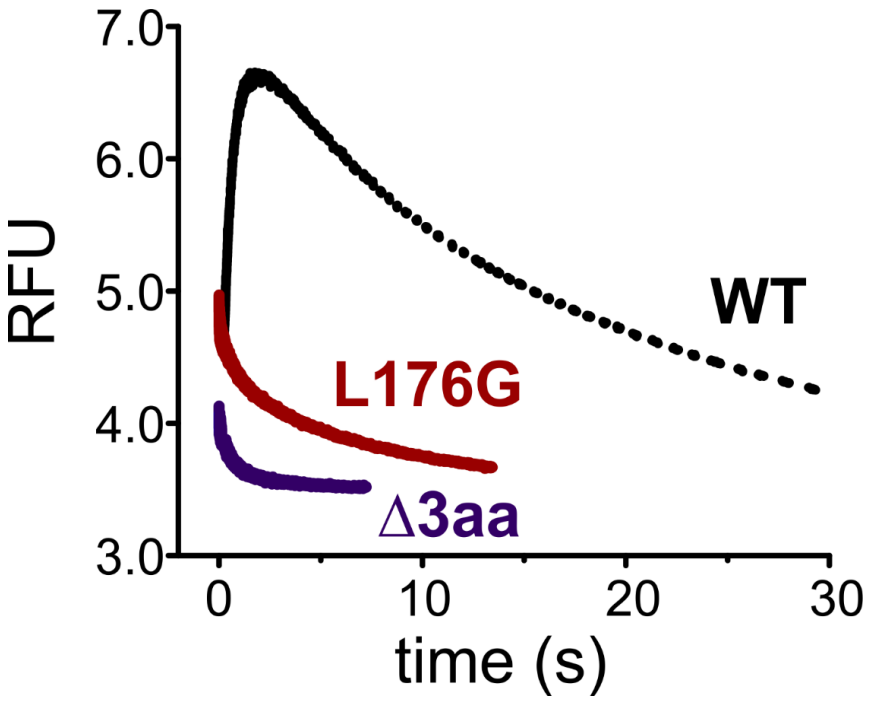


**Figure 2.10** Transient fluorescence changes upon rapid mixing of a wild-type (black), L176G (red) or Δ3aa (blue) OleT-JE:DAUDA ternary complex with excess $H_2O_2$ at 4 °C. Concentrations of OleT-JE and $H_2O_2$ were 10 uM and 5 mM after mixing respectively. An excitation wavelength of 280 nm was used and fluorescence was collected using a 510 nm bandpass filter.

The longer 16-DSA substrate was used as an auxiliary probe to verify the influence of the F-G loop on the substrate-coordination and product release steps. The electron paramagnetic resonance (EPR) spectrum of the doxyl-linked FA is particularly sensitive to the local environment at the nitroxide label. The EPR spectra of OleT:16-DSA complexes, prepared with the wild-type and L176G and Δ3aa OleT mutants, are shown in Figure 2.11. The anisotropic broadening of the spectra and diagnostic shift of the low-field signal, relative to that of free 16-DSA in solution, verified that like DAUDA, the loop mutants are fully capable of binding the FA analog. Fitting of the spectra for the OleT:DAUDA complexes using an anisotropic model (Table 2.3) provided rotational correlations times (RCT or $\tau_c$) for the bound probe.

**Table 2.3:** Fitting parameters for free 16-DSA in solution and for the OleT:16-DSA complexes using EPRSIM-C. An isotropic label:label exchange (LLE) model was used to fit the spectrum of free 16-DSA and an anisotropic tumbling model (MES) that accounts for restricted rotational motion of the nitroxide-label was used to fit the OleT:16-DSA complexes.

| Parameter | Free 16-DSA | Wild-Type | Δ3aa | L176G |
|---|---|---|---|---|
| $T_c$ | 0.112 ns | | | |
| W | 1.5 G | 4 G | 4 G | 4 G |
| $W_{ex}$ | 0.943 G | | | |
| $P_a$ | 1.0778 | 1.0021 | 1.0021 | 1.0018 |
| $P_g$ | 0.99985 | | | |
| thθ | - | 0.55 rad | 0.5 rad | 0.52 rad |
| fiθ | - | 0.33 rad | 0.42 rad | 0.4 rad |
| $t_c$ | - | 0.383 ns | 0.383 ns | 0.338 ns |
| $P_r$ | - | -0.07 | -0.07 | -0.067 |

$T_c$ = isotropic tumbling time; W = broadening constant; $W_{ex}$ = spin exchange rate; $P_a$, $P_g$ = polarity correction terms; thθ = main cone angle; fiθ = asymmetry angle; $t_c$ = effective rotational correlation time; $P_r$ = proticity

The 16-DSA:OleT complexes exhibit very similar RCTs ($\tau_c \sim 0.4$ ns) that are significantly higher than that of 16-DSA in solution ($\tau_c \sim 0.1$ ns). Nonetheless, these RCTs are considerably smaller than those measured for other FA-binding proteins such as lipoxygenase [43] or serum albumin [44] ($\tau_c > 10$ ns). The enhanced mobility suggests that the longer acyl chain (relative to DAUDA) allows the probe to fluctuate around the entry-point of the binding channel of OleT. However, the doxyl group is largely unrestricted in nature.

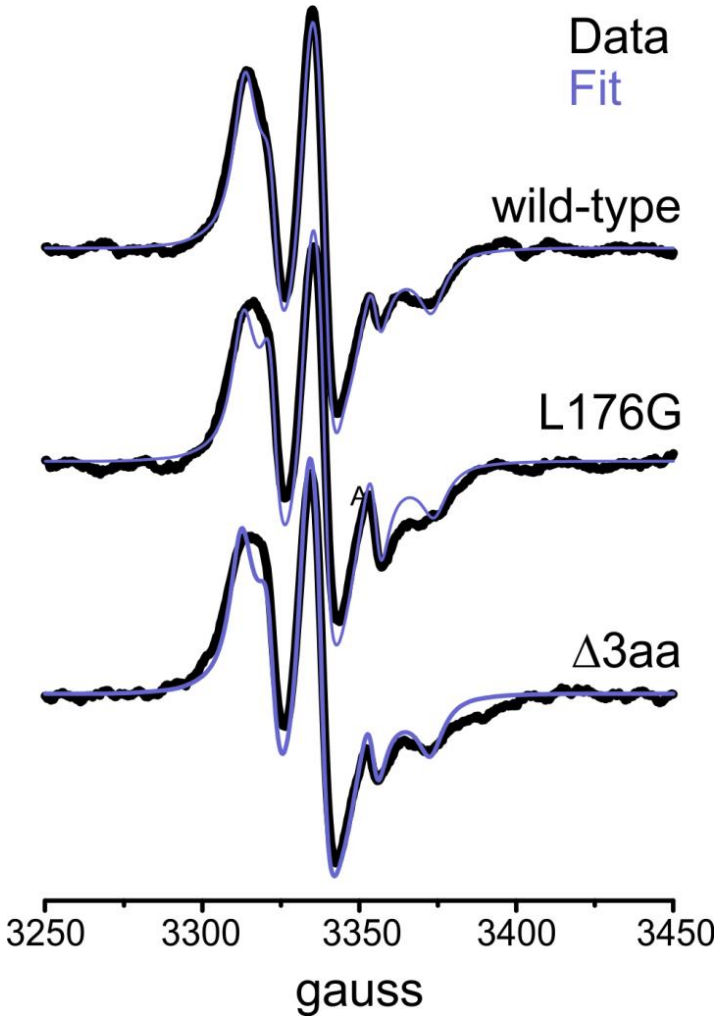


**Figure 2.11** Room temperature electron paramagnetic resonance spectra of 16-DSA:OleT-JE complexes prepared with the wild-type (top), L176G (middle), or Δ3aa mutant enzymes (black). The spectral fitting procedures using EPRSIM-C are described in the methods. The parameters used for fitting are provided in Table 2.3

The ability to readily delineate between the EPR spectra for the bound- and free-DSA probe provides, in principle, a way to determine if the F-G loop synchronizes the release of a longer CL product that more closely approximates native metabolism. The OleT:16-DSA complexes were mixed with varying amounts of $H_2O_2$, and EPR spectra were collected after incubation for one hour at 4°C. Simple spectral addition procedures using the component spectra allowed a determination of the fraction of the label bound to the enzyme, presumably as a product form (Figure 2.12).

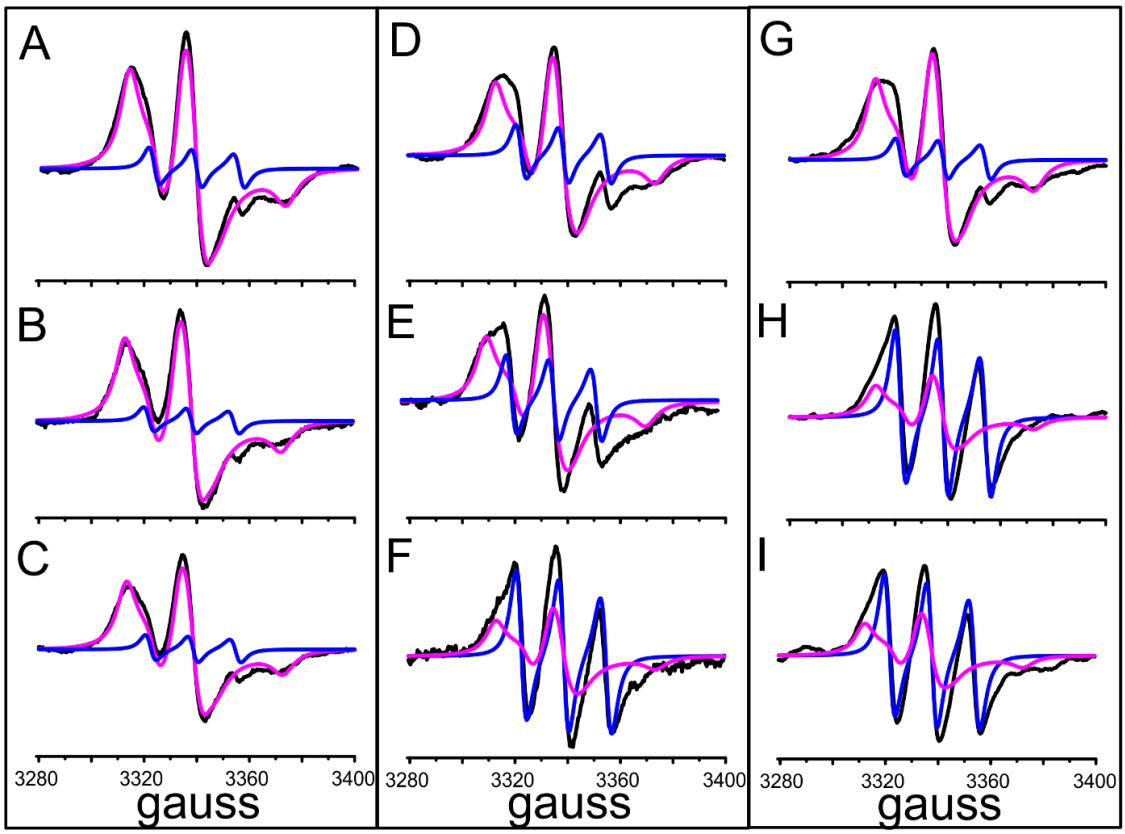


**Figure 2.12** EPR spectra of wild-type (A-C), L176G (D-F), and Δ3AA OleT:16-DSA complexes following the addition of 5 (A, D, G), 10 (B, E, H), or 30 molar (C, F, I) equivalents of $H_2O_2$ and incubation for one hour. The data (black) were fit to bound- (pink) and free- (blue) components using differential weighting of the spectral fitting parameters listed in Table S1.

Although these approaches do not provide as direct of a kinetic read-out for product egress as DAUDA fluorescence, the results clearly show that slow product release is a general feature of OleT and does not solely result from the attached probe (Figure 2.13). For example, despite the addition of 30 molar equivalents of $H_2O_2$ to wild-type OleT:16-DSA, the vast majority of the probe (> 95 %) remained bound to the enzyme. In contrast, paired reactions with the L176G and Δ3aa mutants resulted in a much larger fraction (> 40 %) of the free probe after incubation with the oxidant. Taken together with the fluorescence data and the relatively sluggish steady-state rates for OleT turnover, this implies that

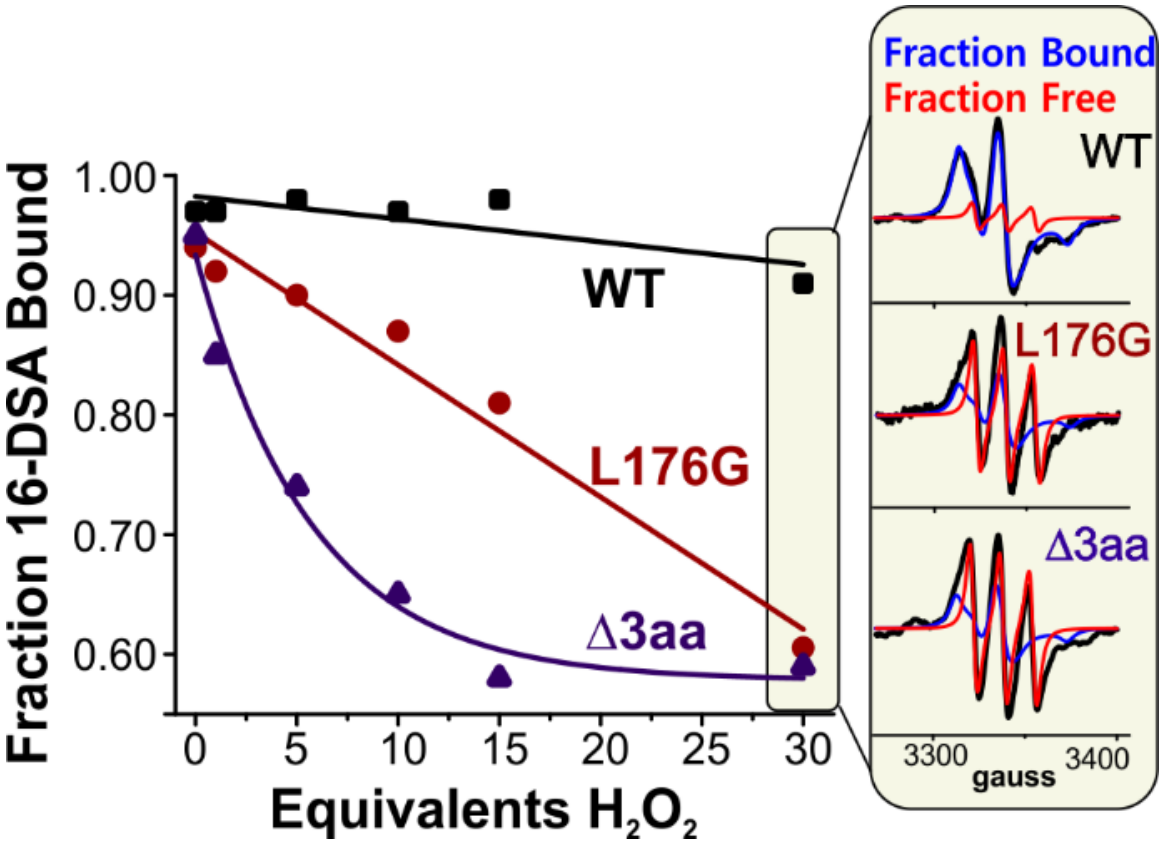


**Figure 2.13** Fraction of 16-DSA bound to wild-type (WT), L176G, and Δ3aa after incubation of the enzyme:substrate complex with $H_2O_2$ after one hour at 4°C. The fraction bound was determined from spectral addition procedures using the fitting parameters determined for the free and bound labels. The inset shows an example of these fitting procedures after the addition of 30 equivalents of $H_2O_2$ to the enzyme:substrate complex.

structural changes at the F-G loop serve to limit the rate of product egress and that this may represent the overall rate-limiting step in OleT catalysis.

### 3.4 Distal control of OleT-JE chemo- and regio-selectivity

Despite lacking a spin-shift, it is evident from the FRET responses upon the addition of DAUDA and the EPR spectra of the OleT:16-DSA complexes, that FA substrates are capable of binding to both the L176G and Δ3aa variants. In the absence of any long-range coordinated effects on the cysteine proximal ligand, which would seem unlikely, this implies that the F-G loop may also influence the binding-modes of substrates or alter the mobility of FAs within the OleT pocket, resulting in more active site hydration. The lack of high-spin conversion with the mutants precludes the detection of Ole-I and Ole-II intermediates, as the hexacoordinate low-spin enzyme only reacts slowly with $H_2O_2$. The array of products formed by the mutants, however, is highly revealing. The metabolic profiles of the labeled FAs and OleT mutants are shown in Table 2 to facilitate comparison with the wild-type. LC-MS analysis of the products obtained from DAUDA metabolism revealed a mixture of at least three new products that were more polar than the substrate (Figure 2.14).

MS of these new species revealed a parent ion at m/z = 451, consistent with introduction of a hydroxyl group, and a progressive decrease in the level of alkene from wild-type, to L176G, to Δ3aa. MS/MS analysis of the alcohols places the regiospecificity of C-H abstraction for most of the alcohol products at the Cβ-H position or further. However, absolute assignment is not possible. Nonetheless, it is evident that introduction

of the loop mutations predisposes OleT towards hydroxylation. The combined loss of anchoring from the substrate-dansyl group and the F-G loop led to more dramatic alterations in the chemoselectivity of 16-DSA oxidations.

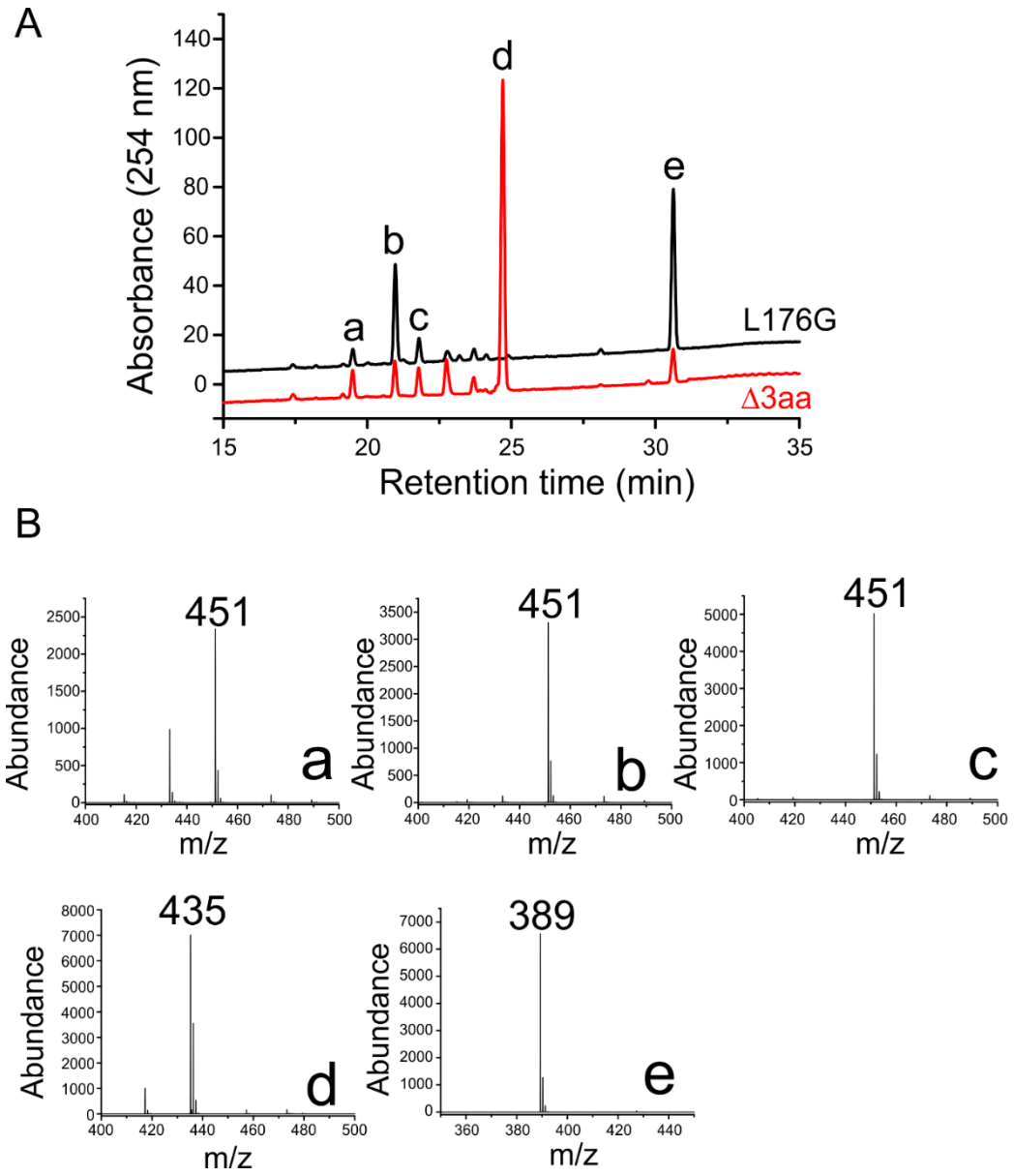


**Figure 2.14** Metabolism of DAUDA by the L176G and Δ3aa OleT mutants. Liquid chromatography absorbance chromatograms of the metabolism of DAUDA (A) and mass spectral fragmentation pattern of the decarboxylated and hydroxylated FA products.

The products from 16-DSA metabolism showed a progressive increase in the total turnover numbers for L176G and Δ3aa, consistent with more efficient steady-state turnover rates due to an acceleration of the product release step. Rather than exhibiting mixed chemoselectivity, GC analysis only revealed the presence of fatty-alcohol metabolites, even though the Cβ regioselectivity of C-H abstraction was largely retained.

The products generated from more traditional FA substrates revealed even more dramatic alterations on the array of products formed (Figure 2.15). The product distributions of the wild-type enzyme are very similar to those recently reported by Munro and colleagues, and demonstrate that even though OleT is capable of decarboxylating a broad range of substrates, the metabolism of $C_{12}$ – $C_{16}$ FAs is accompanied by the presence of a significant fraction of Cβ-alcohols. [13] The L176G mutant results in a tangible loss of decarboxylation activity. With substrate CLs ≤ $C_{14}$, the enzyme exclusively hydroxylates substrates. Loss of stabilization from the F-G loop also results in a significant loss of regiospecificity. For the $C_{12}$ FA substrate, alcohol products were observed that extended as far as the Cε position. A significant fraction (~30 %) of new metabolites were detected that eluted much later than alcohols and had masses (m/z = 415) much larger than those expected for single oxidations. Results from the Δ3aa mutant were comparable to the single amino acid variant. A complete loss of decarboxylation activity occurred with substrates with a CL of $C_{16}$ and lower and wide distribution of fatty alcohol products, many at positions far-removed from the carboxylate-head, were observed.

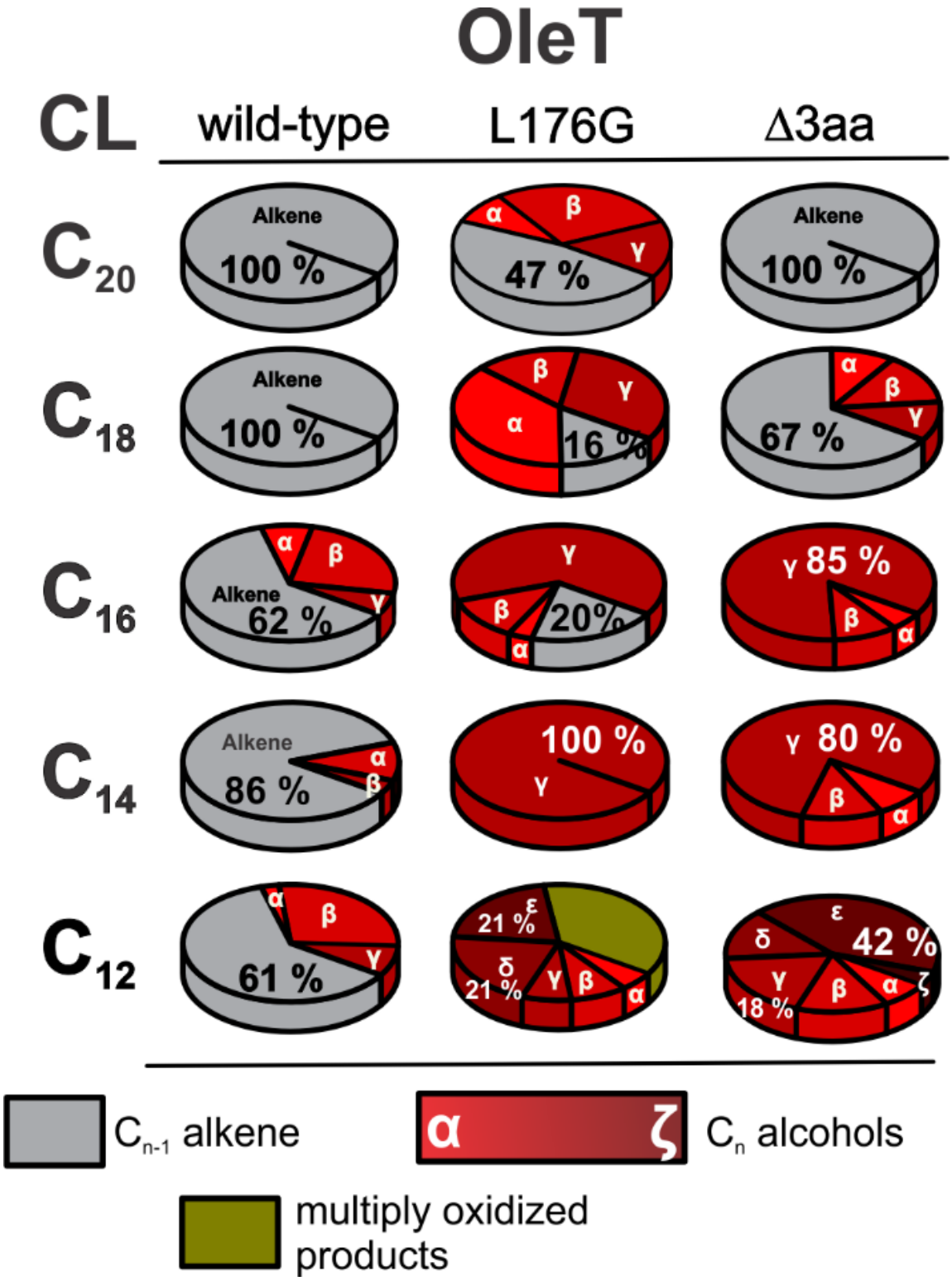


**Figure 2.15** Metabolic profile of wild-type (WT), L176G, and Δ3aa OleT-JE with $C_n$ chain length fatty acid substrates

## 4. Conclusions

We have shown that very subtle alterations on the substrate or protein, at positions quite far from the site of chemistry, can have profound effects on the partitioning of decarboxylation and hydroxylation chemistries in OleT. The FA probes utilized here have revealed a previously unidentified slow product release step that limits turnover by this family of enzymes. Although this slow step can be alleviated through targeted mutagenesis of the F-G loop, such alterations come with a significant price. A single amino acid change in this region converts OleT into a hydroxylase and has significant impact on the regiospecificity of C-H abstraction. This work provides the most compelling evidence to date that the coordination of substrate and a restriction of its mobility within the active site is the most important element for regulating chemical outcome in this family of enzymes.

## 5. References

1. Wong, S. D.; Srnec, M.; Matthews, M. L.; Liu, L. V.; Kwak, Y.; Park, K.; Bell, C. B., 3rd; Alp, E. E.; Zhao, J.; Yoda, Y.; Kitao, S.; Seto, M.; Krebs, C.; Bollinger, J. M., Jr.; Solomon, E. I., Elucidation of the Fe(IV)=O intermediate in the catalytic cycle of the halogenase SyrB2. *Nature* **2013,** *499* (7458), 320-3.

2. Chang, W. C.; Guo, Y.; Wang, C.; Butch, S. E.; Rosenzweig, A. C.; Boal, A. K.; Krebs, C.; Bollinger, J. M., Jr., Mechanism of the C5 stereoinversion reaction in the biosynthesis of carbapenem antibiotics. *Science* **2014,** *343* (6175), 1140-4.

3. Wang, C.; Chang, W. C.; Guo, Y.; Huang, H.; Peck, S. C.; Pandelia, M. E.; Lin, G. M.; Liu, H. W.; Krebs, C.; Bollinger, J. M., Jr., Evidence that the fosfomycin-producing epoxidase, HppE, is a non-heme-iron peroxidase. *Science* **2013,** *342* (6161), 991-5.

4. Tarhonskaya, H.; Szollossi, A.; Leung, I. K.; Bush, J. T.; Henry, L.; Chowdhury, R.; Iqbal, A.; Claridge, T. D.; Schofield, C. J.; Flashman, E., Studies on deacetoxycephalosporin C synthase support a consensus mechanism for 2-oxoglutarate dependent oxygenases. *Biochemistry* **2014,** *53* (15), 2483-93.

5. Rettie, A. E.; Boberg, M.; Rettenmeier, A. W.; Baillie, T. A., Cytochrome P-450-Catalyzed Desaturation of Valproic Acid In vitro. Species Differences, Induction Effects, and Mechanistic Studies. *J Biol Chem* **1988,** *263* (27), 13733-13738.

6. Fukuda, H.; Fujii, T.; Sukita, E.; Tazaki, M.; Nagahama, S.; Ogawa, T., Reconstitution of the isobutene-forming reaction catalyzed by cytochrome P450 and P450 reductase from Rhodotorula minuta: decarboxylation with the formation of isobutene. *Biochem Biophys Res Commun* **1994,** *201* (2), 516-22.

7. Rude, M. A.; Baron, T. S.; Brubaker, S.; Alibhai, M.; Del Cardayre, S. B.; Schirmer, A., Terminal Olefin (1-Alkene) Biosynthesis by a Novel P450 Fatty Acid Decarboxylase from Jeotgalicoccus Species. *Applied and Environmental Microbiology* **2011,** *77* (5), 1718-1727.

8. Rittle, J.; Green, M. T., Cytochrome P450 compound I: capture, characterization, and C-H bond activation kinetics. *Science* **2010,** *330* (6006), 933-7.

9. Grant, J. L.; Hsieh, C. H.; Makris, T. M., Decarboxylation of fatty acids to terminal alkenes by cytochrome P450 compound I. *Journal of the American Chemical Society* **2015,** *137* (15), 4940-3.

10. Grant, J. L.; Mitchell, M. E.; Makris, T. M., Catalytic strategy for carbon−carbon bond scission by the cytochrome P450 OleT. *Proceedings of the National Academy of Sciences* **2016,** *113* (36), 10049-10054.

11. Lee, D. S.; Yamada, A.; Sugimoto, H.; Matsunaga, I.; Ogura, H.; Ichihara, K.; Adachi, S.; Park, S. Y.; Shiro, Y., Substrate recognition and molecular mechanism of fatty acid hydroxylation by cytochrome P450 from Bacillus subtilis. Crystallographic, spectroscopic, and mutational studies. *J Biol Chem* **2003,** *278* (11), 9761-7.

12. Fang, B.; Xu, H.; Liu, Y.; Qi, F.; Zhang, W.; Chen, H.; Wang, C.; Wang, Y.; Yang, W.; Li, S., Mutagenesis and redox partners analysis of the P450 fatty acid decarboxylase OleTJE. *Sci Rep* **2017,** *7*, 44258.

13. Matthews, S.; Belcher, J. D.; Tee, K. L.; Girvan, H. M.; McLean, K. J.; Rigby, S. E. J.; Levy, C. W.; Leys, D.; Parker, D. A.; Blankley, R. T.; Munro, A. W., Catalytic determinants of alkene production by the cytochrome P450 Peroxygenase OleT(JE). *J Biol Chem* **2017,** *292* (12), 5128-5143.

14. Du, J.; Liu, L.; Guo, L. Z.; Yao, X. J.; Yang, J. M., Molecular basis of P450 OleTJE: an investigation of substrate binding mechanism and major pathways. *J Comput Aided Mol Des* **2017,** *31* (5), 483-495.

15. Faponle, A. S.; Quesne, M. G.; de Visser, S. P., Origin of the Regioselective Fatty-Acid Hydroxylation versus Decarboxylation by a Cytochrome P450 Peroxygenase: What Drives the Reaction to Biofuel Production? *Chemistry* **2016,** *22* (16), 5478-83.

16. Dennig, A.; Kuhn, M.; Tassoti, S.; Thiessenhusen, A.; Gilch, S.; Bulter, T.; Haas, T.; Hall, M.; Faber, K., Oxidative Decarboxylation of Short-Chain Fatty Acids to 1-Alkenes. *Angewandte Chemie* **2015,** *54*, 8819-8822.

17. Zachos, I.; Gassmeyer, S. K.; Bauer, D.; Sieber, V.; Hollmann, F.; Kourist, R., Photobiocatalytic decarboxylation for olefin synthesis. *Chem Commun (Camb)* **2015,** *51* (10), 1918-21.

18. Hsieh, C. H.; Huang, X.; Amaya, J. A.; Rutland, C. D.; Keys, C. L.; Groves, J. T.; Austin, R. N.; Makris, T. M., The Enigmatic P450 Decarboxylase OleT Is Capable of, but Evolved To Frustrate, Oxygen Rebound Chemistry. *Biochemistry* **2017,** *56* (26), 3347-3357.

19. Amaya, J. A.; Rutland, C. D.; Makris, T. M., Mixed regiospecificity compromises alkene synthesis by a cytochrome P450 peroxygenase from Methylobacterium populi. *J Inorg Biochem* **2016,** *158*, 11-6.

20. Hsieh, C. H.; Makris, T. M., Expanding the substrate scope and reactivity of cytochrome P450 OleT. *Biochem Biophys Res Commun* **2016,** *476* (4), 462-466.

21. Lelyveld, V. S.; Brustad, E.; Arnold, F. H.; Jasanoff, A., Metal-substituted protein MRI contrast agents engineered for enhanced relaxivity and ligand sensitivity. *Journal of the American Chemical Society* **2011,** *133* (4), 649-51.

22. Morrison, J. F., Kinetics of the reversible inhibition of enzyme-catalysed reactions by tight-binding inhibitors. *Biochim Biophys Acta* **1969,** *185* (2), 269-86.

23. Belcher, J.; McLean, K. J.; Matthews, S.; Woodward, L. S.; Fisher, K.; Rigby, S. E. J.; Nelson, D. R.; Potts, D.; Baynham, M. T.; Parker, D. A.; Leys, D.; Munro, A. W., Structure and biochemical properties of the alkene producing cytochrome P450 OleTJE (CYP152L1) from the Jeotgalicoccus sp. 8456 bacterium. *J. Biol. Chem.* **2014,** *289* (10), 6535-6550.

24. Amaya, J. A.; Rutland, C. D.; Makris, T. M., Mixed regiospecificity compromises alkene synthesis by a cytochrome P450 peroxygenase from Methylobacterium populi. *Journal of Inorganic Biochemistry* **2016,** *158*, 11-16.

25. Štrancar, J.; Koklič, T.; Arsov, Z.; Filipič, B.; Stopar, D.; Hemminga, M. A., Spin Label EPR-Based Characterization of Biosystem Complexity. *Journal of Chemical Information and Modeling* **2005,** *45* (2), 394-406.

26. Sundaramoorthy, M.; Terner, J.; Poulos, T. L., The crystal structure of chloroperoxidase: A heme peroxidase-cytochrome P450 functional hybrid. *Structure* **1995,** *3* (12), 1367-1377.

27. Yi, X.; Conesa, A.; Punt, P. J.; Hager, L. P., Examining the role of glutamic acid 183 in chloroperoxidase catalysis. *J Biol Chem* **2003,** *278* (16), 13855-9.

28. Piontek, K.; Strittmatter, E.; Ullrich, R.; Grobe, G.; Pecyna, M. J.; Kluge, M.; Scheibner, K.; Hofrichter, M.; Plattner, D. A., Structural basis of substrate conversion in a new aromatic peroxygenase: cytochrome P450 functionality with benefits. *J Biol Chem* **2013,** *288* (48), 34767-76.

29. Lee, D. S.; Yamada, A.; Sugimoto, H.; Matsunaga, I.; Ogura, H.; Ichihara, K.; Adachi, S.; Park, S. Y.; Shiro, Y., Substrate recognition and molecular mechanism of fatty acid hydroxylation by cytochrome P450 from Bacillus subtilis - Crystallographic, spectroscopic, and mutational studies. *J Biol Chem* **2003,** *278* (11), 9761-9767.

30. Ramanan, R.; Dubey, K. D.; Wang, B.; Mandal, D.; Shaik, S., Emergence of Function in P450-Proteins: A Combined Quantum Mechanical/Molecular Mechanical and Molecular Dynamics Study of the Reactive Species in the H2O2-Dependent Cytochrome

P450SPalpha and Its Regio- and Enantioselective Hydroxylation of Fatty Acids. *Journal of the American Chemical Society* **2016,** *138* (21), 6786-97.

31. Fujishiro, T.; Shoji, O.; Nagano, S.; Sugimoto, H.; Shiro, Y.; Watanabe, Y., Crystal Structure of H2O2-dependent Cytochrome P450(SP alpha) with Its Bound Fatty Acid Substrate INSIGHT INTO THE REGIOSELECTIVE HYDROXYLATION OF FATTY ACIDS AT THE alpha POSITION. *J Biol Chem* **2011,** *286* (34), 29941-29950.

32. Wilton, D. C., The fatty acid analogue 11-(dansylamino)undecanoic acid is a fluorescent probe for the bilirubin-binding sites of albumin and not for the high-affinity fatty acid-binding sites. *Biochemical Journal* **1990,** *270* (1), 163-166.

33. Matsunaga, I.; Yamada, A.; Lee, D. S.; Obayashi, E.; Fujiwara, N.; Kobayashi, K.; Ogura, H.; Shiro, Y., Enzymatic reaction of hydrogen peroxide-dependent peroxygenase cytochrome P450s: kinetic deuterium isotope effects and analyses by resonance Raman spectroscopy. *Biochemistry* **2002,** *41* (6), 1886-92.

34. Dunn, A. R.; Dmochowski, I. J.; Bilwes, A. M.; Gray, H. B.; Crane, B. R., Probing the open state of cytochrome P450cam with ruthenium-linker substrates. *Proceedings of the National Academy of Sciences* **2001,** *98* (22), 12420-12425.

35. Lee, Y.-T.; Wilson, R. F.; Rupniewski, I.; Goodin, D. B., P450cam visits an open conformation in the absence of substrate. *Biochemistry* **2010,** *49* (16), 3412-3419.

36. Liou, S.-H.; Myers, W. K.; Oswald, J. D.; Britt, R. D.; Goodin, D. B., Putidaredoxin Binds to the Same Site on Cytochrome P450cam in the Open and Closed Conformation. *Biochemistry* **2017**.

37. Poulos, T. L.; Finzel, B. C.; Howard, A. J., High-resolution crystal structure of cytochrome P450cam. *Journal of Molecular Biology* **1987,** *195* (3), 687-700.

38. Haines, D. C.; Tomchick, D. R.; Machius, M.; Peterson, J. A., Pivotal Role of Water in the Mechanism of P450BM-3. *Biochemistry* **2001,** *40* (45), 13456-13465.

39. Li, H.; Poulos, T. L., The structure of the cytochrome p450BM-3 haem domain complexed with the fatty acid substrate, palmitoleic acid. *Nat Struct Mol Biol* **1997,** *4* (2), 140-146.

40. Park, S.-Y.; Yamane, K.; Adachi, S.-i.; Shiro, Y.; Weiss, K. E.; Maves, S. A.; Sligar, S. G., Thermophilic cytochrome P450 (CYP119) from Sulfolobus solfataricus: high resolution structure and functional properties. *Journal of Inorganic Biochemistry* **2002,** *91* (4), 491-501.

41. Scott, E. E.; He, Y. A.; Wester, M. R.; White, M. A.; Chin, C. C.; Halpert, J. R.; Johnson, E. F.; Stout, C. D., An open conformation of mammalian cytochrome P450 2B4 at 1.6-Å resolution. *Proceedings of the National Academy of Sciences of the United States of America* **2003,** *100* (23), 13196-13201.

42. Dodani, S. C.; Kiss, G.; Cahn, J. K.; Su, Y.; Pande, V. S.; Arnold, F. H., Discovery of a regioselectivity switch in nitrating P450s guided by molecular dynamics simulations and Markov models. *Nat Chem* **2016,** *8* (5), 419-25.

43. Wu, F.; Gaffney, B. J., Dynamic behavior of fatty acid spin labels within a binding site of soybean lipoxygenase-1. *Biochemistry* **2006,** *45* (41), 12510-12518.

44. Livshits, V. A.; Marsh, D., Fatty acid binding sites of serum albumin probed by non-linear spin-label EPR. *Biochim Biophys Acta* **2000,** *1466* (1-2), 350-60.

# CHAPTER 3

## STRUCTURAL AND BIOPHYSICAL CHARACTERIZATION OF A P450 DECARBOXYLASE FROM STAPHYLOCOCCUS AUREUS


### Abstract

In the last decade, much effort has been placed in understanding the mechanisms of decarboxylation and hydroxylation in the cytochrome P450 $OleT_{JE}$. Recent work in our group has described the role of the F-G loop in substrate stabilization and its importance in the efficient decarboxylation of fatty acids. Furthermore, we have demonstrated that decarboxylation in $OleT_{JE}$ proceeds through the prototypical ferryl-heme intermediates of P450s. The unusual stability of these transient species is evidence of their role in chemoselectivity; understanding how they are stabilized in the protein framework is a primary focus of our research. Here, we present the structural and functional characterization of an $OleT_{JE}$ homolog from *Staphylococcus aureus* ($OleT_{SA}$) that readily performs C-C bond scission on a broad range of substrates. The crystal structure of eicosanoic-acid bound $OleT_{SA}$ shows the retention of the important secondary elements necessary to suppress oxygen rebound. Moreover, we discuss how the improved stability of the protein at high concentrations will allow the characterization of the catalytically relevant intermediates in decarboxylases of the CYP152 family of P450s.

## 1. Introduction

Olefin production has become one of the most important processes in the chemical industry. As a building block for many products that are used daily, its demand is exponentially growing and does not show any signs of halting. Olefin preparation is mainly accomplished through a steam cracking process, in which the hydrocarbons primarily found in fossil fuels are broken to produce smaller olefin molecules.[2] Although highly efficient, this process requires the input of high temperatures and environmentally harsh conditions. A recent study by Ghanta et al.[3] demonstrated that fuel burning, necessary to produce these conditions, accounts for almost 90% of greenhouse gas (GHG) emissions in the process of ethylene production. As we approach critical levels of GHG, finding alternative techniques to produce alkenes are becoming essential. Alternative routes to produce olefins, like the methanol-to-olefin process (MTO), have been well developed in the past decades; however, they have very poor carbon efficiencies and thus produce immense quantities of GHG.[2]

Intense interest has been put in the research and development of platforms to produce valuable molecules from microorganisms. The so-called advanced generation of biofuels is becoming more viable everyday with the immense growth of biodiesel production from algae.[4] Another method in development is the use of bacteria to produce valuable molecules by hijacking their natural biosynthesis pathways. The engineering of recombinant proteins capable of catalyzing difficult chemistry like C-C bond cleavage has turned these processes into a possible route to replace the extreme conditions necessary in current industrial processes.[5-6] A clear example of this has been the engineering of aldehyde deformylating oxygenase (ADO) from cyanobacteria into *E. coli*, which converts fatty

aldehydes into alkanes and formate.[7] Although much effort has been placed in the development of enzymes capable of such chemistry, there is still much to be done for these systems to become economically viable.

In 2011, $OleT_{JE}$, an enzyme isolated from the *Jeotgalicoccus sp.*, species was shown to produce terminal olefins from fatty acids, a cheap substrate found in abundance in bacteria such as *E. coli*.[8] Although very efficient in the production of long-chain olefins, $OleT_{JE}$ is less efficient in metabolizing shorter substrates into terminal alkenes.[3, 9] This is a requirement in the chemical industry as the most valuable olefins tend to be shorter in chain length.[2] As a part of the CYP152 family of cytochrome P450s, $OleT_{JE}$ is the only P450 that can efficiently decarboxylate a substrate yet also catalyze monooxygenation.[8, 10-11] In fact, as the chain-length is decreased, the chemistry tends to be rerouted onto the hydroxylation pathway. In recent years, great effort has been placed in understanding the catalytic determinants of decarboxylation in $OleT_{JE}$ as it could help harness its powerful chemistry to deploy it in an industry setting. We have shown in our group that C-C bond cleavage in this family of P450s is finely regulated by small modifications in the structure of the protein that extend as far as 17 Å from the active site.[12-13] Furthermore, we have demonstrated that decarboxylation proceeds in a similar manner as prototypical P450s with the formation of the canonical intermediates compound I and compound II.[14-15] These powerful ferryl heme oxidants have been shown to be extremely short-lived in most P450s. In $OleT_{JE}$, their stabilization is of great importance as decarboxylation requires the redirection of the typical "oxygen rebound" chemistry of compound II into what is believed to be the formation of a carbocation substrate through a proton-coupled electron transfer (PCET) pathway.[15] Analysis of the electronic structure of these intermediates in order to understand how they

are stabilized has proven to be a challenge in $OleT_{JE}$ as their study requires the implementation of advanced spectroscopy such as rapid freeze-quench EPR and Mössbauer, both requiring high protein concentrations. Although well behaved at low concentrations, $OleT_{JE}$ becomes highly unstable at high concentrations preventing the use of these spectroscopies for their study.

In this manuscript, we present the biochemical and structural characterization of $OleT_{SA}$, a new ortholog of the CYP152 family of P450s from *Staphylococcus aureus*. This enzyme has the same decarboxylation properties of $OleT_{JE}$ as well as highly similar kinetics of the catalytically relevant intermediates. However, $OleT_{SA}$ exhibits improved solubility at high concentrations and can be readily crystalized. The retained chemistry and improved biochemical features of this enzyme will set-up a new platform to understand the fundamentals chemistry in this family of proteins and uncovers common themes of CYP152s that enable their implementation for the advanced generation of biofuels.

## 2. Experimental Procedures

### 2.1 Reagents and chemicals

All buffers used in this study were purchased from BDH Chemicals. Media components (tryptone, peptone, yeast extract) and ammonium sulfate were acquired from Research Products International (Mount Prospect, Il, USA). Antibiotics were purchased from BioBasic Inc (Markham, ON Canada). Hydrogen peroxide and sodium molybdate was purchased from Sigma Aldrich. The terminal alkene standard, 1-hexadecene was

purchased from TCI chemicals. The hydroxylated fatty acid standard, 2-hydroxyhexadecanoic acid, was purchased from Combi-Blocks (San Diego, CA). Protiated fatty acids and N,O-Bis(trimethylsilyl)trifluoroacetamide (BSTFA)/trimethylchlorosilane (TMCS) (99:1) were purchased from Supelco (Bellefonte, PA, USA). Deuterated fatty acids were purchased from CDN Isotopes. All the crystallography material was obtained from Hampton Reseach (Aliso Viejo, CA, USA). $OleT_{SA}$ gene was synthetized by Bio Basic Inc (Markham, ON Canada).

### 2.2 Cloning, expression and purification of $OleT_{SA}$

The original $OleT_{SA}$ gene was synthesized and codon optimized for *E. coli* expression by Bio Basic Inc. (Markham Ontario). The gene was subcloned onto a kanamycin-resistant T5 plasmid containing a C-terminal HisTag preceded by a TEV cleavage site using NdeI/XhoI restriction sites. The plasmid was transformed onto BL21(DE3) containing the pTF2 plasmid encoding for GroEL/GroES/Tig onto a kanamycin/chloramphenicol LB plate. The next day, one colony was inoculated into 150 mL of modified Terrific Broth (12 g yeast extract, 6 g tryptone, 2 g peptone) supplemented with 50 µg/mL kanamycin and 20 µg/mL chloramphenicol and grown overnight at 37 °C. 10 mL of starter culture were inoculated into 500 mL of modified terrific broth containing 50 µg/mL Kanamycin, 20 µg/mL chloramphenicol, 125 mg/L thiamine and trace metals. The culture was initially grown for ~2 hours at 37 °C until $OD_{600nm}$ = 0.6, at which point the temperature was decreased to 18 °C until the $OD_{600nm}$ reached 1.5. At this point, cultures were induced with 100 µM IPTG, 10 ng/mL tetracycline and 10 mg/L of 5-aminolevulinic acid and grown for an additional 15 hours at 18 °C. The following day,

cultures were centrifuged 10 minutes at 6000 rpm and the pellet was resuspended in 4 mL of Buffer A (50 mM KPi pH 8, 300 mM NaCl and 10 mM imidazole) per gram of pellet. Cells were disrupted using a Branson sonifier and stirred for an hour before centrifuging 30 minutes at 16,000 rpm. The supernatant was loaded onto a previously equilibrated Ni-NTA column, washed with buffer A + 25 mM imidazole and eluted with buffer A + 250 mM imidazole. The eluate was diluted 1:1 with Buffer B (50 mM KPi pH 8, 300 mM NaCl 60 % ammonium sulfate) to reach a final concentration of 30 % ammonium sulfate. The diluted protein was then loaded onto a previously equilibrated Butyl-S-Sepharose column, washed with 10 column volumes of Buffer C (50 mM KPi pH 8, 300 mM NaCl and 30 % ammonium sulfate) and eluted with a gradient over 8 column volumes from buffer C to buffer D (50 mM KPi pH 8). Fractions with a $418_{nm}/280_{nm}$ ratio higher than 1 were pooled and dialyzed against 50 mM KPi pH 8 200 mM NaCl in the presence of 0.1 molar equivalents of TEV protease. The following day, protein was loaded onto a Ni-NTA column equilibrated in dialysis buffer and the flow-through was directly added onto a Q-Sepharose column equilibrated in the same buffer. The column was subsequently washed with 20 column volumes of buffer E (50 mM KPi pH 8, 250 mM NaCl) and eluted with a gradient over 8 column volumes from buffer E to buffer F (50 mM KPi pH 8, 750 mM NaCl). Fractions with a $418_{nm}/280_{nm}$ ratio higher than 1.2 were pooled and dialyzed against 200 mM KPi pH 8. The final yield was 60 mg of protein per liter of culture.

**2.3 Spectroscopy**

*a) UV-Visible Spectroscopy*

Optical spectra were obtained using an HP 8453 spectrophotometer. For substrate titration experiments, 10 µM of protein in 200 mM potassium phosphate ($KH_2PO_4$) pH 7.5

was titrated with sequential additions of a 1 mM fatty acid stock dissolved in 70% ethanol: 30% Triton X-100 (v:v). The following fatty acid stocks were used: eicosanoic acid (C20), octadecanoic acid (C18), hexadecanoic acid (C16), tetradecanoic (C14), dodecanoic acid (C12) and decanoic acid (C10). The amount of ethanol added never exceeded 5 % of the total volume. Fitting of the substrate induced absorption changes, ΔAbs, (at 396 nm and 418 nm) were done with the Morrison equation for tight-binding ligands as previously described.[16] To discard the possibility that the spectral changes resulted from the binding of Triton X-100 present in the fatty acid stock, a control titration was performed using a 70 % ethanol: 30 % Triton X-100 (v:v) stock in the absence of fatty acid. The resulting spin shift was small enough to conclude the spin shifts resulted from the binding the fatty acid rather than from Triton X-100.

*b) EPR spectroscopy*

All EPR samples were treated with 15 molar equivalents of hydrogen peroxide ($H_2O_2$) and incubated at 4 °C for 30 minutes prior to preparation. After treatment, the protein was desalted in 200 mM potassium phosphate ($KH_2PO_4$) pH 7.5 using a PD-10 desalting column to remove any excess hydrogen peroxide. Following buffer exchange, samples were concentrated to 150 µM. For the substrate-bound forms, 1 molar equivalent of eicosanoic acid dissolved in 70 % ethanol:30 % Triton X-100 (v:v) was added and incubated for 1 hour at 4 °C. All the samples were flash-frozen and kept at liquid nitrogen temperatures until further use. EPR spectra were recorded on a X-band Bruker EMXplus spectrometer equipped with an Oxford Instruments liquid helium continuous flow cryostat. Spectra were recorded at a temperature of 15 K, a power of 2 mW and an amplitude of 1 mT.

### 2.4 P450 activity assays

Multiple turnover *in vitro* reactions of P450 with substrate were prepared in 2 mL with the following contents pre-mix: 5 µM P450, 500 µM fatty acid dissolved in DMSO, and 200 mM $K_2HPO_4$ pH 7.5. 1000 molar equivalents of $H_2O_2$ to P450 were stirred into the 2 mL volume above at a rate of 2 mL/hr to a final volume of 4 mL. Steady-state reactions were quenched with 0.5 mL of 12 M HCl after 1 hour. Fatty acid and oxidant concentrations remained unchanged throughout multiple turnover reactions. Internal standards including 1-hexadecene and a $C_{n-2}$ fatty acid relative to the substrate were added to the quenched reaction. The reactions were extracted with an equal reaction volume of chloroform. The organic phases of each reaction were concentrated under a stream of $N_2$ gas to less than 50 µL. Concentrated samples were derivatized with 250 molar equivalents of BSTFA:TMCS (99:1). Samples were incubated at 60 °C for 20 minutes for trimethylsilylation. Following derivitization, samples were analyzed by Gas Chromatography-Mass Spectrometry (GC-MS). GC-MS was performed at the University of South Carolina Mass Spectrometry facility with a Hewlett-Packard HP5890 Gas Chromatograph and an Agilent HP-5 column. The following oven conditions were used to detect products of $C_{20}$ through $C_{16}$ fatty acids: 170 °C for 3 min., a 10 °C/min to 220 °C, a 5 °C/min to 320 °C, and 320 °C for 3 min. The following oven conditions were used to detect products of $C_{14}$ and $C_{12}$ metabolism: 100 °C for 3 min., a 5 °C/min to 250 °C and a 250 °C for 3 min. The response factors between fatty acids, hydroxyl fatty acids and alkenes were determined by analyzing known authentic fatty acids (C18-C10), 2-hydroxyhexadecanoic acid, 1-hexadecene, and 1-undecene standards.

### 2.5 Stopped-flow kinetics

*a) Sample preparation*

All P450s were prepared as previously described.[14-15] Briefly, the enzyme was peroxide-treated with 15 molar equivalents of hydrogen peroxide and desalted into 200 mM $K_2HPO_4$ pH 7.5 on a PD-10 desalting column. All proteins were concentrated and diluted in 200 mM $K_2HPO_4$ pH 7.5 to a final concentration of 20 µM. Three molar equivalents of either protiated or deuterated fatty acid was subsequently and incubated at 4 °C for at least 4 hours to allow proper fatty acid binding. A stock of 50 mM $H_2O_2$ was prepared in $K_2HPO_4$ pH 7.5 and incubated at 4 °C for 4 hours.

*b) Data collection*

Stopped-flow experiments were carried out on an Applied Photophysics Ltd. SX20 stopped-flow spectrophotometer. Briefly, each protein stock was rapidly mixed 1:1 against 50 mM $H_2O_2$ to give a final concentration of 10 µM protein and 25 mM $H_2O_2$ post-mix. Single wavelength traces were collected using a photomultiplier tube (PMT) and full spectral data was acquired using photodiode array (PDA) detection. The decay rates of the catalytically relevant intermediates compound I and compound II were determined using the ProData software package using the PMT traces at 370 nm, 440 nm and 690 nm as previously described.[14-15] The maximal accumulation of the intermediates was determined using singular value decomposition (SVD) using ProKIV and the PDA data as an input.

### 2.6 Crystallography

*a) Initial screen*

To assess initial crystallization conditions, the protein was sent to the Hauptman-Woodward Medical Research Institute where 1536 conditions were tested (soluble screen under oil).[17] Prior to condition screening, the protein was purified as described above and treated with 3 molar equivalents of eicosanoic acid ($C_{20}$). The protein was incubated at 4 °C for an hour and subsequently desalted in 200 mM $K_2HPO_4$ pH 7.5 to remove any excess fatty acid substrate. The P450 was concentrated to roughly 10 mg/ml (~200 µM) and flash-frozen in liquid nitrogen.

*b) Optimized conditions*

Optimized crystals were grown using the hanging-drop vapor diffusion method. Briefly, protein solution at 15 mg/mL was mixed 1:1 against reservoir solution (100 mM HEPES pH 7.5; 100 mM sodium molybdate; 20% PEG 8000) in a total volume of 2 µL. Crystal trays were incubated at 4 °C for two weeks before crystals appeared. Prior to storage, crystals were soaked in reservoir solution supplemented with 20% glycerol as cryoprotectant for 1 minute and subsequently cryo-cooled in liquid nitrogen. For the product-bound forms, the crystal was soaked in reservoir solution + 20% glycerol supplemented with either 1 mM hydrogen peroxide, 300 µM meta-chloroperbenzoic acid (mCPBA) or 500 µM peracetic acid.

*c) Data collection and processing*

X-ray diffraction patterns were collected at the Advanced Photon Source (Lemont, Il, USA), beamline 22-ID, through the Southeast Regional Collaborative Access Team (SER-CAT). Data scaling and integration were done using the HKL-2000 software[18]

package. Structure phasing was done by molecular replacement using the substrate-bound $OleT_{JE}$ structure as a search model (PDB code: 4L40) in the Phenix Phaser program[19]. Initial model building was performed using the Phenix Autobuilder[19] option and manual refinement was done using Coot.[20] Final refinement and validation was done through Phenix Refine and Phenix Validate respectively.[19] Figures were generated using Pymol Molecular Graphics software package (Version 1.3 Schrödinger LLC).

### 2.7 Solubility Assay

Protein solubility was determined using the method developed by Kramer R. et al.[21] Briefly, 20 µM of substrate-free protein in 50 mM $K_2HPO_4$ pH 7.5 was treated with increasing amounts of an ammonium sulfate solution (4 M) at pH 7.5. After each addition, the aliquot was centrifuged to remove any aggregated protein and the absorbance at 418 nm was used to determine the concentration of protein remaining in solution. Taking into account the dilution factor after each ammonium sulfate addition, the common logarithm of the concentration of protein in solution was plotted versus ammonium sulfate concentration. The theoretical solubility of the protein in 50 mM $K_2HPO_4$ pH 7.5 was determined by extrapolation of the linear portion of each curve.

## 3. Results

Previous studies in our group have determined the overall reaction scheme for decarboxylation, including the kinetics for the formation and decomposition of Compound I and II intermediates in $OleT_{JE}$.[14-15] To better understand the origin for the relatively

sluggish reactivity of these intermediates compared to other CYPs, which may be central to reinforce substrate decarboxylation, it is crucial to study their electronic properties. Advanced spectroscopy such as rapid freeze-quench EPR (RFQ-EPR) and Mössbauer requires significantly higher protein concentrations (200 μM to 1 mM) than those used in the transient absorption methods we have utilized previously. This has proven to be a challenge in $OleT_{JE}$, as the protein readily aggregates at these concentrations. To overcome this, we sought to find an ortholog that would retain the essential active site residues necessary for catalysis, but also exhibit improved biochemical properties. An amino acid sequence comparison using the Basic Local Alignment Sequence Tool (BLAST) at NCBI rendered more than 100 hits of proteins possessing 50 % or higher sequence identity to $OleT_{JE}$. From the multiple hits, a cytochrome P450 from *Staphylococcus aureus* was chosen, henceforth named $OleT_{SA}$, with an overall sequence identity of 64%. This protein appears to have all the required catalytic components for fatty acid metabolism, including but not limited to: His85, Ala369 and the extended F-G loop which we have previously demonstrated to be required for efficient decarboxylation in this class of enzymes (Figure 3.1).[9, 12] The active site sequence identity, defined as 10 Å from the catalytic heme-iron, was found to be 95 %. This variation was within the required range for the study and therefore was not expected to have a significant impact on the reactivity nor the chemoselectivity of the enzyme.

### 3.1 Expression and purification of $OleT_{SA}$

The gene with the NCBI reference sequence ID WP_049319149.1 was codon optimized for *E. coli* expression and synthetized by Bio Basic Inc. The initial plasmid


**Figure 3.1** Partial sequence alignment of $OleT_{JE}$ and $OleT_{SA}$ using the Basic Local Alignment Sequence Tool (BLAST) at NCBI. The red boxes correspond to residues that have been shown to participate either in reactivity of in chemoselectivity of the final product.

contained a lac promoter and was transformed into the BL21 *E. coli* strain; however, poor protein expression and yields were obtained.

To overcome these issues, the gene was sub-cloned into a second vector containing a T5 promoter and a kanamycin resistance cassette. The obtained plasmid was co-transformed into BL21(DE3) cells along with the pTF2 plasmid encoding the chaperones GroEL, GroES and Tig, as it has been previously shown the enhancement of protein expression and solubility in $OleT_{JE}$.[9, 12, 14-15] Initial expression trials revealed an elevated expression of the protein in the soluble fraction. Residual amounts of protein were found to be associated with the membrane but were discarded as the yields of the soluble fraction

were sufficient for subsequent purification. A similar association to the membrane was also observed in the purification of CYP-MP, and appears to be general for CYP152s that bind highly hydrophobic substrates.[13] $OleT_{SA}$ was initially purified using nickel nitriloacetic acid (NiNTA) affinity and hydrophobic interaction chromatography (Butyl-Sepharose). Modelling of the protein using the I-TASSER server predicted a disordered C-terminal domain, similar to $OleT_{JE}$.[9] To facilitate crystallization, the polyhistidine tag was removed by TEV cleavage, and the protein was subsequently loaded onto a nickel column to remove TEV and the uncleaved protein. As a final purification step we purified the cleaved protein on a Q-sepharose column and dialyzed it against 200 mM KPi pH 7.5. Using the extinction coefficient at 418 nm $\varepsilon_{418\ nm} = 112\ mM^{-1}cm^{-1}$ corresponding to the heme Soret band and the predicted protein extinction coefficient at 280 nm, we were able to assess the final purity of the protein. The final Reinheitszahl ratio ($A_{418nm}/A_{280nm}$ ratio) was determined to be > 1.2. SDS-PAGE revealed a highly pure protein with a molecular weight of 52 kDa (Figure 3.2).

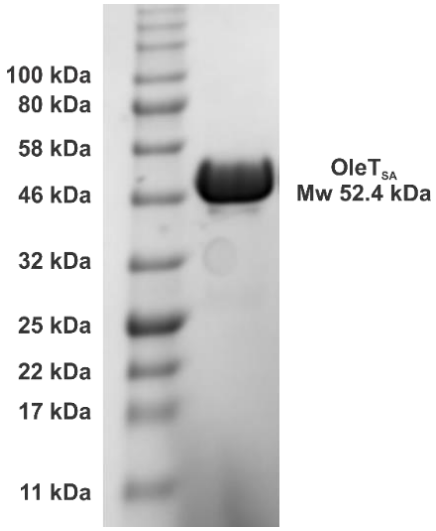


**Figure 3.2** SDS-PAGE gel of $OleT_{SA}$ after a 3-column purification procedure. The apparent molecular weight is consistent to that predicted for the TEV cleaved protein (52.4 kDa).

### 3.2 OleT$_{SA}$ possess similar spectroscopic signatures to OleT$_{JE}$

As it has been well established that the UV-Vis spectra of cytochrome P450s is sensitive to the redox state of the heme as well as the primary coordination sphere.[22] In the absence of substrate, P450s display a Soret band with a maximum absorption between 418 nm and 422 nm depending on the nature of the 6$^{th}$ ligand of the heme ($H_2O$ versus $OH^-$).[13] Upon substrate binding, the sixth ligand is displaced and the Soret band blue-shifts to ~396 nm. UV-Vis spectroscopy of the as purified enzyme displays a maximal absorption at 418 nm with a shoulder at 396 nm, suggesting that OleT$_{SA}$ is purified with an adventitiously-bound substrate (Figure 3.3A). This is unsurprising as *E. coli* produces high amounts of free fatty acids (particularly C16) in the cytoplasm and is a phenomenon that we[12-14] and others[10-11] have noted for several CYP152 enzymes.

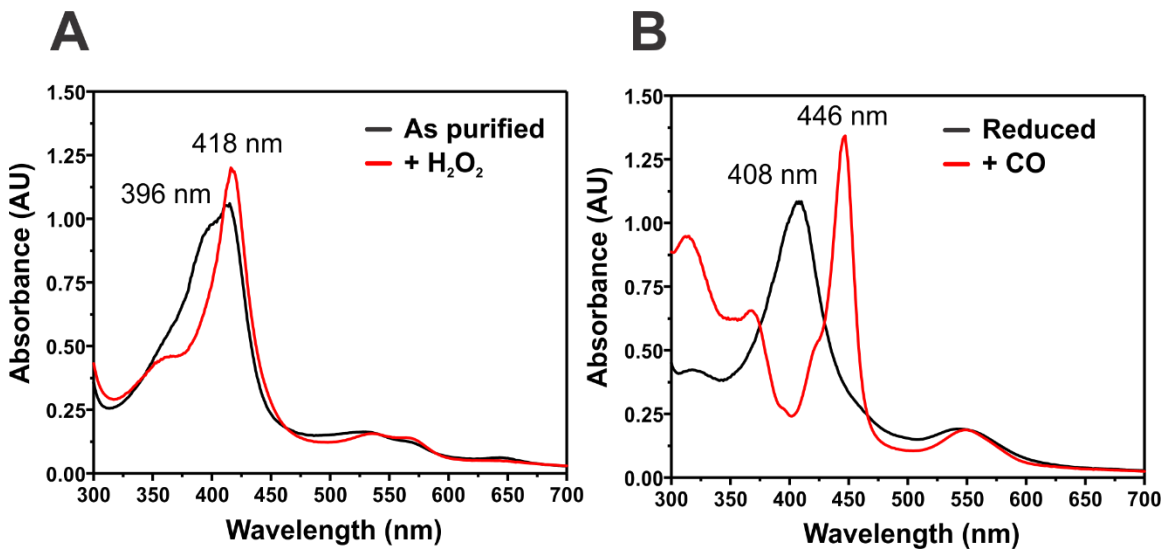


**Figure 3.3** UV-Vis spectra of OleT$_{SA}$. (A) Ferric form of the protein: in black as purified and red hydrogen peroxide treated. (B) Ferrous form of the protein: black corresponds to the reduced protein with dithionite and methyl viologen as a mediator; red corresponds to the reduced form with addition of carbon monoxide.

Upon substrate metabolism that occurs with the addition of hydrogen peroxide, the Soret band shifts to a maximum absorption to 418 nm, indicative of restoration of a water molecule as the 6$^{th}$ ligand to the heme iron. When the protein is reduced with 10 molar equivalents of sodium dithionite, the intensity of the Soret band decreases and has a maximum absorption at 408 nm typical of ferrous P450s (Figure 3.3B). The α and β Q-bands merge into one distinct band at ~550 nm. The addition of carbon monoxide to the reduced protein shifts the main absorption band towards 446 nm, indicating the formation of the carbonmonoxy-bound form of the enzyme and preservation of the thiolate ligated heme. These values are in accordance to what has previously been observed in $OleT_{JE}$.[9] Curiously, the CO-bound form of this enzyme appears to be much more stable in $OleT_{SA}$, and can persist as long as 1 hour. More in-depth studies are needed to confirm the cause for the enhanced stability of the proximal ligand. However, it points towards enhanced properties that can possibly be leveraged for *in vivo* generation of biofuels.

Similar to optical spectroscopy, the EPR spectra of P450s are also highly sensitive to changes in the heme environment, including changes in the hydrogen bonding network and geometry of the heme.[22] As previously noted, the resting state of P450s involves a 6$^{th}$ ligand bound to the heme, this maintains the Fe(III) center in a 6-coordinate low spin state (6cLS) with an S = ½ giving rise to a rhombic signal usually centered at 2.25. The position of the $g_x$, $g_y$ and $g_z$ values is informative of the nature of the 6$^{th}$ ligand and the hydrogen bonding network within the distal and proximal side of the heme. In the case of $OleT_{SA}$ (and $OleT_{JE}$),[9] several $g_z$'s can be detected (Figure 3.4A), suggesting a poorly structured hydrogen bonding network on the distal side of the heme that leads to conformational heterogeneity of the axial water ligand. The same phenomenon is observed in its ortholog.

When substrate is added to the protein and the water molecule is displaced, the Fe(III) center changes to a 5-coordinate high spin state (5cHS) with S = 5/2. This gives rise to a signal with high rhombicity and g values that are usually centered at g ~ 8, 4 and 2. For $OleT_{SA}$ the g values found are 7.89, 3.82 and 1.78; the rhombicity (E/D_ of the S = 5/2 signal is 0.092 and is highly similar to $OleT_{JE}$ (0.091) indicating a conservation of the structural components of the heme in the 5cHS state.[9]

Together, UV-Vis and EPR spectroscopy suggest that the heme environment and geometry within both proteins is very similar between the two enzymes. This may not be surprising given that 95 % of the amino acids in the active site are retained. This similarity may be important as the reactivity of P450s is highly can be highly sensitive to changes in heme geometry and the local microenvironment.

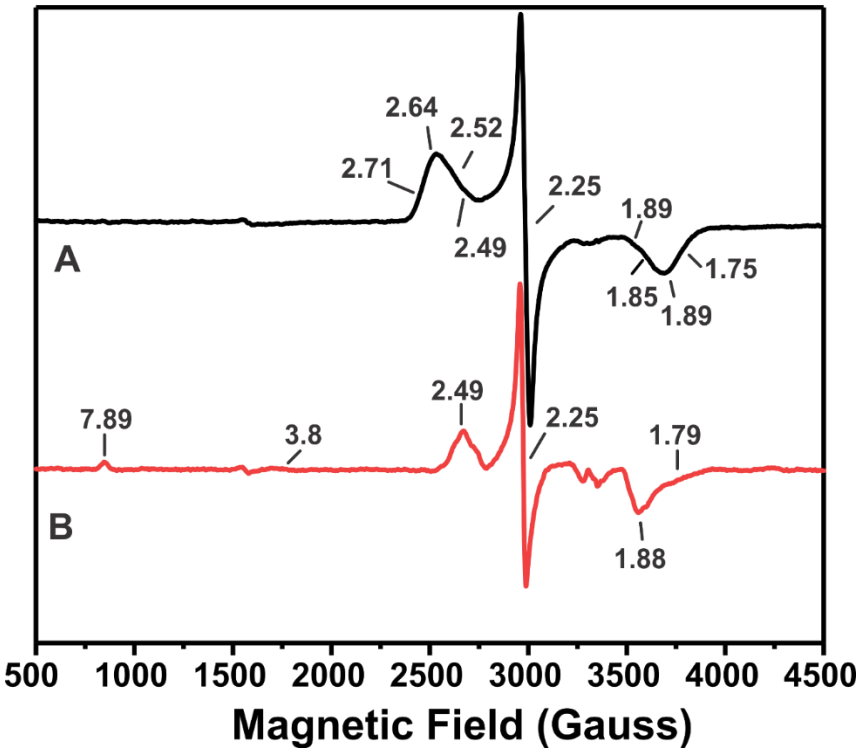


**Figure 3.4** EPR spectra of $OleT_{SA}$. (A) $OleT_{SA}$ substrate-free (B) $OleT_{SA}$ eicosanoic acid bound. Data was collected at a power of 2.5 mW and a modulation amplitude of 1 mT. Temperature was maintained at 12 K.

### 3.3 Binding of fatty acid substrates by OleT $_{SA}$

The versatility of P450s can be explained by their ability to metabolize a large number of substrates.[23] This is especially important for the detoxification of drugs by hepatic P450s in humans.[24] In the CYP152 family of cytochrome P450s, this ability is confined to predominantly linear acyl substrates due to the constraints enforced by the binding pocket. Understanding the substrate scope in decarboxylases undoubtedly impacts their biotechnological potential and will guide mutagenesis strategies to modify the binding pocket of the protein to accept not only linear substrates but perhaps other substrates that can be metabolized to other valuable commodity chemicals.

In OleT$_{SA}$, the transition from a 6cLS to a 5cHS state upon substrate addition facilitates determination of its dissociation constant ($K_D$) using a Morrison quadratic equation that is most accurate for tight binding substrates (Figure 3.5).

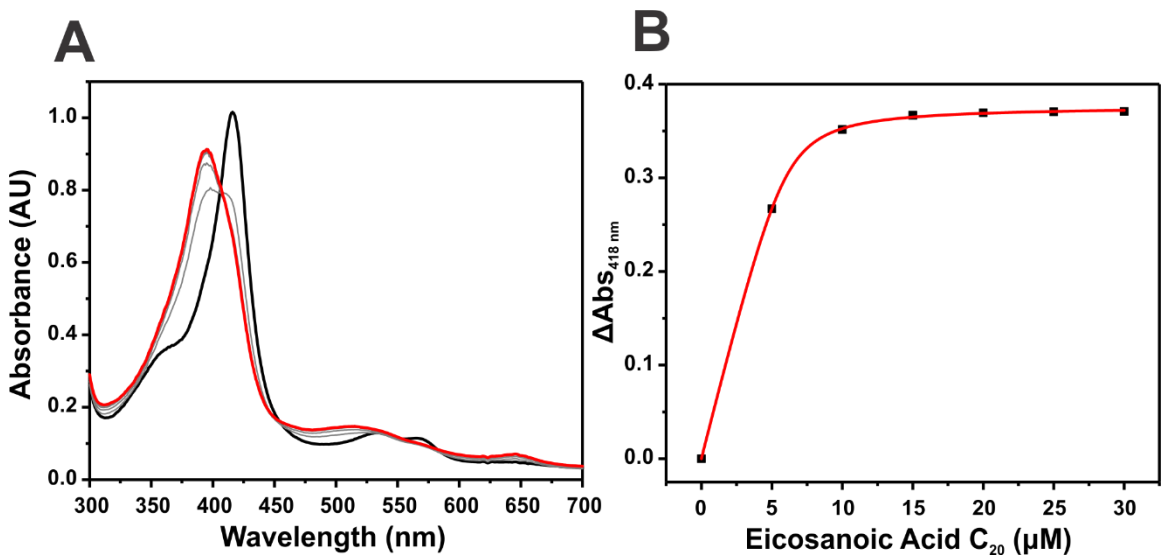


**Figure 3.5** Binding of eicosanoic acid C20 to OleT$_{SA}$. (A) UV-Vis spectra of subsequent additions of C20 fatty acid. Black represents the initial spectra; red represents final spectra. (B) Fitting of Δabsorbance at 418 nm versus fatty acid concentration. Black squares are the actual data and red is the fitting.

In $OleT_{JE}$, longer chain length substrates induce a more pronounced degree of high spin conversion than short chain fatty acids.[25] This most likely derives from the increased mobility of shorter substrates within the active site: longer substrates are more constrained favoring one conformation that reinforces the dissociation of the water ligand, whereas shorter substrates are more dynamic due to their restricted van der Waals contact with the protein framework. This translates to an increase in the dissociation constant in short-chain substrates.[12] The same mechanism can be observed in $OleT_{SA}$ where eicosanoic (C20) or stearic (C18) acid induce an increased 5cHS state with high affinities (Table 3.1). In contrast to $OleT_{JE}$, the change in affinity and 5cHS accumulation between substrates is less pronounced, indicating a more restricted number of conformations adopted by shorter substrates in the binding pocket. This is of great importance as we have previously established that the decarboxylation process starts with hydrogen abstraction from the Cβ position and requires exquisite positioning of the fatty acid within the active site.[12-13] Additionally, it has been observed that the accumulation of the intermediates in $OleT_{JE}$ is proportional to the initial amount of the 5cHS state. We anticipate the decreased dynamics of the substrate in $OleT_{SA}$ favors decarboxylation of shorter chain length substrates and to result in an equal, if not greater, accumulation of the relevant iron-oxo intermediates.

**Table 3.1.** Substrate affinity and 5cHS accumulation in $OleT_{JE}$ and $OleT_{SA}$

| | **$OleT_{SA}$** | | **$OleT_{JE}$** | |
|---|---|---|---|---|
| **Substrate** | **$K_D$ Substrate (μM)** | **High-Spin Heme (%)** | **$K_D$ Substrate (μM)** | **High-Spin Heme (%)** |
| C20 | 0.26 ± 0.50 | 90 | 0.29 ± 0.05 | 90 |
| C18 | 0.32 ± 0.01 | 78 | 0.20 ± 0.05 | 62 |
| C16 | 4.04 ± 2.41 | 73 | 2.20 ± 0.12 | 31 |
| C14 | 2.48 ± 1.63 | 61 | 7.5 ± 0.2 | 49 |
| C12 | 1.51 ± 0.05 | 71 | 2.16 ± 0.70 | 49 |

### 3.4 OleT$_{SA}$ conserves β-regiospecificity and chemoselectivity

To ensure that the metabolic profile of OleT$_{SA}$ was retained, we performed a series of steady state turnover experiments with a panel of saturated fatty acids (C20 through C12). Initial comparison of the chemoselectivity in OleT$_{SA}$ and OleT$_{JE}$ is summarized in Figure 3.6. As shown, exclusive decarboxylation is maintained with long-chain fatty acids (C20 and C18) as expected. Shorter fatty acids (C16 through C12) produce higher amounts of hydroxylated products, as is the case in OleT$_{JE}$.[9]

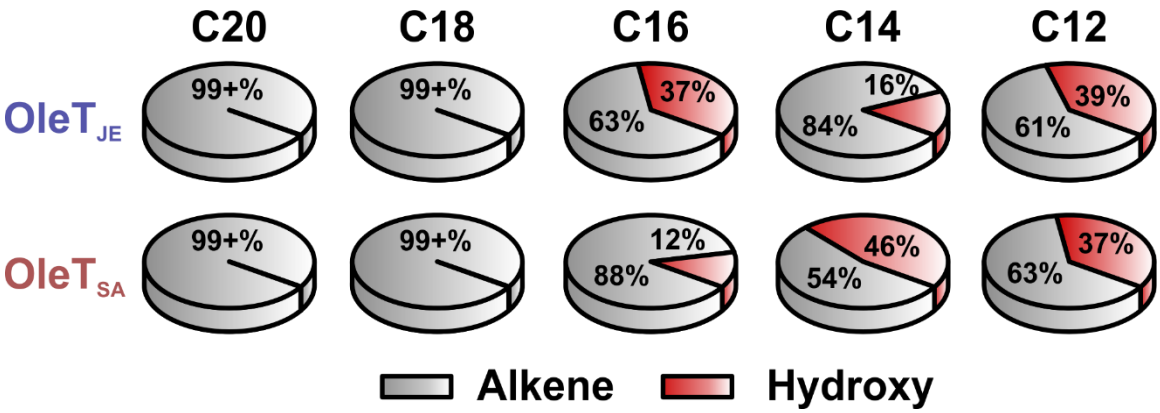


**Figure 3.6** Comparison of the chemoselectivity in OleT$_{JE}$ and OleT$_{SA}$

Small differences can be observed however, with fatty acids C16 and C14, where OleT$_{SA}$ seems to highly favor decarboxylation (88% of the product) in the former and produce more hydroxylated product in the latter (54% of the product). A possible explanation for this shift is the substitution of residue Leu176 in OleT$_{JE}$ to an isoleucine in the protein studied (Figure 3.1). We have shown that small modifications of this residue can lead to highly distorted chemoselectivity and would not be impossible for this residue to cause this shift.[12]

A closer look at the metabolic profile of $OleT_{SA}$ (Table 3.2) also reveals the conservation of the β-regiospecificity. With the exception of myrstic acid (C14), the majority of the alcohol products are predominantly oxidized at the Cβ position. As previously mentioned, hydrogen abstraction at the β position is a requirement for ensuing decarboxylation. Taking this into consideration, at least 90% of the substrate undergoes Cβ-H abstraction for the panel of fatty acid substrates tested here. Previous studies have demonstrated oxidation beyond the β-carbon, and in some cases, subsequent overoxidation of product alcohol to a ketone in $OleT_{JE}$.[13, 26] No such products were detected in $OleT_{SA}$, suggesting that regardless the nature of the substrate, the acyl chain seems to favor no more than a few conformations (α/β-oxidation; decarboxylation). This is further supported by the increased accumulation of the 5cHS state even with short substrates.

**Table 3.2.** Full metabolic profile of $OleT_{SA}$ with a panel of different substrates. Regioselectivity of the alcohol products is represented as percentage of the total hydroxylated products. The $C_\beta$ regiospecificity is defined as the fractional percentage of alkenes and $C_\beta$ alcohols over total products formed by the enzyme.

| Substrate | Alcohol (%) | Alkene (%) | Cβ Regio-selectivity (%) | Conv. (%) | Product accounting (%) |
|---|---|---|---|---|---|
| C20 | 0 | 100 | 100 | 60 | 83 ± 6 |
| C18 | 0 | 100 | 100 | 67.3 | 124 ± 16 |
| C16 | 12.5 (3% α, 97% β) | 77.5 | 99 | 85 | 117 ± 7 |
| C14 | 46 (19% α, 81% β) | 54 | 90 | 100 | 96 ± 1 |
| C12 | 13 (4% α, 96% β) | 87 | 99 | 100 | 90 ± 11 |

### 3.5 The overall crystal structure of $OleT_{SA}$ is conserved

Multiple turnover data have confirmed that $OleT_{SA}$ is a new decarboxylase member from the CYP152 family of P450s. In recent years, much effort has been placed to rationalize the unique chemistry of decarboxylases within this family.[12-13, 25-27] Previous crystallographic studies on $OleT_{JE}$ have attempted to highlight possible structural differences between CYP152 decarboxylases and hydroxylases that may rationalize the source of the divergent chemistries.[9] Comparison of the active site of $OleT_{JE}$ and one of the most studied hydroxylases of this family, P450 BSβ,[11, 28-29] revealed an almost identical active site with only minor substitutions. One of the most studied variations is residue His85 which corresponds to a Gln in P450 BSβ (Figure 3.7).

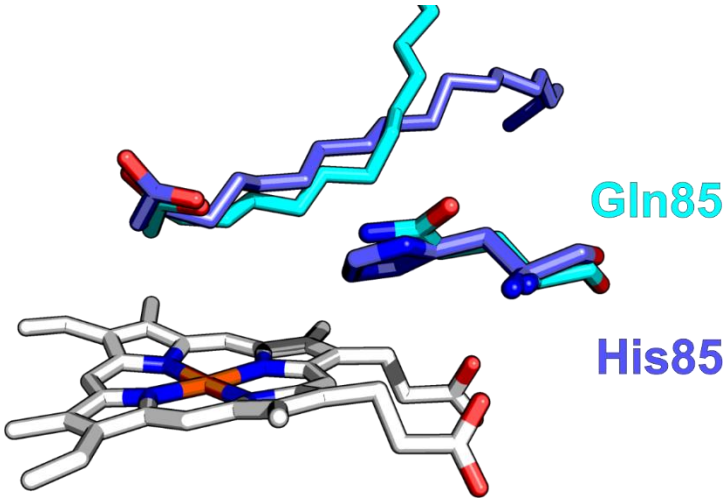


**Figure 3.7** Overlay of the active site of $OleT_{JE}$ and P450 BSβ. $OleT_{JE}$ is represented by the purple structure; P450 BSβ is represented by the cyan trace. The heme from $OleT_{JE}$ is represented in white.

Although there is no clear evidence for the role of this residue in decarboxylation,[25] mutagenesis studies in our group have shown that it is implicated in proper accumulation of 5cHS state of the protein. Furthermore, rapid kinetic studies suggest this residue may also be involved in the stabilization of compound II through hydrogen bonding.[15] Further data analysis is required however, as glutamine can also serve as hydrogen bond donor, although not as efficiently as a histidine.[30] Finally, crystallographic data of $OleT_{JE}$ shows a highly structured hydrogen bonding network in the substrate-bound form between a solvent molecule and residues His85, Arg245 and the fatty acid substrate. This network might be involved in the enhanced hydrogen peroxide activation in decarboxylases.

A second structural difference can be found between the F and G helixes. Decarboxylases from this family have an extended FG loop that allows for proper constraint of the fatty acid substrate.[12] Through van der Waals interactions, Leu176 restraints the mobility of the fatty acid tail. Although the hydrophobic nature of this residue seems to be conserved in P450 BSβ (Val174),[29] the shorter FG loop prevents this residue to come into contact with the fatty acid, conveying a higher mobility to the substrate. In a recent study, we showed the importance of this loop and leucine in decarboxylation.[12]

The structural features described above were a requirement for this study as we wanted to ensure that $OleT_{SA}$ is as similar as possible to $OleT_{JE}$. To determine the crystal structure of $OleT_{SA}$, initial crystallization conditions were obtained using the high throughput (HT) screening facility at the Hauptmann Woodward institute. The crystallization assays were performed using the microbatch crystallization technique under 1536 different conditions.[17] From the HT screening only two conditions rendered positive hits (Figure 3.8A and B): condition A (0.5 M imidazole pH 7.5, PEG 3350 10% w/v) and condition B

(0.1 M sodium molybdate, 0.1 M MES pH 6 and 20% w/v PEG 8000). Initial attempts to reproduce crystals using the microbatch under oil crystallization technique in house were

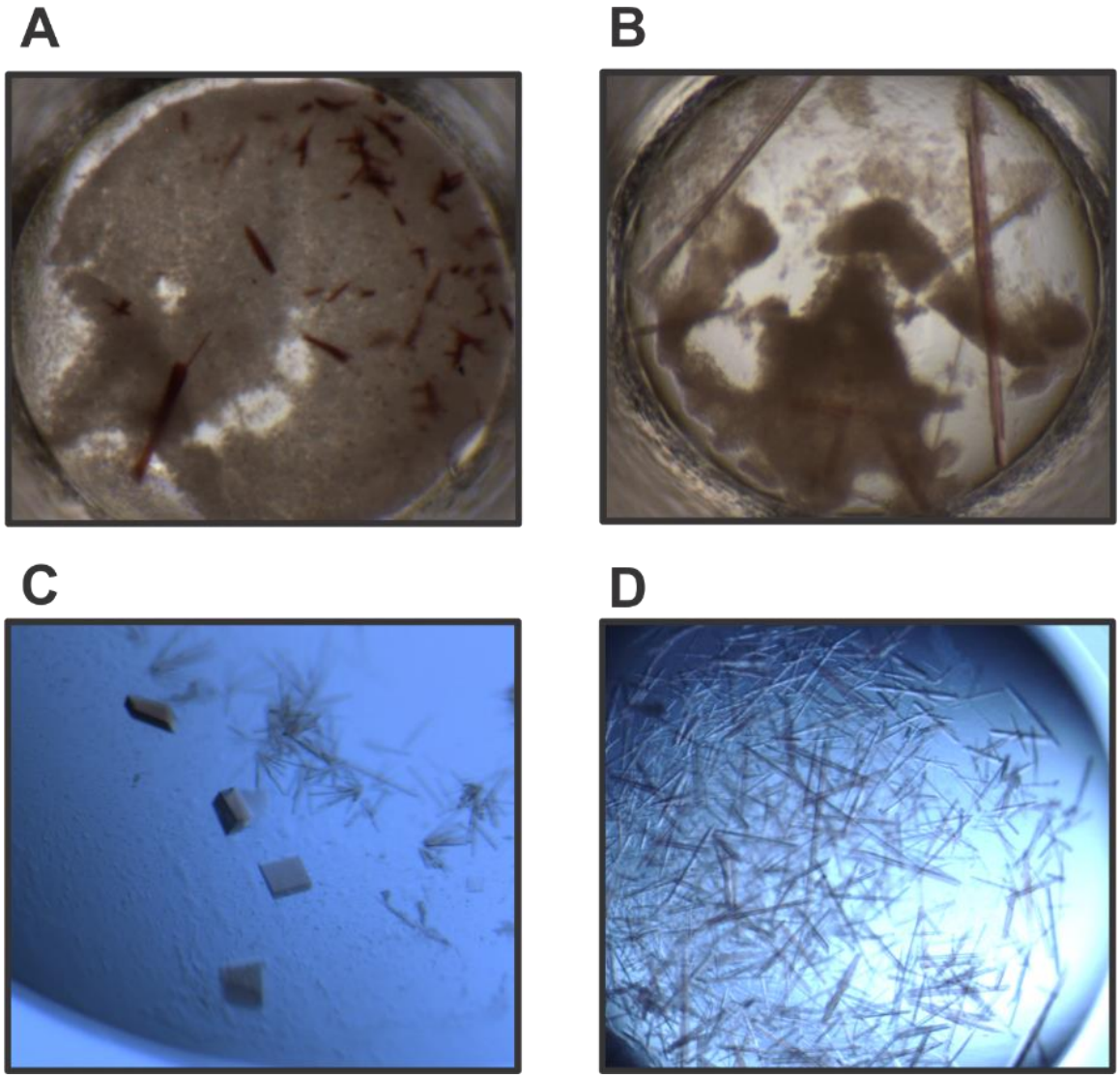


**Figure 3.8** Morphology of $OleT_{SA}$ crystals. (A) Initial condition from HT screening: 0.5 M imidazole pH 7.5, 10% w/v PEG 3350 grown after 3 weeks. (B) Initial condition from HT screening: 0.1 M Sodium Molybdate, 0.1 M MES pH 6; 20% w/v PEG 8000 grown after 3 weeks. (C) Optimized condition from cocktail A: 0.5 M imidazole, 10% w/v PEG 3350, 30% Al's oil. Crystals grown after 1 week. (D) Optimized condition from cocktail B: 0.1 M Sodium Molybdate, 0.1 M HEPES pH 7.5, 20% w/v PEG 8000, 60% Al's oil. Crystals grown after 3 weeks. All the conditions were done using the hanging drop vapor diffusion technique at 4 °C.

unsuccessful due to the lack of reproducibility of the drops. To optimize the conditions, we attempted to crystallize the protein using the hanging drop vapor diffusion technique.

Preliminary crystallization attempts delivered very fragile, poor-quality crystals. For condition A, the use of 30% Al's oil (1:1 silicon oil:paraffin oil) and cold conditions (4 °C) was necessary to decrease the crystallization time and obtain single crystals. The initial morphology provided by the HT screen showed clusters of needles. However, using optimized conditions, single crystals in two morphologies were obtained. Figure 3.8C shows both morphologies, one being cubic shaped and the other one similar to the one obtained under the microbatch condition. Despite the quality of the crystal and the use of several cryosolvents, no X-ray diffraction pattern could be obtained for any of the grown crystals.

The second condition provided by the HT screening was proven to be more challenging to reproduce (Figure 3.8B). Initial attempts using the provided cocktail did not produce any crystal using either crystallization technique.

After several optimization rounds, crystals were grown after 3 weeks by substituting MES for HEPES at pH 7.5 and using 60% Al's oil to minimize nucleation. Figure 3.8D shows a similar morphology of the crystal compared to the initial screen (Figure 3.8B). Single crystals were soaked using mother liquor containing either 20 % glycerol or 20 % sucrose (v:v) as a cryosolvent. X-ray diffraction patterns were obtained at SERCAT and the structure was solved to 3 Å. Electron density analysis showed a highly disordered C-terminal domain as anticipated by the predicted structure. A lack of density for the last 8 amino acids of the protein was obvious. In an attempt to improve the resolution of the structure, we deleted the last 8 amino acids and crystallized the protein in a similar manner. Identical crystal morphology was obtained but the resolution was improved to up to 2.3 Å. Structural parameters and refinement statistics are listed on Tables 3.3 and 3.4.

**Table 3.3.** Data collection statistics

| Data Collection Statistics | OleT$_{SA}$ C20-bound | OleT$_{SA}$ mCPBA |
|---|---|---|
| **Resolution Range (Å)** | 35.74 - 2.2 | 37.29 – 2.55 |
| **Space group** | $C222_1$ | $C222_1$ |
| **Unit cell (a/b/c; Å)** | 69.3 93.7 186.2 | 67.7 94.0 183.7 |
| **(α/β/γ; °)** | 90 90 90 | 90 90 90 |
| **Total reflections** | 209883 (17941) | 168731 (12268) |
| **Unique reflections** | 31159 (3024) | 19508 (1900) |
| **Multiplicity** | 6.7 (5.9) | 8.6 (6.5) |
| **Completeness (%)** | 99.5 (97.3) | 99.8 (98.5) |
| **Mean I/sigma (I)** | 8.2 (1.10) | 11.6 (2.4) |
| **Wilson B-factor (Å$^2$)** | 37.7 | 32.42 |
| **$R_{merge}$** | 0.143 (1.000) | 0.142 (0.555) |
| **$R_{meas}$** | 0.155 (1.100) | 0.151 (0.605) |
| **$R_{pim}$** | 0.0589 (0.4396) | 0.05111 (0.2337) |
| **$CC_{1/2}$** | 0.996 (0.765) | 0.997 (0.851) |
| **CC** | 0.999 (0.931) | 0.999 (0.959) |

**Table 3.4.** Structure refinement statistics

| Structure Refinement Statistics | OleT$_{SA}$ C20-bound | OleT$_{SA}$ mCPBA |
|---|---|---|
| **Reflections used in refinement** | 31122 (2992) | 19503 (1899) |
| **Reflections used for R-free** | 1289 (126) | 1949 (190) |
| **R-work** | 0.2551 (0.3351) | 0.238 (0.226) |
| **R-free** | 0.2927 (0.3876) | 0.300 (0.306) |
| **Number of non-hydrogen atoms** | 3474 | 3582 |
| **Macromolecules** | 3409 | 3409 |
| **Ligands** | 65 | 72 |
| **Protein residues** | 419 | 419 |
| **RMS (Bonds; Å)** | 0.009 | 0.008 |
| **RMS (Angles; °)** | 1.12 | 1.05 |
| **Ramachandran favored (%)** | 94.96 | 94.96 |
| **Ramachandran allowed (%)** | 4.8 | 4.8 |
| **Ramachandran outliers (%)** | 0.24 | 0.24 |

| | | |
|---|---|---|
| **Rotamer outliers (%)** | 5.19 | 5.74 |
| **Clashscore** | 11.16 | 17.71 |
| **Average B-factor (Å$^2$)** | 42.17 | 30.77 |
| **Macromolecules** | 42.23 | 30.56 |
| **Ligands** | 39.42 | 31.4 |

An overlay of the substrate-bound structures of $OleT_{SA}$ and $OleT_{JE}$ (PDB code: 4L40) reveals the conservation of all the secondary structure components of the protein including 11 α-helixes and 2-β sheets. The B-factors shown in Figure 3.9B reveal a relatively rigid protein. The F and G helixes appear to have a higher B-factor, indicating a higher flexibility compared to the rest of the protein. It is well known that these helixes are flexible in P450s as they tend to undergo conformational changes to accommodate their substrate.[31-33] We hypothesize that, although these helixes are more flexible than the rest of the protein, they should not undergo major conformational changes in decarboxylases as the substrate is immobilized by residues in those regions.[12-13] This is further supported by the difficulty for these enzymes in metabolizing non-linear substrates.[34-35] In addition to this, the C-terminal domain of the protein appears to be less flexible as well. In contrast to their hydroxylating orthologs, decarboxylases are able to metabolize long chain fatty acids, suggesting the flexibility of the C-terminal domain of the protein to be involved in the accommodation of longer substrates.

Analysis of the fatty acid binding pocket structure shows the overall conservation of the features present in $OleT_{JE}$, including most of the hydrophobic residues: Tyr24, Val75, Leu79, Ile171, Ile174, Phe293, Val294 and Phe296.[13] Figure 10A and 10B show the overall structure of the FG loop located at the entrance of the binding pocket. The elongated loop seems to be positioned in a similar manner as in $OleT_{JE}$. The distance from the catalytic

center to the residue involved in fatty acid anchoring is 17 Å apart as in $OleT_{JE}$. Ile177 is positioned 4.5 Å from the closest carbon of the acyl chain of the substrate. In $OleT_{JE}$ this distance is shortened to 4 Å and the residue substituted by a leucine. Although both residues have almost identical hydrophobic properties, the distance to the substrate might play an important role in product release and chemoselectivity in $OleT_{SA}$.

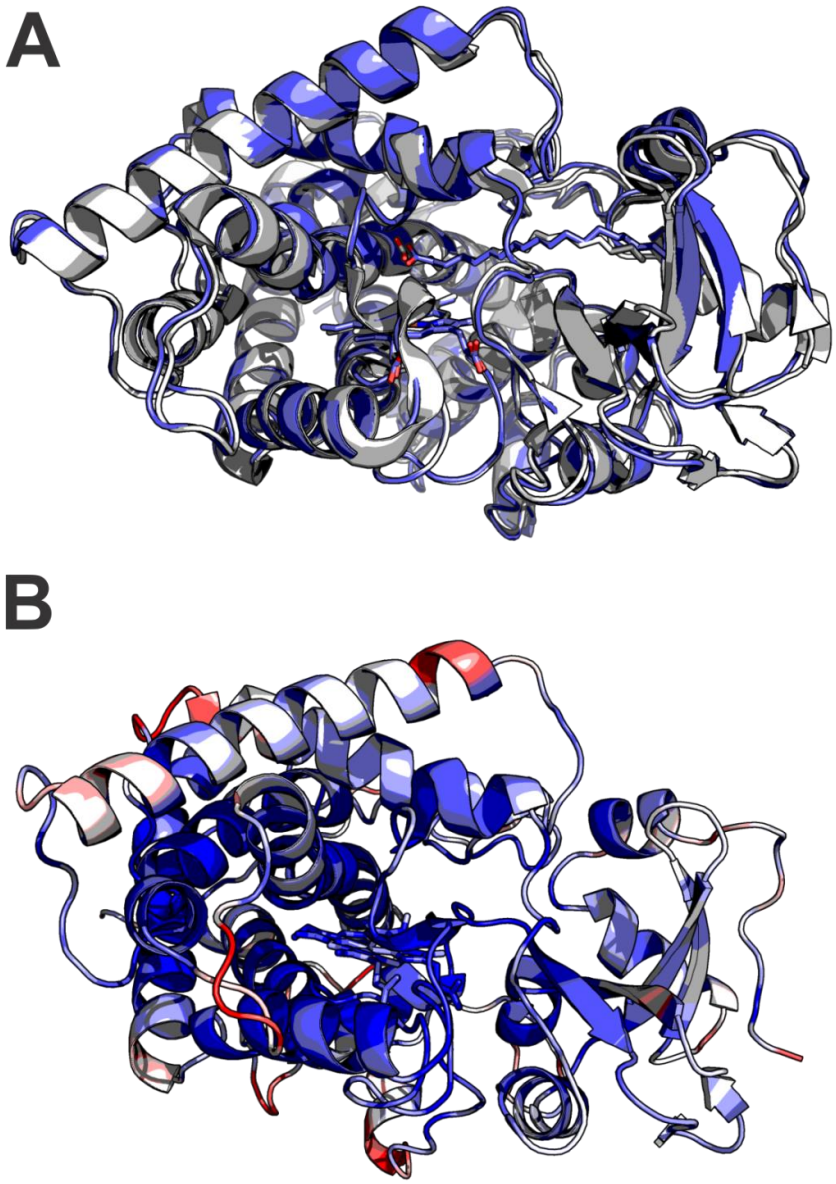


**Figure 3.9** Crystal Structure of $OleT_{SA}$. (A) Overlay of the crystal structure of $OleT_{SA}$ with $OleT_{JE}$ (PDB: 4L40). In purple $OleT_{SA}$ and in white $OleT_{JE}$. (B) Crystal structure of $OleT_{SA}$ colored by B-factors: Blue represents lower B-factors and red higher B-factors.

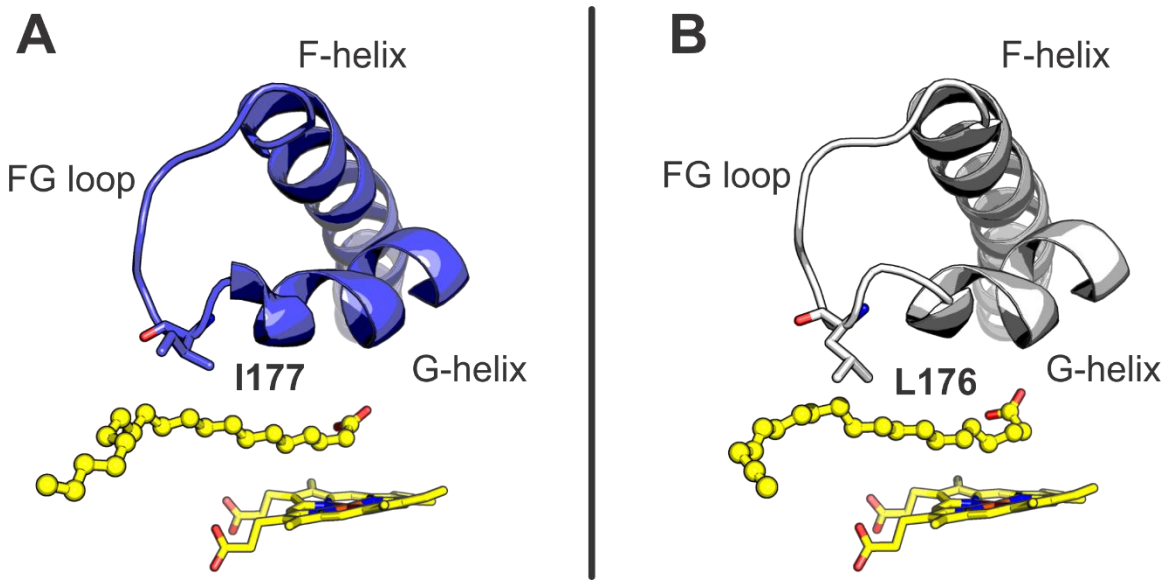


**Figure 3.10** F-G loop structure comparison. (A) F-G loop in $OleT_{SA}$ with eicosanoic acid bound. (B) F-G loop in $OleT_{JE}$ with eicosanoic acid bound.

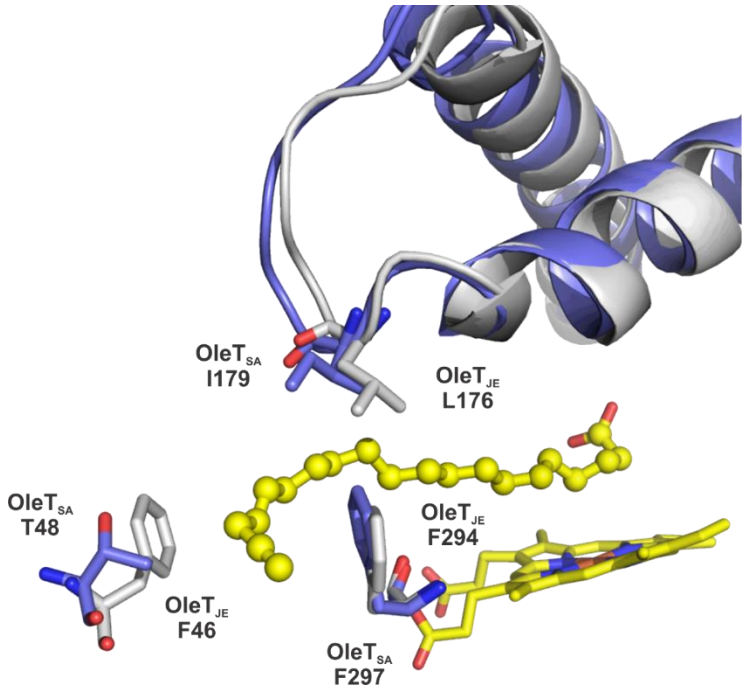


**Figure 3.11** Overlay of the hydrophobic cage in $OleT_{SA}$ and $OleT_{JE}$

In $OleT_{JE}$, residues Phe46, Phe297 and Leu176 serve as a "hydrophobic cage" for the substrate, preventing the rattling of the fatty acid (Figure 3.11). Although there is no direct evidence for the involvement of Phe46 in chemoselectivity, it would appear that this residue would be important in stabilization of the substrate. In contrast, the substitution to a threonine in $OleT_{SA}$ would indicate a possible change in the substrate preference to a shorter-chain fatty acid and an increase in the mobility of the substrate leading to a higher hydroxylation profile. Multiple turnover data demonstrates however, that chemoselectivity with most of the fatty acid substrates is retained, undermining the importance of Thr48. This residue may enable more facile release of the alkene. However, more detailed kinetic and spectroscopic studies are needed to confirm this possible role.

Analysis of the structure of the catalytic center in $OleT_{JE}$ shows a highly structured hydrogen bond network stabilized by Arg245, His85 and the fatty acid substrate. In $OleT_{SA}$ this network seems to be less structured due to a change in the orientation of Arg247 (Figure 3.12). It appears that the $N_{h1}$ atom of the guanidium group of the arginine is 1.5 Å

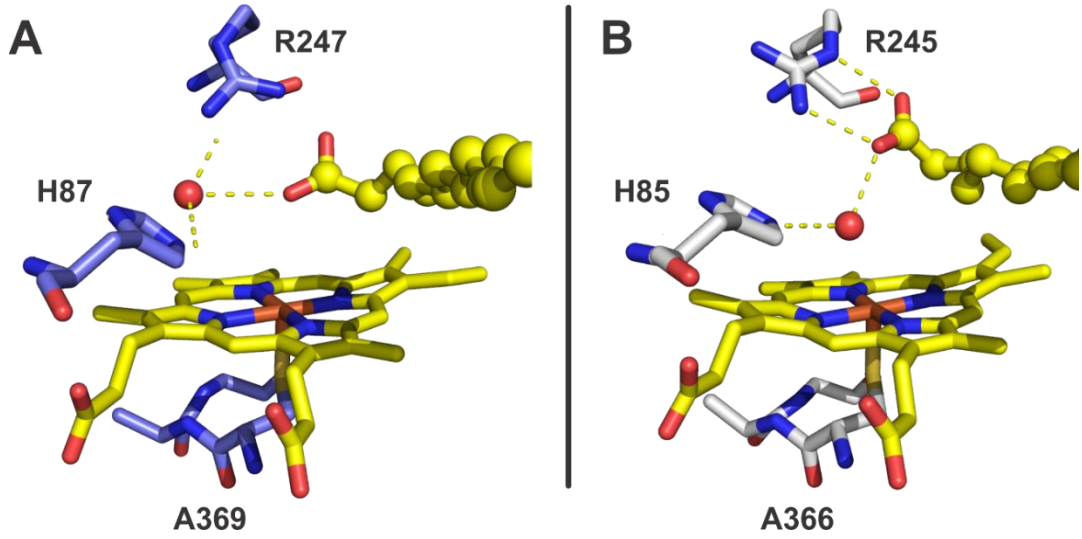


**Figure 3.12** Active-site structure comparison. (A) Crystal structure of the active site in $OleT_{SA}$ with eicosanoic acid bound. (B) Crystal structure of the active site in $OleT_{JE}$ with eicosanoic acid bound (PDB 4L40)

away from the $O_1$ atom of the fatty acid Y-shaped terminus, putting it in direct hydrogen-bonding distance. Additionally, the $N_{h2}$ of the guanidium group is 3.1 Å away from the $O_2$ of the fatty acid substrate. In $OleT_{JE}$, the distance between both oxygens of the fatty acid substrate and the guanidium group is equal at 2.7 Å however, it hydrogen bonds to the $N_{h2}$ and $N_{\varepsilon}$ atoms.

The orientation of the arginine guanidium group in $OleT_{SA}$ is similar to what is observed in the aromatic peroxygenase Aae-APO, suggesting that the precise binding orientation of the fatty acid to Arg245 might be not be required for efficient hydrogen peroxide activation. Additionally, it appears that His87 is 0.6 Å closer to the fatty acid compared to $OleT_{JE}$. Optical and EPR spectroscopy indicate very minor changes in the environment of the protein, suggesting that the highly ordered H-bond network might not be favored in solution.

### 3.6 Increased solubility of $OleT_{SA}$ establishes a new platform for high concentration studies

We have demonstrated that the overall structure and reactivity of $OleT_{SA}$ is similar to $OleT_{JE}$. It is important, however, to determine the stability of the protein at high concentrations as this is a requirement for advanced spectroscopy. A simple study to answer this question was to evaluate the fraction of soluble protein in increasing concentrations of precipitant. A study published by Kramer et al.[21] evaluated the solubility of seven different proteins in two different precipitants, PEG 8000 and ammonium sulfate. Results of this research concluded that, while having very different properties, the nature of the precipitant was irrelevant in the study of protein solubility. Given this result, we

decided to base our study in the utilization of increased concentrations of ammonium sulfate to a protein solution. We evaluated the amount of soluble protein using the heme Soret band at 418 nm and the extinction coefficient $\varepsilon_{418\ nm}$ = 112 $mM^{-1}cm^{-1}$. Briefly, to a 20 µM solution of P450 in 100 mM KPi pH 7.5, we added increasing amount of a saturated solution of ammonium sulfate (4 M). Taking into account the dilution of the sample as we add precipitant, we were able to determine predicted protein solubility in 100 mM KPi pH 7.5. Figure 3.13 shows the logarithm of the soluble fraction of the protein as a function of ammonium sulfate concentration.

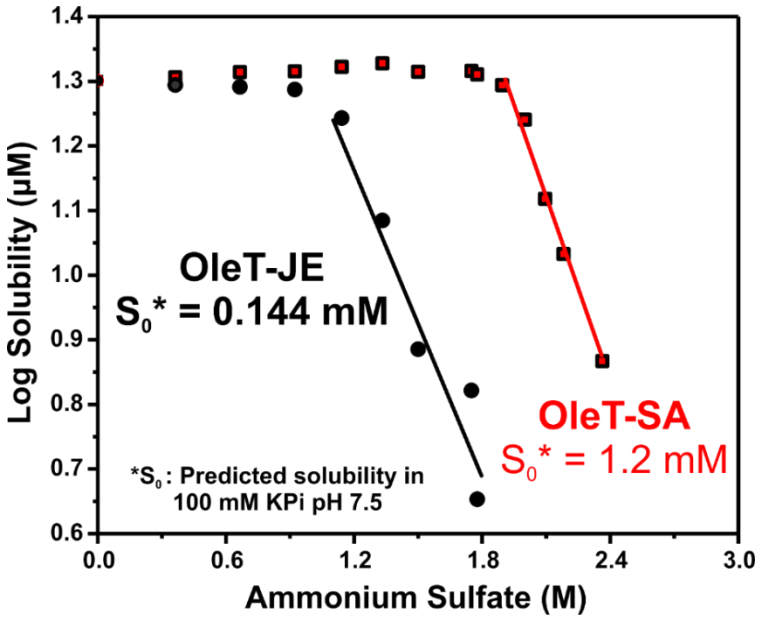


**Figure 3.13** Solubility of decarboxylases in increased concentrations of ammonium sulfate

For each protein, the data shows an initial stationary phase where protein solubility is unaffected by ammonium sulfate. For salts, this region corresponds to the salting-in effect. As the concentration of precipitant is increased, the solubility of the protein decreases and forms a linear decay phase corresponding to the salting-out effect.

**Equation 1** $Log\ S = Log\ So - \beta\ [Ammonium\ Sulfate]$

This region can be fitted to equation 1 where So represents the solubility of protein in the absence of ammonium sulfate and β represents the dependence of solubility of the protein for ammonium sulfate. Projection of the fitting of the salting-out region to the y axis gives the predicted protein solubility in the absence of precipitant. The β factor for OleTSA and OleTJE was determined to be -0.94 M-1 and -0.81 M-1 respectively. Given the high similarity of both proteins, the calculated β-factor was expected to be similar. The predicted solubility for OleTSA was found to be an order of magnitude higher than OleTJE in 100 mM KPi pH 7.5. This is highly similar to our experimental observations, where aggregation

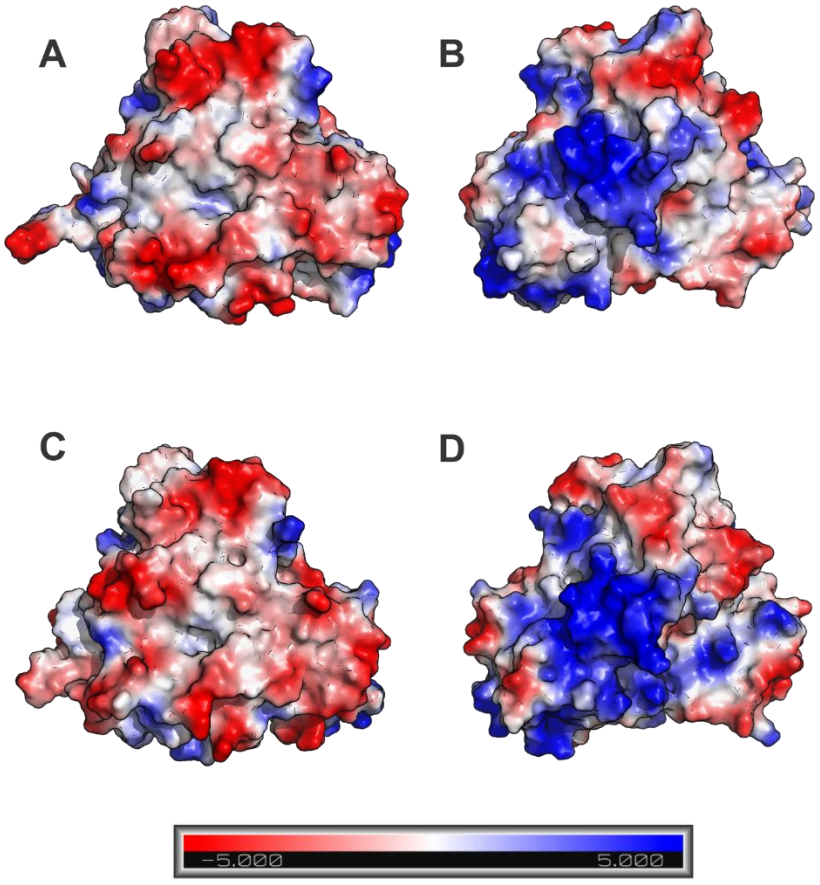


**Figure 3.14** Surface electrostatics comparison between $OleT_{JE}$ and $OleT_{SA}$. (A) and (B) represent $OleT_{JE}$ in two different orientations. (C) and (D) represent $OleT_{SA}$ in two different orientation. Electrostatic potential scale is found at the bottom.

happens at concentrations above 150 µM. In contrast, no solubility problems have been observed in OleTSA, even at concentrations higher than 1.5 mM. Solubility of proteins have been correlated with an increase in the number of negatively charged residues in the protein surface, presumably due to their ability to get into close contact with solvent molecules.21 Surface electrostatics of both decarboxylases seem to be highly similar (Figure 3.14). In addition to this, the predicted isoelectric point between both proteins seems to be almost identical as well (5.2 for OleTSA and 5.7 for OleTJE). Either way, rationalizing the dramatic improvement of solubility in OleTSA may require further structural analysis of both proteins. This feature however, will be invaluable for the study of the electronic properties of the catalytically relevant intermediates in decarboxylases.

### 3.7 Rapid kinetic spectroscopy shows the accumulation of the competent intermediates in OleT$_{SA}$

Cytochrome P450s are amongst nature's most potent catalysts due to their ability to activate inert C-H bonds.[36] The use of a thiolate ligated heme as cofactor allows them to produce powerful oxidants. Theoretical and experimental studies on inorganic complexes suggest that these intermediates could possess redox potentials above 1 V.[37] For a long time, it was hypothesized that these enzymes utilize a ferryl-oxo pi cation radical heme (compound I) as an intermediate for the activation of these inert bonds as suggested by synthetic model compounds.[38-40]

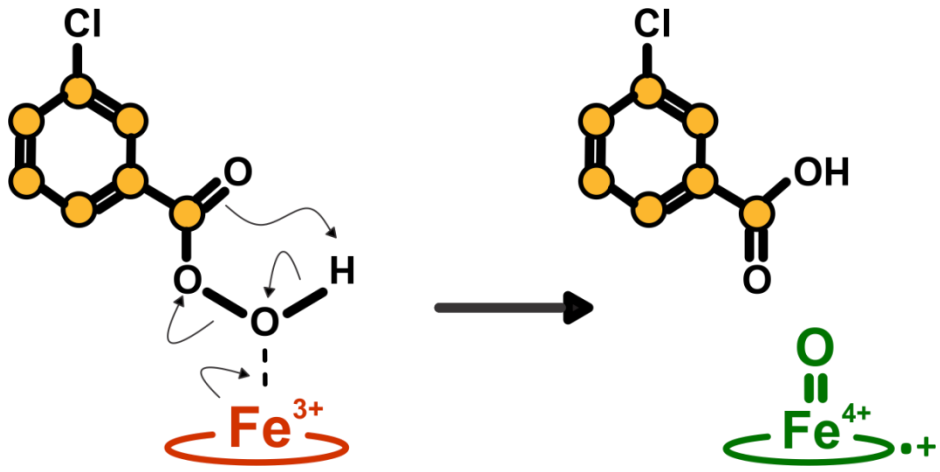


**Scheme 3.1** Formation of compound I by the addition of meta-chloroperoxybenzoic acid (mCPBA)

In 2011, Rittle and Green[41] were able to capture and characterize the Compound I in the thermostable P450 CYP119. The use of meta chloroperoxybenzoic acid allowed them to obtain significant amounts of the intermediates through the reaction in scheme 1, where mCPBA was added to the substrate-free enzyme. This technique bypasses the prototypical catalytic P450 cycle by using the so-called "peroxide shunt". Many attempts to reproduce this technique have been done in other cytochrome P450s but have resulted in only the meager accumulation of compound I.[42-43] It is hypothesized that the presence of redox active residues (Trp and Tyr) near the catalytic site is involved in the stability of this species as it may easily oxidize the protein framework and lead to the rapid disappearance of Compound I.[44] The CYP152 family of P450s has naturally evolved to use hydrogen peroxide as an oxygen and electron donor.[45] With the exception of P450 BM3,[46] it is the only family of cytochrome P450s that does not have an enzymatic redox partner.

The ability of these enzymes to efficiently utilize hydrogen peroxide confers them the ability to rapidly form intermediates.[14-15] Kinetic data of the rapid mixing of mCPBA against these proteins, however, show very low efficiency in the accumulation of intermediates but can slowly react with the enzyme (Figure 3.15). Crystallographic structure of $OleT_{SA}$ substrate-bound soaked in 500 µM mCPBA shows that despite the poor

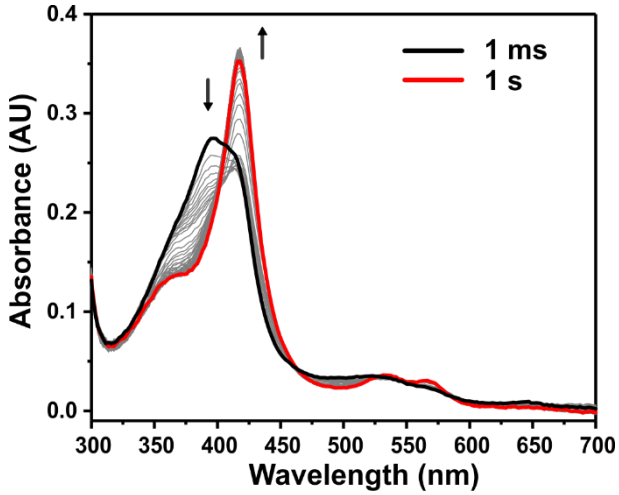


**Figure 3.15** Photodiode array spectra of 20 µM $OleT_{SA}$ eicosanoic acid bound against 200 µM mCPBA. The slow reactivity of the enzyme with mCPBA doesn't allow the accumulation of compound I. Higher concentrations of mCPBA were used but rendered the same result.

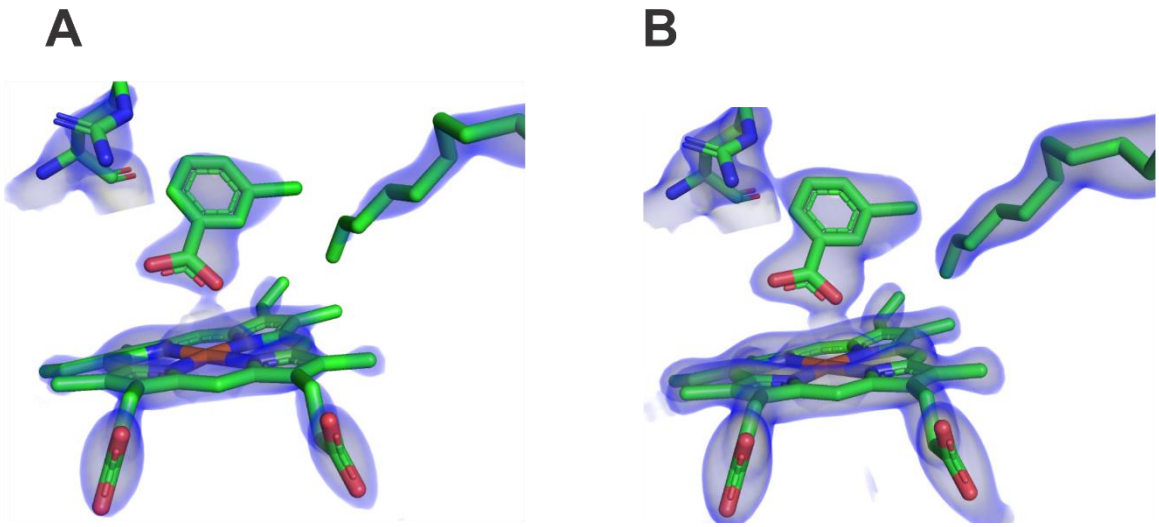


**Figure 3.15** $2F_O$-$F_C$ map of $OleT_{SA}$ substrate bound soaked with 500 µM mCPBA. (A) represents the electron density with a contour level of 2 σ. (B) represents the electron density with a contour level of 1.3 σ.

accumulation of intermediates, the oxidant gets into the pocket and reacts to form meta-chlorobenzoate (Figure 3.16).

Previous work in our group has shown that $OleT_{JE}$ is the first P450 studied in which one is able to prepare a significant amount of compound I in the presence of a substrate using the native oxidant.[14] Stopped-flow kinetic experiments revealed the accumulation of up 70% of the compound I intermediate with a decay rate of ~80 $s^{-1}$ in the presence of a perdeuterated substrate. A significant kinetic isotope effect (KIE) on the decay rates of compound I is observed when the enzyme is prepared with a protiated substrate (3.4) where the decay rate approximates 300 $s^{-1}$. (13 The KIE calculated suggested that decarboxylation is initiated by hydrogen abstraction from the substrate, most likely at the Cβ, followed by the formation a second intermediate that was later identified as a ferryl-hydroxy heme (compound II).[15] Further studies suggest that compound II abstracts a second electron from the fatty acid radical through a proton-coupled electron transfer (PCET) process, forming

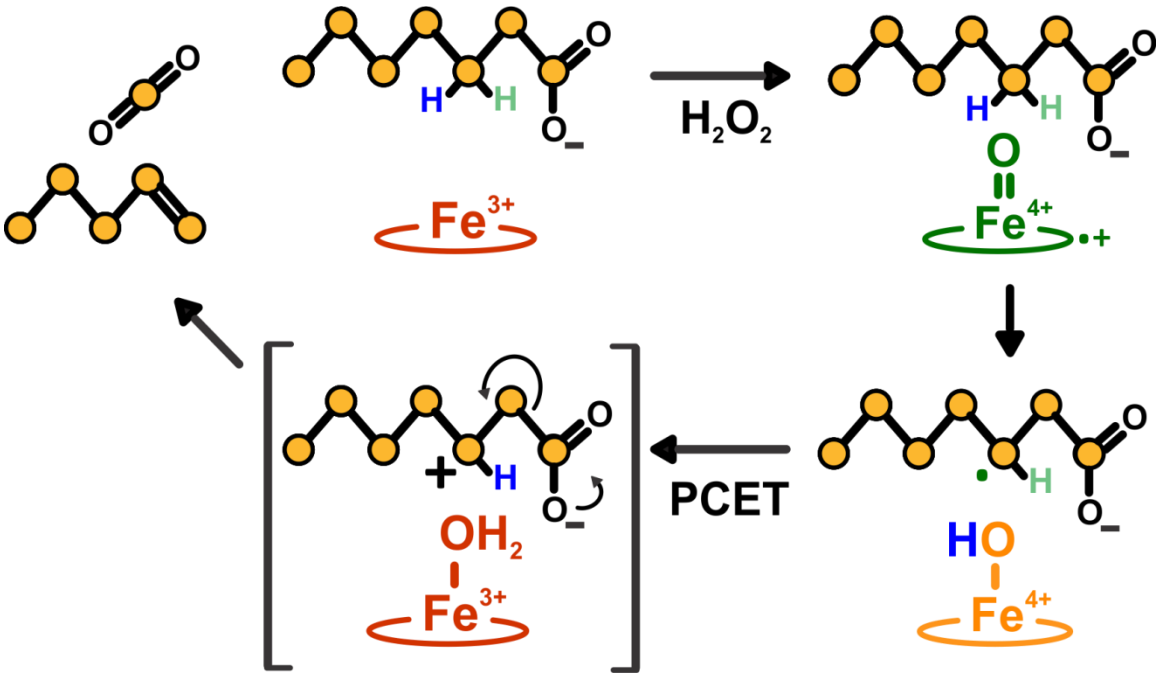


**Scheme 3.2** Catalytic mechanism of decarboxylation in $OleT_{JE}$

a substrate carbocation which is rearranged to render the final decarboxylated product (scheme 2). It has been shown that compound II is highly unstable in prototypical P450s due to the tendency of the hydroxy group to bounce back to the substrate radical in a process termed "oxygen rebound" producing a hydroxylated product.[47] Using norcarane probes as radical clocks, it has been demonstrated that this intermediate is short-lived and decays in no more than a few picoseconds.[16, 47-49] Surprisingly, the decay rate of compound II in $OleT_{JE}$ is lower than 10 $s^{-1}$ implying that this intermediate is stable enough to last for more than 100 miliseconds in the presence of the native substrate.[15] Furthermore, we have shown that this intermediate is no less reactive than typical P450s as the use of norcarane probes indicates very short lifetimes in the absence of native substrate.[16] It is clear, however, that stabilizing this intermediate is essential to divert the oxygen rebound process to the PCET to produce decarboxylated products. Understanding how these intermediates are stabilized and their electronic properties will be informative of the mechanisms of decarboxylation in the CYP152 family of P450s. The retention of reactivity and the increase in stability of $OleT_{SA}$ at high concentrations will be useful in subsequent studies of the reactive intermediates of decarboxylases. To ensure that proper accumulations and decay rates remained untouched, we performed a series of stopped-flow experiments to characterize the kinetics of the intermediates in $OleT_{SA}$. Singular value decomposition (SVD) of the data obtained from kinetic experiments on $OleT_{JE}$ allowed the determination of the pure UV-Vis spectra of all the intermediates in the protein (Figure 3.17).[14-15] Using the characteristic absorption of each intermediate we were able to similarly determine their kinetics in $OleT_{SA}$. Figure 3.16A and 3.16B show the photodiode array data obtained when mixing 20 µM of $OleT_{SA}$-C20 complex (ES) with 10 mM hydrogen peroxide. This was

done in the presence of bound protiated or perdeuterated eicosanoic acid. Preliminary examination of the data shows a complex reaction mechanism involving several intermediates upon mixing. Very distinct traces are obtained from the differentially isotopically labeled fatty acids. Pure spectra of the intermediates show that compound I has a main Soret band centered at 370 nm and a minor charge transfer band at 690 nm arising from the pi cation radical heme moiety. Analysis of the photodiode array data of $OleT_{SA}$ (Figure 18A and 18B) shows a more dramatic accumulation of compound I in the presence of deuterated substrate ($d_{38}$) compared to protiated ($h_{38}$). This is unsurprising as we have established that compound I abstracts a hydrogen atom from the substrate via tunneling event.[14]

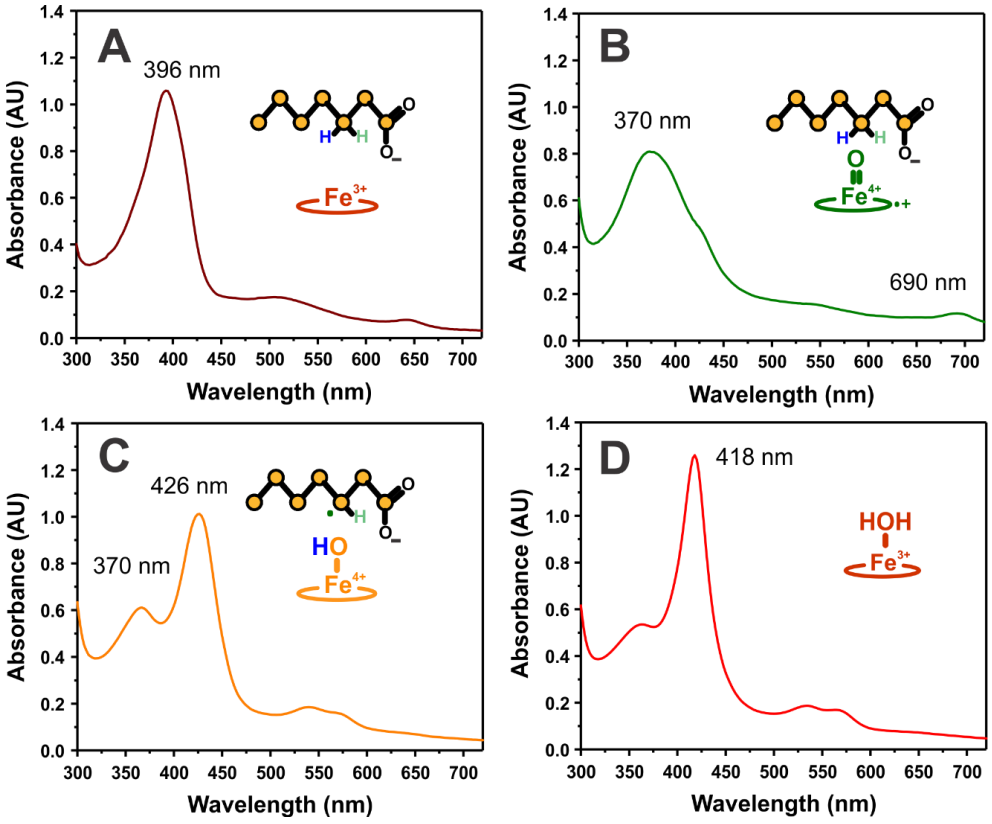


**Figure 3.16** Pure UV-Visible spectra of the catalytically relevant intermediates in $OleT_{JE}$. (A) Ferric 5-coordinate high spin (B) Ferryl-oxo pi cation radical heme (compound I) (C) Ferryl-hydroxy heme (compound II) (D) Ferric 6-coordinate low spin

SVD global analysis indicated the accumulation of ~ 65 % compound I with $d_{38}$-C20 and 40 % with $h_{38}$-C20 respectively. Although not far from the values obtained for $OleT_{JE}$, the latter appears to be slightly lower in the *Staphylococcus* ortholog. A possible explanation for this phenomenon could be that the decay rate of compound II is similar to the decay rate of the ferryl pi cation radical heme, preventing the high accumulation of the intermediate.

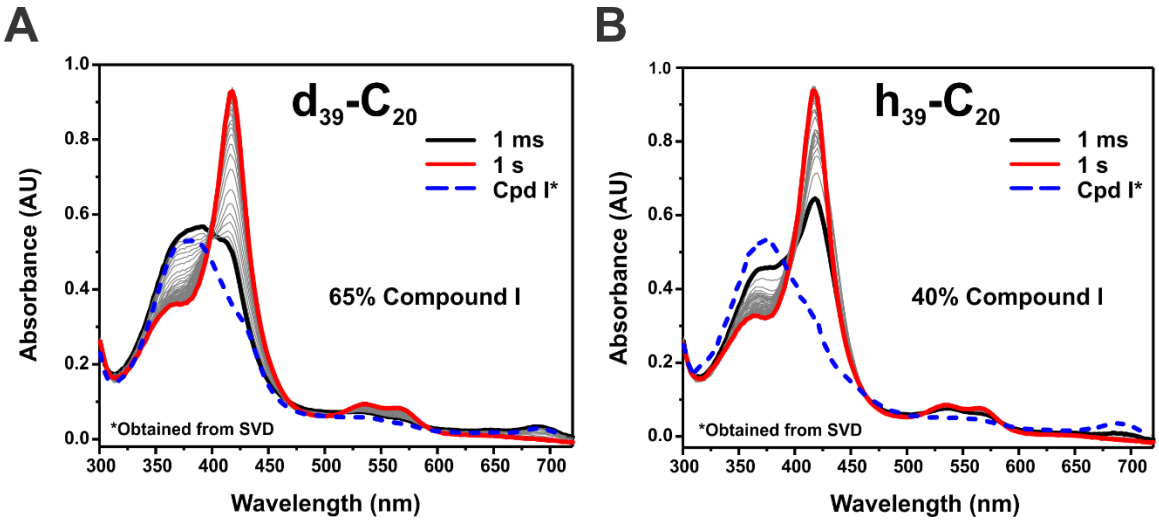


**Figure 3.18** Stopped-flow kinetic spectra of $OleT_{SA}$. (A) Photodiode array trace of 10 µM $OleT_{SA}$ bound to perdeuterated eicosanoic acid against 5 mM $H_2O_2$ (B) Photodiode array trace of 10 µM $OleT_{SA}$ bound to protiated eicosanoic acid against 5 mM $H_2O_2$

To analyze the kinetics of this intermediate, the absorption at 370 nm was monitored as a function of time. A multiphasic kinetic trace was obtained corresponding to compound I decay, however, absorbance contribution from other intermediates might affect the exact determination of the decay rates. To ensure that the kinetics of the intermediates were reliable, we monitored the absorbance at 690 nm which, as previously mentioned, can only arise from the pi-cation radical heme of compound I. A decay rate of 30 s-1 with d39-20

and of 500 s-1 with h39-C20 was determined. The obtained KIEH/D was found to be 16.6; this is a dramatic increase to what has been observed in $OleT_{JE}$. The cause of this change is not evident however, an enhanced hydrogen peroxide activation in $OleT_{SA}$ could be the origin of this phenomenon. As we have previously described,14-15 an apparent dissociation constant for hydrogen peroxide can be obtained by plotting the formation of compound II as a function of hydrogen peroxide concentration.

For $OleT_{JE}$ this apparent $K_D$ was near 80 µM when protiated and deuterated substrates are bound to the enzyme. In $OleT_{SA}$ there is no obvious accumulation of compound II in the $d_{38}$-C20 spectra (Figure 3.19A).

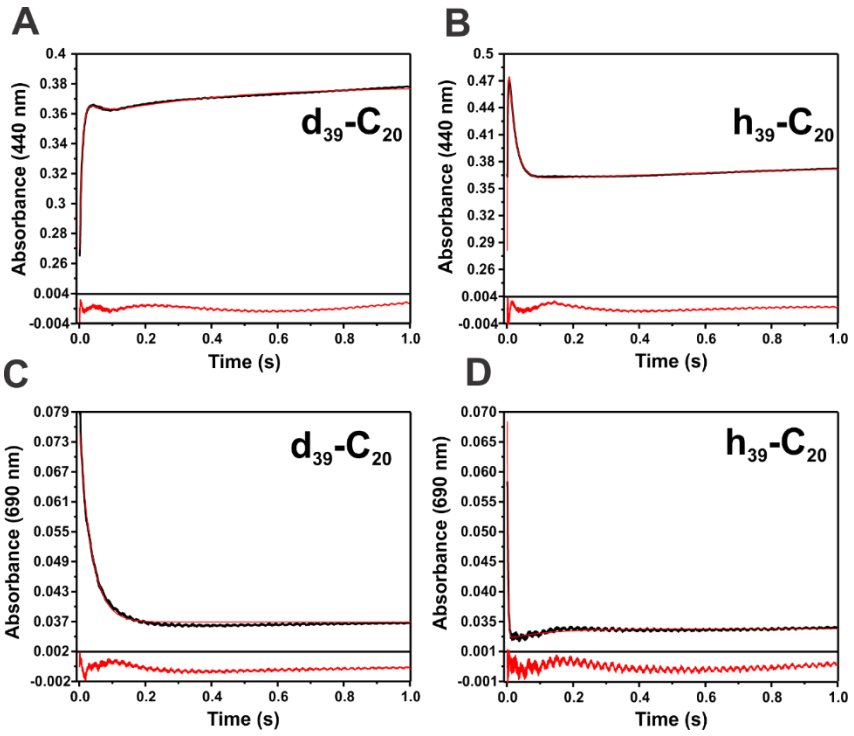


**Figure 3.19** Single wavelength traces of the reaction of 10 µM $OleT_{SA}$ substrate-bound against 5 mM $H_2O_2$. (A) Single wavelength trace at 440 nm of $OleT_{SA}$ bound to perdeuterated eicosanoic acid ($d_{39}$-C20). (B) Single wavelength trace at 440 nm of $OleT_{SA}$ bound to protiated eicosanoic. (C) Single wavelength trace at 690 nm of $OleT_{SA}$ bound to $d_{39}$-C20. (D) Single wavelength trace at 690 nm of $OleT_{SA}$ bound to $h_{39}$-C20.

However, significant accumulation is observed with protiated substrate (Figure 3.19B). SVD analysis determined the accumulation of compound II to be 50% with $h_{38}$-C20. Analysis of the formation rates as a function of hydrogen peroxide can be obtained by monitoring the absorbance at 440 nm as previously described. Figure 3.20 confirms that the apparent dissociation constant is at least 3-fold higher in $OleT_{SA}$. A possible explanation for this might be the unstructured hydrogen bond network in the active site as shown by the crystal structure.

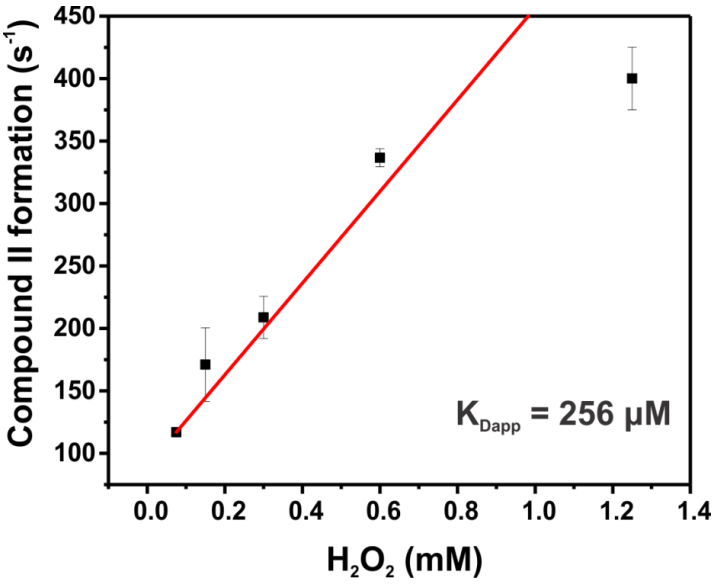


**Figure 3.20** Hydrogen peroxide dependence in the formation of compound II

Further analysis of the absorbance at 440 nm indicate that compound II has a decay rate 53 $s^{-1}$. The decay rate should be the same with deuterated substrate as compound II reactivity is independent of the nature of the hydrogen isotope of the substrate. This decay rates appear to be 5-fold higher than $OleT_{JE}$ but is still within the same order of magnitude, suggesting a similar mechanism of stabilization of the intermediate to allow for the decarboxylation of the substrate. Furthermore, the increased decay rate of this intermediate

explains why the accumulation of compound II with perdeuterated substrate is not obvious, as the decay rate of both intermediates is very similar (35 $s^{-1}$ and 53 $s^{-1}$). Taking all this into consideration, we can conclude that despite having small kinetic differences, the reactivity of the intermediates in $OleT_{SA}$ are similar than in $OleT_{JE}$ and can therefore be used as a platform to study the fundamentals of their chemistry.

## 4. Conclusion

The biophysical and structural characterization of a new decarboxylase of the CYP152 family of P450 has been presented in this manuscript. UV-Vis and EPR spectroscopy indicates that these two proteins have very similar heme environments including the second coordination sphere. This is reflected on the similar reactivity of both proteins with a panel of fatty acids which show that the decarboxylation features are retained. Furthermore, we were able to crystallize and show that both proteins are structurally identical. More importantly, we showed that $OleT_{SA}$ is an order of magnitude more stable than $OleT_{JE}$, and that it can properly accumulate the catalytically relevant intermediates observed in the *Jeotgalicoccus* ortholog. Taking all this into account, $OleT_{SA}$ opens up a new platform for the study of the electronic properties of the catalytically relevant intermediates in decarboxylases from the CYP152 family of cytochrome P450s.

## 5. References

1. Jurrus, E.; Engel, D.; Star, K.; Monson, K.; Brandi, J.; Felberg, L. E.; Brookes, D. H.; Wilson, L.; Chen, J.; Liles, K.; Chun, M.; Li, P.; Gohara, D. W.; Dolinsky, T.; Konecny, R.; Koes, D. R.; Nielsen, J. E.; Head-Gordon, T.; Geng, W.; Krasny, R.; Wei, G. W.; Holst,

M. J.; McCammon, J. A.; Baker, N. A., Improvements to the APBS biomolecular solvation software suite. *Protein Science* **2018,** *27* (1), 112-128.

2. Amghizar, I.; Vandewalle, L. A.; Van Geem, K. M.; Marin, G. B., New Trends in Olefin Production. *Engineering* **2017,** *3* (2), 171-178.

3. Ghanta, M.; Fahey, D.; Subramaniam, B., Environmental impacts of ethylene production from diverse feedstocks and energy sources. *Applied Petrochemical Research* **2014,** *4* (2), 167-179.

4. Brownbridge, G.; Azadi, P.; Smallbone, A.; Bhave, A.; Taylor, B.; Kraft, M., The future viability of algae-derived biodiesel under economic and technical uncertainties. *Bioresource Technology* **2014,** *151*, 166-173.

5. Koppolu, V.; Vasigala, V. K., Role of Escherichia coli in Biofuel Production. *Microbiology insights* **2016,** *9*, 29-35.

6. Wise, C. E.; Grant, J. L.; Amaya, J. A.; Ratigan, S. C.; Hsieh, C. H.; Manley, O. M.; Makris, T. M., Divergent mechanisms of iron-containing enzymes for hydrocarbon biosynthesis. *J. Biol. Inorg. Chem.* **2017,** *22* (2-3), 221-235.

7. Kallio, P.; Pásztor, A.; Thiel, K.; Akhtar, M. K.; Jones, P. R., An engineered pathway for the biosynthesis of renewable propane. *Nature Communications* **2014,** *5*, 4731.

8. Rude, M. A.; Baron, T. S.; Brubaker, S.; Alibhai, M.; Del Cardayre, S. B.; Schirmer, A., Terminal olefin (1-alkene) biosynthesis by a novel p450 fatty acid decarboxylase from Jeotgalicoccus species. *Appl. Environ. Microbiol.* **2011,** *77* (5), 1718-27.

9. Belcher, J.; McLean, K. J.; Matthews, S.; Woodward, L. S.; Fisher, K.; Rigby, S. E. J.; Nelson, D. R.; Potts, D.; Baynham, M. T.; Parker, D. A.; Leys, D.; Munro, A. W., Structure and Biochemical Properties of the Alkene Producing Cytochrome P450 OleT(JE) (CYP152L1) from the Jeotgalicoccus sp. 8456 Bacterium. *The Journal of Biological Chemistry* **2014,** *289* (10), 6535-6550.

10. Fujishiro, T.; Shoji, O.; Nagano, S.; Sugimoto, H.; Shiro, Y.; Watanabe, Y., Crystal structure of H2O2-dependent cytochrome P450SPalpha with its bound fatty acid substrate: insight into the regioselective hydroxylation of fatty acids at the alpha position. *J. Biol. Chem.* **2011,** *286* (34), 29941-50.

11. Lee, D. S.; Yamada, A.; Sugimoto, H.; Matsunaga, I.; Ogura, H.; Ichihara, K.; Adachi, S.; Park, S. Y.; Shiro, Y., Substrate recognition and molecular mechanism of fatty acid hydroxylation by cytochrome P450 from Bacillus subtilis. Crystallographic, spectroscopic, and mutational studies. *J. Biol. Chem.* **2003,** *278* (11), 9761-7.

12. Amaya, J. A.; Rutland, C. D.; Leschinsky, N.; Makris, T. M., A Distal Loop Controls Product Release and Chemo- and Regioselectivity in Cytochrome P450 Decarboxylases. *Biochemistry* **2018,** *57* (3), 344-353.

13. Amaya, J. A.; Rutland, C. D.; Makris, T. M., Mixed regiospecificity compromises alkene synthesis by a cytochrome P450 peroxygenase from Methylobacterium populi. *J. Inorg. Biochem.* **2016,** *158*, 11-6.

14. Grant, J. L.; Hsieh, C. H.; Makris, T. M., Decarboxylation of fatty acids to terminal alkenes by cytochrome P450 compound I. *Journal of the American Chemical Society* **2015,** *137* (15), 4940-3.

15. Grant, J. L.; Mitchell, M. E.; Makris, T. M., Catalytic strategy for carbon-carbon bond scission by the cytochrome P450 OleT. *Proceedings of the National Academy of Sciences of the United States of America* **2016,** *113* (36), 10049-54.

16. Hsieh, C. H.; Huang, X.; Amaya, J. A.; Rutland, C. D.; Keys, C. L.; Groves, J. T.; Austin, R. N.; Makris, T. M., The Enigmatic P450 Decarboxylase OleT Is Capable of, but Evolved To Frustrate, Oxygen Rebound Chemistry. *Biochemistry* **2017,** *56* (26), 3347-3357.

17. Luft, J. R.; Collins, R. J.; Fehrman, N. A.; Lauricella, A. M.; Veatch, C. K.; DeTitta, G. T., A deliberate approach to screening for initial crystallization conditions of biological macromolecules. *Journal of Structural Biology* **2003,** *142* (1), 170-179.

18. Otwinowski, Z.; Minor, W., [20] Processing of X-ray diffraction data collected in oscillation mode. In *Methods Enzymol.*, Academic Press: 1997; Vol. 276, pp 307-326.

19. McCoy, A. J.; Grosse-Kunstleve, R. W.; Adams, P. D.; Winn, M. D.; Storoni, L. C.; Read, R. J., Phaser crystallographic software. *Journal of applied crystallography* **2007,** *40* (Pt 4), 658-674.

20. Emsley, P.; Lohkamp, B.; Scott, W. G.; Cowtan, K., Features and development of Coot. *Acta crystallographica. Section D, Biological crystallography* **2010,** *66* (Pt 4), 486-501.

21. Kramer, Ryan M.; Shende, Varad R.; Motl, N.; Pace, C N.; Scholtz, J M., Toward a Molecular Understanding of Protein Solubility: Increased Negative Surface Charge Correlates with Increased Solubility. *Biophysical Journal* **2012,** *102* (8), 1907-1915.

22. Luthra, A.; Denisov, I. G.; Sligar, S. G., Spectroscopic features of cytochrome P450 reaction intermediates. *Archives of biochemistry and biophysics* **2011,** *507* (1), 26-35.

23. Coon, M. J., Cytochrome P450: nature's most versatile biological catalyst. *Annual review of pharmacology and toxicology* **2005,** *45*, 1-25.

24. Gillam, E. M.; Guengerich, F. P., Exploiting the versatility of human cytochrome P450 enzymes: the promise of blue roses from biotechnology. *IUBMB life* **2001,** *52* (6), 271-7.

25. Matthews, S.; Belcher, J. D.; Tee, K. L.; Girvan, H. M.; McLean, K. J.; Rigby, S. E.; Levy, C. W.; Leys, D.; Parker, D. A.; Blankley, R. T.; Munro, A. W., Catalytic Determinants of Alkene Production by the Cytochrome P450 Peroxygenase OleTJE. *J. Biol. Chem.* **2017,** *292* (12), 5128-5143.

26. Matthews, S.; Tee, K. L.; Rattray, N. J.; McLean, K. J.; Leys, D.; Parker, D. A.; Blankley, R. T.; Munro, A. W., Production of alkenes and novel secondary products by P450 OleTJE using novel H2 O2 -generating fusion protein systems. *FEBS letters* **2017,** *591* (5), 737-750.

27. Zachos, I.; Gassmeyer, S. K.; Bauer, D.; Sieber, V.; Hollmann, F.; Kourist, R., Photobiocatalytic decarboxylation for olefin synthesis. *Chemical Communications (Cambridge)* **2015,** *51* (10), 1918-21.

28. Matsunaga, I.; Yamada, A.; Lee, D. S.; Obayashi, E.; Fujiwara, N.; Kobayashi, K.; Ogura, H.; Shiro, Y., Enzymatic reaction of hydrogen peroxide-dependent peroxygenase cytochrome P450s: kinetic deuterium isotope effects and analyses by resonance Raman spectroscopy. *Biochemistry* **2002,** *41* (6), 1886-92.

29. Shoji, O.; Fujishiro, T.; Nagano, S.; Tanaka, S.; Hirose, T.; Shiro, Y.; Watanabe, Y., Understanding substrate misrecognition of hydrogen peroxide dependent cytochrome

P450 from Bacillus subtilis. *JBIC Journal of Biological Inorganic Chemistry* **2010,** *15* (8), 1331-1339.

30. Rhys, N. H.; Soper, A. K.; Dougan, L., The Hydrogen-Bonding Ability of the Amino Acid Glutamine Revealed by Neutron Diffraction Experiments. *The Journal of Physical Chemistry B* **2012,** *116* (45), 13308-13319.

31. Poulos, T. L., Cytochrome P450 flexibility. *Proceedings of the National Academy of Sciences of the United States of America* **2003,** *100* (23), 13121-2.

32. Muralidhara, B. K.; Negi, S.; Chin, C. C.; Braun, W.; Halpert, J. R., Conformational Flexibility of Mammalian Cytochrome P450 2B4 in Binding Imidazole Inhibitors with Different Ring Chemistry and Side Chains: SOLUTION THERMODYNAMICS AND MOLECULAR MODELING. *Journal of Biological Chemistry* **2006,** *281* (12), 8051-8061.

33. Hendrychova, T.; Anzenbacherova, E.; Hudecek, J.; Skopalik, J.; Lange, R.; Hildebrandt, P.; Otyepka, M.; Anzenbacher, P., Flexibility of human cytochrome P450 enzymes: molecular dynamics and spectroscopy reveal important function-related variations. *Biochimica et biophysica acta* **2011,** *1814* (1), 58-68.

34. Faponle, A. S.; Quesne, M. G.; de Visser, S. P., Origin of the Regioselective Fatty-Acid Hydroxylation versus Decarboxylation by a Cytochrome P450 Peroxygenase: What Drives the Reaction to Biofuel Production? *Chemistry (Weinheim an der Bergstrasse, Germany)* **2016,** *22* (16), 5478-83.

35. Yang, J.; Nie, Q.; Liu, H.; Xian, M.; Liu, H., A novel MVA-mediated pathway for isoprene production in engineered E. coli. *BMC biotechnology* **2016,** *16*, 5.

36. Denisov, I. G.; Makris, T. M.; Sligar, S. G.; Schlichting, I., Structure and chemistry of cytochrome P450. *Chemical reviews* **2005,** *105* (6), 2253-77.

37. Takahashi, A.; Kurahashi, T.; Fujii, H., Redox Potentials of Oxoiron(IV) Porphyrin π-Cation Radical Complexes: Participation of Electron Transfer Process in Oxygenation Reactions. *Inorganic Chemistry* **2011,** *50* (15), 6922-6928.

38. Groves, J. T.; Haushalter, R. C.; Nakamura, M.; Nemo, T. E.; Evans, B. J., High-valent iron-porphyrin complexes related to peroxidase and cytochrome P-450. *J. Am. Chem. Soc.* **1981,** *103* (10), 2884-2886.

39. Groves, J. T.; Watanabe, Y., Reactive iron porphyrin derivatives related to the catalytic cycles of cytochrome P-450 and peroxidase. Studies of the mechanism of oxygen activation. *J. Am. Chem. Soc.* **1988,** *110* (25), 8443-8452.

40. Shaik, S.; Hirao, H.; Kumar, D., Reactivity of high-valent iron-oxo species in enzymes and synthetic reagents: a tale of many states. *Accounts of chemical research* **2007,** *40* (7), 532-42.

41. Rittle, J.; Green, M. T., Cytochrome P450 compound I: capture, characterization, and C-H bond activation kinetics. *Science (New York, N.Y.)* **2010,** *330* (6006), 933-7.

42. Egawa, T.; Shimada, H.; Ishimura, Y., Evidence for Compound I Formation in the Reaction of Cytochrome-P450cam with m-Chloroperbenzoic Acid. *Biochemical and Biophysical Research Communications* **1994,** *201* (3), 1464-1469.

43. Raner, G. M.; Thompson, J. I.; Haddy, A.; Tangham, V.; Bynum, N.; Ramachandra Reddy, G.; Ballou, D. P.; Dawson, J. H., Spectroscopic investigations of intermediates in the reaction of cytochrome P450(BM3)-F87G with surrogate oxygen atom donors. *Journal of inorganic biochemistry* **2006,** *100* (12), 2045-53.

44. Spolitak, T.; Dawson, J. H.; Ballou, D. P., Reaction of ferric cytochrome P450cam with peracids: kinetic characterization of intermediates on the reaction pathway. *J. Biol. Chem.* **2005,** *280* (21), 20300-9.

45. Munro, A. W.; McLean, K. J.; Grant, J. L.; Makris, T. M., Structure and function of the cytochrome P450 peroxygenase enzymes. *Biochem. Soc. Trans.* **2018,** *46* (1), 183-196.

46. Munro, A. W.; Leys, D. G.; McLean, K. J.; Marshall, K. R.; Ost, T. W.; Daff, S.; Miles, C. S.; Chapman, S. K.; Lysek, D. A.; Moser, C. C.; Page, C. C.; Dutton, P. L., P450 BM3: the very model of a modern flavocytochrome. *Trends Biochem. Sci.* **2002,** *27* (5), 250-7.

47. He, X.; de Montellano, P. R. O., Radical Rebound Mechanism in Cytochrome P-450-catalyzed Hydroxylation of the Multifaceted Radical Clocks α- and β-Thujone. *Journal of Biological Chemistry* **2004,** *279* (38), 39479-39484.

48. Auclair, K.; Hu, Z.; Little, D. M.; Ortiz de Montellano, P. R.; Groves, J. T., Revisiting the Mechanism of P450 Enzymes with the Radical Clocks Norcarane and Spiro[2,5]octane. *J. Am. Chem. Soc.* **2002,** *124* (21), 6020-6027.

49. Kumar, D.; de Visser, S. P.; Sharma, P. K.; Cohen, S.; Shaik, S., Radical clock substrates, their C-H hydroxylation mechanism by cytochrome P450, and other reactivity patterns: what does theory reveal about the clocks' behavior? *Journal of the American Chemical Society* **2004,** *126* (6), 1907-20.

# CHAPTER 4

## STOICHIOMETRIC PREPARATION AND REACTIVITY OF COMPOUND I IN THE DECARBOXYLASE OLET-SA


**Abstract**

Cytochrome P450s are amongst nature's most versatile catalysts. The thiolate-ligated heme cofactor has allowed these enzymes to become essential biological tools for organisms to activate molecular oxygen and metabolize inert molecules. Previous P450 research has demonstrated how these enzymes can catalyze multiple chemistries on the same types of substrate, ranging from simple epoxidations to decarboxylations. The origin of this multiplicity can be attributed to the highly tunable nature of their heme-cofactor, where small changes in heme environment and geometry can have large repercussions on protein reactivity. In decarboxylases from the CYP152 family of P450s, the unusual stability of the catalytically relevant ferryl-heme intermediates allows these enzymes to redirect their chemistry from the P450 prototypical hydroxylation to the decarboxylation of their fatty acid substrate. In this study, we discuss how small alterations of the heme geometry in $OleT_{SA}$ translate to reactivity. Through a concerted effort of optical and EPR spectroscopy, resonance Raman and crystallography we demonstrate how small alteration in the distal pocket leads to a change in heme conformation, which at its turn, lead to a change in the spin equilibrium of the protein and the reactivity of its ferryl-heme intermediates.

## 1. Introduction

Cytochrome P450s constitute a superfamily of proteins present in all kingdoms of life.[1] The functional diversity of their thiolate-ligated heme prosthetic group has allowed these enzymes to become biological tools for organisms to activate molecular oxygen and metabolize a plethora of substrates. These proteins catalyze a highly diverse set of difficult reactions including but not limited to hydroxylations, epoxidations, nitrifications, and decarboxylations, among many others.[2-3] In humans, the versatility of these proteins is exemplified by their ability to metabolize 75 % of exogenous molecules such as drugs and other xenobiotics[4], as well as their essential role in the metabolism of endogenous molecules such as bile acids and steroids.[5-7] Current and previous research on P450s has focused on the elucidation of their mechanisms to chemically modify substrates, as they have shown to be essential elements in almost all organisms. The understanding of the chemistry of these enzymes has led to the development of therapeutic and biotechnological tools that range from anti-cancer drug treatments in humans[8] to their implementation in oil biodegradation.[9]

Many cytochrome P450s can perform multiple types of chemistries on a single substrate.[10-11] Deciphering the multiplicity of the chemistry in these enzymes has become an important focus of P450 research. In the last decade, this focus is highlighted in the elucidation of the catalytic determinants for decarboxylation in the CYP152 family of P450s.[12-15] This family of proteins was initially functionally characterized as fatty acid hydroxylases.[16-17] In 2011, a member of this family, $OleT_{JE}$, from the *Jeotgalicoccus sp*. bacteria, was shown to also catalyze the decarboxylation of a fatty acid substrate to a terminal alkene and $CO_2$.[18] Previous research in our group has been highly focused on determining the features that

give rise to decarboxylation in this family of enzymes. Using a panel of orthologs from this family, we have been able to show the importance of substrate positioning in the decarboxylation process.[14] Furthermore, we have demonstrated the functionality of the omnipresent F-G loop in maintaining the positioning of the substrate for proper decarboxylation.[13] Although much has been understood in the chemistry of these proteins, there are still some ambiguous details regarding the molecular determinants for C-C bond cleavage. Kinetic studies on $OleT_{JE}$ have revealed that the decarboxylation process proceeds using the prototypical high-valent ferryl-heme intermediates of P450s (compound I and compound II).[19-20] Moreover, we have shown that the stabilization of compound II in particular is necessary to allow a proton-coupled electron transfer (PCET) process between this intermediate and a substrate radical, producing what is believed to be a transient substrate carbocationic intermediate that allows for decarboxylation.[20] It is evident that understanding the unique ability of $OleT_{JE}$ to stabilize these intermediates is a major focal point for establishing the mechanisms of decarboxylation.

The optical properties of the heme cofactor in cytochrome P450s facilitate their study using optical spectroscopy.[21] While much information can be derived regarding the redox state of the heme and its environment, advanced spectroscopies such as electron paramagnetic resonance (EPR) and Mössbauer are necessary to further understand the electronic properties of the prosthetic group, particularly for transient reaction intermediates. These techniques however, require preparations that require a high concentration of protein and substrate and to obtain an intermediate in the purest form possible. Given the hydrophobic nature of both the substrate and protein, decarboxylases from the CYP152 family often tend to be poorly soluble and aggregate at higher concentrations. We have addressed this

limitation in chapter 3 of this dissertation through the characterization of $OleT_{SA}$, a new member of this family from *Staphylococcus aureus*. $OleT_{SA}$ possesses the same metabolic profile as $OleT_{JE}$ but is at least an order of magnitude more soluble. Moreover, we have revealed the importance of the initial spin state of the heme cofactor for accumulation of the transient intermediates in decarboxylases. We established that in order to attain maximal accumulation of compound I and compound II, $OleT_{SA}$ needs to be in the 5-coordinate high spin state (5cHS) to efficiently activate the native $H_2O_2$ oxidant and yield Compound I. To slow down the reactivity of Compound I, however, low temperatures are required. Notably, the 6-coordinate low spin (6cHS) to 5cHS spin-state transition is disfavored under these conditions. In this study, we characterize a mutation on the axial side of the heme cofactor ("cys-pocket") in $OleT_{SA}$ that alters the spin-state equilibrium of the protein, allowing for the stoichiometric accumulation of Compound I at extremely high concentrations. Through multiple spectroscopies and crystallographic studies, we demonstrate that the origin of this alteration in spin-equilibrium is a distortion in the heme planarity that is caused from altering an alanine to a bulkier proline residue. This research establishes a platform to understand the mechanisms of transient intermediate stabilization in decarboxylases from the CYP152 family, and more generally the cytochrome P450 reaction coordinate, at a level of detail that has been unattainable to date.

## 2. Experimental Procedures

### 2.1 Reagents and chemicals

All buffers used in this study were purchased from BDH chemicals. Hydrogen peroxide and sodium dithionite were purchased from Sigma Aldrich. Eicosanoic

($C_{20}H_{40}O_2$), octadecanoic ($C_{18}H_{36}O_2$), hexadecanoic ($C_{16}H_{32}O_2$), dodecanoic ($C_{12}H_{24}O_2$), were purchased from Supelco Analytical. Deuterated fatty acids were purchased from CDN Isotopes. P450 BSβ was a generous gift from Dr. Michael T. Green.

### 2.2 Mutagenesis of P450 BSβ and $OleT_{SA}$

The point mutation glutamine to histidine at position 85 in P450 BSβ was generated by PCR using the following primer and its reverse complement with the mutated codon underlined:

5' GGTGTTAATGCAATTCACGGTATGGATGGTAGC 3'

The point mutation of proline to alanine at position 364 in P450 BSβ was generated by PCR using the following primers with the mutated codon underlined and using either wild-type or BSβ_Q85H as a template:

5' TTGTGCGGGTGAAGGTATTACCATTGAAGTGA 3' Fwd

5' CACCCGCACAACGATGACCTTTTTCTGCATGAC 3' Rev

The point mutation alanine to proline at position 369 in $OleT_{SA}$ was generated by PCR using the following primers with the mutated codon underlined:

5' GTTGCCCTGGCGAGTGGATGACCATTATCATTATG 3' Fwd

5' GCCAGGGCAACGATGGTTGGTATAGTAGTCACCAC 3' Rev

Following PCR, plasmids were digested by DpnI for 1 hour at 37 °C to remove the parental plasmid. Following digestion, plasmids were transformed into *Escherichia coli* XL1 Blue. Resulting mutations were verified by sequencing at EtonBio Inc. (North Carolina).

### 2.3 Expression and purification of $OleT_{SA}$ and its variant

Expression and purification of both $OleT_{SA}$ wild-type and A369P were identical to the protocol previously described in Chapter 3. The final yields for both proteins were 80 mg of protein per liter of culture. The $R_Z$ ratio ($A_{418}/A_{280}$) was greater than 1.2, indicating a high degree of purity and heme incorporation into both variants.

### 2.4 Expression and purification of P450 BSβ and its variants

Expression of P450 BSβ wild-type, Q85H and Q85H/A366P was done in a similar manner as $OleT_{SA}$. Briefly, the plasmids were transformed onto BL21(DE3) containing the pTF2 plasmid encoding for GroEL/GroES/Tig onto a kanamycin/chloramphenicol LB plate. One colony was inoculated into 150 mL of modified Terrific Broth (12 g yeast extract, 6 g tryptone, 2 g peptone) supplemented with 50 µg/mL kanamycin and 20 µg/mL chloramphenicol and grown overnight at 37 °C. 10 mL of starter culture were inoculated into 500 mL of modified terrific broth containing 50 µg/mL kanamycin, 20 µg/mL chloramphenicol, 125 mg/L thiamine and trace metals. The culture was initially grown for ~2 hours at 37 °C until $OD_{600nm}$ = 0.8, at which point the temperature was decreased to 18 °C until the $OD_{600nm}$ reached 1.5. At this point, cultures were induced with 100 µM IPTG, 10 ng/mL tetracycline and 10 mg/L of 5-aminolevulinic acid and grown for an additional 15 hours at 18 °C. The following day, cultures were centrifuged 10 minutes at 6000 rpm and the pellet was resuspended in 4 mL of Buffer A (50 mM KPi pH 8, 300 mM NaCl and 10 mM imidazole) per gram of pellet. Cells were disrupted using a Branson sonifier and stirred for an hour before centrifuging 30 minutes at 16,000 rpm. The supernatant was loaded onto a previously equilibrated Ni-NTA column, washed with buffer A + 25 mM

imidazole and eluted with buffer A + 250 mM imidazole. The eluate was diluted 1:1 with Buffer B (50 mM KPi pH 8, 300 mM NaCl 60% ammonium sulfate) to reach a final concentration of 30% ammonium sulfate. The diluted protein was then loaded onto a previously equilibrated Butyl-S-Sepharose column, washed with 10 column volumes of Buffer C (50 mM KPi pH 8, 300 mM NaCl and 30% ammonium sulfate) and eluted with a gradient over 8 column volumes from buffer C to buffer D (50 mM KPi pH 8). Fractions with a $418_{nm}/280_{nm}$ ratio higher than 1.3 were pooled and dialyzed against 50 mM KPi pH 8 200 mM NaCl. Proteins were concentrated to 200 µM, flash frozen in liquid nitrogen and stored at -80 °C until further use. Final yields for all three variants were similar at around 65 mg of protein per liter of culture. The theoretical $R_Z$ ratio is 1.6 and is not far from what was obtained, indicating a highly pure protein preparation.

### 2.3 Spectroscopy

*a) UV-visible*

UV-visible spectra were obtained using an Agilent HP 8453 spectrophotometer. 10 µM of protein in 200 mM potassium phosphate ($KH_2PO_4$) pH 7.5 was used to titrate fatty acids dissolved in 70% ethanol: 30% Triton X-100 (v:v). The amount of ethanol added never exceeded 5% of the total volume. Dissociation constants were determined by plotting the change in absorbance at 418 nm and 396 nm and fitting them into the Morrison equation for tight binding as previously described.[15] All the absorbance changes can be attributed to the fatty acid binding as titrations with pure Triton X-100 did not induce any spin change. The ferrous forms of the protein were prepared by the addition of 50 µM of sodium dithionite to a solution of 10 µM P450 supplemented with 500 nM methyl viologen under

anaerobic conditions. The carbonmonoxy adduct was prepared by bubbling carbon monoxide for thirty seconds to the ferrous for of the protein.

*b) EPR spectroscopy*

EPR spectroscopy was performed as previously described (chapter 3). All the substrate-free forms of the proteins were prepared by the addition of 15 molar equivalents of hydrogen peroxide and incubation for 30 minutes prior to treatment with Biobeads SM-2 to remove any adventitiously bound hydrophobic molecules. After treatment, the protein was desalted in 200 mM potassium phosphate ($KH_2PO_4$) pH 7.5 using a PD-10 desalting column to remove any excess hydrogen peroxide. All the substrate-bound forms contained 1 molar equivalent of the indicated fatty acid dissolved in 70% ethanol:30% Triton X-100 (v:v). Final protein concentrations were 200 µM. All the samples were flash-frozen and kept at liquid nitrogen temperatures until further use. EPR spectra were recorded on a X-band Bruker EMXplus spectrometer equipped with an Oxford Instruments liquid helium continuous flow cryostat. Spectra were recorded at a temperature of 15 K, a power of 2 mW and an amplitude of 1 mT.

*c) Magnetic Circular Dichroism (MCD) spectroscopy*

Substrate-free and C20 fatty acid bound $OleT_{SA}$ samples were prepared as described above, using 10 µM enzyme. Ferrous carbonmonoxy P450 adducts were prepared by combining 10 µM $OleT_{SA}$ (substrate-free or C20-bound) with 500 nM methyl viologen. The solution was made anaerobic by purging with $N_2$ gas. Carbon monoxide gas was bubbled into the solution, and the protein was reduced to the ferrous state with sodium dithionite. MCD spectra were obtained on a Jasco J-815 CD spectrometer with a 1.4-Tesla

electromagnet. The sample was maintained at 3 ºC using a Lauda-Brinkmann RM6 recirculating water bath.

*d) Resonance Raman Spectroscopy*

Resonance Raman studies on $OleT_{SA}$ was performed by Dr. Yilin Liu and Prof. James Kincaid at Marquette University. The following experimental procedures were used. All proteins were centrifuged to remove any precipitation before measurements. The ferric proteins were diluted to 100 µM with 200mM KPi pH 7.5 and transferred to NMR tubes for measurements. Two molar equivalents of hydrogen peroxide were added to the substrate-free sample to keep protein in the low spin state. To prepare the ferrous CO adducts, 70 µL of 150 µM proteins (wild-type $OleT_{SA}$, theA369P mutant, and their substrate-bound forms) were transferred into NMR tubes (WG-5 Economy, Wilmad), respectively, sealed with a rubber septum. The ferrous CO complexes were prepared by saturation the sample with CO gas prior to the injection of excess sodium dithionite solution.

The spectra of ferric samples were obtained using 406.7 nm excitation line, which was provided by a Kr+ laser (Coherent Innova Sabre Ion Laser) with a Spex 1269 spectrometer equipped with a Spec-10 LN liquid nitrogen cooler detector (Princeton Instruments). The spectra of ferrous CO complexes were measured using 441.6 nm excitation line from a He-Cd laser (IK series He-Cd laser, Kimmon Koha Co., Ltd). The slit width was 150 µm for all the measurements except for high-frequency measurement on ferrous CO samples, where it was increased to 250 µm facilitating detection of the weaker intensity ν(C-O) modes. The laser power for ferric and ferrous samples was kept around 13mW, whereas spectra of the ferrous CO complexes were obtained using ~1 mW to avoid

photodissociation. All samples were measured in spinning NMR tubes, where a cylindrical focusing lens was used to avoid local heating and protein degradation. Spectra were calibrated with fenchone and acetone-d6 (for calibration with high frequency above 1700 $cm^{-1}$), and processed with Grams AI software. It is important to note that the substrate-bound CO samples precipitated after 20-30 minutes during measurement under a 1 mW laser power, showing low signal/noise ratios in the CO region.

### 2.4 Temperature-dependent UV-visible spectroscopy and analysis

Experiments were performed by Olivia Manley and the following experimental methods are credited to her. Substrate-free $OleT_{SA}$ (WT or A369P) was prepared by incubating 10 µM of the as-purified enzyme with 3 molar equivalents of $H_2O_2$ to turn over adventitiously bound fatty acids. The enzyme-substrate complex was prepared by incubating 10 µM of the as-purified enzyme with 3 molar equivalents of the desired fatty acid at 4 °C for at least 4 hours to allow for complete fatty acid binding. The absorbance spectra of the samples were obtained at various temperatures using a Cary 400 Bio UV-visible spectrophotometer equipped with a PolyScience circulating water bath. The pyridine hemochromogen assay[22] was used to determine the extinction coefficients of the Soret peak of pure HS and LS samples ($\varepsilon_{394}$ = 106.5 $mM^{-1}$ $s^{-1}$ and $\varepsilon_{418}$ = 56.6 $mM^{-1}$ $s^{-1}$ for HS; $\varepsilon_{394}$ = 62.5 $mM^{-1}$ $s^{-1}$, $\varepsilon_{418}$ = 112.8 $mM^{-1}$ $s^{-1}$ for LS; and $\varepsilon_{406}$ = 86.8 $mM^{-1}$ $s^{-1}$ for both HS and LS as 406 nm corresponds to the isosbestic point). In a similar manner to the analysis of P450cam by Sligar,[23] these extinction coefficients were used to calculate the fraction of the enzyme in the HS and the LS states for each sample. The equilibrium constants were determined by K = [HS]/[LS] for each sample and were modeled to an

Arrhenius temperature dependence to produce a linear van't Hoff plot, from which the enthalpy and entropy of the equilibrium constants were determined. For T = 20 °C, the Gibb's free energy and the equilibrium constant representative of the spin shift equilibrium ($K_{spin}$) were calculated.

### 2.5 Crystallography

*a) Sample preparation*

A solution of $OleT_{SA}$ A369P with a RZ ratio of 1.3 was treated with 2 molar equivalents of eicosanoic acid and incubated for 2 hours at 4 °C. The protein was subsequently buffer-exchanged in 200 mM KPi pH 7.5 with a PD-10 desalting column and treated for 2 hours at 4 °C with Biobeads SM-2 to remove any remaining fatty acid and Triton X-100. The protein was finally concentrated to 600 µM (~30 mg/mL) and flash frozen in liquid nitrogen until further use.

*b) Crystallization conditions*

Crystals were grown in a similar manner as the wild-type enzyme (chapter 3). Briefly, 1 µL of protein was diluted with 1 µL of mother liquor (100 mM HEPES pH 7.5; 100 mM sodium molybdate; 20 % PEG 8000) in a total volume of 2 µL. Hanging-drop trays were incubated at 4 °C for three weeks for optimum crystal growth. Crystals were harvested and soaked in mother liquor supplemented with 20 % glycerol as a cryoprotectant and cryo-cooled in liquid nitrogen.

*c) Data collection and processing*

Data collection was performed at the Advanced Photon Source (Lemont, Il, USA), beamline 22-ID, through the Southeast Regional Collaborative Access Team (SER-CAT).

Integration and scaling of the data was done using the HKL-2000 software package.[24] Structure phasing was done by molecular replacement using the substrate-bound $OleT_{SA}$ structure as an initial model (described in chapter 3) in the Phenix Phaser program.[25] Model building was done by using the original wild-type enzyme as a scaffold using WinCoot.[26] Final refinement and validation was done through Phenix Refine and Phenix Validate respectively.[25] All the figures were generated using Pymol Molecular Graphics software package (Version 1.3 Schrödinger LLC).

Heme out-of-plane distortion values were determined using the Normal-Coordinate Structure Decomposition software developed by Shelnutt.[27]

### 2.6 Stopped-flow kinetics

To prepare $OleT_{SA}$ for stopped-flow experiments, adventitiously bound FAs were removed by treating the protein with 15 molar equivalents of $H_2O_2$, and the protein was subsequently desalted into 200 mM KPi at pH 7.5. All proteins were then concentrated to ~200 µM and diluted in 200 mM KPi at pH 7.5 to a final concentration of 20 µM. Proteins were then incubated with two molar equivalents of FA substrate from and incubated at 4 °C for at least 4 hours to allow fatty acid binding; ethanol concentration did not exceed 5% of the total volume. A stock of 10 mM $H_2O_2$ was prepared in 200 mM KPi at pH 7.5 and incubated at 4 °C prior to use. Stopped-flow experiments were carried out on an Applied Photophysics Ltd. SX20 stopped-flow spectrophotometer. Briefly, each protein stock was rapidly mixed 1:1 against 10 mM $H_2O_2$ for a final concentration of 10 µM protein and 5 mM $H_2O_2$ post-mix. Single wavelength traces were collected using a photomultiplier tube

and full spectrum data using a photodiode array. Data processing was done as previously described (chapter 3).

### 3. Results

Kinetic studies in our lab have allowed us to establish the overall catalytic mechanism for decarboxylation in OleT.[19-20, 28] Scheme 1 shows a compilation of the general reaction sequence for decarboxylation. The initial state of the protein involves a water molecule as a sixth ligand of the heme, in what is termed the 6-coordinate low-spin state (6cLS). Upon substrate binding, the water molecule is displaced and the heme undergoes a transition to a 5-coordinate high spin state (5cHS). When hydrogen peroxide is rapidly mixed to the enzyme-substrate complex, $OleT_{SA}$ forms the initial transient intermediate compound I. This ferryl pi-cation radical heme is a powerful oxidant that

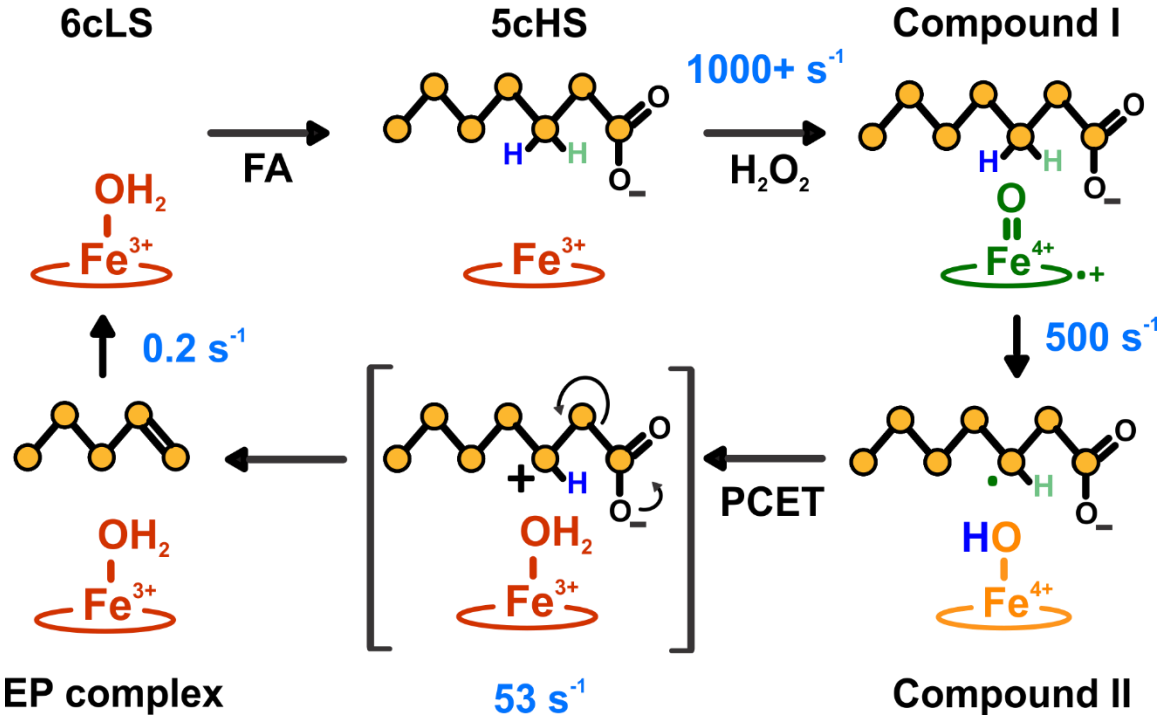


**Scheme 4.1** Decarboxylation mechanism in $OleT_{SA}$ with protiated eicosanoic acid bound with observed kinetic rate constants derived from transient absorption studies.

proceeds to abstract a hydrogen from the β-carbon of the fatty acid to form a substrate radical and compound II. The protonated ferryl-heme is then involved in a proton-coupled electron transfer (PCET) between this intermediate and the substrate radical to render the final decarboxylated product. The atypically low decay rate constants for both intermediates has allowed their detailed kinetic characterization. Their unusual stability is a hallmark for their involvement in the decarboxylation process in CYP152 enzymes.

Further studies on these intermediates however, has been hampered by the strenuous conditions required for rapid freeze-quench methods for their capture. In order to maximize their accumulation, it is imperative for the protein to be in the 5cHS state before rapidly mixing with hydrogen peroxide. This feat is practically complex as it requires the solubilization of long chain fatty acids and a promotion of spin-state conversion despite the low temperatures necessary for intermediate stability. A possible route to circumvent this problem would be to disrupt the spin-state equilibrium ($K_{spin}$) to favor the 5cHS state. Previous studies have shown that changes in the heme environment can lead to alterations in the $K_{spin}$ in other P450s.[29-30] A clear example of this type of alteration has been observed in $P450_{coh}$ where the placement of hydrophobic residues on the distal pocket results in an increased accumulation of the 5cHS state.[30] These residue changes however, were also shown to affect substrate selectivity and thus the final metabolized product.

In CYP152 enzymes, alterations of an active site histidine (H87 in $OleT_{SA}$) have been shown to affect high-spin accumulation. Mutagenic conversion of His85 in $OleT_{JE}$ to a glutamine residue (reminiscent of hydroxylases from this family; Figure 4.1A) resulted in a lower accumulation of the 5cHS even in the presence of substrate.[12] Preliminary data

in our group showed that the analogous mutation (glutamine to histidine) in the P450 BSβ hydroxylase results in an increased accumulation of the 5cHS state of the protein (Figure 4.4.1B) supporting the involvement of this residue in maintaining spin-state equilibrium.

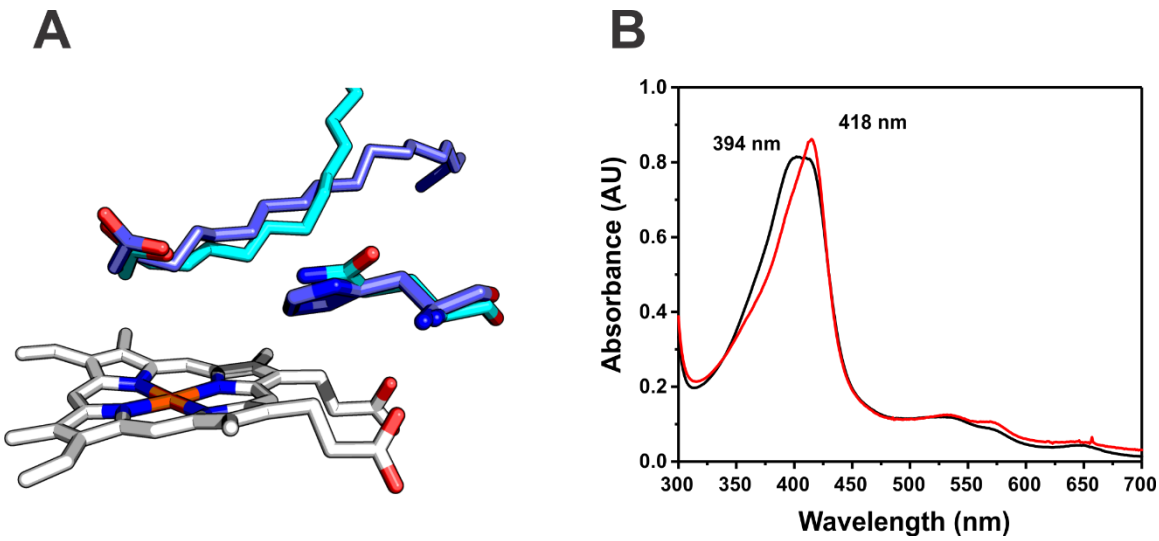


**Figure 4.1** Effect of the mutation of residue 85 in P450 BSβ hydroxylase. (A) Crystal structure of $OleT_{SA}$ and P450 BSβ. In purple $OleT_{SA}$ and in cyan P450 BSβ. (B) UV-Vis spectroscopy of the maximal 5cHS accumulation in P450 BSβ wild type (red) and P450 BSβ Q85H.

Although mutagenesis data suggest that changes in the distal heme environment might be effective in modulating the $K_{spin}$ in these enzymes, this is not the most efficient approach. The high dependence of the decarboxylation process on substrate positioning limits this strategy as any disruption could lead to the hydroxylation of the substrate and the loss of intermediate stabilization.

Another approach to alter the $K_{spin}$ is to alter the hydrogen bonding environment of the Fe-S bond. In a recent study by Krest et al,[31] the authors described the importance of the H-bonding network on the "cys-pocket" for regulating P450 reactivity. They

demonstrated that a weaker hydrogen bonding network leads to a shorter Fe-S bond length which in turn leads to greater reactivity in P450s compared to chloroperoxidases. Extensive research has also been done on CYP2B4 where the change of a phenylalanine residue to a histidine on the proximal side of the heme leads to changes in the redox potential and other properties of the protein.[32-33] Although there is no direct evidence that the H-bonding network is specifically involved in modulation of the spin-state equilibrium, it is clear that subtle changes might affect it.

Hydroxylases from the CYP152 family, like P450 BSβ and P450 SPα, possess a proline residue that is adjacent to the cysteine ligand, whereas decarboxylases often possess an alanine residue. The crystal structure of these proteins shows a change in the hydrogen bonding network of the Fe-S bond (Figure 4.2), with decarboxylases having an additional hydrogen bond to the thiol which would translate to weaker reactivity. The strong differences in 5cHS accumulation between hydroxylases and decarboxylases remains

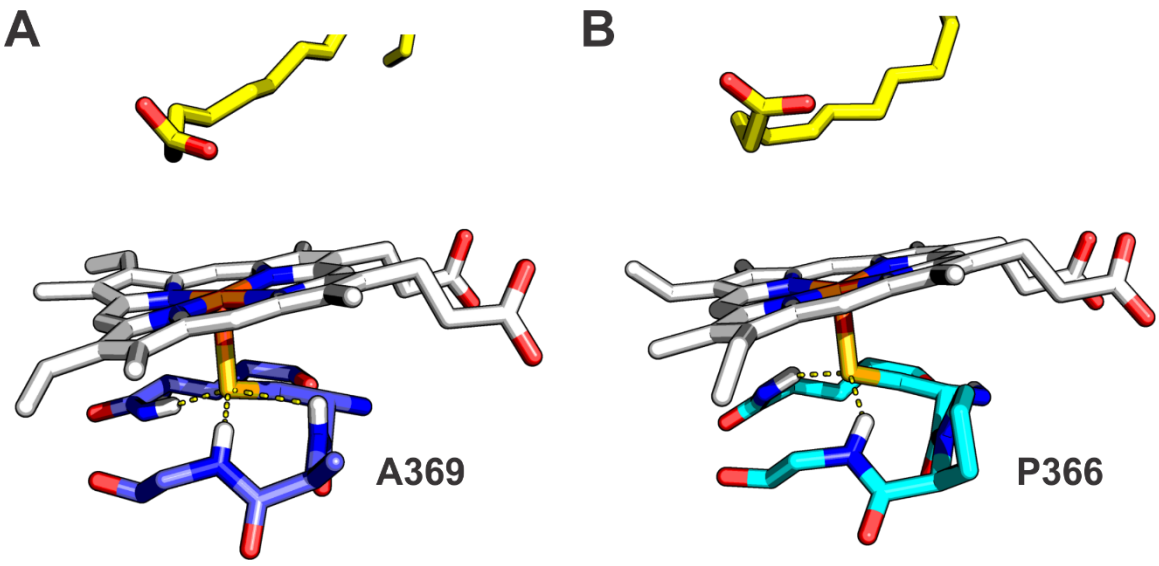


**Figure 4.2** Crystal structure of the "cys-pocket" H-bonding network in $OleT_{SA}$ and P450 BSβ. (A) $OleT_{SA}$; 3 hydrogen bonds are shown to the Fe-S stretch coming from residues A369, G370 and Q357. (B) P450 BSβ (PDB code: 1IZO); 2 hydrogen bonds are shown to the Fe-S stretch coming from residues G367 and Q352.

highly uncharted. It is clear however, that these types of interactions might somehow be involved in the spin equilibrium of CYP152 enzymes. To explore the effects of such changes, we studied the effects of the mutation $OleT_{SA}$ A369P and P450 BSβ P366A.

### 3.1 The proline to alanine mutation of residue 366 in P450 BSβ disrupts the spin equilibrium favoring the 6cLS state

As shown in Figure 4.1B, wild-type P450 BSβ can only accumulate 42% 5cHS even in the presence of an excess of the native substrate hexadecanoic acid. In $OleT_{SA}$ the accumulation of the 5cHS form with its corresponding native substrate (presumed to be eicosanoic acid such as in $OleT_{JE}$) is at least 2-fold larger than for BSβ. Given the high similarity of the active of both enzymes, this suggests that modulation of the spin equilibrium is done by single residues near the heme. To understand the effects of Pro366 in 5cHS accumulation, we mutated this residue to the alanine found in the decarboxylases of this family. We anticipated that if this residue is involved in spin-equilibrium it would

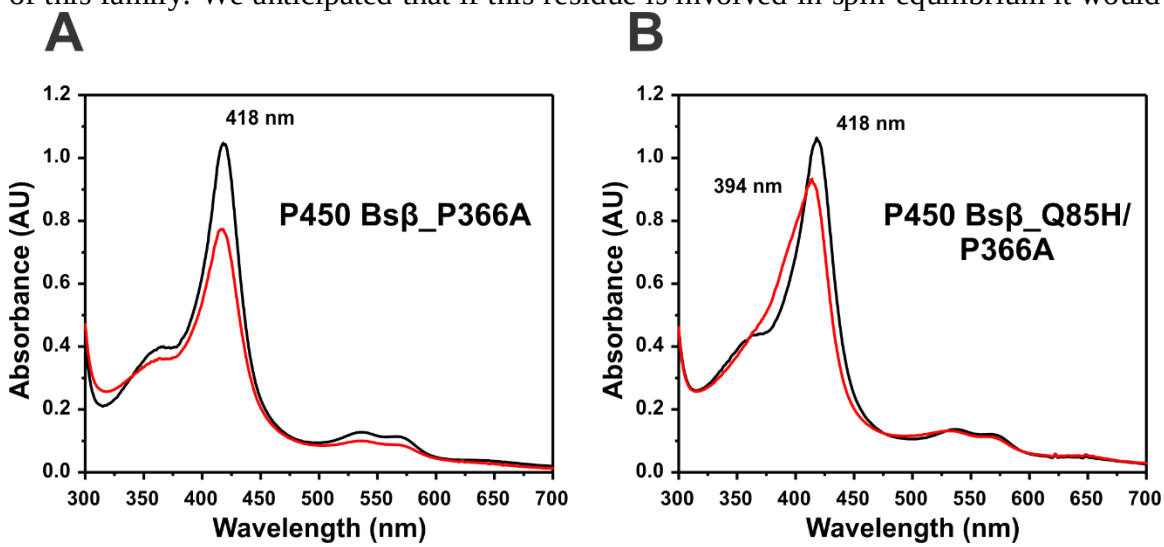


**Figure 4.3** UV-Vis absorption spectra of P450 BSβ mutants. (A) P450 BSβ_P366A; black represents the substrate-free form and red in the presence of excess hexadecanoic acid. (B) P450 BSβ_Q85H/P366A; black represents the substrate free form and red in the presence of excess hexadecanoic acid.

favor the 5cHS state like in $OleT_{SA}$ and $OleT_{JE}$. Since it has already been shown that residue Gln85 in P450 BSβ is involved in the spin transition, we also produced the double mutant Q85H/P366A to discard any involvement of the glutamine in the process. Figure 4.3 shows the UV-Vis spectra of both mutants in their substrate-free form and in the presence of excess hexadecanoic acid.

As is evident from the spectra, the 5cHS accumulation, which is monitored by an increase in the absorbance at 394 nm, is highly affected by the proline to alanine change. In the substrate-free form, both the single and double mutant show a maximum Soret absorbance at 418 nm, consistent with a water molecule as a 6$^{th}$ ligand to the Fe(III) center. Upon substrate addition, a small spin transition can be observed in the single mutant to a final 5cHS accumulation of 23 %. This is a 20% decrease to what is observed in the wild-type enzyme (Figure 4.1B). A similar change can be observed in the double mutant in which the maximal 5cHS accumulation is 41 %. This is again a 20 % decrease to what is observed for the single Q85H mutant.

**Table 4.1** Maximal 5cHS accumulation for P450 BSβ and $OleT_{SA}$ and all their variants determined at 20 °C.

| **% 5-coordinate high spin accumulation** | | | | | | |
|---|---|---|---|---|---|---|
| **Substrate** | **P450 BSβ** | **P450 BSβ Q85H** | **P450 BSβ P366A** | **P450 BSβ Q85H/P366A** | **$OleT_{SA}$** | **$OleT_{SA}$ A369P** |
| **C20** | ND* | ND* | ND* | ND* | 90 | 100 |
| **C16** | 42 | 64 | 23 | 41 | 73 | 95 |
| **C12** | 40 | 55 | 15 | 40 | 71 | 90 |

* not detected

Similar trends are obtained with other fatty acid substrates (Table 4.1), supporting the notion of the involvement of this residue in modulating $K_{spin}$. Although still unclear how

these mutations affect the $K_{spin}$ of the protein, the data suggests that the analogous mutation in decarboxylases would favor the 5cHS accumulation. To our knowledge, such effects have never been observed in other P450s. Further studies on the engagement of this residue in spin transition is necessary.

### 3.2 Alanine to proline change of residue 369 in $OleT_{SA}$ highly favors the 5cHS state of the protein

To further examine the involvement of residue 369 in decarboxylases, we mutated Ala369 in $OleT_{SA}$ to a proline and examined its high spin accumulation. Figure 4.4 shows the UV-Vis spectra of the mutant in both the ferric and ferrous state, as well as its carbon-monoxy ferrous form. The 5cHS accumulations with different fatty acids are compiled in table 4.1

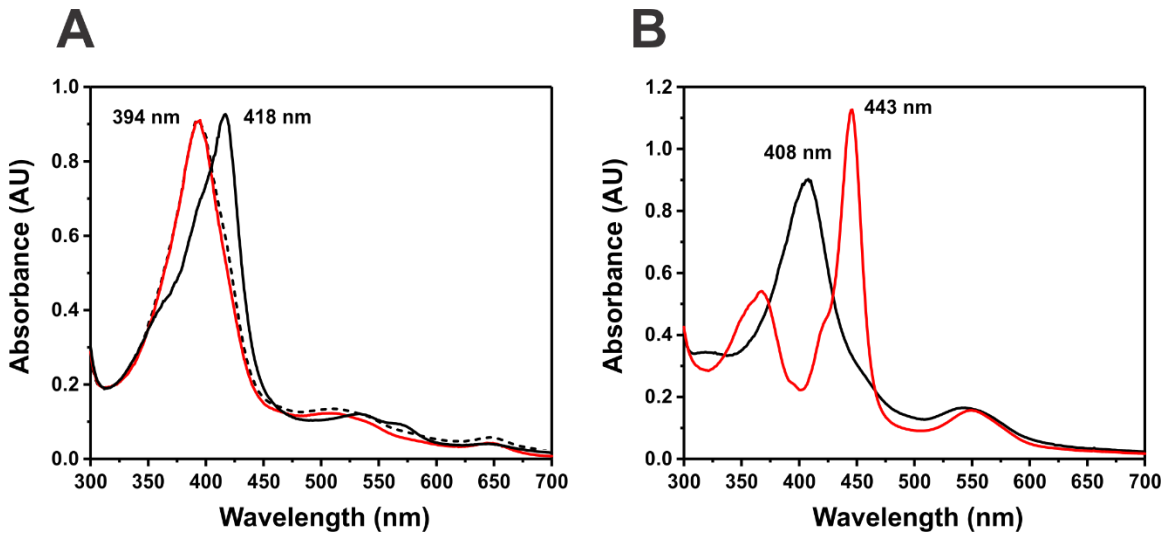


**Figure 4.4** UV-Vis spectra of $OleT_{SA}$ A369P. (A) Ferric spectra; black represents the enzyme in the substrate-free form, black dashed line represents the enzyme in the "as-purified" form and red represents the enzyme with an excess of eicosanoic acid. (B) Ferrous spectra; black represents the enzyme in the ferrous form and red the carbon monoxy ferrous enzyme.

Initial examination of the spectra of the as purified protein (Figure 4.4A, black dashed line), indicates that 90 % of the protein is purified in the 5cHS state. This phenomenon has also been seen in the wild-type enzyme due to the presence of adventitiously bound fatty acids from *E. coli*, predominantly C16, although to a much lesser extent (chapter 3). This could be due to the presence of a larger amount of fatty acid in the protein preparation, which seems unlikely, a shift of the spin-state equilibrium or a change in the dissociation constant ($K_D$) of the enzyme for its substrate. Addition of hydrogen peroxide to remove any bound substrate induces the full transition to a 6cLS state with a water bound as a $6^{th}$ ligand in CYP152 enzymes. The $OleT_{SA}$ A369P mutant shows however, the presence of 20% 5cHS even in high excess of hydrogen peroxide (Figure 4.4A, black line). This is highly indicative of a change in the heme environment favoring the 5cHS state even in the absence of substrate. Addition of eicosanoic acid in excess fully drives the protein to the 5cHS compared to wild-type where 90% is observed. Although this change is subtle, the low temperatures required for the rapid freeze-quench conditions are expected to decrease the high spin accumulations by about 20% in both proteins due to the temperature dependence of spin conversion, in which case this subtle change will become important. The thermodynamic behavior of the spin transition is addressed in the following section.

The transition observed with other fatty acid substrates highly indicates that the enzyme now favors the 5cHS both in the substrate-free and substrate-bound form. A possibility of the higher accumulation can be explained by an increased affinity of the enzyme for fatty acids. Given the fact that we have not changed any residue involving fatty acid binding and that the substrate does not directly ligate to the Fe(III) center, it seems highly unlikely that this would be the case. Table 4.2 shows the dissociation constants determined from the

absorbance change at 418 nm and their fitting using the Morrison equation for tight binding. This data shows very minimal changes in the $K_D$ of the wild-type enzyme and the mutant, demonstrating that the affinity remains unaffected.

**Table 4.2** Dissociation constants of a panel of fatty acids for $OleT_{SA}$ wild-type and $OleT_{SA}$ A369P.

| | $K_D$ (μM) | | Fold change from WT |
|---|---|---|---|
| **Substrate** | **Wild-Type** | **A369P** | |
| **C20** | 0.26 ± 0.52 | 0.34 ± 0.02 | 1.31 |
| **C18** | 0.32 ± 0.01 | 0.24 ± 0.01 | 0.75 |
| **C16** | 4.04 ± 2.41 | 1.49 ± 0.02 | 0.36 |
| **C14** | 2.48 ± 1.63 | 1.24 ± 0.02 | 0.5 |
| **C12** | 1.51 ± 0.05 | 1.21 ± 0.02 | 0.8 |

To ensure that the thiolate ligated heme moiety has been preserved in the mutant, we prepared the carbon-monoxy ferrous complex which shows maximal accumulation at 443 nm, confirming the preservation protein integrity (Figure 4.4B). This data demonstrates that residue 369 is involved in the accumulation of the 5cHS of the heme in CYP152 enzymes and goes in accordance to what was observed in the analog P450 BSβ mutation. Understanding the thermodynamic parameters and origin of this alteration is essential for its implementation in high resolution spectroscopy.

### 3.3 The spin equilibrium $K_{spin}$ is highly altered in $OleT_{SA}$_A369P

In cytochrome P450 chemistry, the equilibrium constant $K_{spin}$ is defined as the ratio of the 5cHS fraction over the 6cLS fraction determined from the absorbances at 394 nm and 418 nm respectively. Unlike the dissociation constant of fatty acids ($K_D$), the equilibrium constant $K_{spin}$ gives information about the spin equilibrium of the system

irrespective of the presence of substrate. Hence, it can provide valuable information on which spin conformation is favored on a specific P450 at given conditions. This equilibrium constant gives information about which spin conformation is favored at certain conditions. In most P450s, $K_{spin}$ has a high temperature dependence originating from pure

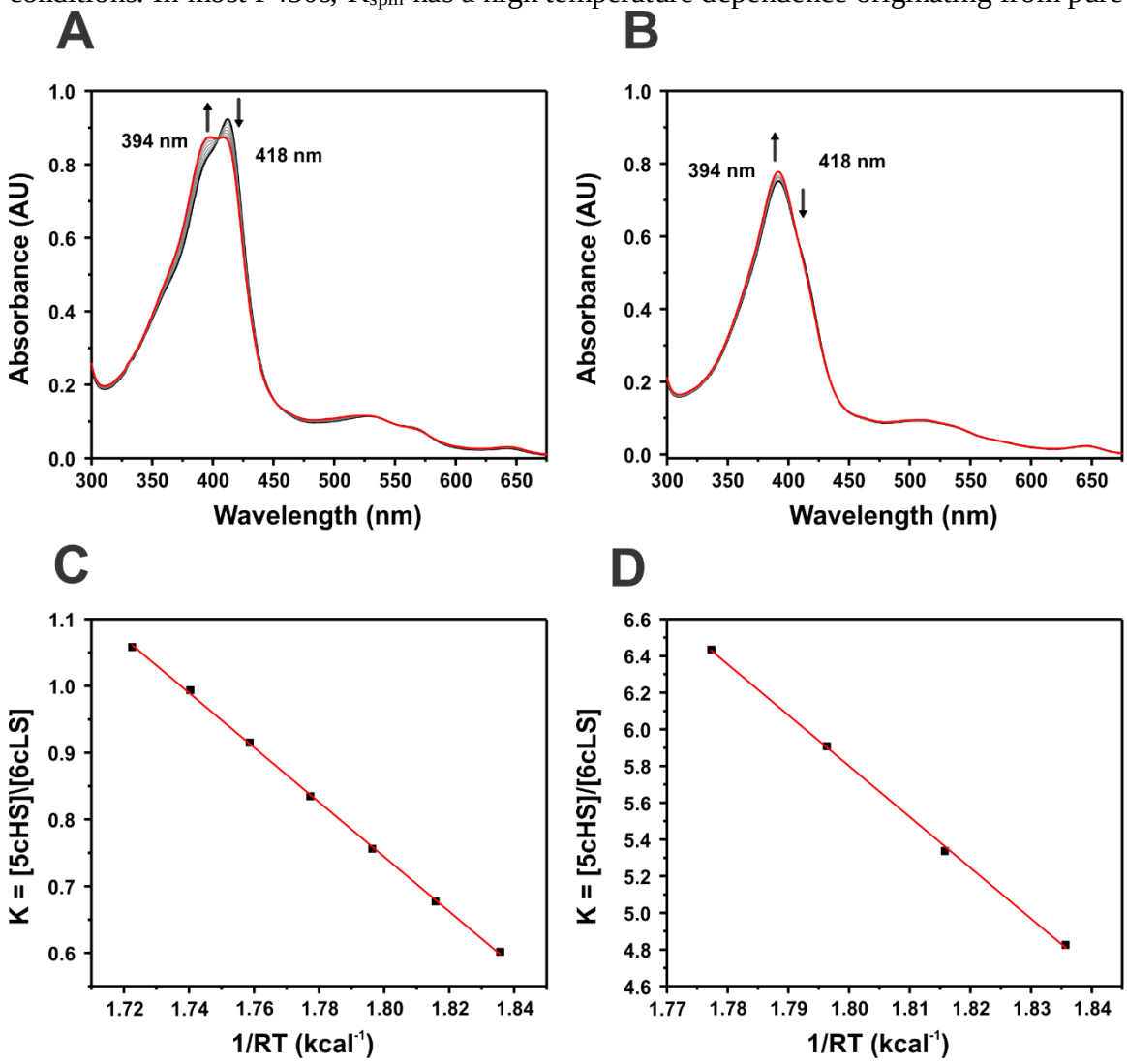


**Figure 4.5** High-spin temperature dependence. (A) UV-Vis spectra of $OleT_{SA}$ wild type as a function of temperature in the presence of dodecanoic acid. Black line represents the protein at 4 °C and red represents the protein at 20 °C. (B) UV-Vis spectra of $OleT_{SA}$_A369P wild type as a function of temperature in the presence of dodecanoic acid. Black line represents the protein at 4 °C and red represents the protein at 20 °C. (C) Van't Hoff plot derived from the temperature dependence of the equilibrium constant of $OleT_{SA}$ in the presence of dodecanoic acid. (D) Van't Hoff plot derived from the temperature dependence of the equilibrium constant of $OleT_{SA}$_A369P in the presence of dodecanoic acid.

electronic rearrangements of the heme as well as global structural changes from the protein and substrate.[34] The generation of van't Hoff plots from $K_{spin}$ as a function of temperature is necessary to derive thermodynamic parameters of the spin transition and are specific for each cytochrome P450.

Spectroscopic data indicates that the A369P mutation in $OleT_{SA}$ highly affects the 5cHS accumulation at room temperature. Dissociation constant determination from different fatty acids indicate that there is no significant change in the $K_D$ of the mutant compared to the wild-type, indicating that the affinity has remained unaffected in the mutant and that the $K_{spin}$ change is most likely coming from a change in the heme properties. To compare the thermodynamic parameters of this spin transition between both proteins, we calculated $K_{spin}$ at different temperatures and generated the corresponding van't Hoff plots.[23]

**Table 4.3** Thermodynamic parameters for $OleT_{SA}$ and A369P with C20 and C12 fatty acids. $K_{spin}$ and ΔG values were calculated at 20 °C.

| Protein | Substrate | $K_{spin}$ | ΔG (kcal.mol$^{-1}$) | ΔH (cal.mol$^{-1}$) | ΔS (cal.mol$^{-1}$.K$^{-1}$) |
|---|---|---|---|---|---|
| **$OleT_{SA}$** | **-** | $4.8 \pm 0.9 \times 10^{7}$ | 10.0 ± 2.0 | 23.0 ± 3.0 | 35.2 ± 0.5 |
| | **C20** | $3.65 \pm 0.09 \times 10^{3}$ | 4.8 ± 0.1 | 8.2 ± 0.2 | 16.3 ± 0.3 |
| | **C12** | $6.15 \pm 0.30 \times 10^{3}$ | 5.1 ± 0.2 | 10.0 ± 0.3 | 17.4 ± 0.6 |
| **$OleT_{SA}$ A369P** | **-** | $1.6 \pm 0.2 \times 10^{8}$ | 11.0 ± 1.0 | 24.0 ± 2.0 | 38.0 ± 0.4 |
| | **C20** | $7.15 \pm 0.28 \times 10^{8}$ | 11.9 ± 0.5 | 18.4 ± 0.6 | 40.5 ± 1.0 |
| | **C12** | $4.28 \pm 0.13 \times 10^{4}$ | 6.2 ± 0.2 | 9.85 ± 0.20 | 21.2 ± 0.4 |

Figure 4.5 A and B show a representative UV-Vis spectrum of both the wild-type and A369P enzyme in the presence of a short-chain fatty acid (dodecanoic acid) as a function of temperature. As it shown by the spectra, the fraction of 5cHS in the mutant is much more accentuated in the mutant compared to wild-type. Figure 4.5C and D show the van't Hoff

plot generated from the equilibrium constant determined from these spectra. Table 4.3 compiles all of the thermodynamic parameters derived from these plots of the enzyme with eicosanoic acid (a long-chain fatty acid and native substrate), dodecanoic acid and the substrate-free enzyme.

Enthalpy values indicate that the 6cLS to 5cHS transition is endothermic as observed in the UV-Vis spectra. Theoretical investigation from the entropic changes between low-spin and high-spin in other heme-containing proteins determined the ΔS associated with this transition to be ~2 cal/mol K.[35] In $OleT_{SA}$ these changes are significantly larger, suggesting the involvement of a protein or substrate conformational change in addition to the electronic rearrangement. The entropy change originating from a substrate conformational change should be identical in both wild-type and mutant as the nature of the substrate is the same. In the case of a structural rearrangement that derives from the protein itself, the ΔS should be highly similar, if not identical, as it is very unlikely the alanine to proline mutation induces a major alteration in protein structure. If the heme properties have been altered however, the difference in ΔS values between WT and mutant should be evident but modest and should be in the same order of magnitude as to what has been postulated to be the ΔS of the pure electronic spin transition in other ferrihemoproteins (2 cal/mol K).[35] In the substrate-free form the difference between ΔS in the WT and mutant enzyme is ~3 cal/mol K. This small difference suggests a change of the heme electronic structure has occurred Similar values are obtained with dodecanoic acid, following the same trend of a subtle increase in the entropy change. In the case of the eicosanoic acid-bound A369P however, the entropy change is two-fold higher than in wild-type and much more significant than in the substrate-free or dodecanoic acid-bound enzymes. We have

previously shown that long-chain substrates induce protein conformational changes in $OleT_{JE}$ as the protein needs to accommodate its pocket for binding of the substrate.[13] The fact that the entropy change with eicosanoic acid is much higher would be expected however, the large shift of the ΔS in the mutant is rather surprising as it would indicate that the mutation affects this conformational change. A possible explanation would be that this major shift in protein structure might accentuate the observed change in the heme electronic structure in the substrate-free form by inducing a variation of the geometry of the heme. Although this data clearly demonstrates a change in the ΔS of the spin transition, it would be naïve to assign this difference to a single parameter. In any case, $K_{spin}$ values appear to be at least an order of magnitude higher in all forms of the A369P mutant compared to wild-type, conclusively showing that this mutation alters the spin-state equilibrium to favor the high-spin state of the protein. Further examination of these changes is necessary to uncover where this spin transition is originating from. Possibilities of this alteration might include a change in the Fe-S bond strength, a change in the geometry of the heme or more major protein conformational rearrangements. These possibilities are discussed below.

### 3.4 $OleT_{SA}$_A369P has an apolar cavity and an altered heme geometry

Magnetic circular dichroism (MCD) and electron paramagnetic resonance (EPR) are highly informative techniques in cytochrome P450 spectroscopy providing specific fingerprints of defined heme environments, including ligands, polarity and geometry of the heme.[21] Andersson et al demonstrated that when the carbonmonoxy ferrous form of P450s with a well-hydrated pocket (like P450terp) is analyzed by MCD spectroscopy, it tends to absorb at higher wavelengths compared to P450s with more hydrophobic cavities (such as

that for P450cam).[36] Given the hydrophobic nature of the binding pocket in $OleT_{SA}$, it is expected that the cavity would be more dehydrated compared to other P450s. Figure 4.6A, black line, shows that the carbon-monoxy ferrous form of the substrate-free $OleT_{SA}$ enzyme has a positive absorbance at 441 nm, this is similar to the value found in P450cam which has a maximal absorbance at 443 nm,[36] supporting a non-polar pocket. Since the spin shift in P450s involves the loss of a water ligand from the Fe(III) center, the A369P mutant which has a higher propensity to be in the 5cHS state should have a less polar pocket than the wild-type $OleT_{SA}$. MCD spectra of the carbon-monoxy ferrous form of the enzymes showed very minimal changes (roughly 1 nm) between the WT and A369P mutant, suggesting that the hydration of the pocket might be retained. Although the A369P mutant favors the 5cHS state, the solvent molecule might not be completely absent, which would explain the relatively unperturbed MCD spectra.

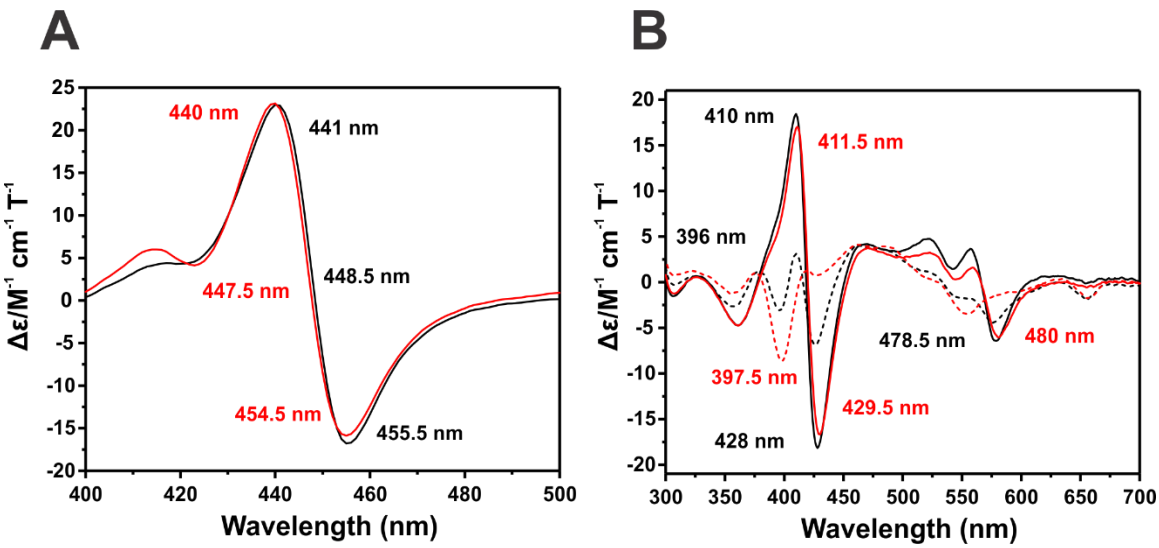


**Figure 4.6** MCD spectra of $OleT_{SA}$ wild-type and A369P. (A) MCD spectra of the carbon-monoxy ferrous forms. Black trace represents wild-type, red trace represents A369P. (B) MCD spectra of the ferric forms of $OleT_{SA}$. Black solid line represents wild-type substrate-free; red solid line represents A369P substrate-free; black dashed line represents wild-type bound to C20 fatty acid; red dashed line represents A369P bound to C20 fatty acid.

Figure 4.6B shows the MCD spectrum of the ferric forms of the enzyme in the absence and presence of eicosanoic acid. In all cases, the spectrum of the A369P mutant is red-shifted by 1.5 nm. Given the fact that MCD spectroscopy is unaffected by changes in the protein conformation unless they affect the heme, it can be speculated that the prosthetic group of the A369P mutant has a different conformation. The same phenomenon has been observed in other ferrihemoproteins such as cytochrome c.[37] Further MCD using near-IR absorbances is necessary as there are distinct S ($\pi$) → Fe charge transfer contributions in that region that could give information on the strength of the Fe-S bond.[38-39]

EPR spectra of both proteins in the substrate-free and substrate-bound form shows significant changes in the S = 5/2 signal. Figure 4.7 shows the EPR spectrum of $OleT_{SA}$ and the A369P mutant. The black trace corresponds to the substrate-free and the red trace to the eicosanoic acid bound form.

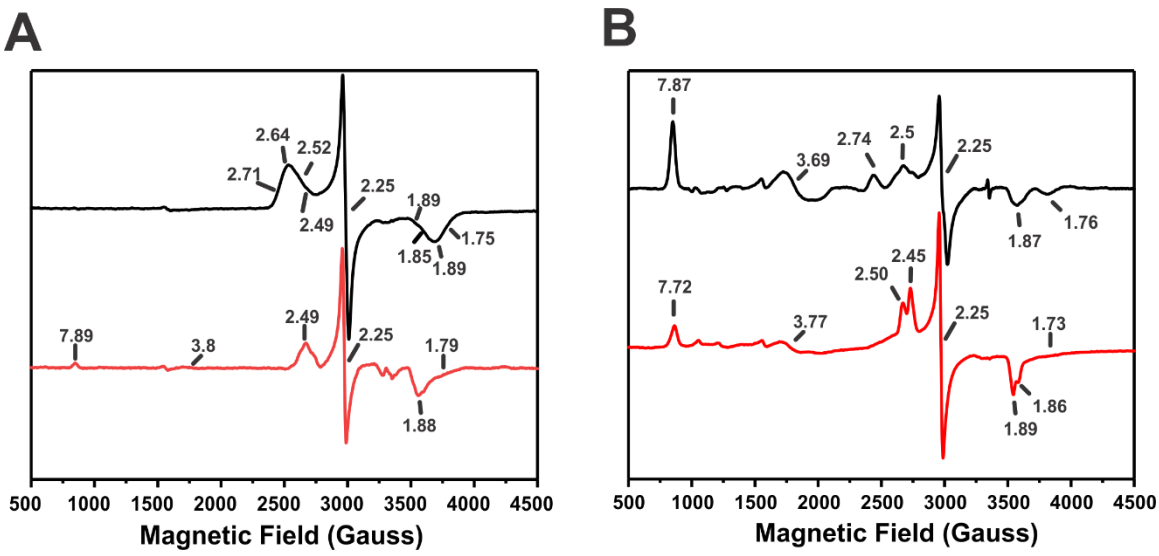


**Figure 4.7** EPR spectra of $OleT_{SA}$ wild-type and A369P mutant. (A) EPR spectrum of $OleT_{SA}$ wild-type. The black trace represents the substrate-free form of the enzyme and red trace the eicosanoic acid bound form. (B) EPR spectrum of $OleT_{SA}$ A369P. Black trace represents the substrate-free form and red trace the eicosanoic acid bound form.

Initial examination of the EPR spectrum of the A369P mutant reveals the presence of a high fraction of a rhombic signal typical of a S = 5/2 (5cHS) with g values of 7.87, 3.69 and 1.76 for the substrate-free form and 7.72, 3.77 and 1.73 for the C20 bound respectively. In the absence of substrate, the former is substantially higher than in wild-type, which displays a rhombic signal typical of a spin system with S = 1/2 (6cLS). The low spin signal of the EPR spectrum of the A369P mutant displays a similar trend as the wild-type with multiple $g_z$ values, which suggest a highly disordered water network on the distal side of the heme. When substrate is added, the S = 5/2 signal corresponding to the 5cHS state is decreased in the A369P mutant. This is conflicting as to what is often expected since the substrate should drive the protein to the 5cHS state. In fact, it appears that the addition of substrate highly structures the hydrogen bond network of the distal side of the heme as only 2 $g_z$ values are now evident in the S = ½ signal.

The most important factor that can be derived from this data however, is the fact that the rhombicity of the S = 5/2 signal of the C20-bound $OleT_{SA}$_A369P enzyme is substantially decreased compared to the wild-type. This type of change has been seen in the F429H mutation in CYP2B4. Davydov R et al.[40] demonstrated that this mutation decreases the rhombicity of the S = 5/2 EPR signal. Although this change might be due to a change in the H-bonding network of the proximal side of the heme in $OleT_{SA}$, it can also originate from a change in the heme geometry. In addition to this, the rhombicity of the substrate-free form is higher than with substrate bound, suggesting that the long-chain fatty acid distorts the heme. This supports the idea discussed in the previous section that the conformational change induced by C20 fatty acid might accentuate the change of the electronic structure of the heme. The data so far suggests that the largest structural changes

derive from alterations in heme geometry rather than changes in the H-bonding network of the proximal side of the protein. Higher resolution spectroscopy is necessary to elucidate these phenomena.

### 3.5 Resonance Raman indicates a change in the vinyl orientation of the heme in the A369P mutant

One of the most sensitive techniques for P450s is resonance Raman spectroscopy. Information about the spin-state of the heme, as well as oxidation state of the Fe center and geometry of the heme can be derived with this technique.[21] Moreover, the relative strength of the Fe-S bond can be derived from the analysis of the carbon-monoxy ferrous form of P450s which would conclusively say whether the strength of the bond has changed. Figure 4.8 shows the high-frequency region of the wild-type and A369P enzymes in the presence of C20 and C12 fatty acids. The oxidation marker at 1374 $cm^{-1}$ indicate that all samples are in the ferric state as expected. Spin-state markers of the 5cHS form at 1489 $cm^{-1}$, 1565 $cm^{-1}$ and 1626 $cm^{-1}$ indicate that the A369P mutant (Figure 4.8B) contains substantially more 5cHS heme than the wild-type, even in the substrate free form. The accumulations of the 5cHS state were determined by employing the derived resonance Raman scattering cross-section of the 1489 $cm^{-1}$ spin state marker of P450cam, using the ratio of $I_{HS/LS} = 1.24$.[41] These values seem to be in accordance to what was determined in the optical spectroscopy studies at low temperature.

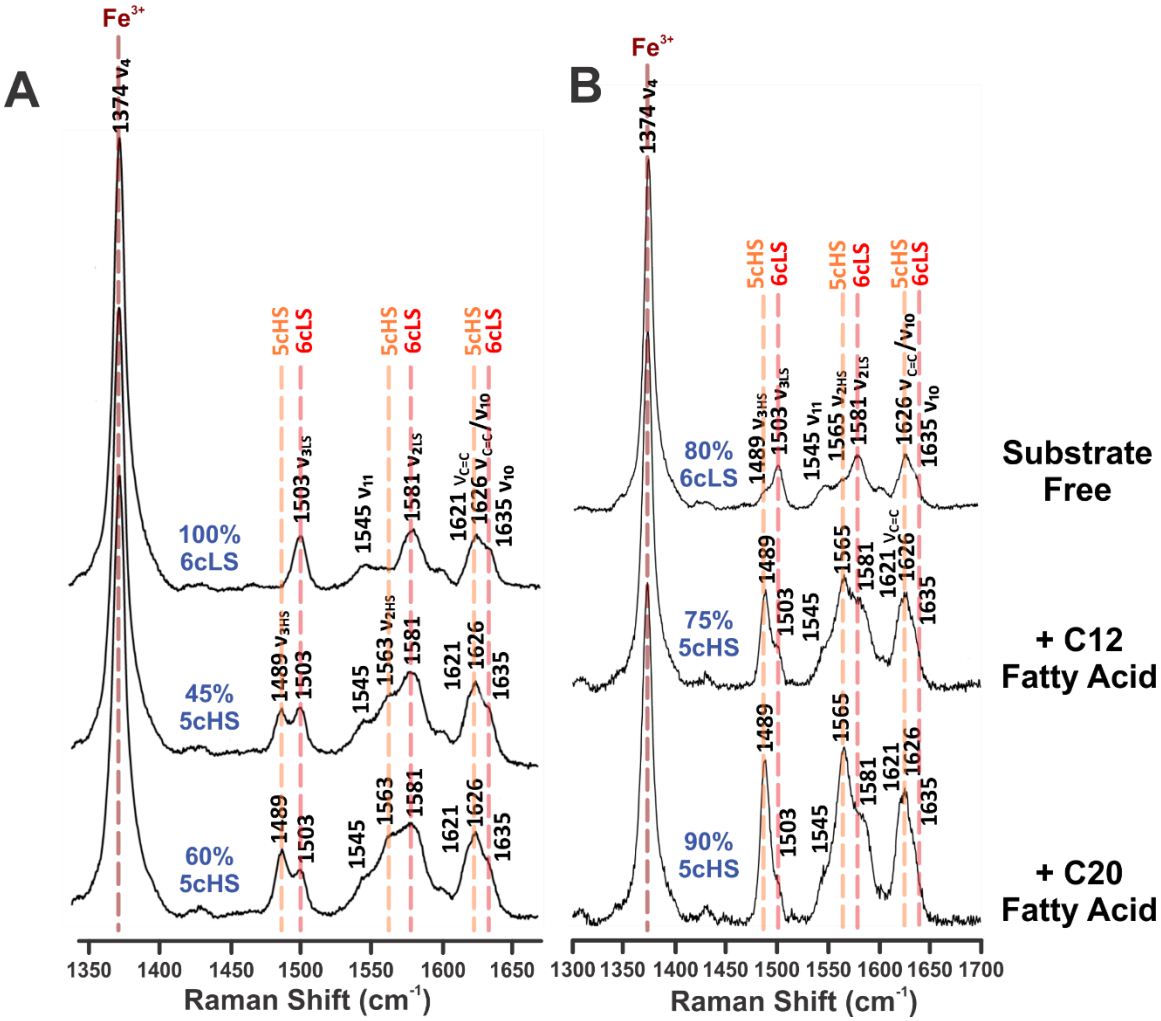


**Figure 4.8** High-frequency region of the resonance Raman spectra of $OleT_{SA}$ and $OleT_{SA}$_A369P. (A) $OleT_{SA}$ wild-type. (B) $OleT_{SA}$_A369P. Oxidation marker at 1374 $cm^{-1}$ is represented in scarlet. Spin state marker of the 5cHS form at 1489 $cm^{-1}$, 1563 $cm^{-1}$ and 1626 $cm^{-1}$ is presented in orange. Spin state marker of the 6cLS form at 1503 $cm^{-1}$, 1581 $cm^{-1}$ and 1635 $cm^{-1}$ are marked in red.

Figure 4.9 shows the low-frequency region of the resonance Raman scattering for the wild-type and A369P enzyme in the presence of eicosanoic acid. Interestingly, the porphyrin out-of-plane modes occurring at 307 $cm^{-1}$, 332 $cm^{-1}$, 496 $cm^{-1}$, 695 $cm^{-1}$ and 713 $cm^{-1}$ indicate a highly distorted heme cofactor. A similar pattern is seen both with C12 fatty acid

bound and the substrate-free form. The most pronounced change, however, is seen between 400 – 440 $cm^{-1}$ , a region that corresponding to the vinyl bending modes.

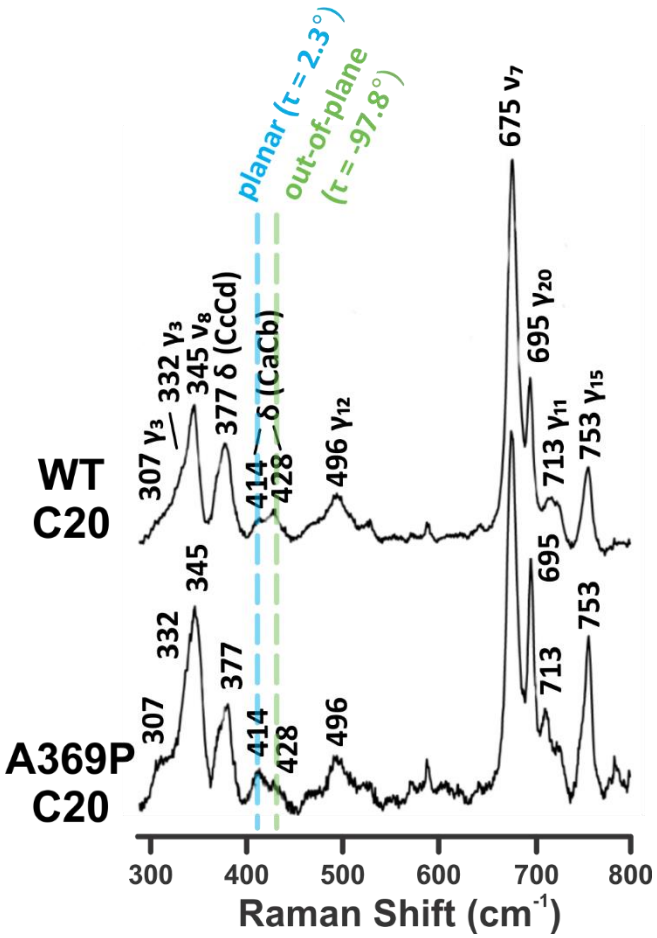


**Figure 4.9** Resonance Raman scattering of the low-frequency region of $OleT_{SA}$ and $OleT_{SA}$_A369P. Bending mode corresponding to a planar vinyl orientation is highlighted in cyan at 414 $cm^{-1}$. Bending mode corresponding to an out-of-plane vinyl orientation is highlighted in green at 428 $cm^{-1}$.

The resonance Raman spectrum shows the wild-type enzyme having a higher intensity at 428 $cm^{-1}$ relative to 414 $cm^{-1}$. Based on assignments from myoglobin and other P450s,[42] the latter correlates to a planar orientation of the vinyl groups of the heme, whereas the former corresponds to a more out-of-plane orientation, indicating that the wild-type favors

a planar orientation of the vinyl modes. In the A369P mutant, this tendency is reversed, favoring the out-of-plane orientation. This conclusively indicates that the geometry of the heme is affected in the A369P mutant by changing the orientation of the vinyl modes.

As previously mentioned, one of the most important factors that can be determined using resonance Raman is the strength of the Fe-S bond of the heme. Scattering of the carbon-monoxy ferrous adducts can help determine the strength of this bond by measuring the changes of the internal modes of the Fe-CO fragment which depend on the extent of the $d\pi$ (Fe) to CO ($\pi^*$) backbonding donation.[43] Figure 4.10 and 11 show the low- and high-frequency resonance Raman spectra respectively of the carbon-monoxy adducts in the presence and absence of fatty acids. In the substrate-free wild-type enzyme, a single Fe-CO fragment can be detected with the $\nu$(Fe-C) frequency observed at 478 $cm^{-1}$ and the corresponding $\nu$(C-O) mode observed at the higher frequency of 1943 $cm^{-1}$. The A369P mutant exhibits a change in the Raman shift to 482 $cm^{-1}$ in the low-frequency region and to 1938 $cm^{-1}$ in the high-frequency region, suggesting a change in the Fe-CO bond. Binding of C12 fatty acid to the wild-type enzyme gives rise to two distinct frequencies at 477 and 489 $cm^{-1}$ whereas the mutant gives rise to only one at 486 $cm^{-1}$, indicating that C12 fatty acid most likely interacts with the CO adduct allowing two conformations in the wild-type and only one in the A369P mutant.[44] This effect is reversed with C20 fatty acid where the mutant exhibits two conformers whereas the wild-type only one, suggesting that the conformation of the fatty acid is highly flexible in the active site and is chain length dependent. Such dependence however, appears to have changed in the A369P mutant. A reasonable explanation for this could be the change in heme geometry and could explain

the effects observed with the thermodynamic data where large differences in the ΔS between the WT and A369P can be observed with C20 fatty acid but not with C12.

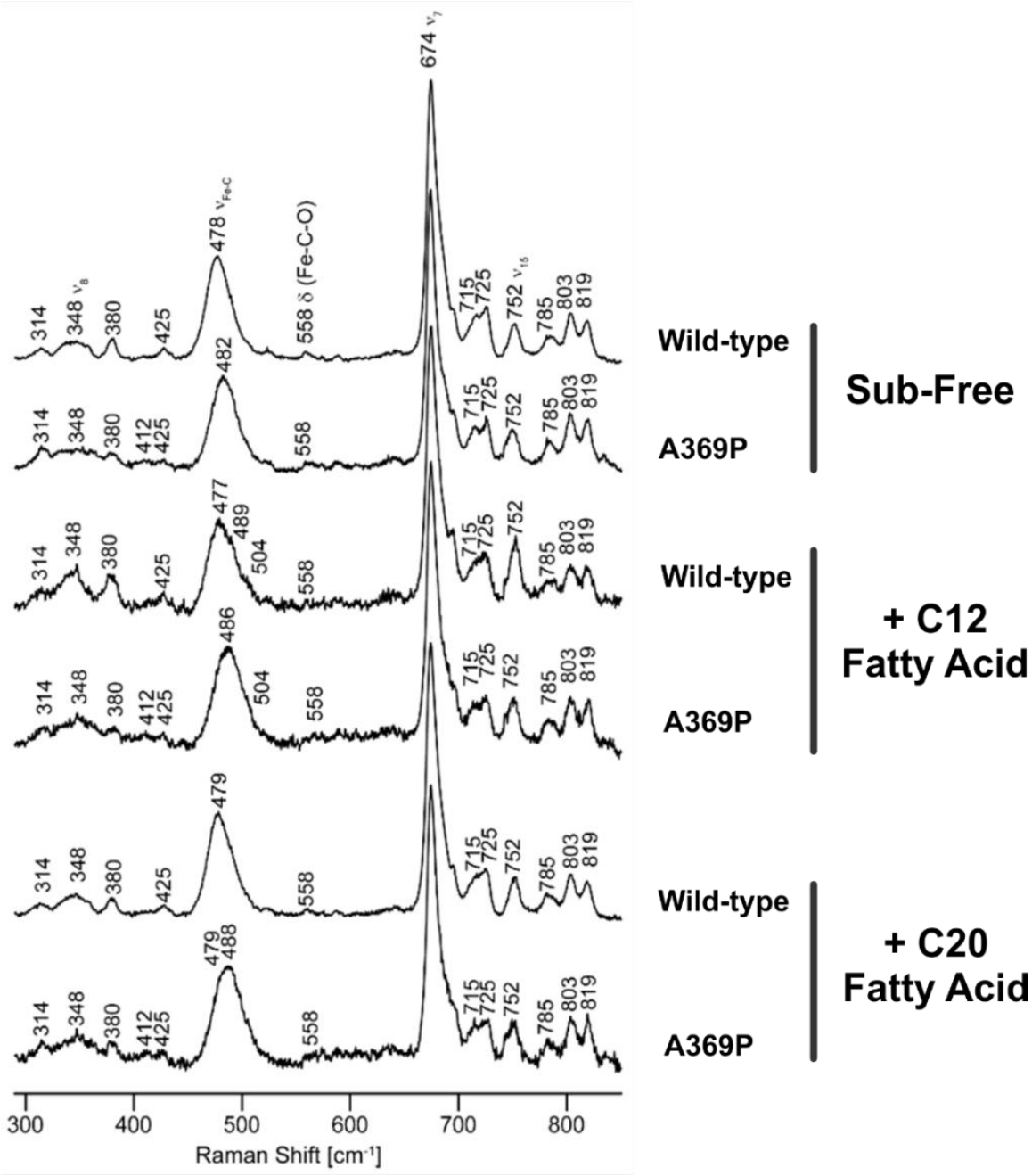


**Figure 4.10** Low-frequency region of the resonance Raman spectra of the carbon-monoxy ferrous adducts of $OleT_{SA}$ and $OleT_{SA}$_A369P

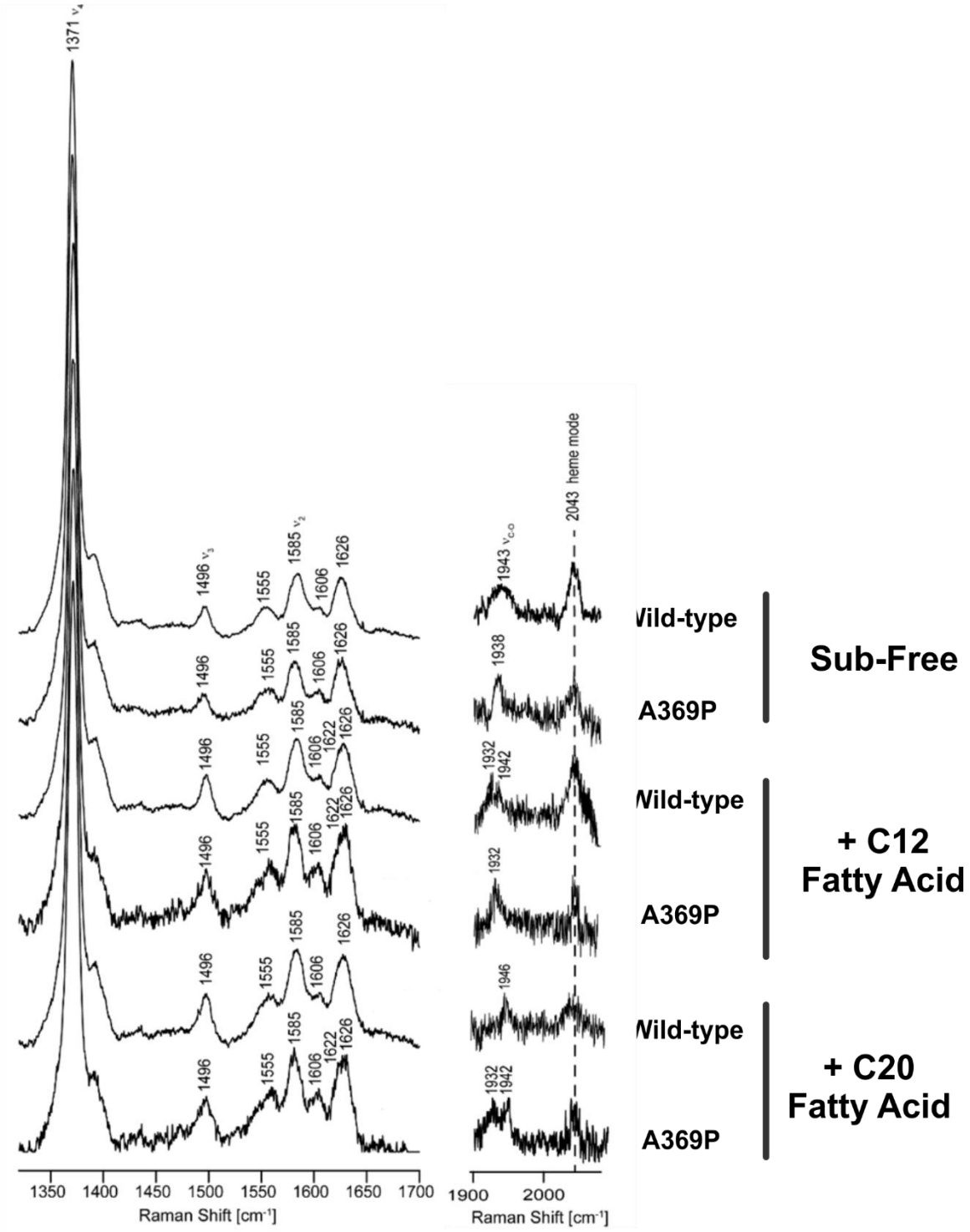


**Figure 4.11** High-frequency region of the resonance Raman spectra of the carbon-monoxy ferrous adducts of $OleT_{SA}$ and $OleT_{SA}$_A369P

Further examination of the H-bonding network to the Fe-S bond can be derived by plotting the inverse backbonding correlation line between the ν(Fe-C) and ν(CO) frequencies as shown in Figure 4.12.

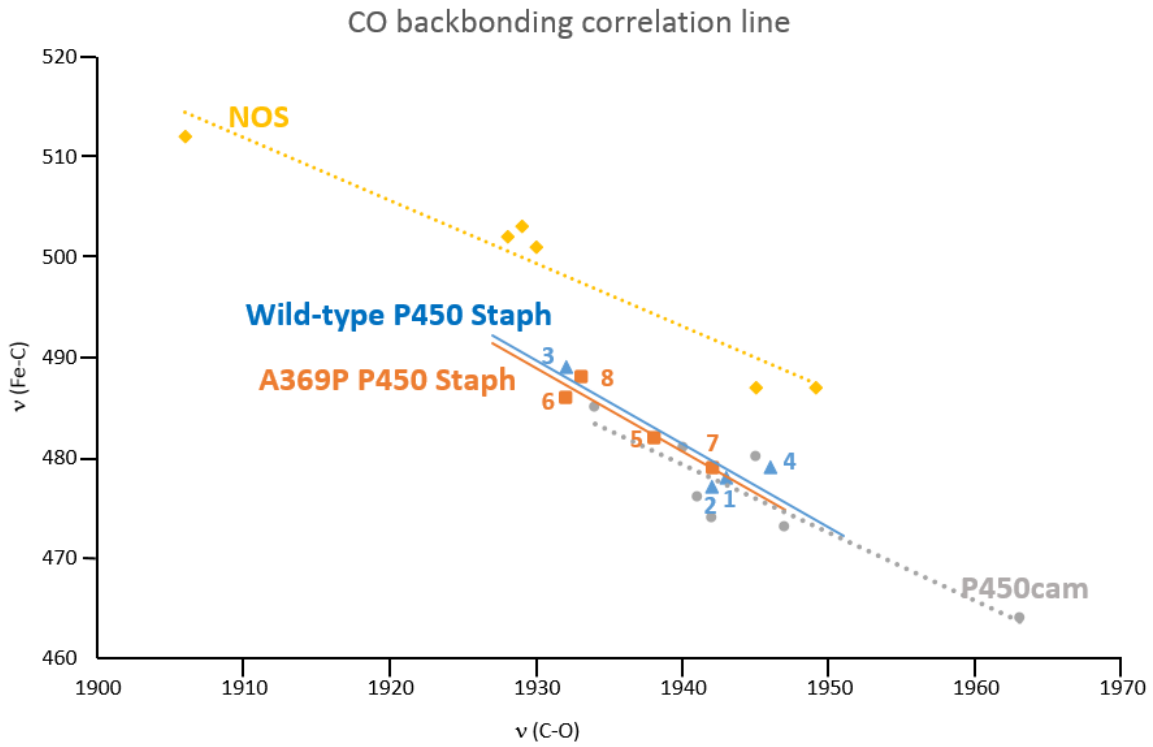


**Figure 4.12** CO backbonding correlation line. Yellow squares correspond to data points for nitric oxide synthase (NOS), grey circles correspond to data points for P450cam; blue triangles correspond to $OleT_{SA}$; orange squares correspond to $OleT_{SA}$_A369P

It has been established that P450cam possesses a stronger donor thiolate ligand compared to nitric oxide synthase (NOS) enzymes.[43-44] The change in strength arises from the fact that a tryptophan residue on the cys-pocket of NOS enzymes is hydrogen bonded to the proximal cysteine sulfur, thus weakening the Fe-S bond.[45-46] In the CO backbonding correlation, line this manifests in P450cam having a line well below that of NOS. In $OleT_{SA}$, this line is comparable to P450cam indicating that the strength of the thiolate

ligand donation is comparable and significantly stronger than NOS. The A369P mutant follows a very similar correlation to the wild-type enzyme, suggesting that there is no significant change in the electronic properties of the thiolate ligand. This indicates that if there is a change in the H-bonding network of the cys-pocket of the mutant, it may only have minimal effects in the strength of the Fe-S bond.

Summarizing the resonance Raman data, it can be concluded that the A369P mutation does not significantly affect the hydrogen bonding network of the Fe-S bond as previously anticipated. Rather, the larger effects are comprised of changes in the heme geometry that in turn cause changes to $K_{spin}$. It is important, however, to directly examine the ν(Fe-S) modes as this would give a more definitive answer on whether the Fe-S bond has been changed.

### 3.6 Crystal structure of $OleT_{SA}$ A369P shows a change in heme geometry

To further investigate the changes in heme properties, we determined the crystal structure of the $OleT_{SA}$ A369P mutant at a resolution of 2.3 Å. The data statistics for the crystal structure can be found on table 4.4. The crystal structure of $OleT_{SA}$ wild-type is the same as the one discussed in chapter 3 as well as the statistics corresponding to that structure. Similar conditions were used to crystallize the A369P mutant. The only difference was the use of a higher protein concentration in the crystallization tray. The concentration was increased to 30 mg/mL, twice the amount used for the wild-type. Crystals obtained were significantly larger than in wild-type and were singular.

**Table 4.4** Data collection and structure refinement statistics of $OleT_{SA}$ A369P

| Data Collection Statistics | $OleT_{SA}$_A369P C20-bound |
|---|---|
| **Resolution Range (Å)** | 35.57 - 2.3 |
| **Space group** | $C222_1$ |
| **Unit cell (a/b/c; Å)** | 68.7 94.9 185.1 |
| **(α/β/γ; °)** | 90 90 90 |
| **Total reflections** | 210112 (19367) |
| **Unique reflections** | 27174 (2687) |
| **Multiplicity** | 7.7 (7.2) |
| **Completeness** | 99.5 (99.9) |
| **Mean I/sigma (I)** | 8.7 (1.5) |
| **Wilson B-factor ($Å^{2)}$** | 32.4 |
| **$R_{merge}$** | 0.144 (0.922) |
| **$R_{meas}$** | 0.154 (0.994) |
| **$R_{pim}$** | 0.05462 (0.3658) |
| **$CC_{1/2}$** | 0.997 (0.771) |
| **CC** | 0.999 (0.933) |
| **Structure Refinement Statistics** | **$OleT_{SA}$_A369P C20-bound** |
| **Reflections used in refinement** | 27169 (2686) |
| **Reflections used for R-free** | 1058 (104) |
| **R-work** | 0.2191 (0.2932) |
| **R-free** | 0.2386 (0.3043) |
| **Number of non-hydrogen atoms** | 3669 |
| **Macromolecules** | 3411 |
| **Ligands** | 65 |
| **Protein residues** | 419 |
| **RMS (Bonds; Å)** | 0.011 |
| **RMS (Angles; °)** | 1.2 |
| **Ramachandran favored (%)** | 96.16 |
| **Ramachandran allowed (%)** | 3.84 |
| **Ramachandran outliers (%)** | 0 |
| **Rotamer outliers (%)** | 0 |
| **Clashscore** | 12.75 |
| **Average B-factor ($Å^2$)** | 36.22 |
| **Macromolecules** | 36.35 |

The crystal structure of the A369P mutant reveals the conservation of all the secondary structural elements of the protein. No significant changes can be seen in the region directly below the heme where the residue 369 sits. This is unsurprising as the alanine to proline mutation is not very stringent as demonstrated by its presence in other CYP152 enzymes. Preliminary analysis of the active site of the protein, showed that the electron density of the heme cofactor is more concave compared to the wild-type (Figure 4.13).

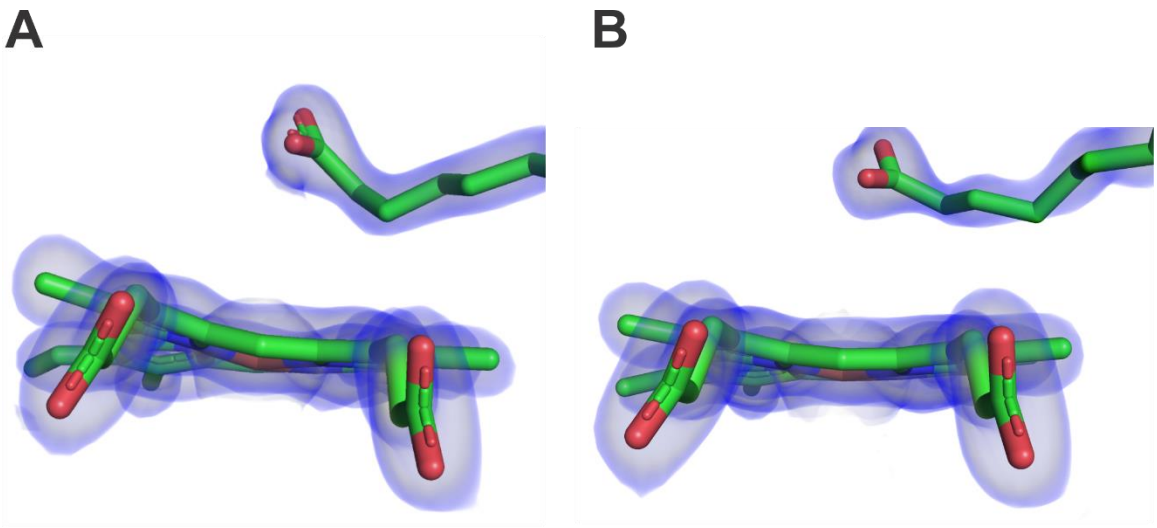


**Figure 4.13** $2F_O$-$F_C$ map of the heme in (A) $OleT_{SA}$_A369P and (B) $OleT_{SA}$ wild-type. The contour level is set at 1.6 σ.

The change in heme planarity was further examined by measuring the torsion angle between one of the vinyl groups, the Fe center and the methyl group opposite to the vinyl group. Figure 4.14 A and B show the angle change between the wild type and the mutant enzyme. The A369P variant shows an angle of 154.2° compared to the 169.7° shown in the WT. The difference in torsion angles confirms the distortion of the heme to a more saddled configuration. These geometric properties can be analyzed in more detail by using the Normal-Coordinate Structural Decomposition (NSD) software developed by Shelnutt.[27] By entering the coordinates of the crystal structure, this program gives

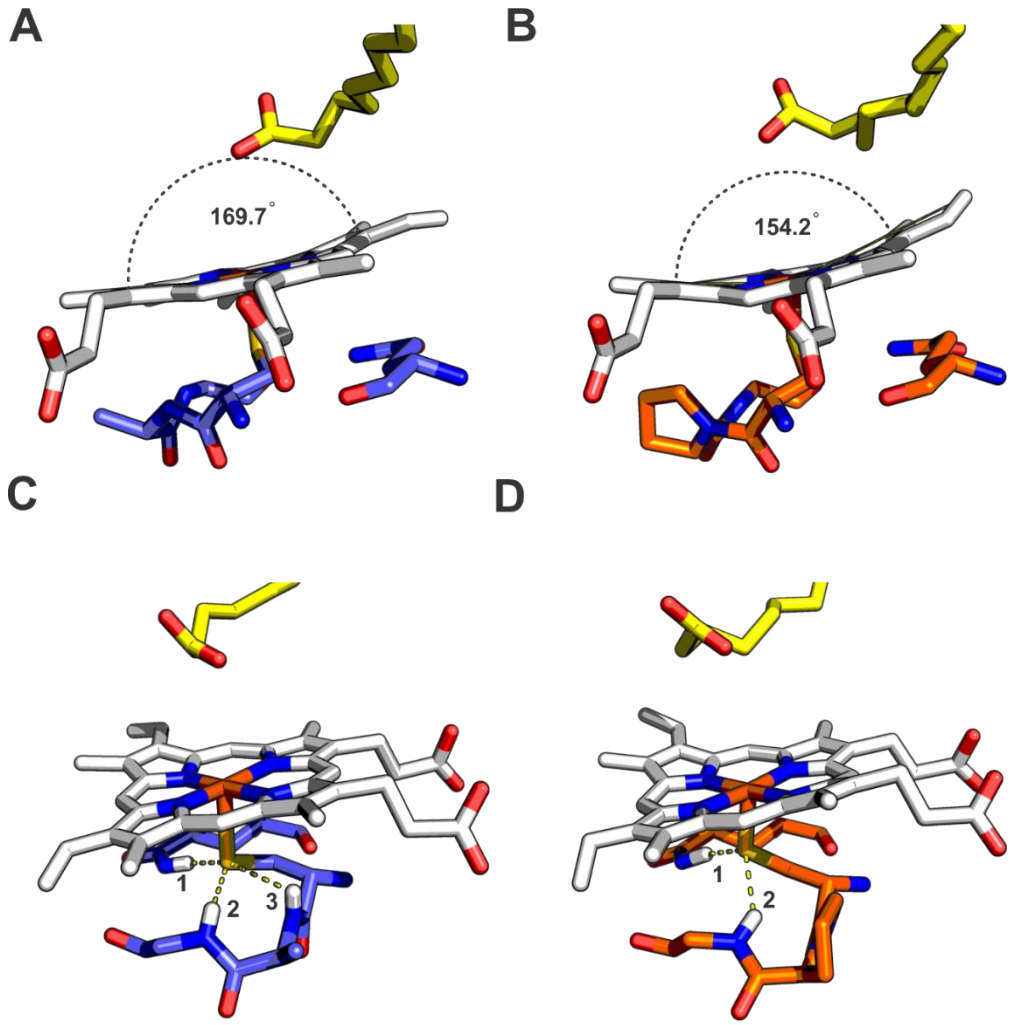


**Figure 4.14** Crystal structure of the active site of $OleT_{SA}$ and the A369P mutant. (A) $OleT_{SA}$ wild-type showing the distortion angle. (B) $OleT_{SA}$ A369P showing the distortion angle. (C) $OleT_{SA}$ wild-type showing the change in the H-bonding network to the Fe-S bond. $d_{H1\text{-}S}$ = 2.8 Å; $\theta_{N\text{-}H1\text{-}S}$ = 142°; $d_{H2\text{-}S}$ = 3 Å; $\theta_{N\text{-}H2\text{-}S}$ = 121°; $d_{H3\text{-}S}$ = 3.4 Å; $\theta_{N\text{-}H3\text{-}S}$ = 83° (D) $OleT_{SA}$ A369P showing the change in the H-bonding network to the Fe-S bond. $d_{H1\text{-}S}$ = 2.7 Å; $\theta_{N\text{-}H1\text{-}S}$ = 150°; $d_{H2\text{-}S}$ = 2.5 Å; $\theta_{N\text{-}H2\text{-}S}$ = 141°.

quantitative information about the out-of-plane distortion (Doop) and which heme conformation is favored in the heme (saddled, planar, propeller, ruffled etc). Analysis of the crystal structure of both protein variants indicated an out-of-plane distortion of 1 Å versus 0.8 Å in the wild-type enzyme. This is a significant change as seen in other heme-containing proteins [47] and indeed large enough to alter the electronic properties of the heme.

Additionally, these results indicate that the heme in the A369P mutant favors more a saddled conformation compared to the wild-type where a ruffled conformation is more prevalent. Analysis of the hydrogen bonding network of the cys-pocket of the wild-type enzyme shows three residues within H-bonding distance of the Fe-S bond. H1 represented in Figure 4.14C 1 originates from the $N_{\varepsilon 2}$ atom of Gln357 with a distance of 2.8 Å and a N-H-S angle of 142°; H2 originates from the amide hydrogen of Gly370 at a distance of 3 Å to the S atom and an angle of 121°. The last bond (H3) originates from the amide hydrogen of Ala369 and is 3.4 Å from the thiolate ligand with an angle of 83°; this is in the limit of hydrogen bonding distance, suggesting that this residue might not play a significant role in reactivity. In the A369P mutant, H3 is missing due to the elimination of the hydrogen from the amide of the proline residue. H1 seems to be mostly unaffected as the distance is 2.7 Å and the angle 150°; H2 however, seems to be have been placed 0.5 Å closer to the Fe-S bond with a steeper angle of 141°.

The crystal structure of the $OleT_{SA}$ A369P mutant shows a clear disruption in the geometric conformation of the heme. This data correlates well with results derived from resonance Raman, MCD and EPR spectroscopies. It is also clear that the A369P mutant has a disrupted hydrogen bonding network in the proximal side of the heme. However, this change is not evident in any of the spectroscopies performed thus far. More in-depth analysis of the Fe-S bond must be done in order to clarify the effects of this change on the donation properties of the thiolate ligand.

Although we have changed the $K_{spin}$ of the heme by altering its geometry, it is necessary to correlate these changes to the reactivity of the protein as it would be expected that these alterations would affect the redox potential of the heme.

### 3.7 The change in heme geometry in $OleT_{SA}$ A369P allows for the stoichiometric preparation of compound I

The main goal of this study has been to modify the protein to obtain large amounts of the catalytically relevant intermediates in $OleT_{SA}$ to allow their electronic characterization using high resolution spectroscopy. A mutation in the residue adjacent to the functional cysteine of the protein from an alanine residue to a bulkier proline induces an alteration in the spin-state equilibrium of the enzyme favoring the 5cHS state of the heme. This alteration can be attributed to a change in the geometry and conformation of the heme as indicated by the crystal structure and resonance Raman analysis. Previous studies on other heme-containing enzymes have shown that the heme conformation is very important in the reactivity of the protein.[47] This is unsurprising as P450s naturally change the conformation of their heme upon substrate binding. This change in conformation allows them to decrease their redox potential to allow electron transfer from their natural redox partner.[48-49] In addition to this, previous literature has shown that changes in heme conformation can affect the affinity for small molecules like $O_2$, $CN^-$ and NO thus changing the reactivity of the protein.[47, 50] From all this, it can be speculated that the mutation in $OleT_{SA}$ would have an effect in the overall reactivity of the protein. In accordance to what has been published, it is possible that the more saddled conformation of the heme would decrease the affinity of the protein for hydrogen peroxide. It is also possible that the catalytically relevant intermediates to have different reactivities. To clarify these suppositions, we performed stopped-flow spectroscopy with $OleT_{SA}$ A369P in the presence of protiated eicosanoic acid ($h_{39}$-C20) or deuterated eicosanoic acid ($d_{39}$-C20). All the conditions are identical to what was previously described in chapter 3 with the wild-type

enzyme. Briefly, 20 µM of protein-substrate complex were rapidly mixed with 10 mM hydrogen peroxide and the spectrum was monitored using a photodiode array (PDA) for the full spectrum or a photomultiplier tube (PMT) for single wavelength traces.

Initial look at the PDA spectra obtained from the reaction of $d_{39}$-C20 bound OleTSA mutant and excess $H_2O_2$ (Figure 4.15A) reveals the almost stoichiometric accumulation of the compound I species as determined by singular value decomposition analysis. This is a 25 % increase to what is observed with the wild-type enzyme. Moreover, no compound II accumulation can be observed in either variant of the protein. As discussed in the previous chapter, the lack of compound II accumulation can be explained by the higher decay rate of the compound II species compared to the initial compound I species in the wild-type enzyme. It would appear that this same effect is observed in the mutant.

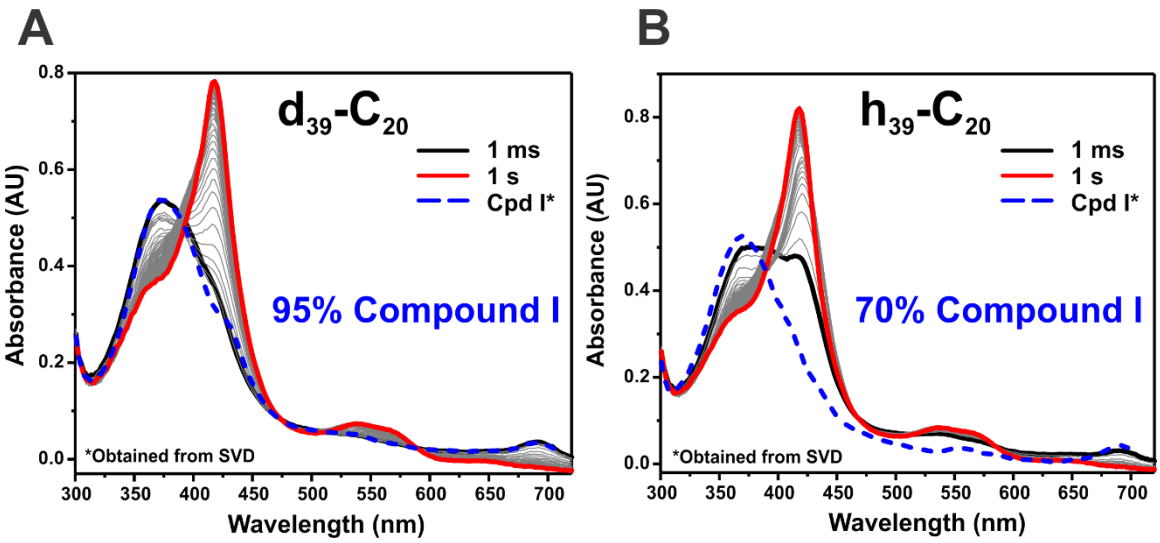


**Figure 4.15** Photodiode array spectra of 10 µM $OleT_{SA}$ A369P-substrate complex rapidly mixed with 5 mM hydrogen peroxide. (A) PDA spectra of $OleT_{SA}$ A369P bound to perdeuterated eicosanoic acid. (B) PDA spectra of $OleT_{SA}$ A369P bound to protiated eicosanoic acid. Initial trace is shown in black; final trace is shown in red; SVD analysis of the pure compound I species is shown in dashed blue.

Analysis of the $h_{39}$-C20 reaction indicates a similar trend in the accumulation of compound I with the A369P mutant accumulating 70% compared to the 50% observed in the wild-type enzyme. Further evaluation of the spectra reveals the accumulation of 80 % of the compound II intermediate compared to the 50 % in the wild-type enzyme under similar conditions. The higher accumulation of compound II with protiated substrate is expected as the decay rate of compound I is largely increased due to the kinetic isotope effect.

Overall it appears that the A369P mutant is able to accumulate substantially higher concentrations of both intermediates compared to wild-type. As we previously discussed, we anticipate that the higher accumulation is caused by the shift in the $K_{spin}$ of the heme favoring more the 5cHS state. To determine the decay rates of both intermediates, we monitored the single wavelength traces at 690 nm (cpd I) and at 440 nm (cpd II) as described in the previous chapter. Figure 4.16 shows the representative traces of both protiated and perdeuterated substrate bound OleTSA_A369P. The final rates and accumulations are summarized in table 4.5.

**Table 4.5** Accumulation and decay rates of transient intermediates of $OleT_{SA}$ and $OleT_{SA}$ A369P.

| | | **$d_{39}$-C20** | | **$h_{39}$-C20** | |
|---|---|---|---|---|---|
| | | **WT** | **A369P** | **WT** | **A369P** |
| **Compound I** | **Max Accumulation (%)** | 65 | 95 | 40 | 70 |
| | **Decay Rate (s-1)** | 38 | 19 | 513 | 368 |
| **Compound II** | **Max Accumulation (%)** | - | - | 50 | 80 |
| | **Decay Rate (s-1)** | - | - | 53 | 19 |

| | | | | | |
|---|---|---|---|---|---|
| **5cHS at 4 C** | **Max Accumulation (%)** | 75 | 95 | 75 | 95 |

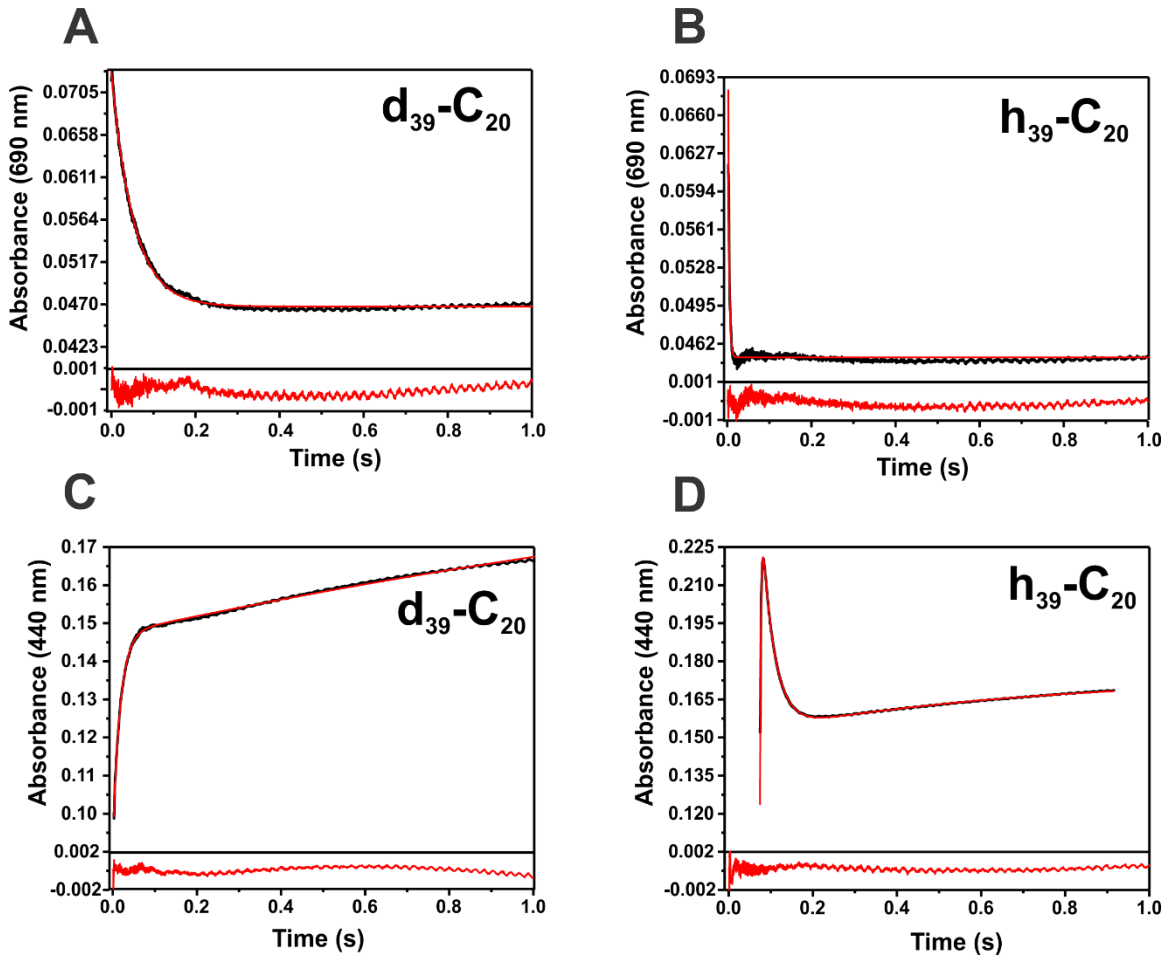


**Figure 4.16** Representative traces of the absorbance at 690 nm (compound I) and 440 nm (compound II). (A) Single wavelength trace at 690 nm of $OleT_{SA}$ A369P perdeuterated acid bound. (B) Single wavelength trace at 690 nm of $OleT_{SA}$ perdeuterated acid bound. (C) Single wavelength trace at 690 nm of $OleT_{SA}$ A369P protiated acid bound. (D) Single wavelength trace at 690 nm of $OleT_{SA}$ protiated acid bound.

As described in table 4.5, the decay rate of both intermediates seems to have changed in the A369P mutant. In the case of the compound I intermediate, a two-fold lower decay rate can be observed with perdeuterated substrate in the A369P mutant. A similar decrease is observed with the protiated substrate. The change in the decay rates appears to be subtle but confirms that the A369P mutant has a slightly less reactive compound I species. The observed kinetic isotope effect ($k_H/k_D$) also appears to be altered as it was determined to be 19 for the A369P mutant compared to 13 in the wild-type enzyme. A more substantial effect can be observed in the decay rates of compound II as the A369P mutant also shows a 2.5-fold less reactive intermediate.

Although the stability of compound I and II appears to have changed in the mutant, they are still within the same order of magnitude as in the wild-type enzyme. The increased stability of the intermediates could in principle serve to promote an increase of decarboxylation activity as compound II would have a higher chance to perform PCET step with the substrate radical. This needs to be confirmed by multiple turnover assays and is currently a work in progress.

To examine the effects of the alteration in heme geometry on the affinity of hydrogen peroxide for the enzyme, we plotted the formation rates of compound I with the deuterated eicosanoic acid bound enzymes as a concentration of hydrogen peroxide. Figure 4.17 indicates that the wild-type enzyme can activate hydrogen peroxide better than the mutant as revealed by the steeper slope. This goes in accordance to what is seen in other ferrihemoproteins where a saddled conformation of the heme leads to a decrease in affinity for $O_2$ binding.[50] A possible explanation for this is that the more concave form of the porphyrin hampers the initial binding of hydrogen peroxide.

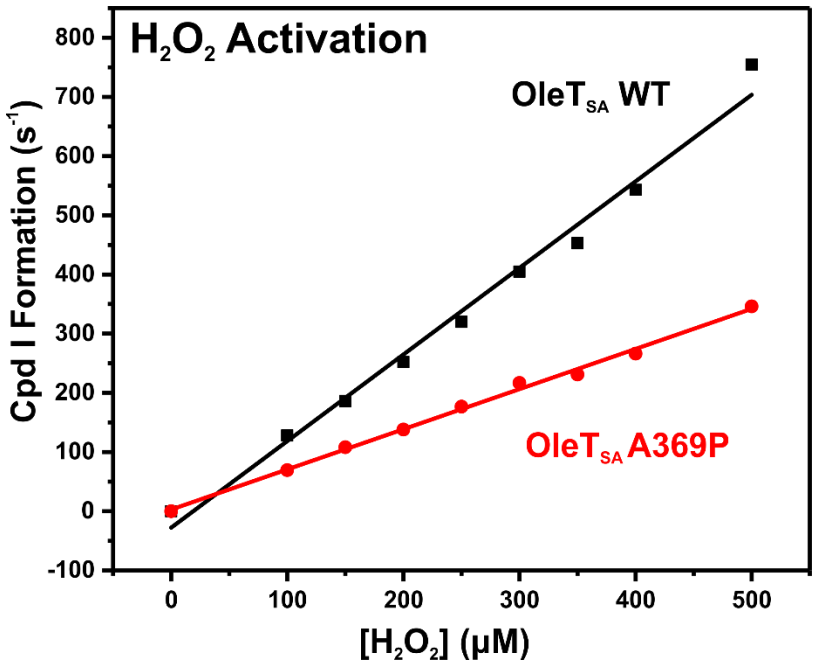


**Figure 4.17** Hydrogen peroxide activation in $OleT_{SA}$. Black trace represents the wild-type enzyme and the red trace represents the A369P mutant.

All the data shown so far indicates that the mutated form of the enzyme can accumulate the catalytically relevant intermediates better than the wild-type form. The enhanced accumulation of these intermediates can be partially explained by their increased stabilization as the decay rates appear to be lower in the A369P mutant however, this does not fully account for the high disparity in the accumulation of compound I and compound II. A second parameter that could explain this phenomenon is a better affinity for hydrogen peroxide. As we previously discussed, this is not the case as the hydrogen peroxide activation of the A369P is decreased and should lead to a lower accumulation of compound I. It is rational to attribute the change in accumulation to the change in the spin equilibrium of the protein which highly favors the 5cHS state.

The capture of the transient intermediates in $OleT_{SA}$ using rapid freeze-quench is necessary for their study using advanced spectroscopy. Usually, the "dead-time" of this instrument

tends to be in the order of 10 milliseconds. In other words, maximal accumulation of the intermediate is necessary at 10 ms to avoid any mixture of the species. Figure 4.18 shows the speciation plots of the wild type and the A369P mutant as a function of time. Figure 4.18A and B clearly demonstrates that the A369P mutant with perdeuterated eicosanoic acid is more suited for the capture of the compound I intermediate, as it shows that at 10

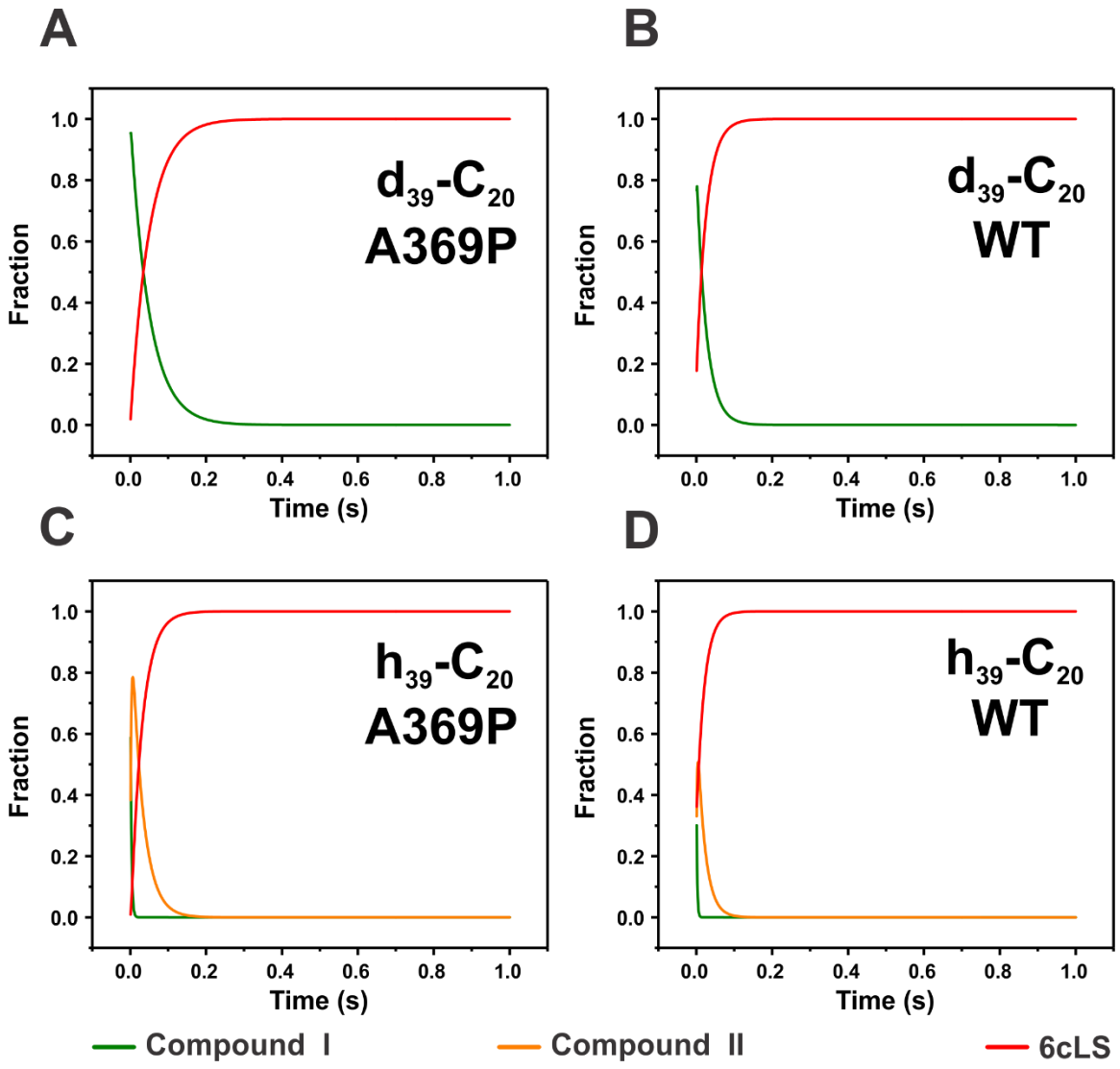


**Figure 4.18** Speciation plots of $OleT_{SA}$ wild-type and A369P. (A) Speciation plot of the A369P mutant with deuterated eicosanoic acid. (B) Speciation plot of the wild-type enzyme with perdeuterated eicosanoic acid. (C) Speciation plot of the A369P mutant with protiated eicosanoic acid. (D) Speciation plot of the wild-type enzyme with protiated eicosanoic acid. Green traces correspond to compound I; Orange traces correspond to compound II; red traces correspond to the 6cLS.

ms 80 % of the protein is in the compound I state compared to only 57% in the wild-type enzyme. This can also be described for the compound II intermediate with protiated eicosanoic acid. Figure 4.18C and D describe the fraction of each intermediate as a function of time and indicates that at 10 ms 75% of the protein is in the compound II state compared to only 49% in the wild-type enzyme. The speciation plots conclusively indicate that the intermediates in $OleT_{SA}$ A369P are suitable for their capture using rapid freeze-quench.

In addition to the required accumulation of the species, high protein concentrations are also necessary to capture these intermediates for their EPR and Mössbauer analysis. In chapter 3 we approached this problem by describing the improved stability of $OleT_{SA}$ at high concentration compared to the highly studied $OleT_{JE}$. Figure 4.19 shows the PDA trace of $OleT_{SA}$ and the mutant in the presence of perdeuterated eicosanoic acid. This trace reveals the stoichiometric accumulation of compound I even at a concentration of 100 µM post-mix and conclusively shows that the protein is now well suited for high resolution spectroscopy.

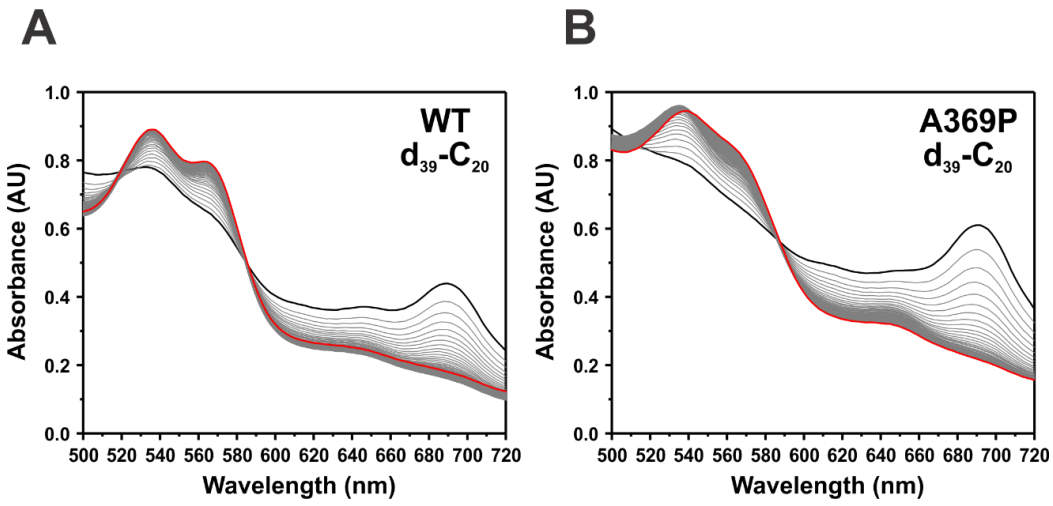


**Figure 4.19** High concentration stopped-flow of $OleT_{SA}$. (A) $OleT_{SA}$ wild-type 100 µM post-mix bound to perdeuterated eicosanoic acid. (B) $OleT_{SA}$ A369P 100 µM post-mix bound to perdeuterated eicosanoic acid. The intensity of the absorbance of compound I (690 nm) is accentuated in A369P.

## 4. Conclusion

Decarboxylases from the CYP152 family of P450s are fascinating enzymes. Their ability to catalyze multiple chemistries on single substrates is remarkable. The biotechnological potential of these enzymes however, rely on their ability to completely funnel their chemistry into the decarboxylation process to produce suitable amounts of terminal olefins and only small amount of (undesirable) hydroxylated side-products. Although much progress has been made to understand the origin of this chemistry multiplicity, there is still many properties of the proteins that need to be deciphered. Although we have previously shown the importance of substrate positioning and protein conformational rearrangements on the decarboxylation process, we are still unable to understand how this protein is able to stabilize its catalytically relevant intermediates compound I and II. To this day, the ability to study the electronic properties of these intermediates has been hampered by the demanding conditions of the rapid-freeze quench process: high protein and substrate concentration. We approached the former in the previous chapter by identifying a more stable decarboxylase. In this chapter, we addressed the latter by altering the Kspin of $OleT_{SA}$ to favor the 5cHS accumulation. A change from an alanine to a proline induces a change in the geometry of the heme to a more saddled conformation, which, at its turn, is translated to a change in the spin-state of the protein allowing higher accumulation of the transient intermediates of $OleT_{SA}$. This study ultimately establishes a new platform for the study of the electronic properties of the ferryl species in decarboxylases of this family. Ongoing experiments include redox potential studies, activity assays and EPR/Mössbauer studies of the transient species. Further

examination of the effects of this mutation will provide a better understanding of the effects of heme conformation in P450s.

**5. References**


1. Danielson, P. B., The cytochrome P450 superfamily: biochemistry, evolution and drug metabolism in humans. *Curr. Drug Metab.* **2002,** *3* (6), 561-97.

2. Guengerich, F. P.; Munro, A. W., Unusual cytochrome p450 enzymes and reactions. *Journal of Biological Chemistry* **2013,** *288* (24), 17065-73.

3. Guengerich, F. P., Common and uncommon cytochrome P450 reactions related to metabolism and chemical toxicity. *Chem. Res. Toxicol.* **2001,** *14* (6), 611-50.

4. Wang, J. F.; Chou, K. C., Molecular modeling of cytochrome P450 and drug metabolism. *Curr. Drug Metab.* **2010,** *11* (4), 342-6.

5. Zimniak, P.; Waxman, D. J., Liver Cytochrome P450 Metabolism of Endogenous Steroid Hormones, Bile Acids, and Fatty Acids. In *Cytochrome P450*, Schenkman, J. B.; Greim, H., Eds. Springer Berlin Heidelberg: Berlin, Heidelberg, 1993; pp 123-144.

6. Hrycay, E.; Forrest, D.; Liu, L.; Wang, R.; Tai, J.; Deo, A.; Ling, V.; Bandiera, S., Hepatic bile acid metabolism and expression of cytochrome P450 and related enzymes are altered in Bsep (-/-) mice. *Mol. Cell. Biochem.* **2014,** *389* (1-2), 119-32.

7. Lorbek, G.; Lewinska, M.; Rozman, D., Cytochrome P450s in the synthesis of cholesterol and bile acids--from mouse models to human diseases. *The FEBS journal* **2012,** *279* (9), 1516-33.

8. Fujita, K., Cytochrome P450 and anticancer drugs. *Curr. Drug Metab.* **2006,** *7* (1), 23-37.

9. Peixoto, R. S.; Vermelho, A. B.; Rosado, A. S., Petroleum-Degrading Enzymes: Bioremediation and New Prospects. *Enzyme Research* **2011,** *2011*, 7.

10. Bonomo, S.; Jorgensen, F. S.; Olsen, L., Mechanism of Cytochrome P450 17A1-Catalyzed Hydroxylase and Lyase Reactions. *J. Chem. Inf. Comput. Sci.* **2017,** *57* (5), 1123-1133.

11. Mak, P. J.; Gregory, M. C.; Denisov, I. G.; Sligar, S. G.; Kincaid, J. R., Unveiling the crucial intermediates in androgen production. *Proceedings of the National Academy of Sciences* **2015,** *112* (52), 15856-15861.

12. Matthews, S.; Belcher, J. D.; Tee, K. L.; Girvan, H. M.; McLean, K. J.; Rigby, S. E.; Levy, C. W.; Leys, D.; Parker, D. A.; Blankley, R. T.; Munro, A. W., Catalytic Determinants of Alkene Production by the Cytochrome P450 Peroxygenase OleTJE. *Journal of Biological Chemistry* **2017,** *292* (12), 5128-5143.

13. Amaya, J. A.; Rutland, C. D.; Leschinsky, N.; Makris, T. M., A Distal Loop Controls Product Release and Chemo- and Regioselectivity in Cytochrome P450 Decarboxylases. *Biochemistry* **2018,** *57* (3), 344-353.

14. Amaya, J. A.; Rutland, C. D.; Makris, T. M., Mixed regiospecificity compromises alkene synthesis by a cytochrome P450 peroxygenase from Methylobacterium populi. *J. Inorg. Biochem.* **2016,** *158*, 11-16.

15. Hsieh, C. H.; Huang, X.; Amaya, J. A.; Rutland, C. D.; Keys, C. L.; Groves, J. T.; Austin, R. N.; Makris, T. M., The Enigmatic P450 Decarboxylase OleT Is Capable of, but Evolved To Frustrate, Oxygen Rebound Chemistry. *Biochemistry* **2017,** *56* (26), 3347-3357.

16. Matsunaga, I.; Sumimoto, T.; Ueda, A.; Kusunose, E.; Ichihara, K., Fatty acid-specific, regiospecific, and stereospecific hydroxylation by cytochrome P450 (CYP152B1) from Sphingomonas paucimobilis: substrate structure required for alpha-hydroxylation. *Lipids* **2000,** *35* (4), 365-71.

17. Matsunaga, I.; Ueda, A.; Fujiwara, N.; Sumimoto, T.; Ichihara, K., Characterization of the ybdT gene product of Bacillus subtilis: novel fatty acid beta-hydroxylating cytochrome P450. *Lipids* **1999,** *34* (8), 841-6.

18. Belcher, J.; McLean, K. J.; Matthews, S.; Woodward, L. S.; Fisher, K.; Rigby, S. E.; Nelson, D. R.; Potts, D.; Baynham, M. T.; Parker, D. A.; Leys, D.; Munro, A. W., Structure and biochemical properties of the alkene producing cytochrome P450 OleTJE (CYP152L1) from the Jeotgalicoccus sp. 8456 bacterium. *Journal of Biological Chemistry* **2014,** *289* (10), 6535-50.

19. Grant, J. L.; Hsieh, C. H.; Makris, T. M., Decarboxylation of fatty acids to terminal alkenes by cytochrome P450 compound I. *Journal of the American Chemical Society* **2015,** *137* (15), 4940-3.

20. Grant, J. L.; Mitchell, M. E.; Makris, T. M., Catalytic strategy for carbon-carbon bond scission by the cytochrome P450 OleT. *Proceedings of the National Academy of Sciences* **2016,** *113* (36), 10049-54.

21. Luthra, A.; Denisov, I. G.; Sligar, S. G., Spectroscopic features of cytochrome P450 reaction intermediates. *Arch. Biochem. Biophys.* **2011,** *507* (1), 26-35.

22. Berry, E. A.; Trumpower, B. L., Simultaneous determination of hemes a, b, and c from pyridine hemochrome spectra. *Anal. Biochem.* **1987,** *161* (1), 1-15.

23. Sligar, S. G., Coupling of spin, substrate, and redox equilibriums in cytochrome P450. *Biochemistry* **1976,** *15* (24), 5399-5406.

24. Otwinowski, Z.; Minor, W., [20] Processing of X-ray diffraction data collected in oscillation mode. In *Methods Enzymol.*, Academic Press: 1997; Vol. 276, pp 307-326.

25. McCoy, A. J.; Grosse-Kunstleve, R. W.; Adams, P. D.; Winn, M. D.; Storoni, L. C.; Read, R. J., Phaser crystallographic software. *J. Appl. Crystallogr.* **2007,** *40* (Pt 4), 658-674.

26. Emsley, P.; Lohkamp, B.; Scott, W. G.; Cowtan, K., Features and development of Coot. *Acta Crystallogr. Sect. D. Biol. Crystallogr.* **2010,** *66* (Pt 4), 486-501.

27. Shelnutt, J. A., Normal-coordinate structural decomposition and the vibronic spectra of porphyrins. *Journal of Porphyrins and Phthalocyanines* **2001,** *5* (3), 300-311.

28. Munro, A. W.; McLean, K. J.; Grant, J. L.; Makris, T. M., Structure and function of the cytochrome P450 peroxygenase enzymes. *Biochem. Soc. Trans.* **2018,** *46* (1), 183-196.

29. Bonifacio, A.; Groenhof, A. R.; Keizers, P. H.; de Graaf, C.; Commandeur, J. N.; Vermeulen, N. P.; Ehlers, A. W.; Lammertsma, K.; Gooijer, C.; van der Zwan, G., Altered spin state equilibrium in the T309V mutant of cytochrome P450 2D6: a spectroscopic and computational study. *J. Biol. Inorg. Chem.* **2007,** *12* (5), 645-54.

30. Iwasaki, M.; Juvonen, R.; Lindberg, R.; Negishi, M., Alteration of high and low spin equilibrium by a single mutation of amino acid 209 in mouse cytochromes P450. *Journal of Biological Chemistry* **1991,** *266* (6), 3380-2.

31. Krest, C. M.; Silakov, A.; Rittle, J.; Yosca, T. H.; Onderko, E. L.; Calixto, J. C.; Green, M. T., Significantly shorter Fe-S bond in cytochrome P450-I is consistent with greater reactivity relative to chloroperoxidase. *Nature chemistry* **2015,** *7* (9), 696-702.

32. Yang, Y.; Zhang, H.; Usharani, D.; Bu, W.; Im, S.; Tarasev, M.; Rwere, F.; Pearl, N. M.; Meagher, J.; Sun, C.; Stuckey, J.; Shaik, S.; Waskell, L., Structural and functional characterization of a cytochrome P450 2B4 F429H mutant with an axial thiolate-histidine hydrogen bond. *Biochemistry* **2014,** *53* (31), 5080-91.

33. Mancini, G.; Zazza, C., F429 Regulation of Tunnels in Cytochrome P450 2B4: A Top Down Study of Multiple Molecular Dynamics Simulations. *PloS one* **2015,** *10* (9), e0137075.

34. Jovanovic, T.; Farid, R.; Friesner, R. A.; McDermott, A. E., Thermal equilibrium of high- and low-spin forms of cytochrome P450 BM-3: repositioning of the substrate? *Journal of the American Chemical Society* **2005,** *127* (39), 13548-52.

35. George, P.; Beetlestone, J.; Griffith, J. S., Ferrihemoprotein Hydroxides: A Correlation Between Magnetic and Spectroscopic Properties. *Reviews of Modern Physics* **1964,** *36* (1), 441-458.

36. Andersson, L. A.; Johnson, A. K.; Peterson, J. A., Active site analysis of P450 enzymes: comparative magnetic circular dichroism spectroscopy. *Arch. Biochem. Biophys.* **1997,** *345* (1), 79-87.

37. Weber, C.; Michel, B.; Bosshard, H. R., Spectroscopic analysis of the cytochrome c oxidase-cytochrome c complex: circular dichroism and magnetic circular dichroism measurements reveal change of cytochrome c heme geometry imposed by complex formation. *Proceedings of the National Academy of Sciences* **1987,** *84* (19), 6687-6691.

38. Conner, K. P.; Schimpf, A. M.; Cruce, A. A.; McLean, K. J.; Munro, A. W.; Frank, D. J.; Krzyaniak, M. D.; Ortiz de Montellano, P.; Bowman, M. K.; Atkins, W. M., Strength of axial water ligation in substrate-free cytochrome P450s is isoform dependent. *Biochemistry* **2014,** *53* (9), 1428-34.

39. Galinato, M. G. I.; Spolitak, T.; Ballou, D. P.; Lehnert, N., Elucidating the Role of the Proximal Cysteine Hydrogen-Bonding Network in Ferric Cytochrome P450cam and Corresponding Mutants Using Magnetic Circular Dichroism Spectroscopy. *Biochemistry* **2011,** *50* (6), 1053-1069.

40. Davydov, R.; Im, S.; Shanmugam, M.; Gunderson, W. A.; Pearl, N. M.; Hoffman, B. M.; Waskell, L., Role of the Proximal Cysteine Hydrogen Bonding Interaction in Cytochrome P450 2B4 Studied by Cryoreduction, Electron Paramagnetic Resonance, and Electron-Nuclear Double Resonance Spectroscopy. *Biochemistry* **2016,** *55* (6), 869-83.

41. Mak, P. J.; Zhu, Q.; Kincaid, J. R., Using resonance Raman cross-section data to estimate the spin-state populations of cytochromes P450. *Journal of Raman Spectroscopy* **2013,** *44* (12), 1792-1794.

42. Marzocchi, M. P.; Smulevich, G., Relationship between heme vinyl conformation and the protein matrix in peroxidases. *Journal of Raman Spectroscopy* **2003,** *34* (10), 725-736.

43. Uno, T.; Nishimura, Y.; Makino, R.; Iizuka, T.; Ishimura, Y.; Tsuboi, M., The resonance Raman frequencies of the Fe-CO stretching and bending modes in the CO complex of cytochrome P-450cam. *Journal of Biological Chemistry* **1985,** *260* (4), 2023-6.

44. Jung, C.; Hoa, G. H.; Schroder, K. L.; Simon, M.; Doucet, J. P., Substrate analogue induced changes of the CO-stretching mode in the cytochrome P450cam-carbon monoxide complex. *Biochemistry* **1992,** *31* (51), 12855-62.

45. Fan, B.; Wang, J.; Stuehr, D. J.; Rousseau, D. L., NO synthase isozymes have distinct substrate binding sites. *Biochemistry* **1997,** *36* (42), 12660-5.

46. Wang, J.; Stuehr, D. J.; Rousseau, D. L., Interactions between substrate analogues and heme ligands in nitric oxide synthase. *Biochemistry* **1997,** *36* (15), 4595-606.

47. Li, D.; Stuehr, D. J.; Yeh, S.-R.; Rousseau, D. L., Heme Distortion Modulated by Ligand-Protein Interactions in Inducible Nitric-oxide Synthase. *Journal of Biological Chemistry* **2004,** *279* (25), 26489-26499.

48. Ma, J. G.; Zhang, J.; Franco, R.; Jia, S. L.; Moura, I.; Moura, J. J.; Kroneck, P. M.; Shelnutt, J. A., The structural origin of nonplanar heme distortions in tetraheme ferricytochromes c3. *Biochemistry* **1998,** *37* (36), 12431-42.

49. Olea, C., Jr.; Kuriyan, J.; Marletta, M. A., Modulating heme redox potential through protein-induced porphyrin distortion. *Journal of the American Chemical Society* **2010,** *132* (37), 12794-5.

50. Bikiel, D. E.; Forti, F.; Boechi, L.; Nardini, M.; Luque, F. J.; Martí, M. A.; Estrin, D. A., Role of Heme Distortion on Oxygen Affinity in Heme Proteins: The Protoglobin Case. *The Journal of Physical Chemistry B* **2010,** *114* (25), 8536-8543.

# APPENDIX A

## REPRINT PERMISSION FOR CHAPTERS I AND II